

AD 631777



DEUTSCHE FORSCHUNGSANSTALT
FÜR LUFT- UND RAUMFAHRT E.V.
INSTITUT FÜR FLUGMECHANIK
PROF. DR. H. BLENK

FINAL REPORT
PARACHUTE CANOPIES DURING INFLATION

H.-D. Melzig
P. K. Schmidt

code 1

CLEARINGHOUSE FOR FEDERAL SCIENTIFIC AND TECHNICAL INFORMATION			
Hardcopy	Microfiche		
\$ 4.00	\$ 1.00	137 pp	XX
ARCHIVE COPY			

PROCESSING COPY

DDC
RECEIVED
APR 27 1966
D

BRAUNSCHWEIG

September 1965

AF EOAR

September 1965

FINAL REPORT
PARACHUTE CANOPIES DURING INFLATION

H.-D. MELZIG
P. K. SCHMIDT

DEUTSCHE FORSCHUNGSANSTALT FÜR LUFT- UND RAUMFAHRT
INSTITUT FÜR FLÜGMECHANIK
BRAUNSCHWEIG, GERMANY

The research reported in this document has been sponsored by the
AERONAUTICAL SYSTEMS DIVISION, AFSC through the European Office,
Office of Aerospace Research, United States Air Force.

FOREWORD

This Technical Report was prepared by the Institut für Flugmechanik of the Deutsche Forschungsanstalt für Luft- und Raumfahrt e. V. (DFL) under USAF Contract Nr. AF 61(052)-681. The work was sponsored by the Air Force Flight Dynamics Laboratory, Research and Technology Division, AFSC, through the European Office, Office of Aerospace Research, USAF. The work was administered by the European Office, Office of Aerospace Research, USAF, in Brussels, Belgium, Major W. C. Whicher and Major W. T. Campbell, Contracting Officers, and was directed technically by the Recovery and Crew Station Branch, AF Flight Dynamics Laboratory, RTD, AFSC, Mr. R. J. Berndt, Project Engineer.

The research effort was initiated in April 1963 and completed in April 1965, and was conducted under Project Nr. 6065 "Performance and Design of Deployable Aerodynamic Decelerators", and Task Nr. 606503, "Parachute Aerodynamics and Structures."

The manuscript was released by the authors in September 1965 for publication.

ABSTRACT

An experimental investigation and correlative analysis were conducted to determine the pressure distribution over the surface of parachute canopies during the period of inflation for the infinite mass case and to correlate pressure coefficients with inflating canopy shapes. Parachute canopy models of Circular Flat, 10% Extended Skirt, Ringslot, and Ribbon designs were tested under infinite mass conditions in a 9 x 12 ft low speed wind tunnel. External and internal pressure values were measured at various locations over the surface of the model canopies throughout the period of inflation, and generalized canopy profile shapes were obtained by means of photographic analysis.

Pressure coefficients derived for the steady state (fully open canopy) are quite comparable to the results of previous measurements. Peak pressure values during the unsteady period of inflation were found to be up to 5 times as great as steady state values.

The relationships between the pressure distribution and time for each of the canopy models deployed at free-stream velocities between 70 and 160 ft/sec are presented in detail and correlated with changing canopy shape. A complete shape analysis is made and a mathematical model is proposed.

T A B L E O F C O N T E N T S

<u>Section</u>	<u>Page</u>
1. Introduction	1
2. Test Conditions	2
A. Parachute Models	2
B. Test Facilities and Test Method	3
C. Test Procedure	7
3. Results and Analysis	8
A. Canopy Pressure Distribution	9
B. Canopy Shape Analysis	70
4. Summary and Recommendations	98
5. References	99
Appendixes	
I. Parachute Canopy Models	100
II. Comparative Pressure Coefficient Versus Time Relationships (plottings and original recordings)	115
III. Pressure Distribution on Gore Center Line	121

ILLUSTRATIONS

<u>Figure No</u>	<u>Page</u>
1. Test arrangement in the windtunnel	4
2. Pressure transducer	5
3. Error in % of 0.3 psi output versus g-loading for the 3 axes of attack	5
4. Frequency response of pressure transducer	6
5. Linearity and calibration of pressure transducer . .	6
6. Reproducibility of experiments	10
7. c_{pd} and filling versus time, Circular Flat, $v_o = 70$ ft/sec	16
8. c_{pi} and filling versus time, Circular Flat, $v_o = 70$ ft/sec	17
9. c_{pe} and filling versus time, Circular Flat, $v_o = 70$ ft/sec	18
10. c_{pd} and filling versus time, Circular Flat, $v_o = 100$ ft/sec	19
11. c_{pi} and filling versus time, Circular Flat, $v_o = 100$ ft/sec	20
12. c_{pe} and filling versus time, Circular Flat, $v_o = 100$ ft/sec	21
13. c_{pd} and filling versus time, Circular Flat, $v_o = 130$ ft/sec	22
14. c_{pi} and filling versus time, Circular Flat, $v_o = 130$ ft/sec	23

ILLUSTRATIONS (cont.)

<u>Figure No.</u>		<u>Page</u>
15.	c_{pe} and filling versus time, Circular Flat, $v_o = 130$ ft/sec	24
16.	c_{pd} and filling versus time, Circular Flat, $v_o = 160$ ft/sec	25
17.	c_{pd} and filling versus time, Extended Skirt, $v_o = 70$ ft/sec	26
18.	c_{pi} and filling versus time, Extended Skirt, $v_o = 70$ ft/sec	27
19.	c_{pe} and filling versus time, Extended Skirt, $v_o = 70$ ft/sec	28
20.	c_{pd} and filling versus time, Extended Skirt, $v_o = 100$ ft/sec	29
21.	c_{pi} and filling versus time, Extended Skirt, $v_o = 100$ ft/sec	30
22.	c_{pe} and filling versus time, Extended Skirt, $v_o = 100$ ft/sec	31
23.	c_{pd} and filling versus time, Extended Skirt, $v_o = 130$ ft/sec	32
24.	c_{pi} and filling versus time, Extended Skirt, $v_o = 130$ ft/sec	33
25.	c_{pe} and filling versus time, Extended Skirt, $v_o = 130$ ft/sec	34
26.	c_{pd} and filling versus time, Extended Skirt, $v_o = 160$ ft/sec	35
27.	c_{pi} and filling versus time, Extended Skirt, $v_o = 160$ ft/sec	36
28.	c_{pe} and filling versus time, Extended Skirt, $v_o = 160$ ft/sec	37

ILLUSTRATIONS (cont.)

<u>Figure No</u>		<u>Page</u>
29.	c_{pd} and filling versus time, FIST, $v_o = 70$ ft/sec	38
30.	c_{pi} and filling versus time, FIST, $v_o = 70$ ft/sec	39
31.	c_{pe} and filling versus time, FIST, $v_o = 70$ ft/sec	40
32.	c_{pd} and filling versus time, FIST, $v_o = 100$ ft/sec	41
33.	c_{pi} and filling versus time, FIST, $v_o = 100$ ft/sec	42
34.	c_{pe} and filling versus time, FIST, $v_o = 100$ ft/sec	43
35.	c_{pd} and filling versus time, FIST, $v_o = 130$ ft/sec	44
36.	c_{pi} and filling versus time, FIST, $v_o = 130$ ft/sec	45
37.	c_{pe} and filling versus time, FIST, $v_o = 130$ ft/sec	46
38.	c_{pd} and filling versus time, FIST, $v_o = 160$ ft/sec	47
39.	c_{pi} and filling versus time, FIST, $v_o = 160$ ft/sec	48
40.	c_{pe} and filling versus time, FIST, $v_o = 160$ ft/sec	49
41.	c_{pd} and filling versus time, Ringslot, $v_o = 70$ ft/sec	50
42.	c_{pi} and filling versus time, Ringslot, $v_o = 70$ ft/sec	51
43.	c_{pe} and filling versus time, Ringslot, $v_o = 70$ ft/sec	52
44.	c_{pd} and filling versus time, Ringslot, $v_o = 100$ ft/sec	53
45.	c_{pi} and filling versus time, Ringslot, $v_o = 100$ ft/sec	54
46.	c_{pe} and filling versus time, Ringslot, $v_o = 100$ ft/sec	55
47.	c_{pd} and filling versus time, Ringslot, $v_o = 130$ ft/sec	56
48.	c_{pi} and filling versus time, Ringslot, $v_o = 130$ ft/sec	57
49.	c_{pe} and filling versus time, Ringslot, $v_o = 130$ ft/sec	58
50.	c_{pd} and filling versus time, Ringslot, $v_o = 160$ ft/sec	59
51.	c_{pi} and filling versus time, Ringslot, $v_o = 160$ ft/sec	60
52.	c_{pe} and filling versus time, Ringslot, $v_o = 160$ ft/sec	61

ILLUSTRATIONS (cont.)

<u>Figure No</u>	<u>Page</u>
53. c_p versus D_p/D_o for Circular Flat, $v_o = 70$ and 100 ft/sec	62
54. c_p versus D_p/D_o for Circular Flat, $v_o = 130$ and 160 ft/sec	63
55. c_p versus D_p/D_o for Extended Skirt, $v_o = 70$ and 100 ft/sec	64
56. c_p versus D_p/D_o for Extended Skirt, $v_o = 130$ and 160 ft/sec	65
57. c_p versus D_p/D_o for FIST, $v_o = 70$ and 100 ft/sec	66
58. c_p versus D_p/D_o for FIST, $v_o = 130$ and 160 ft/sec	67
59. c_p versus D_p/D_o for Ringslot, $v_o = 70$ and 100 ft/sec	68
60. c_p versus D_p/D_o for Ringslot, $v_o = 130$ and 160 ft/sec	69
61. Photographic Shape, phase I for Circular Flat	75
62. Photographic Shape, phase II for Circular Flat . . .	76
63. Idealized Photographic Shape symbols	77
64. Parameters of Idealized Photographic Shape versus time for Circular Flat, $v_o = 70$ ft/sec	78
65. Parameters of Idealized Photographic Shape versus time for Circular Flat, $v_o = 100$ ft/sec	79
66. Parameters of Idealized Photographic Shape versus time for Circular Flat, $v_o = 130$ ft/sec	80
67. Parameters of Idealized Photographic Shape versus time for Circular Flat, $v_o = 160$ ft/sec	81
68. Parameters of Idealized Photographic Shape versus time for Extended Skirt, $v_o = 70$ ft/sec	82
69. Parameters of Idealized Photographic Shape versus time for Extended Skirt, $v_o = 100$ ft/sec	83

ILLUSTRATIONS (cont.)

<u>Figure No</u>		<u>Page</u>
70.	Parameters of Idealized Photographic Shape versus time for Extended Skirt, $v_0 = 130$ ft/sec	84
71.	Parameters of Idealized Photographic Shape versus time for Extended Skirt, $v_0 = 160$ ft/sec	85
72.	Parameters of Idealized Photographic Shape versus time for FIST, $v_0 = 70$ ft/sec	86
73.	Parameters of Idealized Photographic Shape versus time for FIST, $v_0 = 100$ ft/sec	87
74.	Parameters of Idealized Photographic Shape versus time for FIST, $v_0 = 130$ ft/sec	88
75.	Parameters of Idealized Photographic Shape versus time for FIST, $v_0 = 160$ ft/sec	89
76.	Parameters of Idealized Photographic Shape versus time for Ringslot, $v_0 = 70$ ft/sec	90
77.	Parameters of Idealized Photographic Shape versus time for Ringslot, $v_0 = 100$ ft/sec	91
78.	Parameters of Idealized Photographic Shape versus time for Ringslot, $v_0 = 130$ ft/sec	92
79.	Parameters of Idealized Photographic Shape versus time for Ringslot, $v_0 = 160$ ft/sec	93
80.	Parameters of Idealized Photographic Shape versus time for Circular Flat, $v_0 = 70, 100, 130$ and 160 ft/sec	94
81.	Parameters of Idealized Photographic Shape versus time for Extended Skirt, $v_0 = 70, 100, 130$ and 160 ft/sec	95
82.	Parameters of Idealized Photographic Shape versus time for FIST, $v_0 = 70, 100, 130$ and 160 ft/sec . .	96

ILLUSTRATIONS (cont.)

<u>Figure No</u>	<u>Page</u>
83. Parameters of Idealized Photographic Shape versus time for Ringslot, $v_0 = 70, 100, 130$ and 160 ft/sec	97
84. 53.5" model of a Circular Flat parachute	101
85. 62.0" model of a 10 % Extended Skirt parachute . . .	102
86. 53.5" model of a Circular Flat FIST parachute . . .	103
87. 53.5" model of a Ringslot parachute	104
88. c_p versus time for differential, internal and external pressure, Circular Flat, $v_0 = 70$ ft/sec	106
89. c_p versus time for differential, internal and external pressure, Circular Flat, $v_0 = 100$ ft/sec	107
90. c_p versus time for differential, internal and external pressure, Circular Flat, $v_0 = 130$ ft/sec	108
91. c_p versus time for differential, internal and external pressure, Extended Skirt, $v_0 = 70$ ft/sec	109
92. c_p versus time for differential, internal and external pressure, Extended Skirt, $v_0 = 100$ ft/sec	110
93. c_p versus time for differential, internal and external pressure, Extended Skirt, $v_0 = 130$ ft/sec	111
94. c_p versus time for differential, internal and external pressure, Extended Skirt, $v_0 = 160$ ft/sec	112
95. c_p versus time for differential, internal and external pressure, FIST, $v_0 = 70$ ft/sec	113
96. c_p versus time for differential, internal and external pressure, FIST, $v_0 = 100$ ft/sec	114
97. c_p versus time for differential, internal and external pressure, FIST, $v_0 = 130$ ft/sec	115
98. c_p versus time for differential, internal and external pressure, FIST, $v_0 = 160$ ft/sec	116

ILLUSTRATIONS (cont.)

<u>Figure No</u>	<u>Page</u>
99. c_p versus time for differential, internal and external pressure, Ringslot, $v_o = 70$ ft/sec	117
100. c_p versus time for differential, internal and external pressure, Ringslot, $v_o = 100$ ft/sec	108
101. c_p versus time for differential, internal and external pressure, Ringslot, $v_o = 130$ ft/sec	109
102. c_p versus time for differential, internal and external pressure, Ringslot, $v_o = 160$ ft/sec	120
103. c_{pd} and filling versus time, Ringslot, $v_o = 100$ ft/sec .	122
104. c_{pd} and filling versus time, Ringslot, $v_o = 100$ ft/sec	123
105. c_{pd} and filling versus time, Ringslot, $v_o = 100$ ft/sec	124

T A B L E S

<u>Table</u>	<u>Page</u>
1. Peak and steady state values for c_p and D_p and corresponding times	14
2. Approximations to the 4th power for phase II	73

1. INTRODUCTION

Minimum weight and packing volume are basic requirements for parachute canopies for any application. To meet these requirements, knowledge of the stress distribution in the canopy is a prerequisite for the parachute designer. This applies in particular to the period of transient force generation, the parachute filling or opening process. In order to accomplish a valid determination of the canopy stress distribution and since attempts to measure the actual stresses in parachute canopies during the transient state have not been successful, the pressure distribution over the surface of an inflating parachute canopy must be known to yield a basis for the calculation. In addition, the shape and shape changes which a parachute canopy undergoes during the period of inflation must be known so that the calculation procedure may be generalized.

For the steady state condition, that is for the fully inflated parachute canopy, the calculation of stresses in the canopy has been attempted by Jones [1] and by Topping et al [2]. Only recently, an approach was developed by Heinrich and Jamison [3] to predict the canopy stress distribution for the transient state. Although this calculation approach considers synthesized canopy profile shapes through which the canopy evolves during the period of inflation, pressure coefficients were based upon results obtained during steady state measurements on these synthesized canopy shapes.

A great difficulty for all steady state considerations is that maximum stresses occur during the rapidly occurring canopy shape changes of the filling process, and pressure and stress values can vastly exceed steady state values.

A number of attempts have been made in the past to measure the actual pressure versus time relationships during the process of inflation. These attempts, however, have been unsuccessful primarily due to the non-availability of a pressure sensing method or device which would yield accurate results under the acceleration levels encountered

during canopy inflation.

By means of a specially developed pressure transducer it has now become possible to measure pressure values at various locations on the canopy. In addition, an analysis was made of the changing canopy shape and related to the changing pressure distribution. The experimental investigation and correlative analysis were conducted for the case of parachute opening under infinite mass conditions, the case where there is no or only a relatively small velocity decay during the period of canopy inflation. Although the results of this investigation do not apply to all cases of parachute application, they do represent a major step towards a better knowledge of the parachute opening dynamics.

2. TEST CONDITIONS

A. Parachute Canopy Models

The investigation was performed on parachute canopy models of 4 basic types or design:

1. Solid cloth, circular flat type
2. Solid cloth, 10% flat extended type
3. Ringslot type
4. Flat circular ribbon (FIST) type

The solid cloth, circular flat type canopy model was based upon the design of the personnel type (C-9) canopy, incorporated 28 gores, and had a nominal diameter (D_0) of 53.5 inches.

The design of the solid cloth, 10% flat extended skirt type canopy model was based upon that of the troop type (T-10) canopy. The model incorporated 30 gores and had a nominal diameter (D_0) of 62.0 inches.

The ringslot and flat circular ribbon (FIST) type canopy models were fabricated of 24 gores with a geometric porosity of 16% for the ringslot and 18% for the flat circular (FIST) types. The ringslot type canopy model was constructed of 5 cloth rings and 1 vertical tape in each gore, the FIST type canopy model was constructed with 27 horizontal ribbons and 4 vertical tapes in each gore. These models had a nominal diameter (D_0) of 53.5 inches.

The cloth used in the fabrication of the canopy models met the German Kennblatt 1004 (Perlon; nominal cloth permeability at 1/2 inch H₂O: 130 cfm/ft²; weight: 1.45 oz/yd²).

Drawings of the four models are included in Appendix I.

B. Test Facilities and Test Method

All experimental investigations were performed in the 9 x 12 ft low speed wind tunnel of the Deutsche Forschungsanstalt für Luft- und Raumfahrt e.V. (DFL) in Braunschweig.

A schematic presentation of the test arrangement is shown in Figure 1. The canopy models were mounted in the wind tunnel test section in a stretched-out position, but prevented from inflating by two leather clamps, one enclosing the skirt and the other enclosing the middle section of the canopy. The wind tunnel was then brought up to specific speeds (70, 100, 130 and 160 ft/sec) and the clamps were suddenly released by burning a thin wire and by the action of springs attached to the clamps. Upon release of the clamps, the canopy models were free to inflate.

The distribution of the local pressure (internal, external and differential) over the canopy model from skirt to vent was measured by strain gage type pressure transducers attached to the canopy surface at specific locations. The pressure transducers were developed by the Deutsche Forschungsanstalt für Luft- und Raumfahrt. A view of the pressure transducer is shown in Figure 2. The physical specifications of the sensing element are: weight 0.2 oz, diameter 1.2 inches, thickness 0.35 inches, capacity ± 0.5 psi.

Each sensing element is temperature and acceleration compensated. Errors in per cent of output under applied pressures of 0.3 psi as a function of g-loadings applied statically in three mutually perpendicular planes are shown in Figure 3. The influence of accelerations up to 200 g's is below 3% of the full scale output of the transducer.

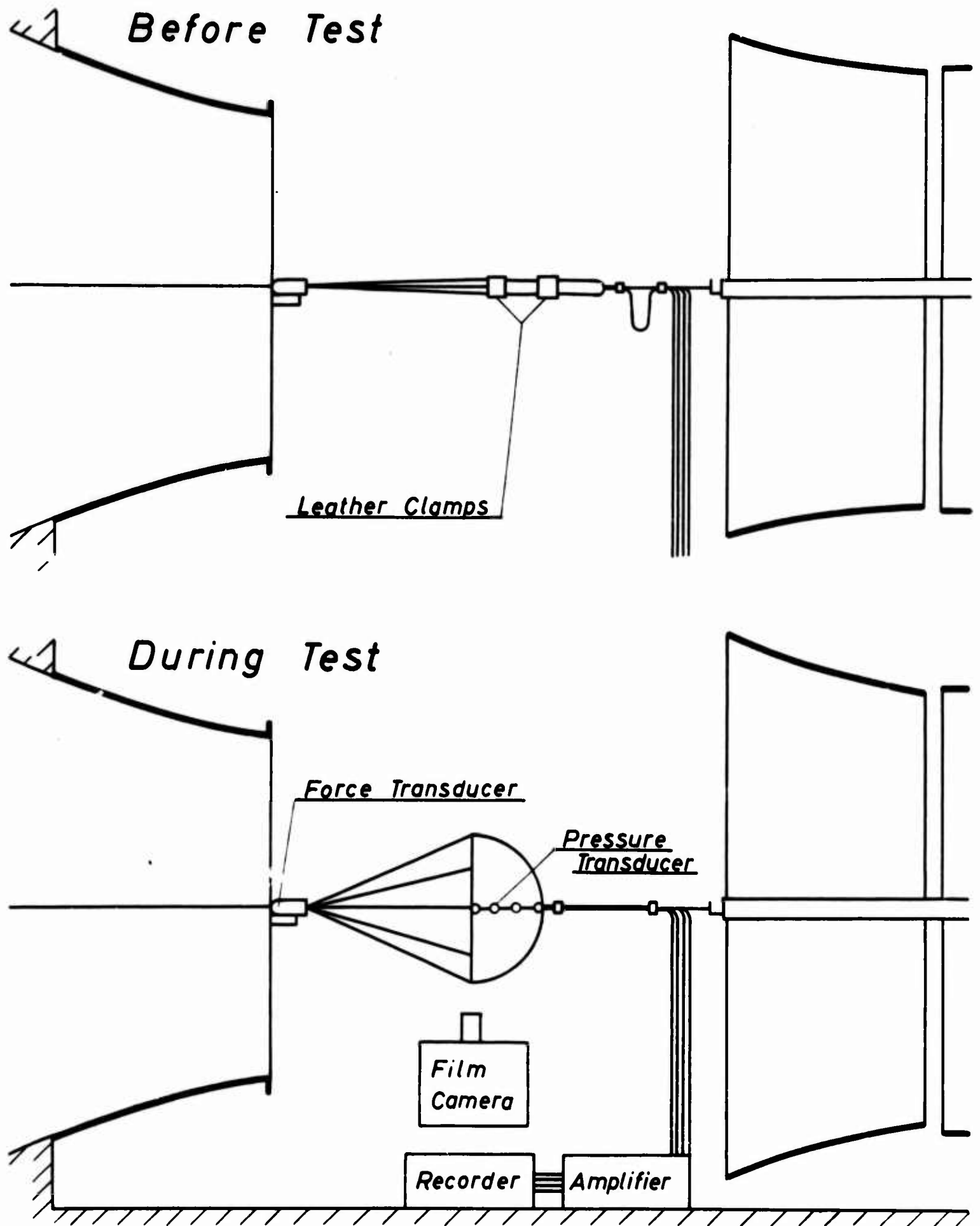


Figure 1 Test Arrangement in the Windtunnel

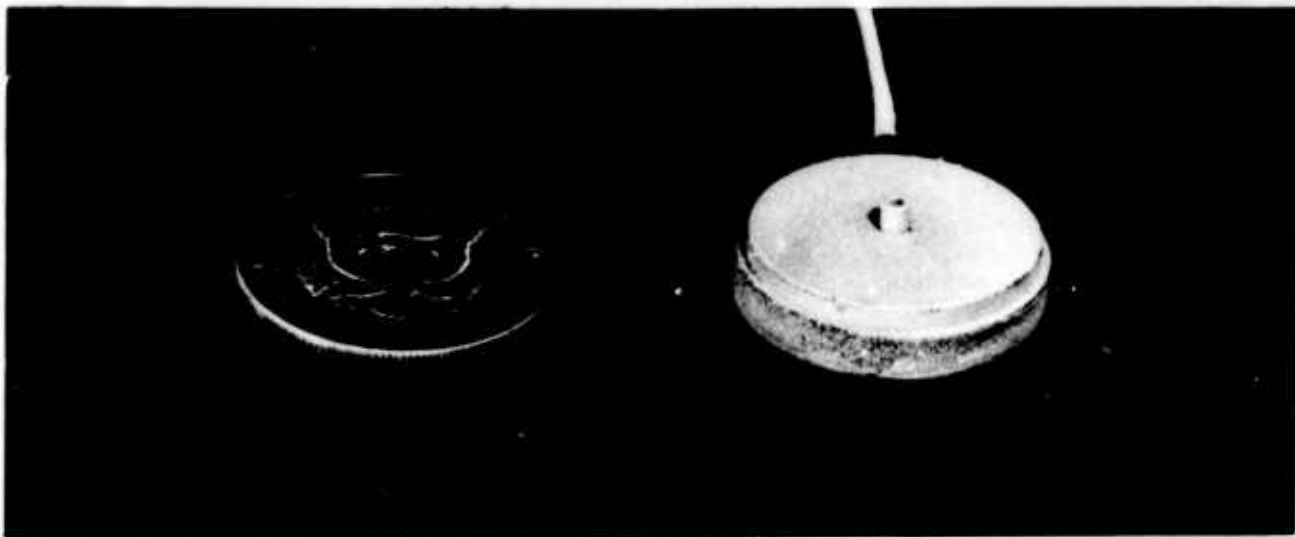


Figure 2 Pressure Transducer

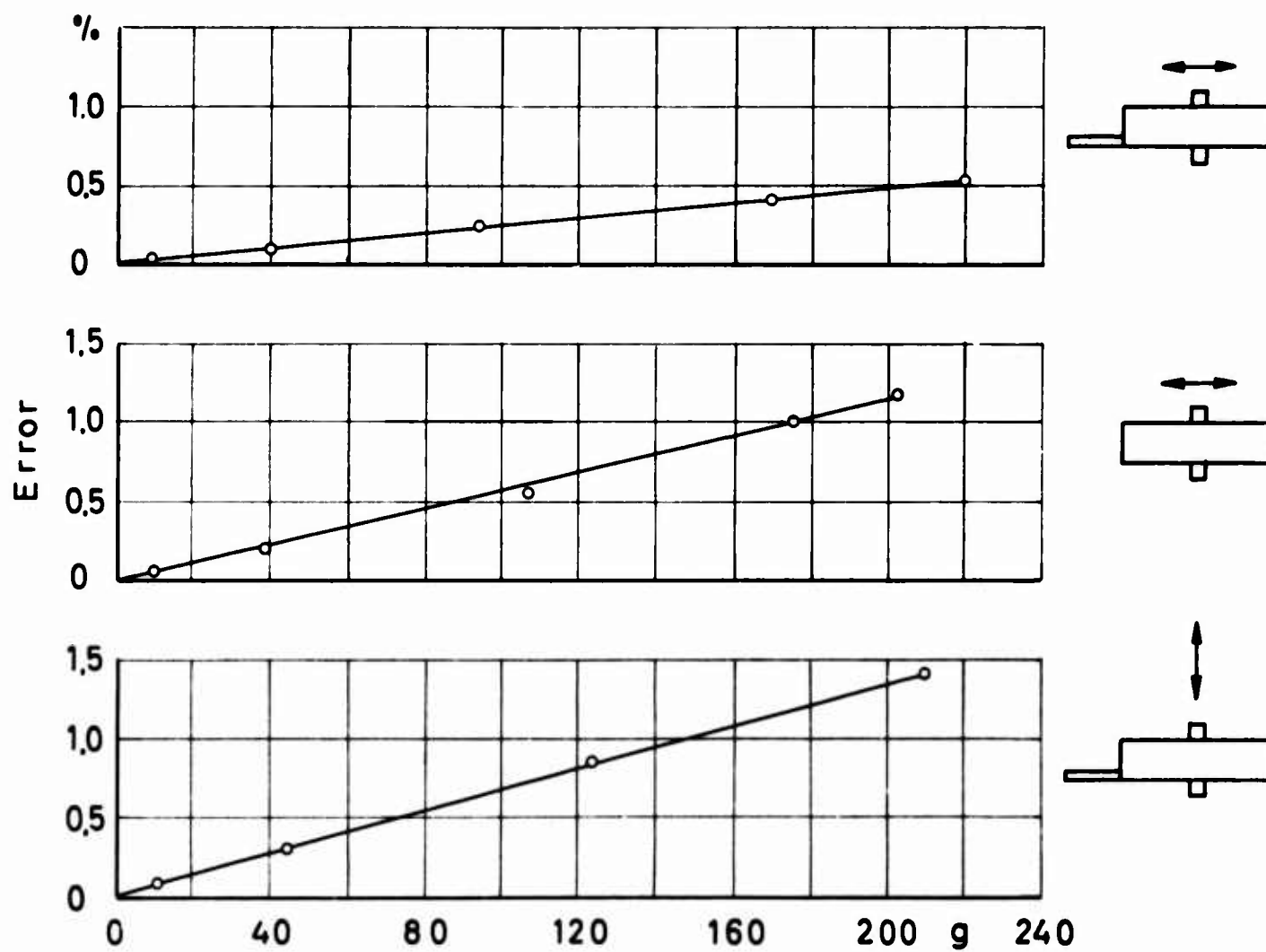


Figure 3 Error in % of 0.3 psi Output Versus g-Loading for the 3 Axes of Attack

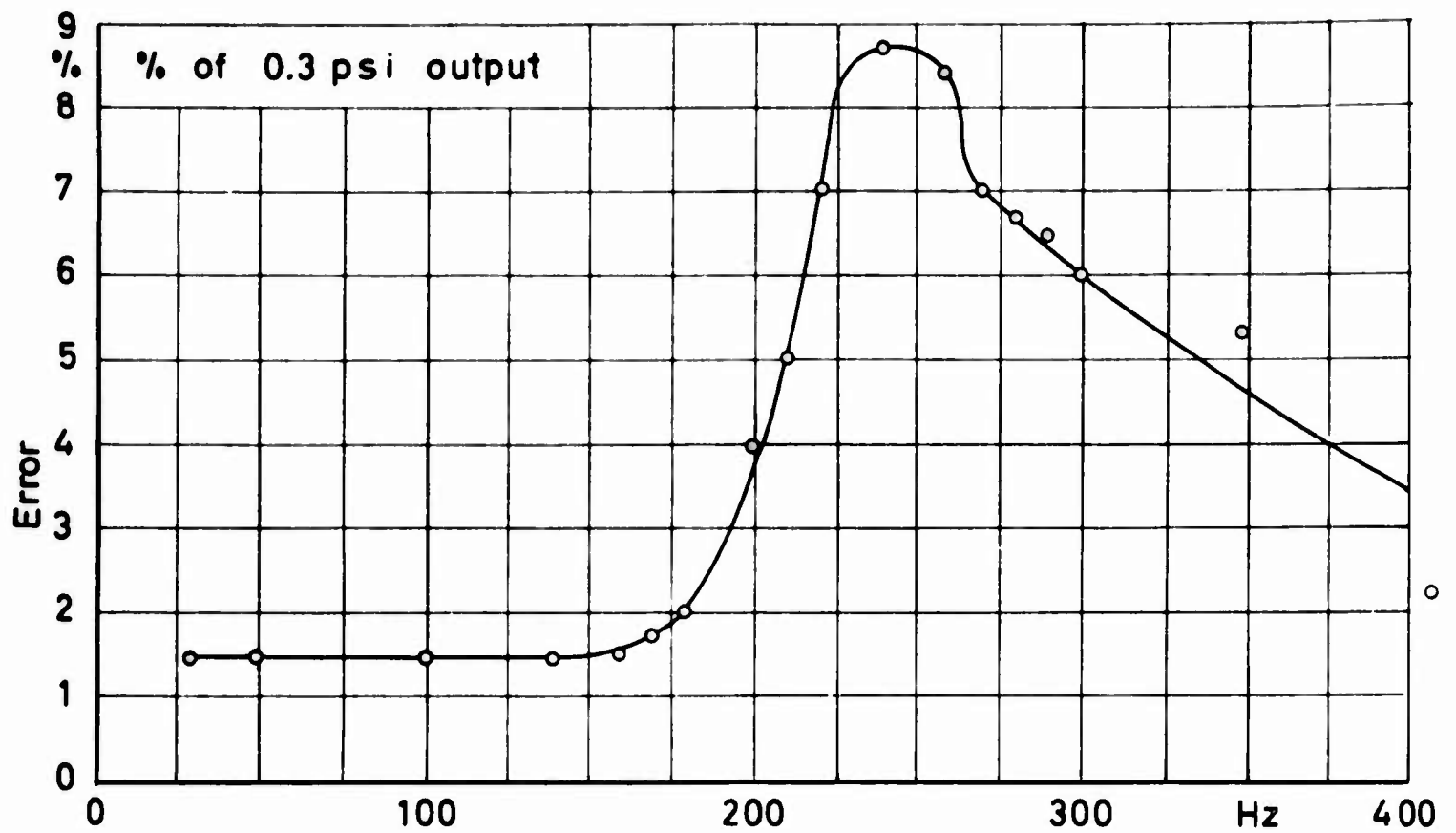


Figure 4 Frequency Response of Pressure Transducer

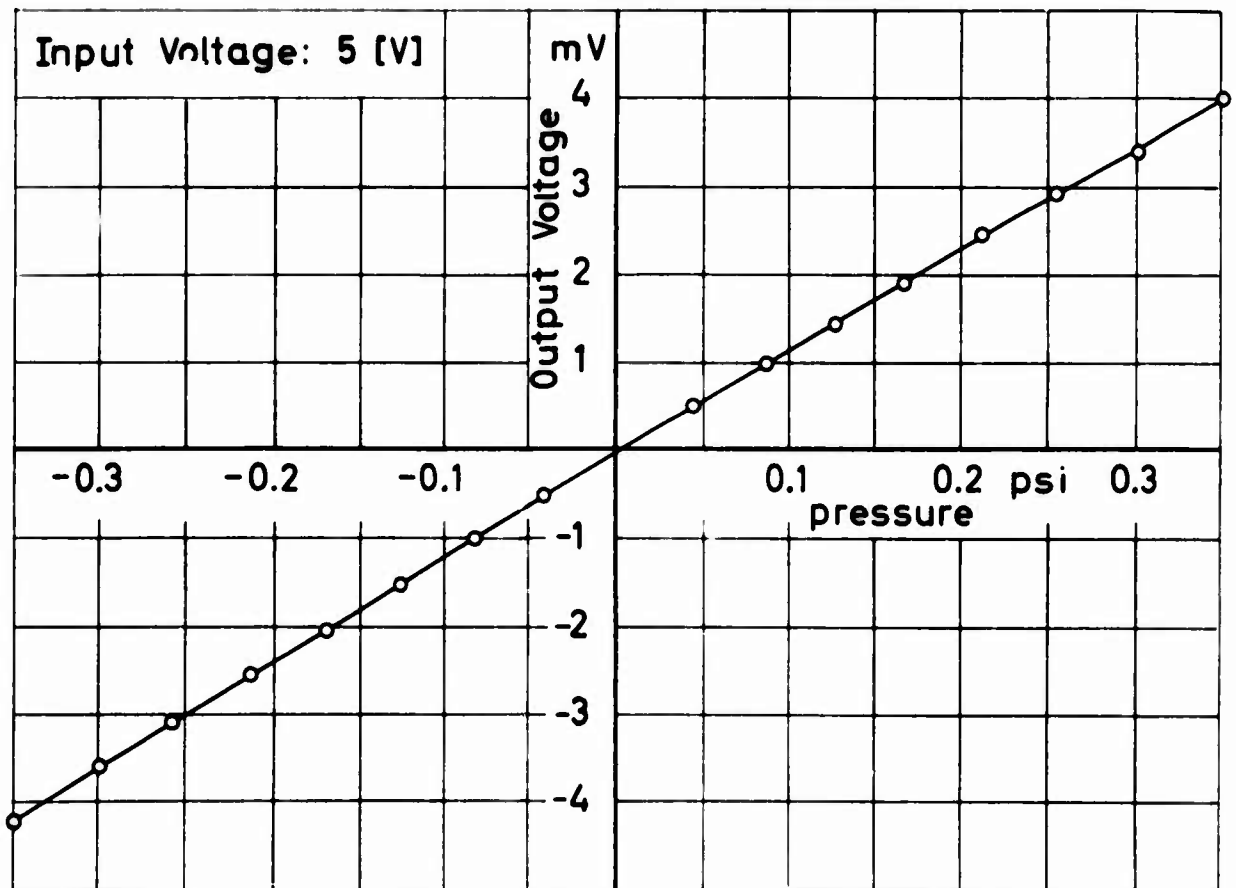


Figure 5 Linearity and Calibration of Pressure Transducer

Since accelerations experienced on the parachute canopy during inflation are not static but dynamic, that is portions of the cloth surface may move or oscillate with frequencies up to 100 cps, the frequency response of the transducer must be considered in order to determine the total introduced error under dynamic conditions. As indicated in Figure 4, the point of resonance of the transducer is approximately 250 cps with a maximum error of 9 % of the total output at an applied pressure of 0.3 psi. Up to an applied frequency of 170 cps, this error is only 1.5 %. Output voltage and linearity of the pressure transducer over a range of applied pressures are shown in Figure 5.

In addition to the pressure values, the forces generated by the parachute canopy were also recorded as measured by a strain gage type tensiometer. Hottinger carrier systems were used for the electronic measurements and the resulting signals recorded on a light-beam oscillograph Honeywell Visicorder.

C. Test Procedure

A total of four pressure transducers were located along the cord center lines of the canopies and distributed 90 degrees apart around the surface of the canopies because of weight influences. In addition, the location of the transducers was staggered in a manner shown in Figures 7 through 52 to obtain pressure measurements near the skirt, near the vent, and at two intermediate positions on the canopy. Additional measurements were made for comparative purposes with the transducers located along the gore center line (Figures 103 thru 105).

The complete filling process was photographed from one side by a high speed camera with 100 frames per second. From the photographic record, canopy profile shapes and projected canopy diameter values were obtained.

At the time of removal of the clamps setting the canopy free to inflate (time $t = 0$), a time base signal of 50 cps was initiated

and recorded on both the oscillogram and the photographic film for synchronization purposes.

The internal, external, and differential pressure values were measured and recorded during different runs. For the measurements of the internal and external pressures, the barometric pressure was conducted by tubings to the outer and inner pressure taps of the transducer, respectively.

A total of four separate measurements were made for each condition in order to determine the repeatability of the measurements and obtain valid average data. Thus, four equal test runs for each of the four canopy types at four different speeds to obtain three different pressure (differential, internal, external) versus time relationships were performed for a total of 192 wind tunnel test runs.

In order to obtain background data on the acceleration distribution over the parachute canopies during the period of inflation, acceleration measurements were performed on each of the four canopy types for each of the four deployment speed conditions. For this purpose, miniature strain gage type accelerometers of approximately the same size and weight as those of the pressure transducers were located at the same points on the canopies where pressure measurements were taken. Maximum values were measured on the solid cloth flat circular type canopy models at a location near the canopy skirt which at the largest deployment speed (160 ft/sec) is accelerated at the beginning of inflation at approximately 50 g's and decelerated at the end of inflation at approximately 200 g's.

3. RESULTS AND ANALYSIS

The two major objectives of the program were:

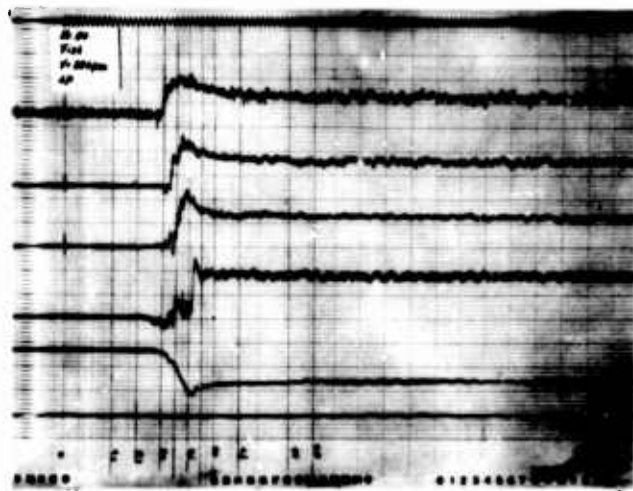
1. To determine the characteristic relationships between the pressure and time for each of the four canopy types,
2. To correlate the pressure values and canopy shape at any point during canopy inflation.

In addition, a detailed analysis of the canopy shape development for the period of canopy inflation under infinite mass operating conditions was to be attempted.

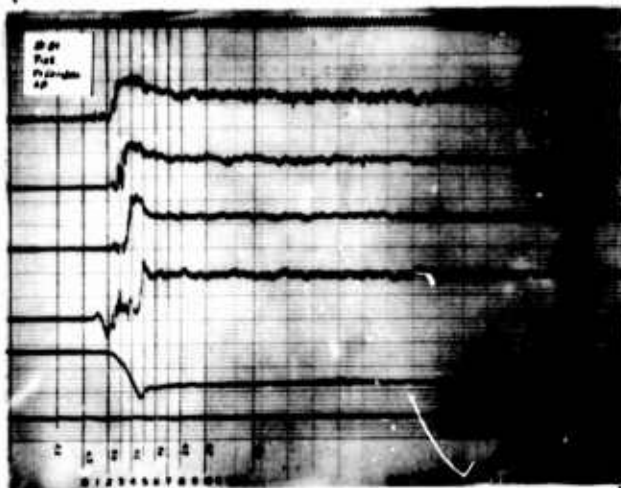
A. Canopy Pressure Distribution

Reproductions of actual oscillograph records obtained from the tests are shown in Figure 6. These records represent the registration obtained on a flat circular ribbon type (FIST) canopy during four different test runs conducted at the same deployment condition of 130 ft/sec. Analyzing these registrations, two general statements may be made:

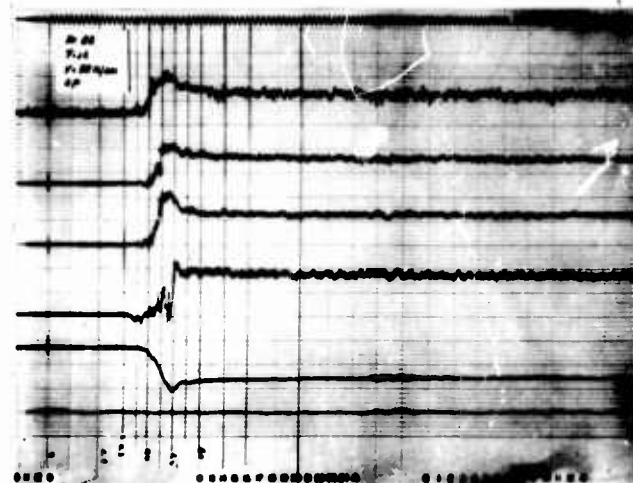
1. The reproducibility of the four measurements made at any one test condition was relatively good. This applies in particular to the solid cloth type canopies. Therefore, since no significant deviations occurred the results of only one measurement for each canopy type and deployment condition are included in this report.
2. As the original recordings illustrate, the pressures fluctuated during the steady state period (canopy fully inflated) due to flow conditions. During the unsteady period (canopy inflation), some fluctuations can occur due to the unsteady movement of the canopy material, in particular in the skirt area; however the mean values show increasing pressures with a more or less prominent peak. The determination of mean steady state values was sometimes difficult due to fluctuations in the pressure values and since actual steady state conditions were not reached immediately after canopy inflation, but several seconds later. To avoid cable breakage and other damages to the test set-up, especially at the high deployment velocity, the wind tunnel was shut down immediately after canopy filling was completed. To obtain more accurate steady state values, readings should be taken for at least five seconds during the steady state period. In general, however, the steady state values obtained are quite comparable to the results of former measurements [4] .



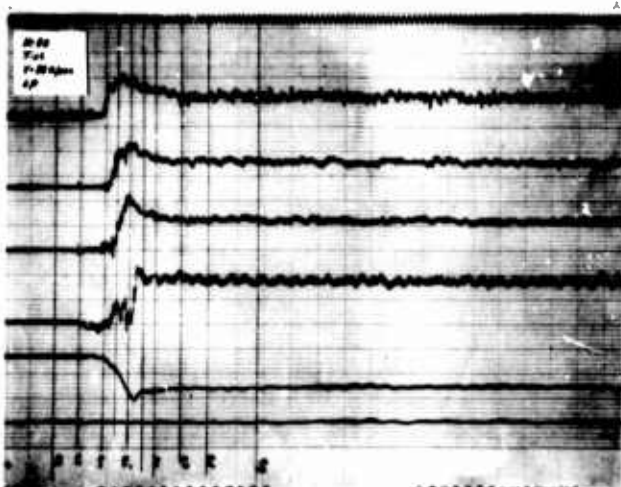
Run No.
80



81



82



83

Figure 6
Reproducibility of experiments.
Original registrations of
4 different runs under the
same initial condition of
 $v_0 = 130$ ft/sec for FIST.

The local pressures measured on the surface of the canopies were differential pressures, Δp , since atmospheric pressure was conducted by tubing to one of the ports of the pressure transducers. For open test section wind tunnels, the atmospheric pressure can be assumed to be equal to the static pressure of the airflow. The pressure values measured are expressed in coefficient form by relating these to the dynamic pressure of the airflow. Thus

$$c_p = \frac{\Delta p}{q}.$$

As mentioned above, the differential, internal, and external pressure distributions were measured. For each of the canopy types and test conditions, the differential, internal, and external pressure coefficients (c_{pd} , c_{pi} , and c_{pe}) for the four locations on the canopy were generalized (smoothed) and are plotted as a function of time in Figures 7 thru 52. In order to correlate pressure values to canopy shape, the instantaneous projected canopy diameter, D_p , was evaluated from the photographic recordings. Therefore, the relationship between projected canopy diameter ratio, D_p/D_o , as a function of time is shown also for each test run. A presentation of all three pressure coefficient (c_{pd} , c_{pi} , c_{pe}) versus time relationships for each test condition together with reproductions of the original oscillograph recordings is included in Appendix II.

In general, the pressure peak occurs first in the canopy vent area and travels very rapidly towards the skirt area. The pressure peaks occur slightly prior to the time at which the canopy reaches its fully inflated shape for the first time. For the solid cloth type canopy models, the pressure peaks from vent to skirt follow very rapidly one another, being separated in time only approximately 1/100 of a second. The last peak in the skirt area occurs at almost exactly the time at which the canopy is fully inflated. For the geometric porosity type canopies, the peak separation time is somewhat greater, for the FIST type canopy approximately 5/100 to 1/10 of a second, for the ringslot type canopy 1/10 of a second or more. The last peak in

the area of the canopy skirt is again close to but before the fully inflated projected canopy diameter is reached for the first time.

Aside from the determination of pressure versus time relationships and pressure distributions, the determination of the magnitude of the pressure peaks is a significant result of this program. For comparative purposes, a pressure factor, F_p , can be defined which is the ratio between the maximum value of the pressure coefficient, c_{pmax} , and the value of the steady state pressure coefficient, c_{pst} , or

$$F_p = \frac{c_{pmax}}{c_{pst}}$$

A compilation of all maximum and steady state pressure coefficient values (c_{pmax} and c_{pst}) at the four locations on the four canopy types, the time increment between occurrence of pressure peaks in the areas of canopy vent and skirt, and the time at which the fully inflated projected canopy diameter, D_p , is reached for the first time is given in Table I for each of the four deployment speed conditions, v_o .

The steady state pressure coefficients, c_{pst} , in the area of the canopy skirt are approximately 1.0 for the internal and -0.7 for the external pressures, resulting in a differential pressure coefficient of 1.7. This is true for the extended skirt, FIST, and ringslot type canopies. These values are comparable to the results obtained by Heinrich [4]. For the circular flat type canopy steady state pressure coefficients of up to 1.5 for the internal, -1.0 for the external, and 2.5 for the differential pressures were obtained. These values are high and there is a wide variation of all values acquired on this canopy type. More tests appear to be necessary to verify the findings.

On the circular flat type canopy, peak differential pressures during inflation reached approximately three times the steady values at full canopy inflation. In one test, a pressure factor of 5.4 was even

obtained at a location near the canopy skirt. At the higher deployment velocities of 130 and 160 ft/sec, the pressure factor decreased slightly due to the slightly lower peak pressure coefficient and the somewhat higher steady state pressure coefficient values.

For the extended skirt type canopy, differential pressure factors from 2.5 at a location near the canopy vent to 3.6 at a location near the canopy skirt were found. Again as for the circular flat type canopy, the pressure factors decreased with increasing deployment velocity. At a deployment velocity of 160 ft/sec, the pressure factors varied from a value of 2.1 to 2.8 from the location near the canopy vent to one near the skirt.

For the geometric porosity type canopies, the pressure factors are remarkably lower. The maximum pressure factor obtained on the flat circular ribbon (FIST) type canopy was 2.3, decreasing to 1.7 at the highest deployment velocity. For the ringslot type canopy, the maximum pressure factor was approximately 1.6, with no significant differences between the low and the high deployment velocities. For the geometric porosity type canopies, there was no significant difference in the magnitude of the pressure factor for locations near the canopy vent or the skirt.

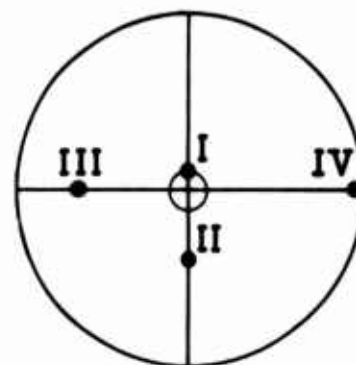
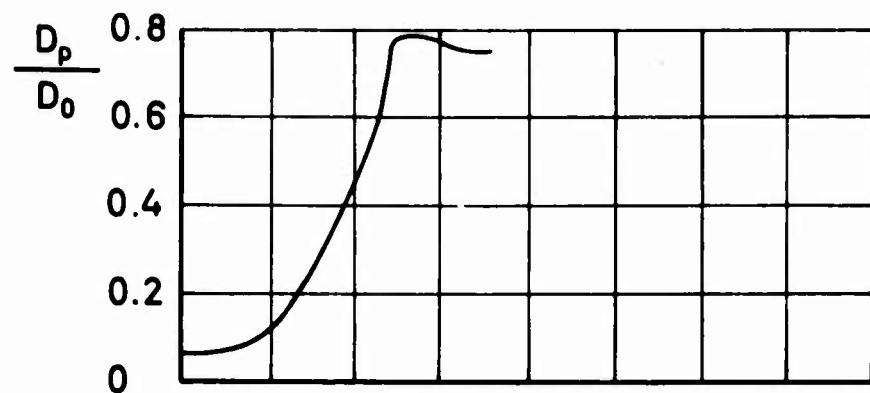
Absolute filling times of each of the canopy types decrease with increasing deployment velocity as can be seen from the Figures and from the tabulated data in Table I. The filling times are shortest for the circular flat type canopy, become longer for the extended skirt and FIST ribbon type canopies, and are longest for the ringslot type canopy.

A correlation between pressure changes and changing canopy shape may be obtained from Figures 53 thru 60 in which the pressure coefficients (c_{pd} , c_{pi} , c_{pe}) are plotted as a function of the projected canopy diameter ratio, D_p/D_o . These diagrams clarify the pressure-shape relationship. For the circular flat type canopy, the curves for the four locations of the pressure sensing elements run very close together, thus indicating a very quick filling of the canopy. These relationships

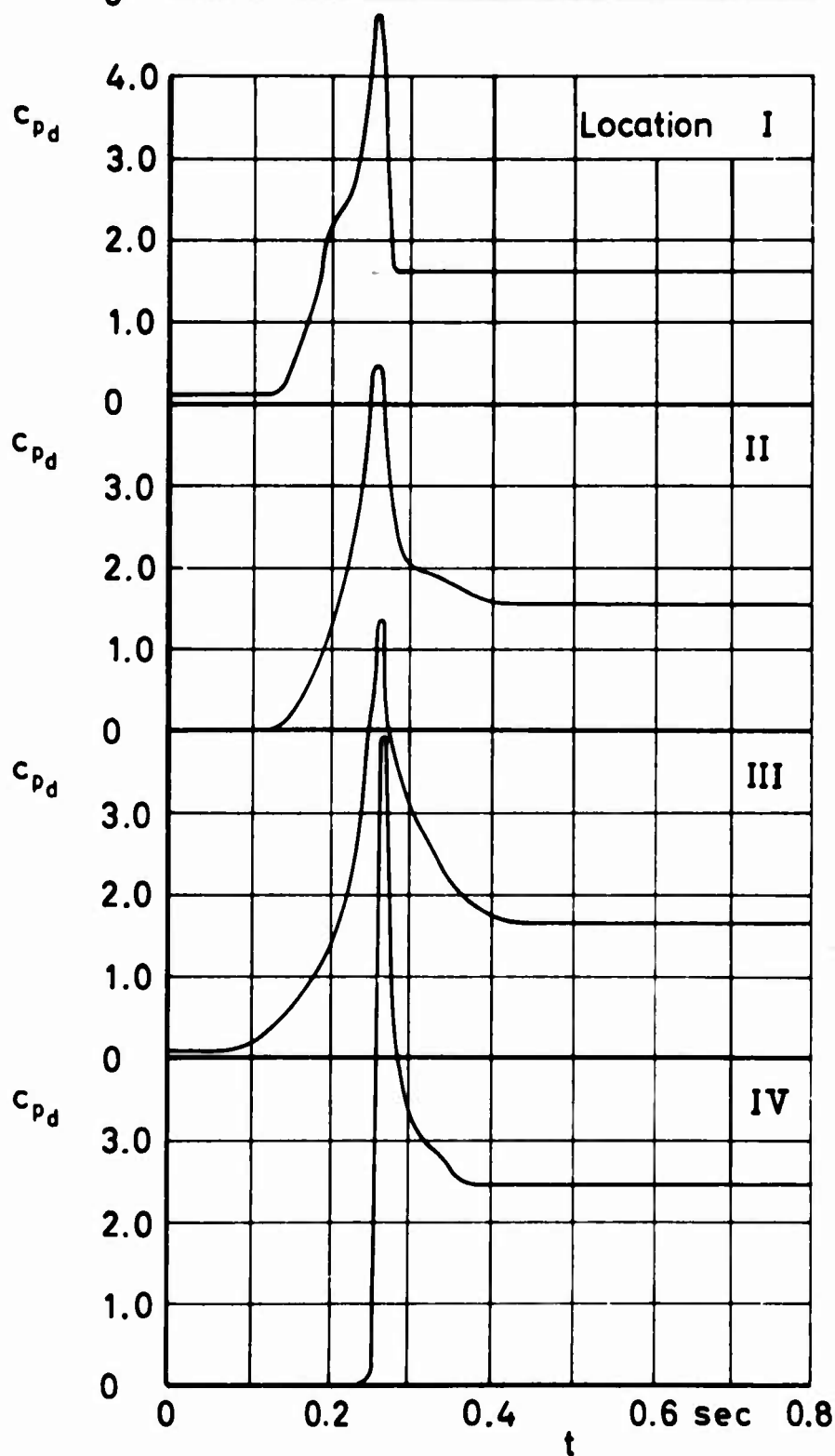
Table 1 Peak and Steady State Values for c_p and D_p and corresponding times

Model	Pressure	Run No.	v_0 ft/sec	I (Vent)		II		III		IV (Skirt)		t at peaks I-IV 1/10 sec	
				Max.	Steady	Max.	Steady	Max.	Steady	Max.	Steady	t at Peak D_p 1/10 sec	
Circular Flat	Differential	182	70	4.8	1.6	4.5	1.6	5.4	1.7	7.9	1.5	2.6-2.7	2.6
		183	100	4.2	1.6	4.6	1.8	4.3	1.8	6.6	2.5	2.1-2.2	2.2
		167	150	4.6	2.0	3.9	1.9	3.5	1.9	5.5	2.7	1.6	1.7
		191	160	2.9	2.1	3.0	1.9	3.4	1.7	4.8	2.4	1.4-1.5	1.4
	Internal	194	70	3.1	1.0	2.7	1.0	3.3	1.0	2.5	1.0	2.4	2.5
		200	100	3.6	1.4	4.0	1.6	3.4	1.5	2.8	1.4	1.9-2.0	2.0
		203	150	2.3	1.1	2.7	1.1	2.5	1.1	2.0	0.8	1.4	1.6
	External	211	70	-1.2	-0.4	-2.3	-0.6	-2.6	-0.5	-4.7	-1.2	2.3-2.9	3.0
		216	100	-1.2	-0.6	-2.0	-0.6	-2.3	-0.7	-2.7	-1.0	2.0-2.1	2.2
		218	150	-1.4	-0.5	-2.4	-0.5	-2.0	-0.8	-3.6	-0.8	1.5-1.6	1.7
Extended Skirt	Differential	159	70	2.7	1.1	4.1	1.4	4.8	1.4	5.8	1.6	3.0-3.5	3.5
		144	100	3.5	1.4	3.4	1.4	3.7	1.7	5.5	1.6	2.6-2.7	2.9
		148	150	3.5	1.5	3.5	1.5	3.2	1.6	3.7	1.5	2.3-2.4	2.5
		153	160	3.0	1.2	2.6	1.2	2.9	1.4	3.9	1.4	1.8-2.0	2.3
	Internal	157	70	3.2	0.8	3.1	0.8	2.3	0.9	2.5	0.9	3.5-3.6	3.5
		160	100	2.8	0.8	2.7	0.7	2.8	0.8	2.5	0.8	2.6-2.8	2.9
		163	150	3.0	1.5	3.0	1.5	2.7	1.5	2.7	1.5	2.7-2.8	2.8
		166	160	2.9	1.3	3.2	1.2	2.9	1.4	2.9	1.4	2.1	2.1
	External	221	70	-2.1	-1.1	-2.4	-1.4	-2.3	-0.9	-3.8	-1.5	3.4-3.8	3.7
		226	100	-1.1	-0.4	-1.3	-0.5	-2.4	-0.5	-3.0	-0.6	2.6-3.0	3.1
		231	150	-1.4	-0.5	-1.1	-0.3	-2.3	-0.5	-2.1	-0.5	1.0-2.2	2.2
		235	160	-0.9	-0.5	-1.8	-0.5	-1.5	-0.5	-2.2	-0.7	1.2-2.0	2.0
FIST	Differential	72	70	1.9	0.8	1.9	1.1	2.3	1.1	2.1	1.7	2.5-3.5	4.0
		76	100	1.7	0.9	2.1	1.0	2.5	1.2	2.4	1.8	1.7-2.5	3.0
		82	150	1.7	0.9	1.5	1.0	1.9	1.2	2.4	1.8	1.3-1.8	2.3
		86	160	1.5	0.9	1.9	1.2	2.2	1.3	2.1	1.7	1.3-1.8	2.1
	Internal	101	70	1.3	0.7	1.4	0.9	1.6	1.0	1.3	0.9	3.1-3.4	3.7
		97	100	1.3	0.8	1.5	0.9	1.5	1.0	1.4	0.9	2.5-2.9	3.2
		92	150	1.2	0.7	1.3	0.9	1.3	1.0	1.1	0.9	1.8-2.4	2.8
		88	160	1.2	0.8	1.5	1.0	1.4	1.0	1.0	0.8	1.1-1.7	2.2
	External	104	70	-0.7	-0.4	-1.3	0.7	-1.3	-0.4	-1.5	-0.7	2.8-3.6	3.6
		110	100	-1.5	-0.5	-1.7	-0.9	-0.7	-0.3	-0.8	-0.3	2.2-2.8	2.9
		117	150	-0.7	-0.3	-0.9	-0.4	-0.9	-0.4	-1.3	-0.8	1.0-1.8	2.0
		119	160	-0.7	-0.3	-0.8	-0.4	-1.1	-0.4	-1.3	-0.7	1.2-1.8	
Ringslot	Differential	7	70	1.3	0.9	1.7	1.1	1.9	1.4	2.0	1.6	1.8-3.4	4.2
		10	100	1.4	1.0	1.9	1.1	1.8	1.4	1.8	1.6	1.0-3.9	4.0
		14	150	1.2	0.9	2.0	1.2	1.6	1.3	1.4	1.3	1.4-2.5	3.0
		18	160	1.3	0.9	1.7	1.1	1.6	1.3	1.6	1.2	1.2-2.4	2.5
	Internal	22	70	1.0	0.6	1.4	0.9	1.2	1.0	1.0	0.9	2.3-3.3	3.9
		30	100	1.1	0.6	1.5	1.1	1.2	1.0	1.1	0.9	2.0-3.1	3.4
		51	150	1.1	0.6	1.4	1.0	1.0	0.9	0.8	0.7	1.5-2.8	2.5
		26	160	1.1	0.7	1.4	1.1	1.1	0.9	0.9	0.8	1.0-2.5	2.5
	External	34	70	-0.6	-0.4	-1.3	-0.3	-1.5	-0.4	-1.3	-0.4	2.0-4.0	4.0
		39	100	-0.7	-0.3	-0.9	-0.3	-0.8	-0.4	1.1	-0.4	2.0-3.4	4.0
		42	150	-0.8	-0.3	-1.2	-0.2	-0.8	-0.4	-0.9	-0.6	1.4-3.0	3.0
		47	160	-0.9	-0.4	-1.5	-0.3	-1.2	-0.3	-1.2	-0.7	1.1-2.3	3.0

show a slow increase in pressure at the beginning of inflation, with a rapid build-up in pressure immediately prior to achieving first full canopy inflation. A different characteristic is observed on the ringslot type canopy. The four curves representing the four pressure points from the canopy vent to the skirt are spread. Although the curves show a rapid increase in pressure at each location, they indicate that the canopy shape change does only slowly follow increasing pressures. The trends for the extended skirt and FIST ribbon type canopies are located between these two extreme trends.



Location of pressure transducers on cord center line

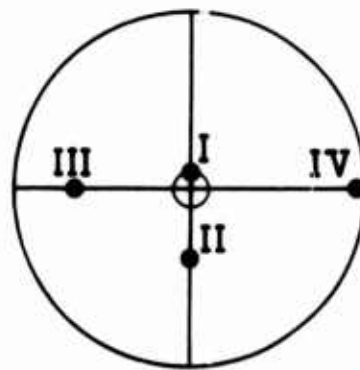
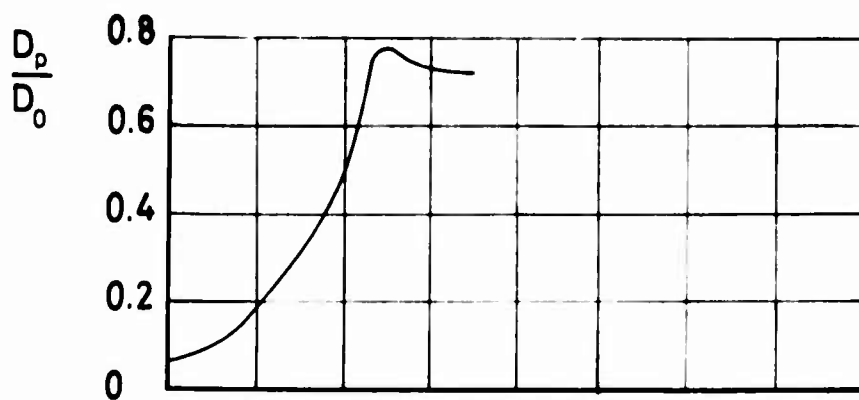


Circular Flat

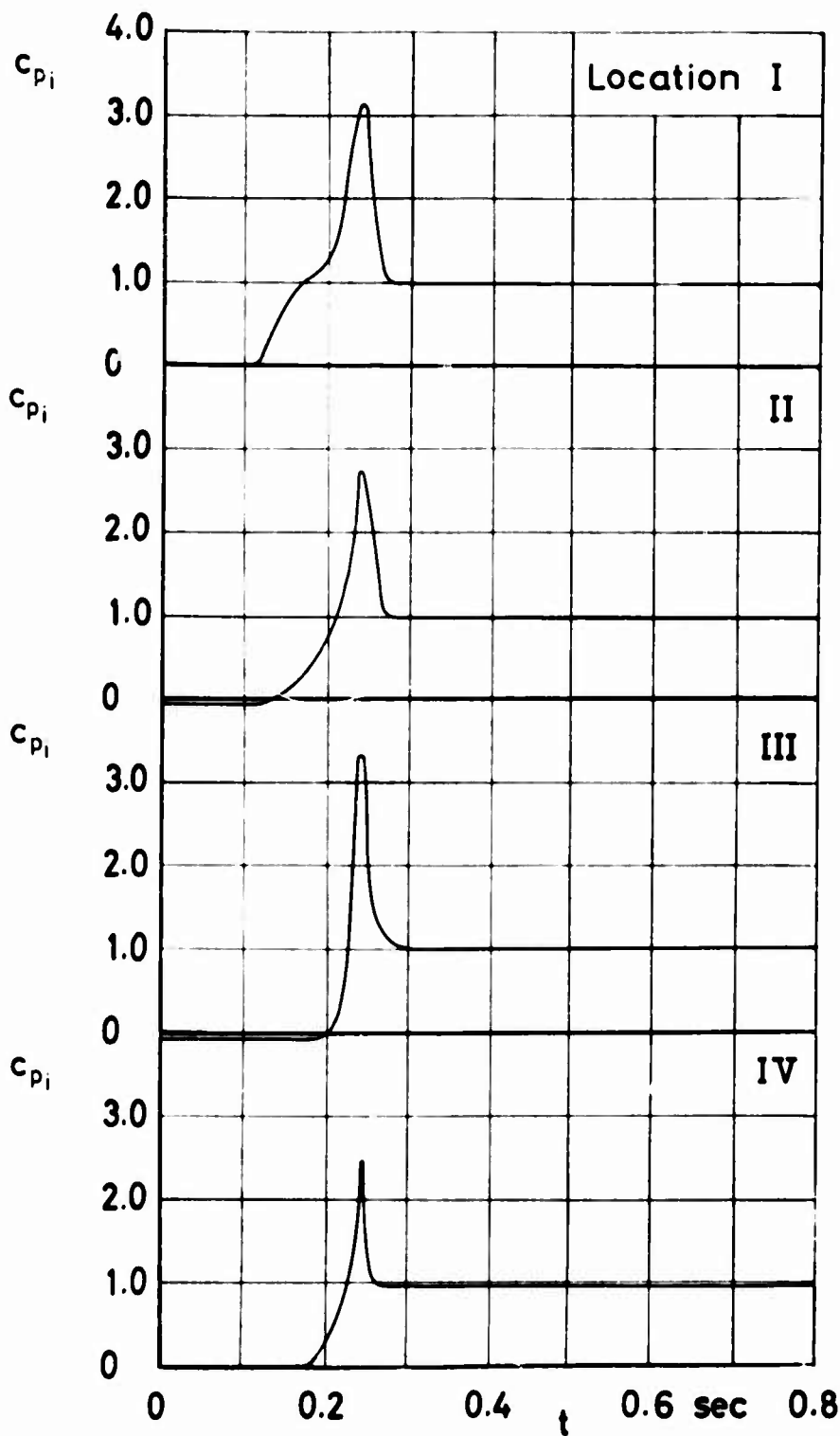
Figure 7 c_{p_d} and filling versus time

$v_0 = 70 \text{ ft/sec}$

Run No. 182



Location of pressure transducers on cord center line

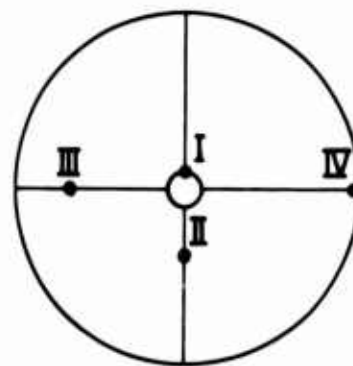
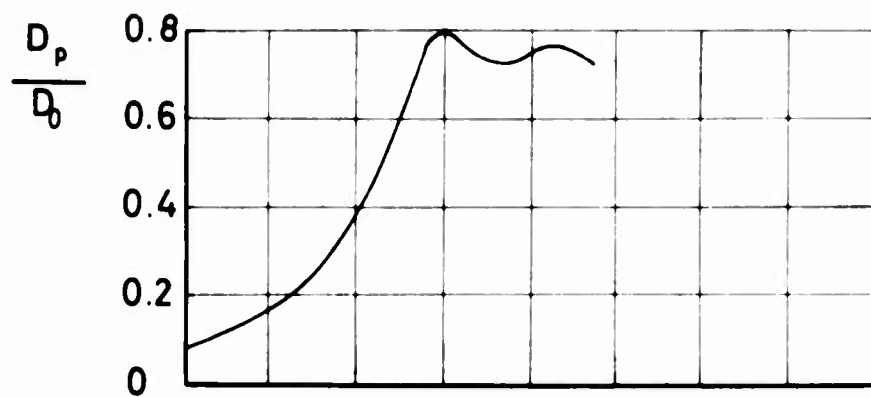


Circular Flat

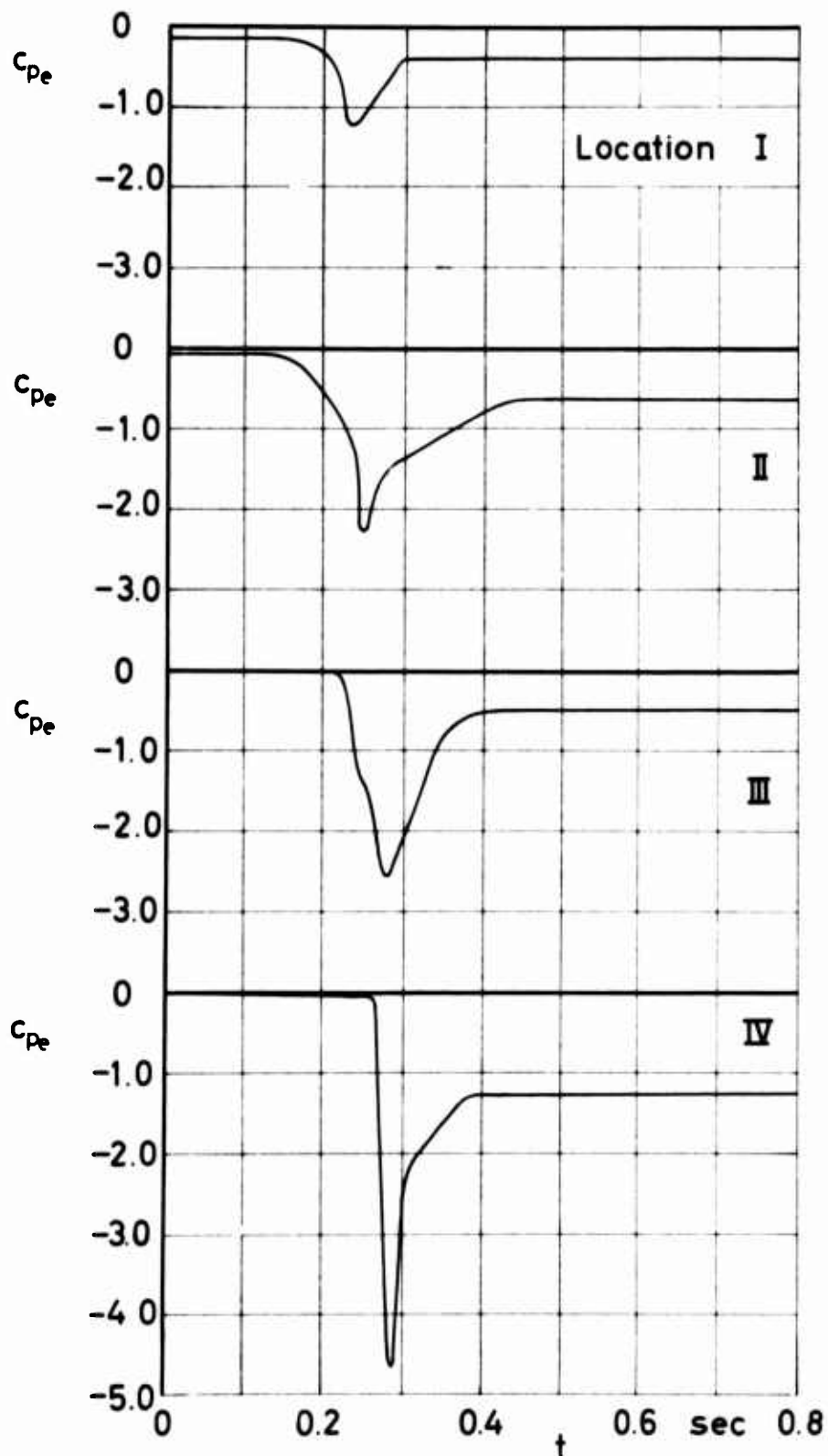
Figure 8 c_{pi} and filling versus time

$v_0 = 70$ ft/sec

Run No. 194



Location of pressure transducers on cord center line

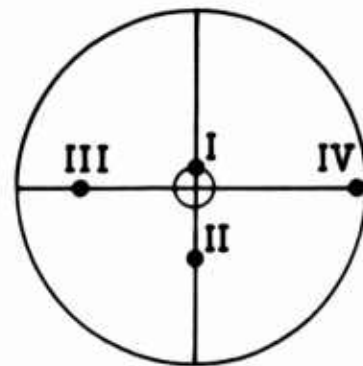
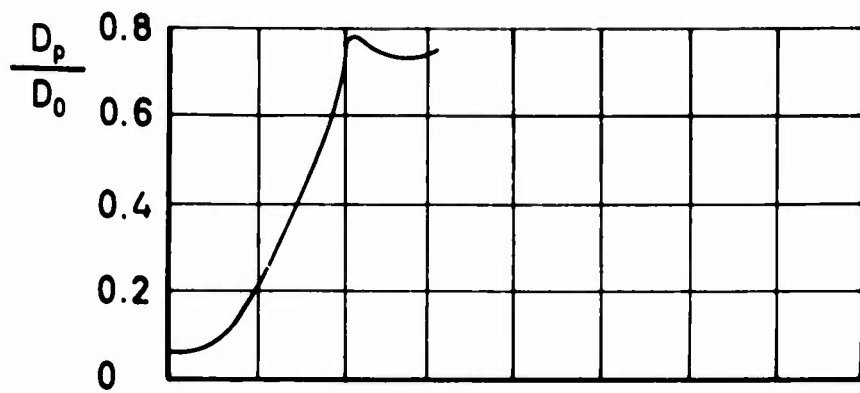


Circular Flat

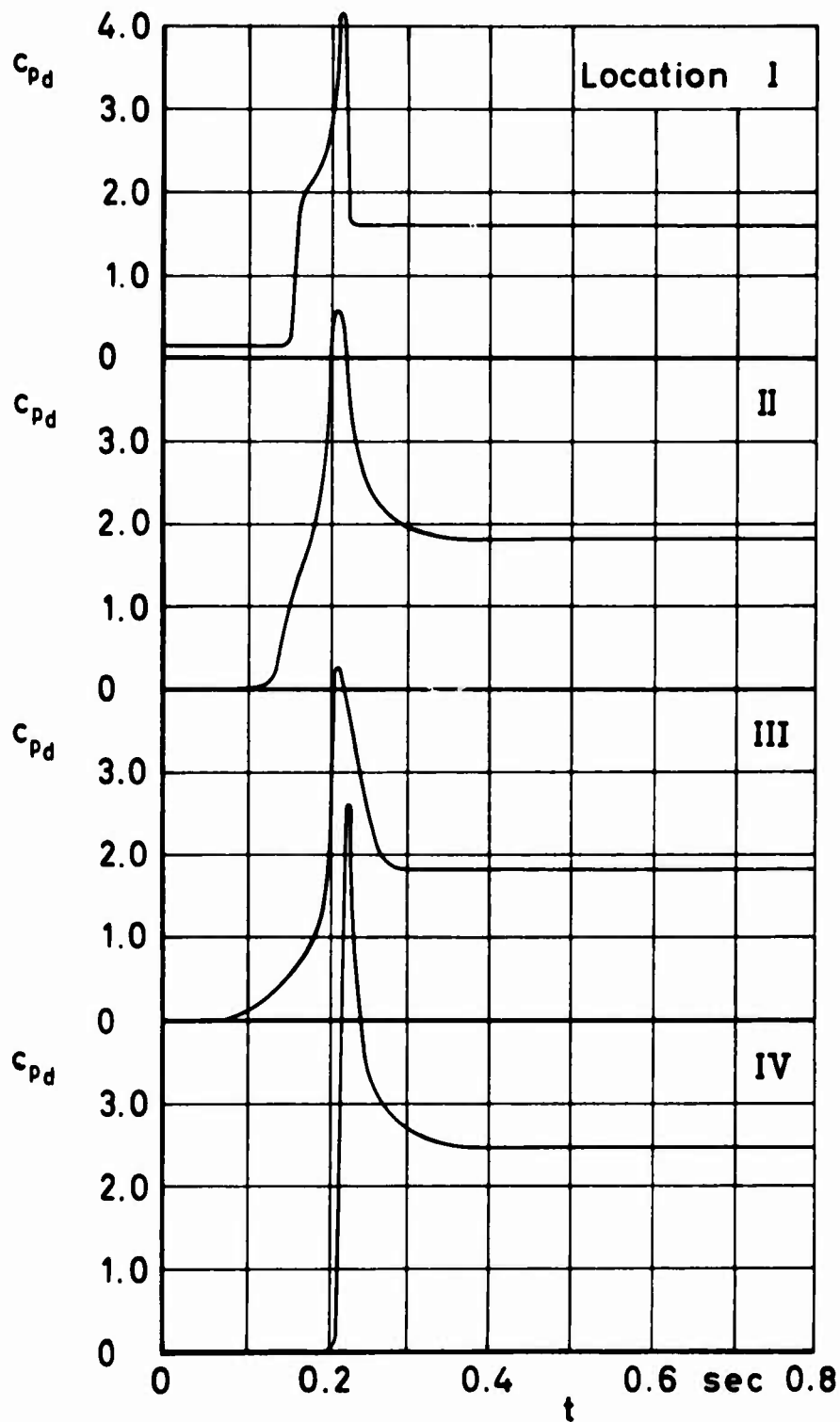
Figure 9 c_{pe} and filling versus time

$v_0 = 70 \text{ ft/sec}$

Run No. 211



Location of pressure transducers on cord center line

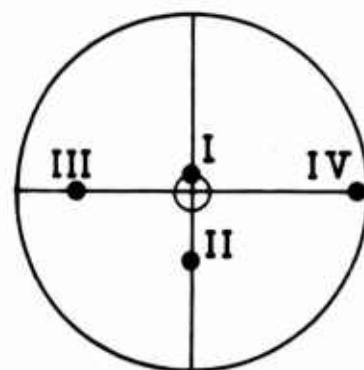
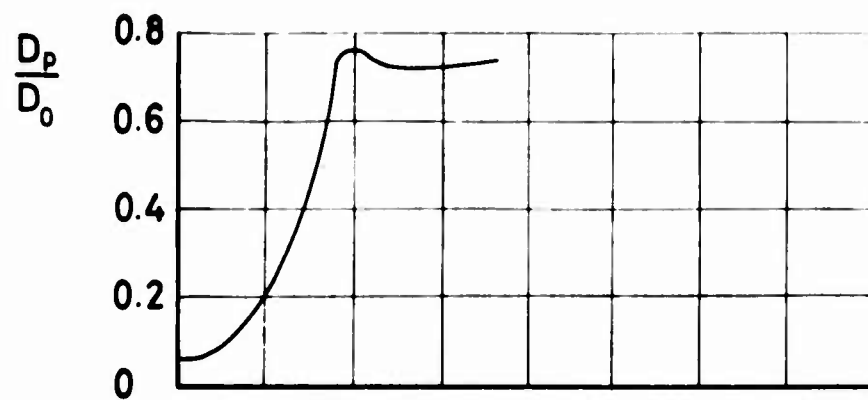


Circular Flat

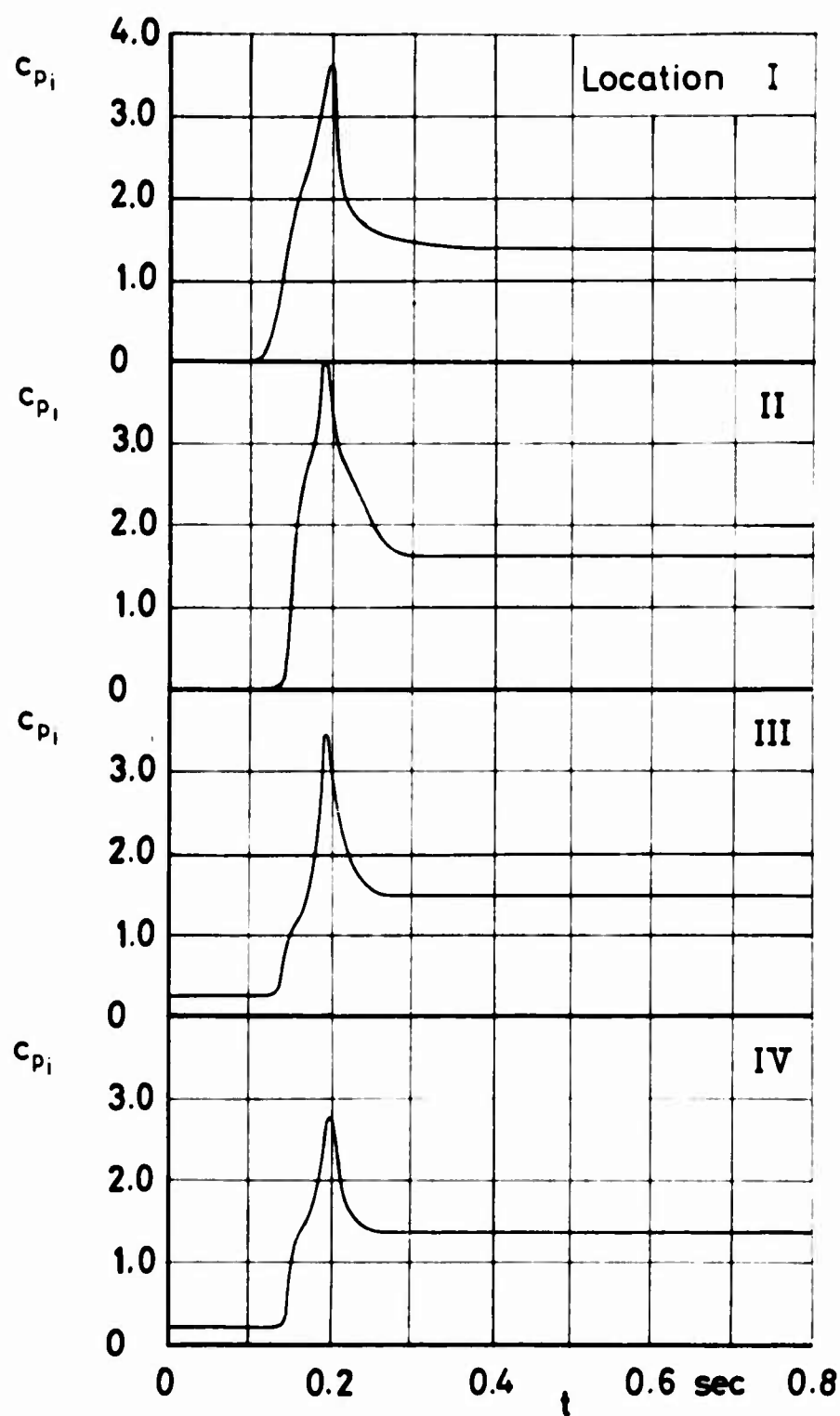
Figure 10 c_{pd} and filling versus time

$v_0 = 100$ ft/sec

Run No. 183

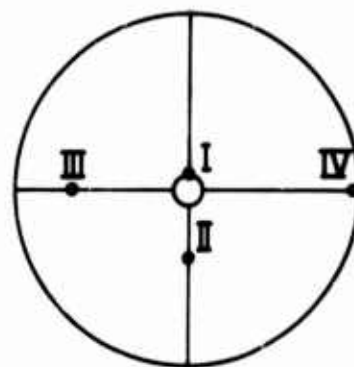
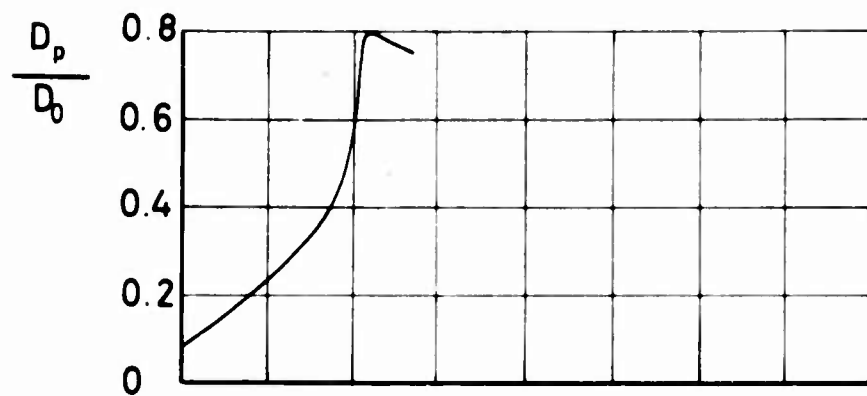


Location of pressure transducers on cord center line

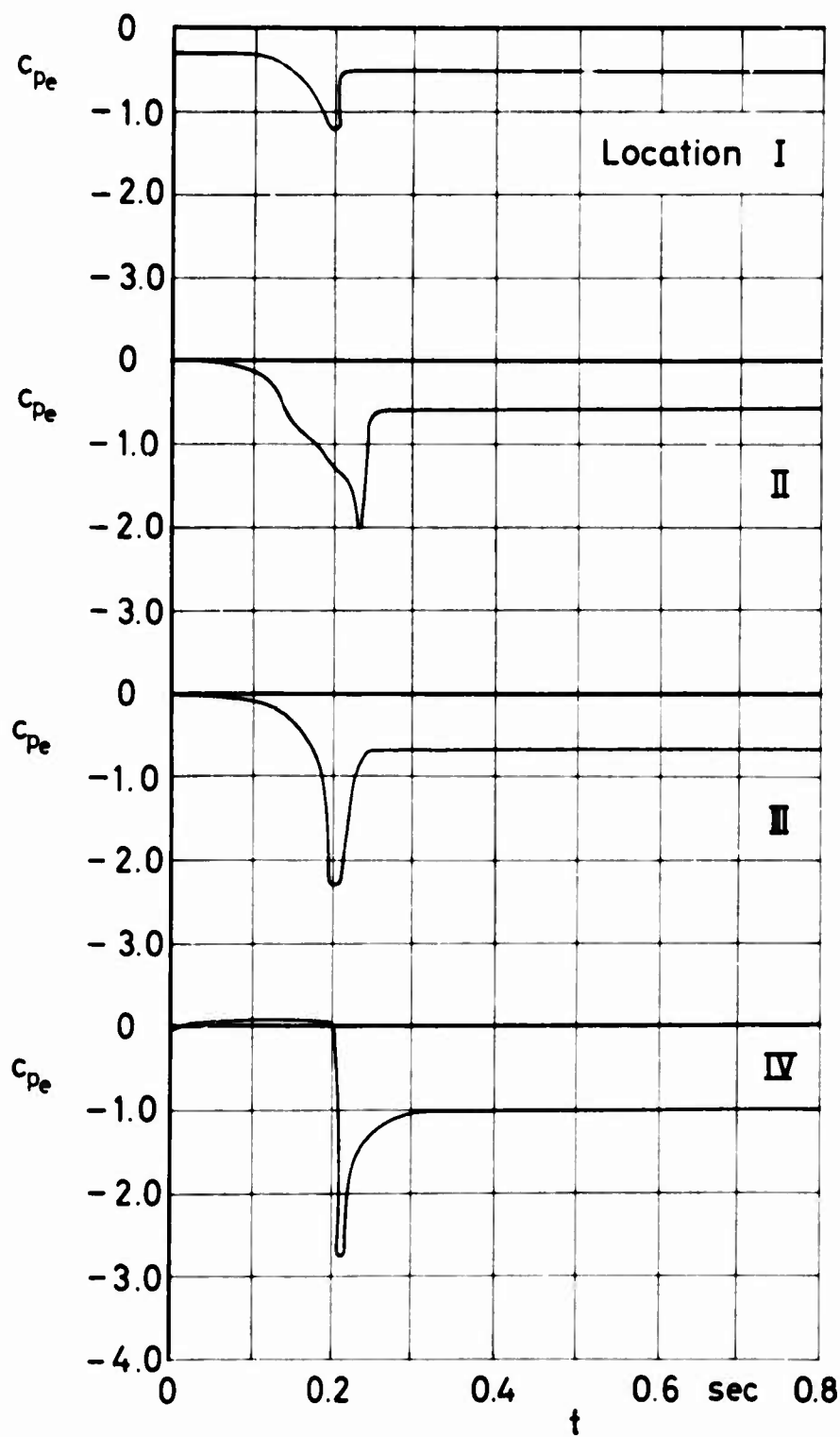


Circular Flat

Figure 11 c_{pi} and filling versus time
 $v_0 = 100$ ft/sec
 Run No. 200



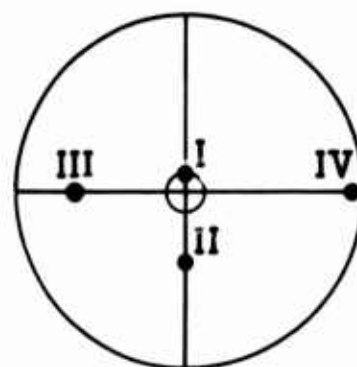
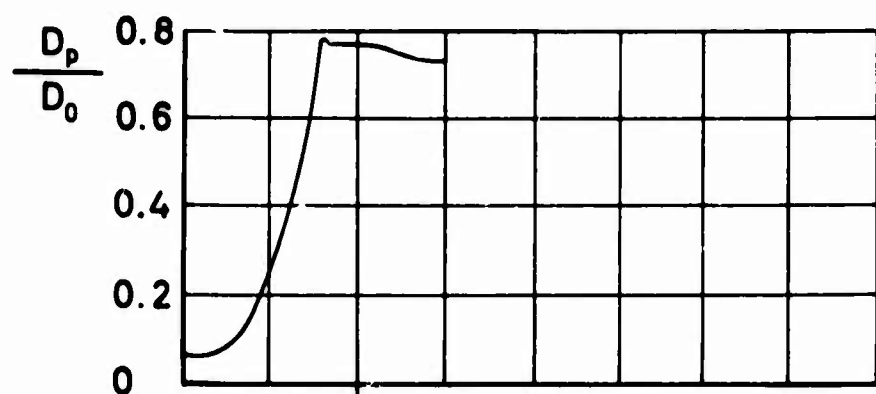
Location of pressure transducers on cord center line



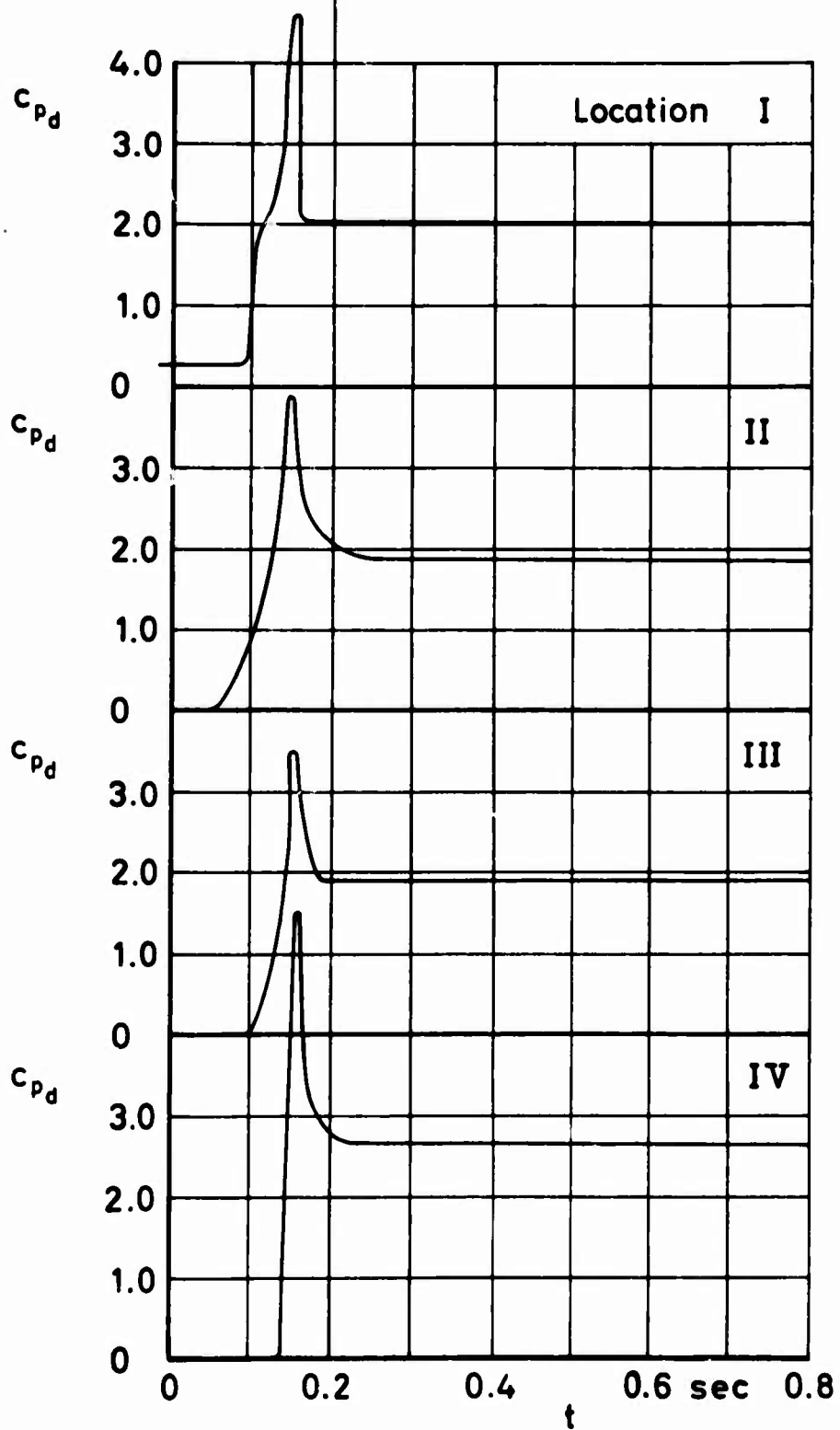
Circular Flat

Figure 12 c_{pe} and filling versus time

$v_0 = 100 \text{ ft/sec}$
Run No. 216



Location of pressure transducers on cord center line

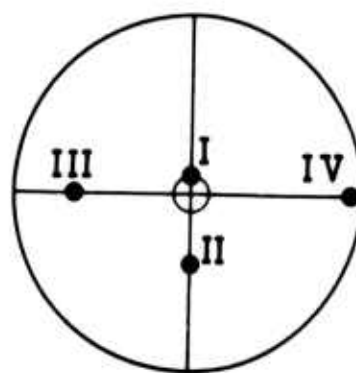
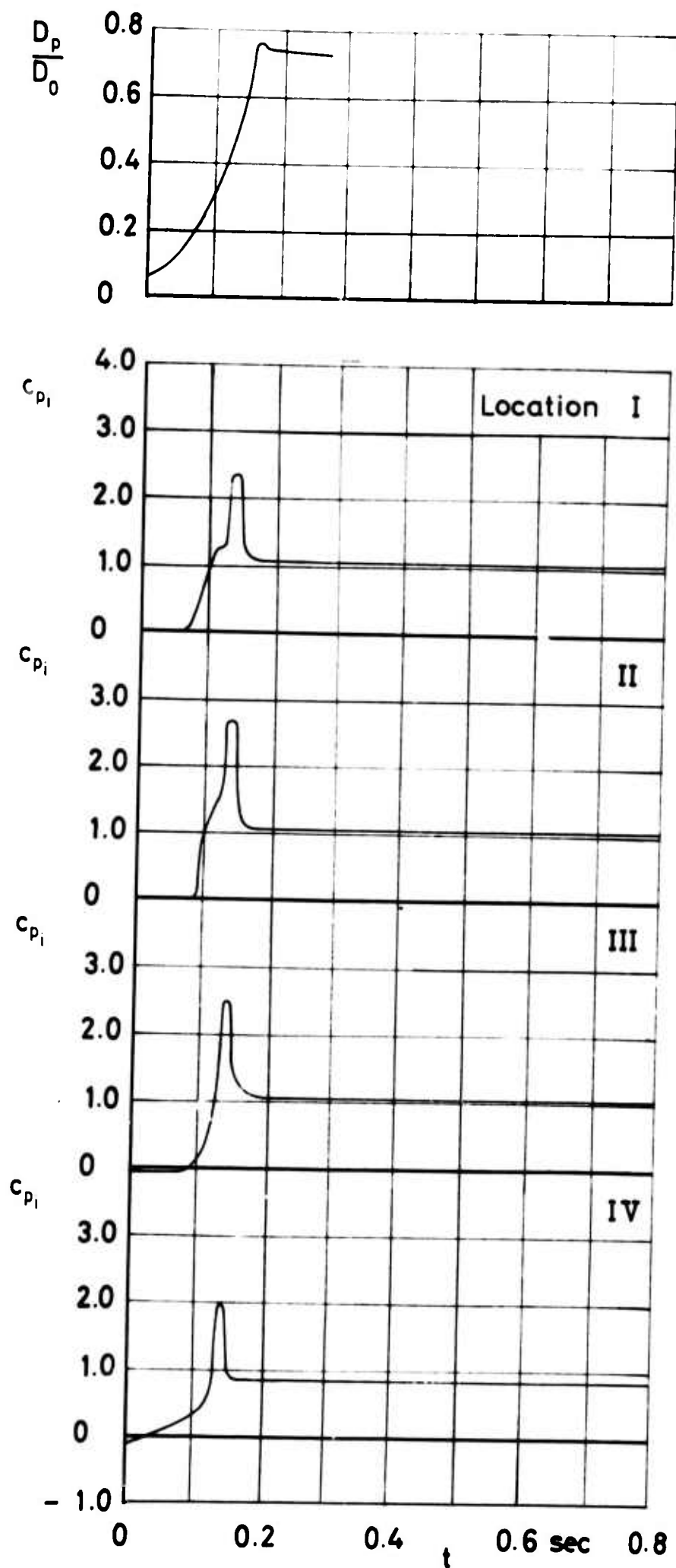


Circular Flat

Figure 13 c_{pd} and filling versus time

$v_0 = 130$ ft/sec

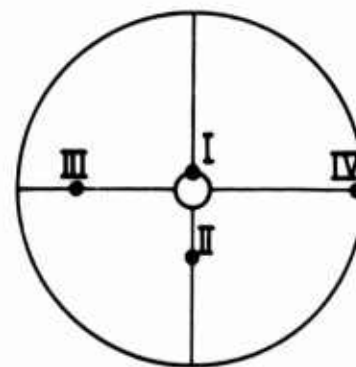
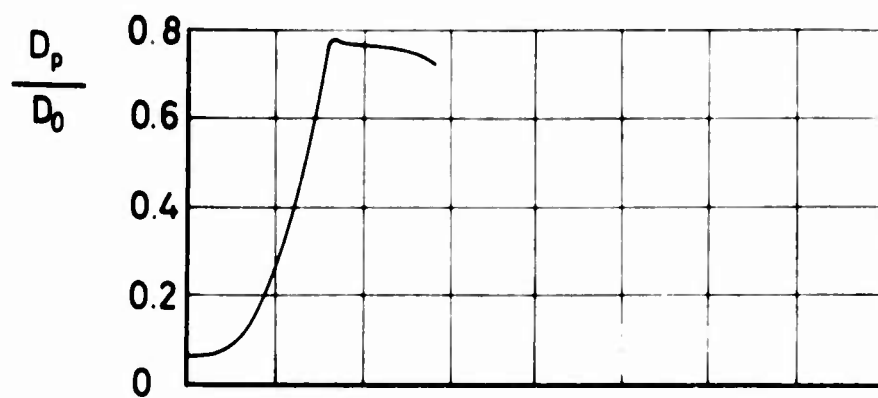
Run No. 167



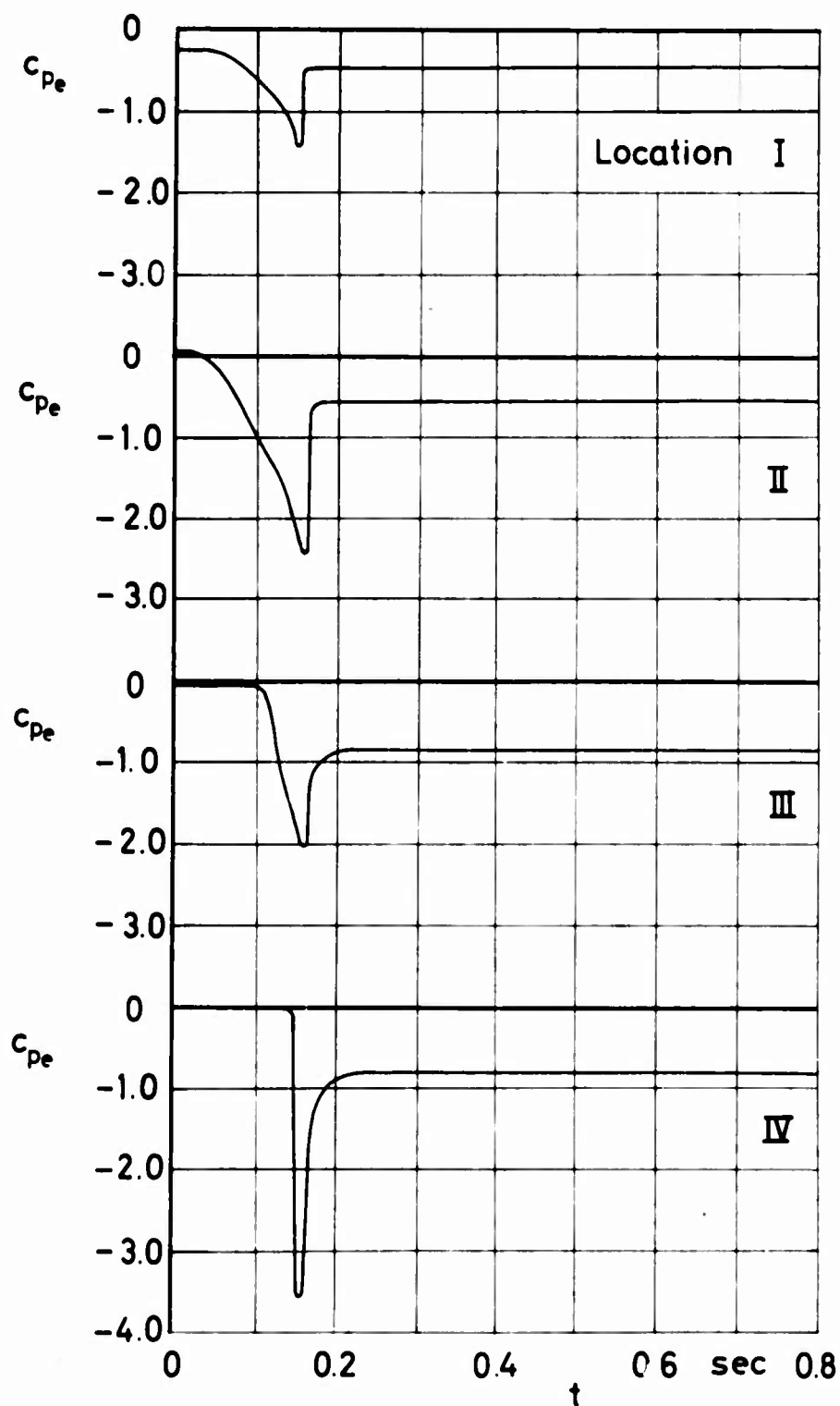
Location of pressure
transducers on
cord center line

Circular Flat

Figure 14 c_{p_i} and
filling versus time
 $v_0 = 130$ ft/sec
Run No. 203



Location of pressure transducers on cord center line

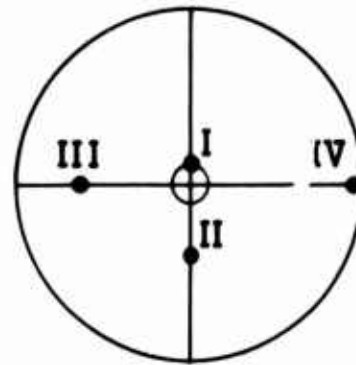
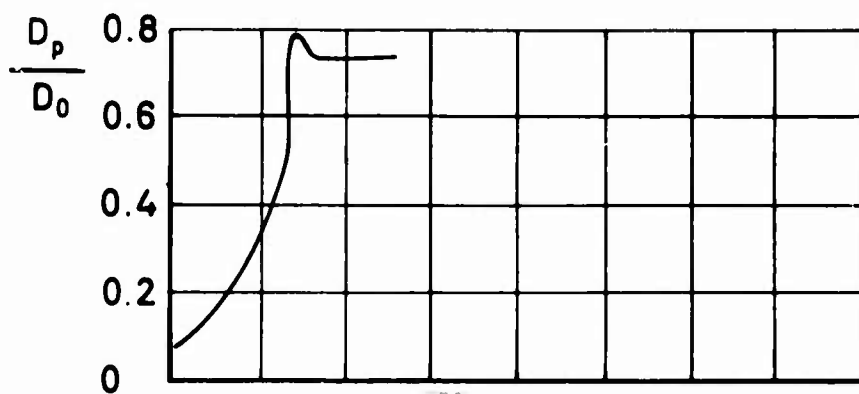


Circular Flat

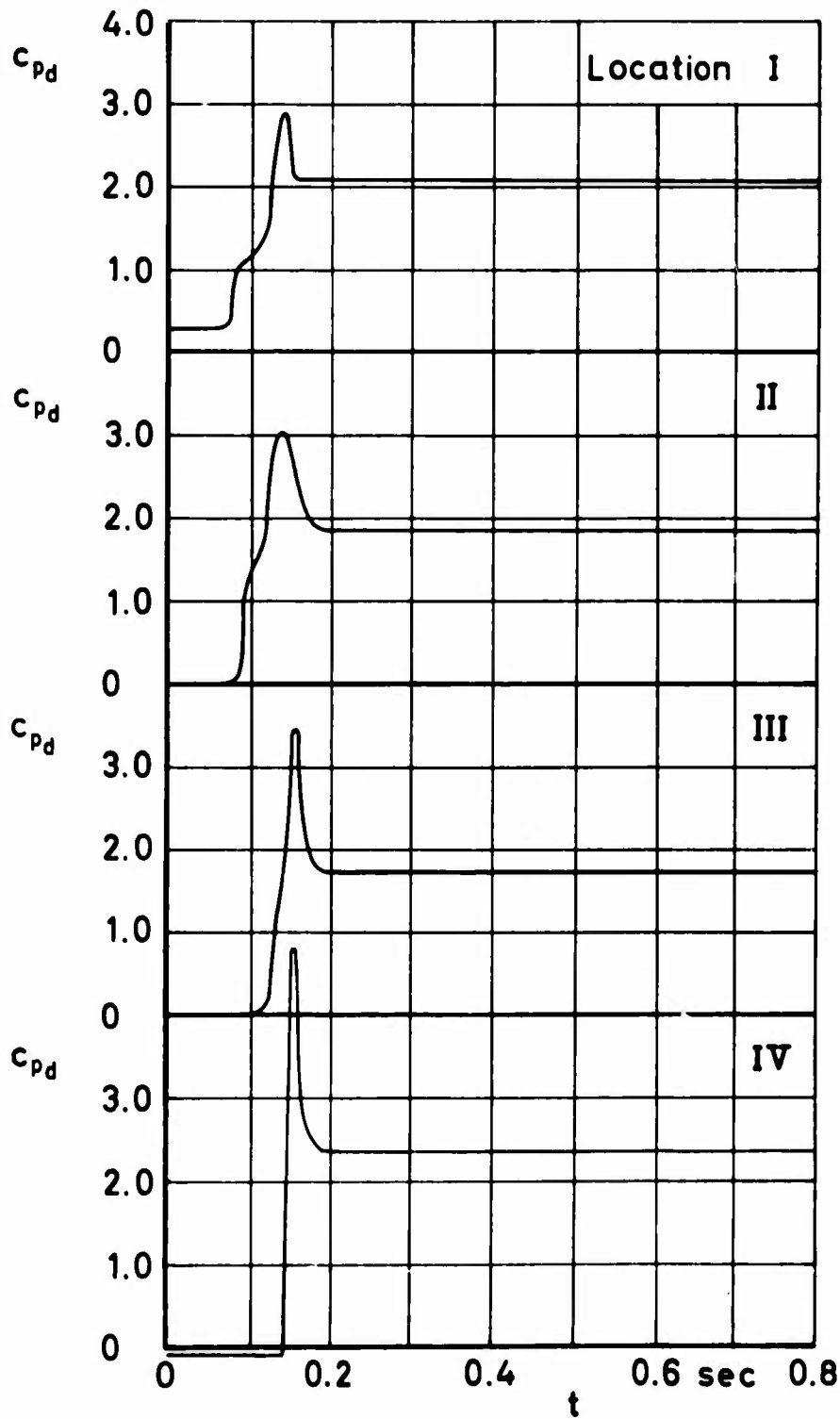
Figure 15 c_{pe} and filling versus time

$v_0 = 130 \text{ ft/sec}$

Run No. 218



Location of pressure transducers on cord center line

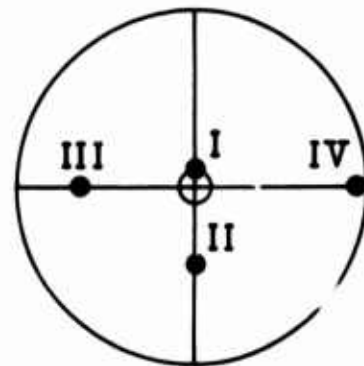
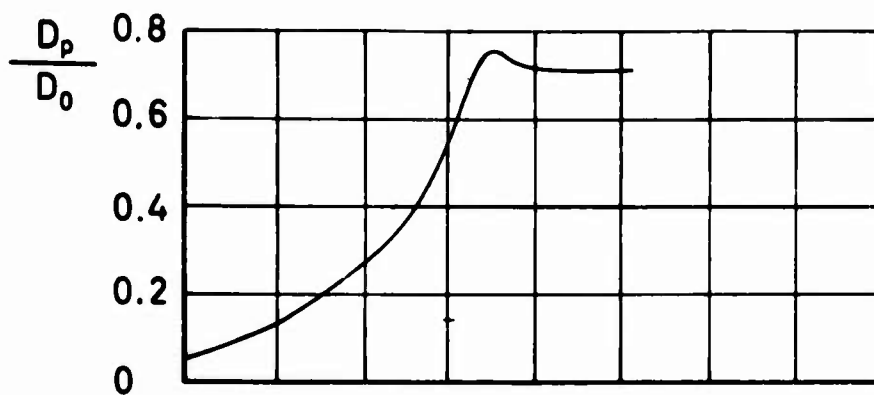


Circular Flat

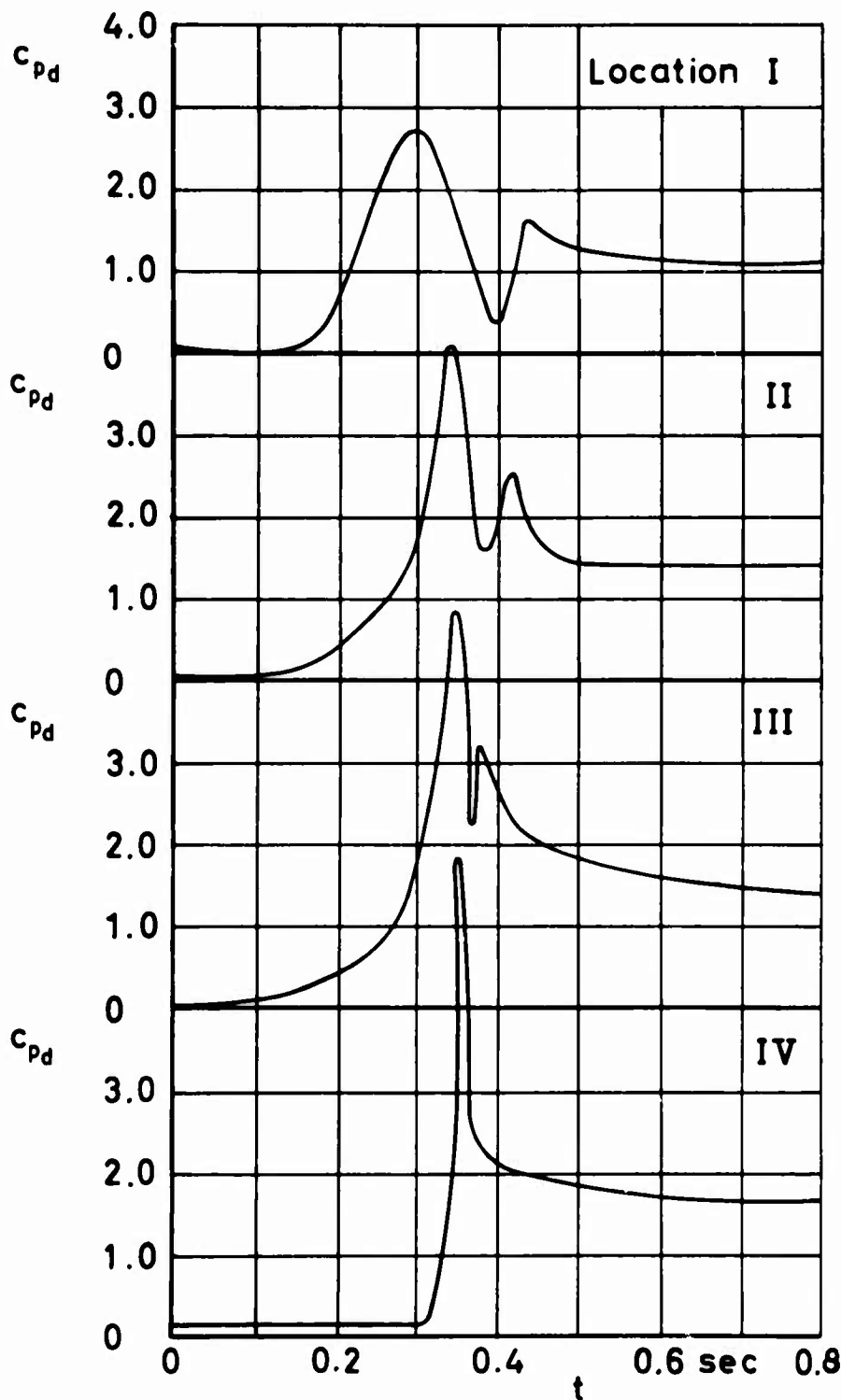
Figure 16 c_{pd} and filling versus time

$v_0 = 160$ ft/sec

Run No. 191



Location of pressure transducers on cord center line

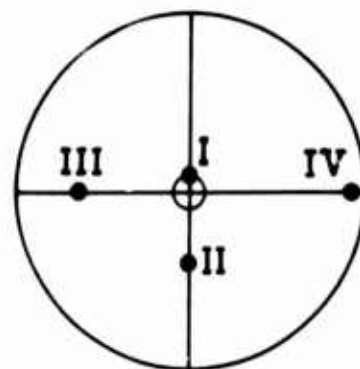
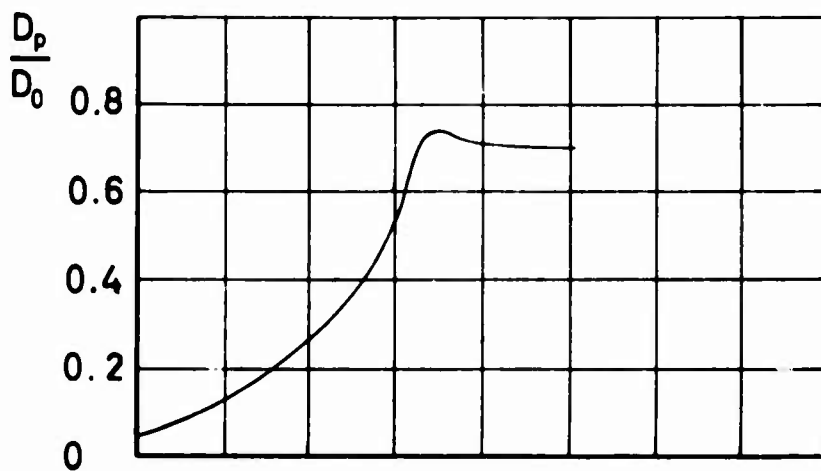


Extended Skirt

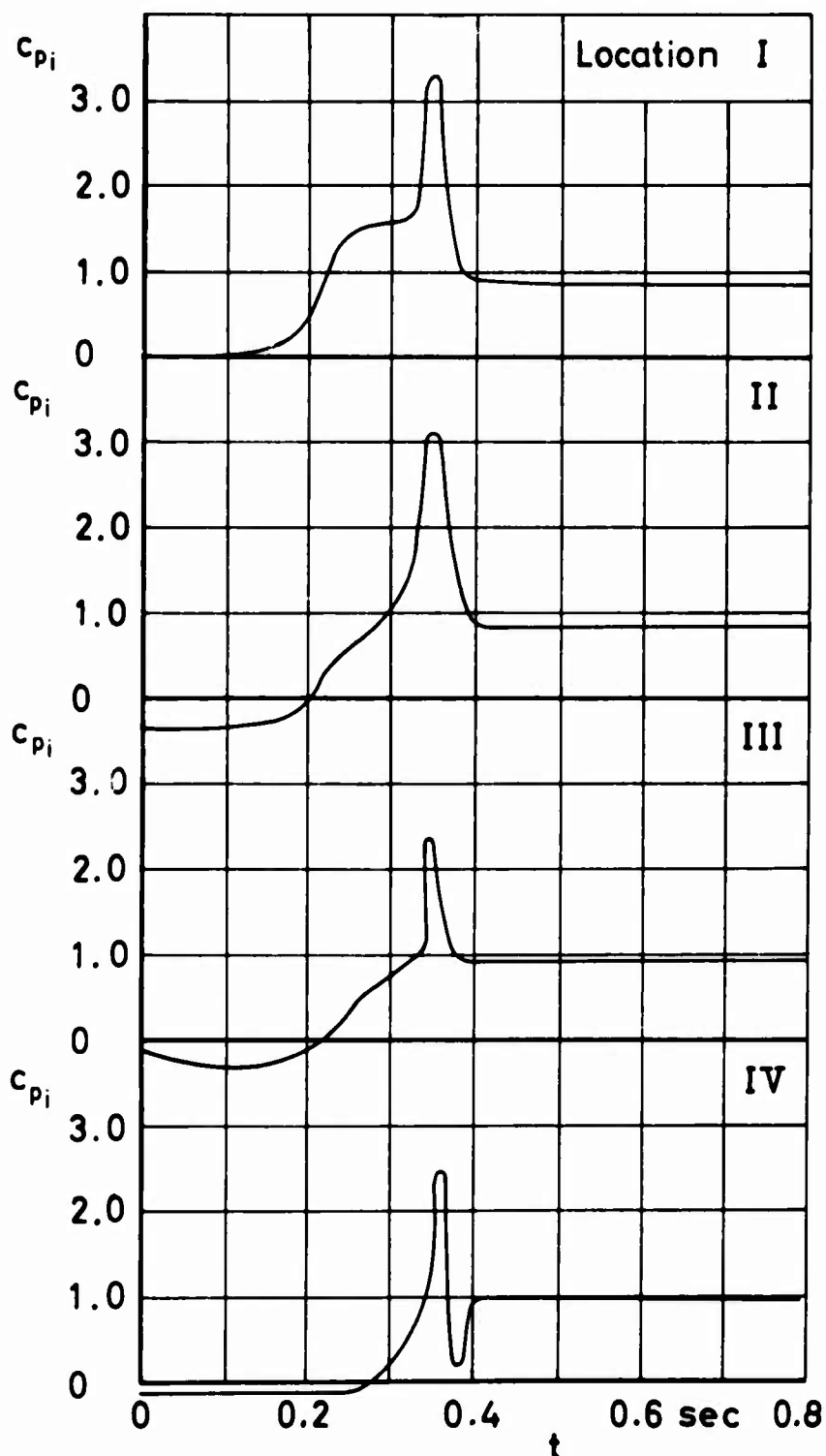
Figure 17 c_{p_d} and filling versus time

$v_0 = 70 \text{ ft/sec}$

Run No.139

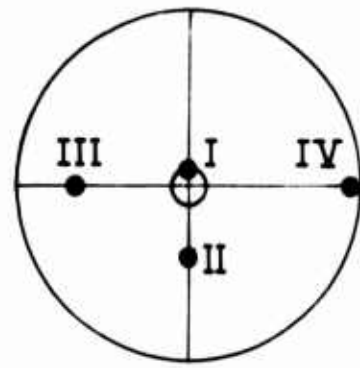
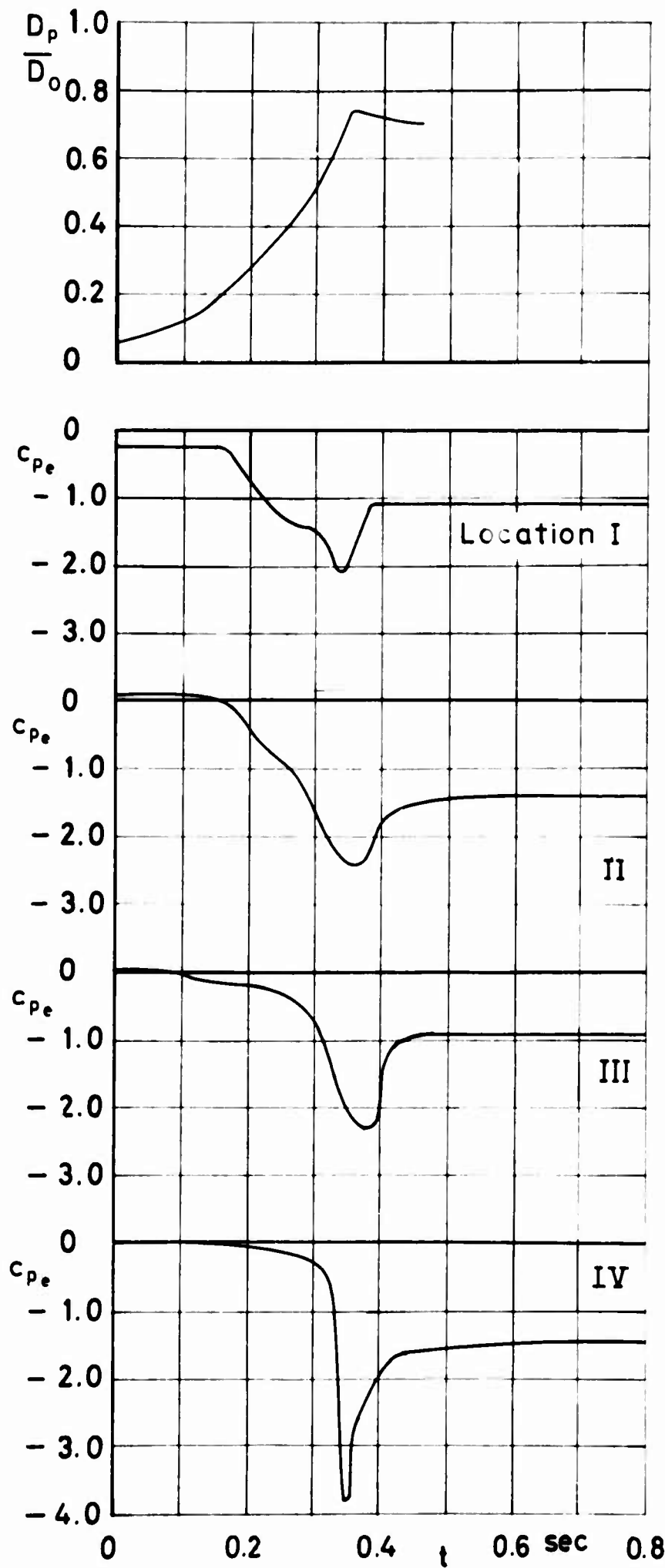


Location of
pressure trans-
ducers on
cord center line



Extended
Skirt

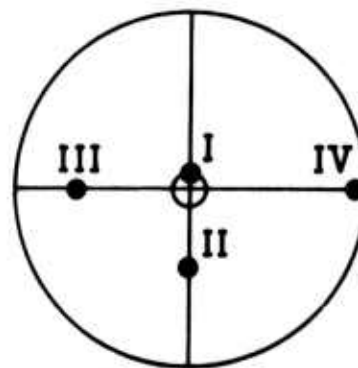
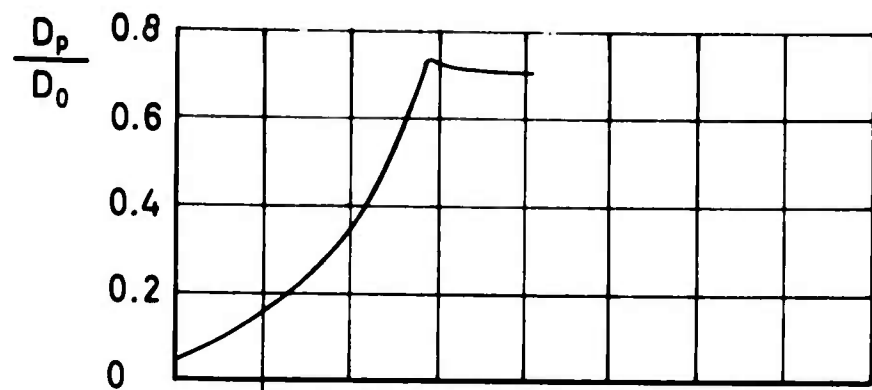
Figure 18 c_{pi}
and filling
versus time
 $v_0 = 70$ ft/sec
Run No.157



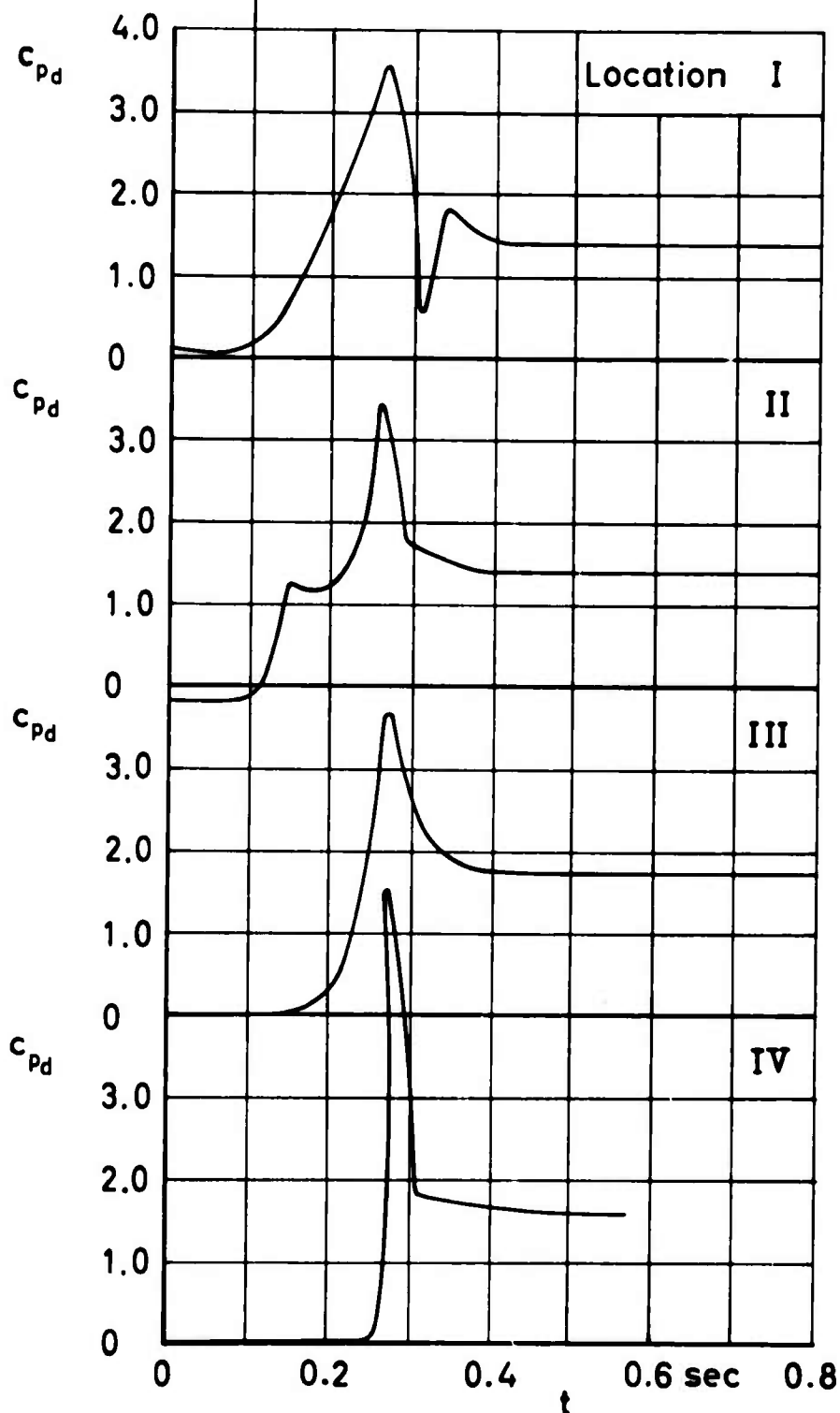
Location of
pressure trans-
ducers on
cord center line

Extended
Skirt

Figure 19 C_{pe}
and filling
versus time
 $v_0 = 70$ ft/sec
Run No 221



Location of pressure transducers on cord center line

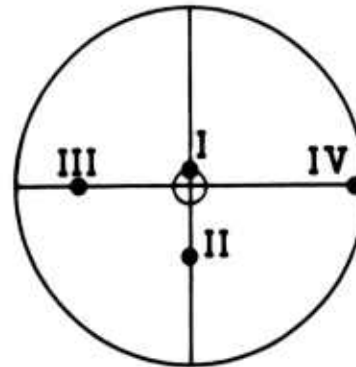
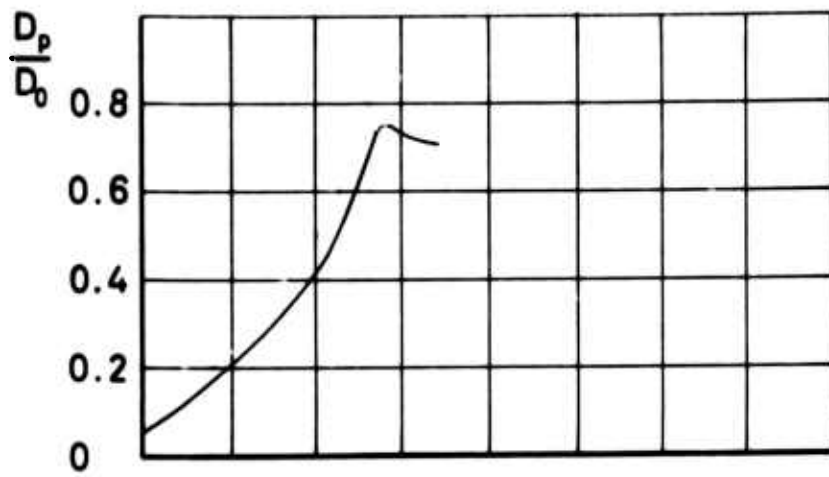


Extended Skirt

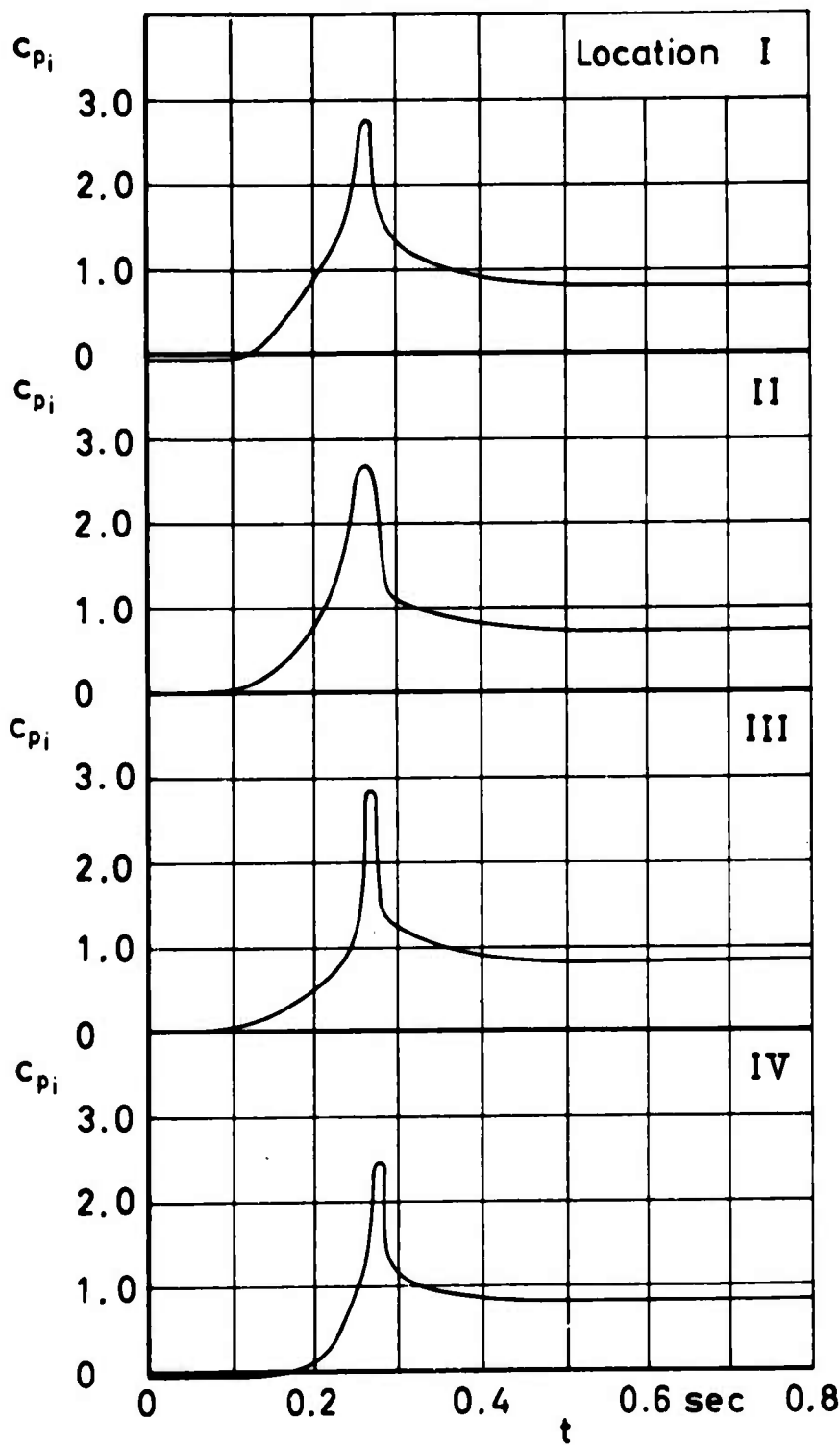
Figure 20 c_{p_d} and filling versus time

$v_0 = 100 \text{ ft/sec}$

Run No.144

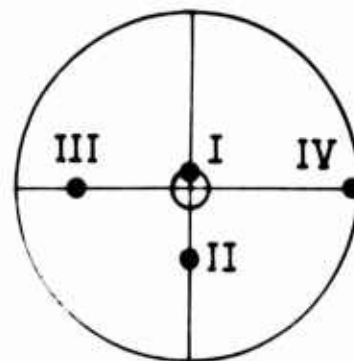
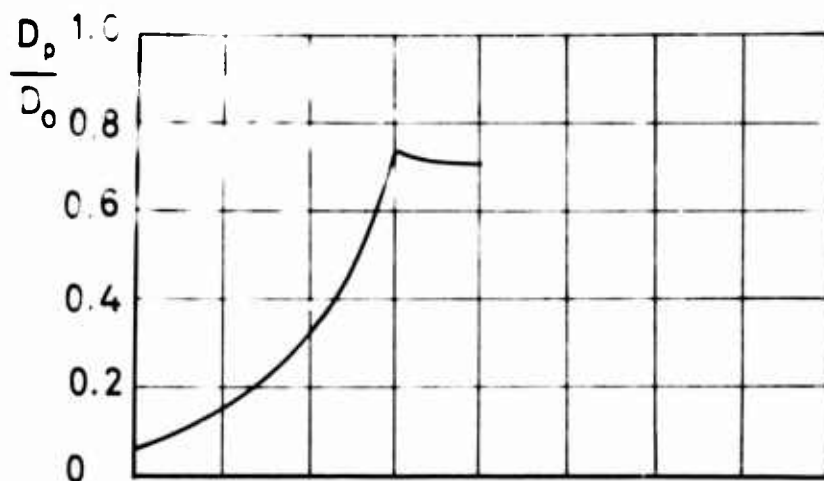


Location of
pressure trans-
ducers on
cord center line

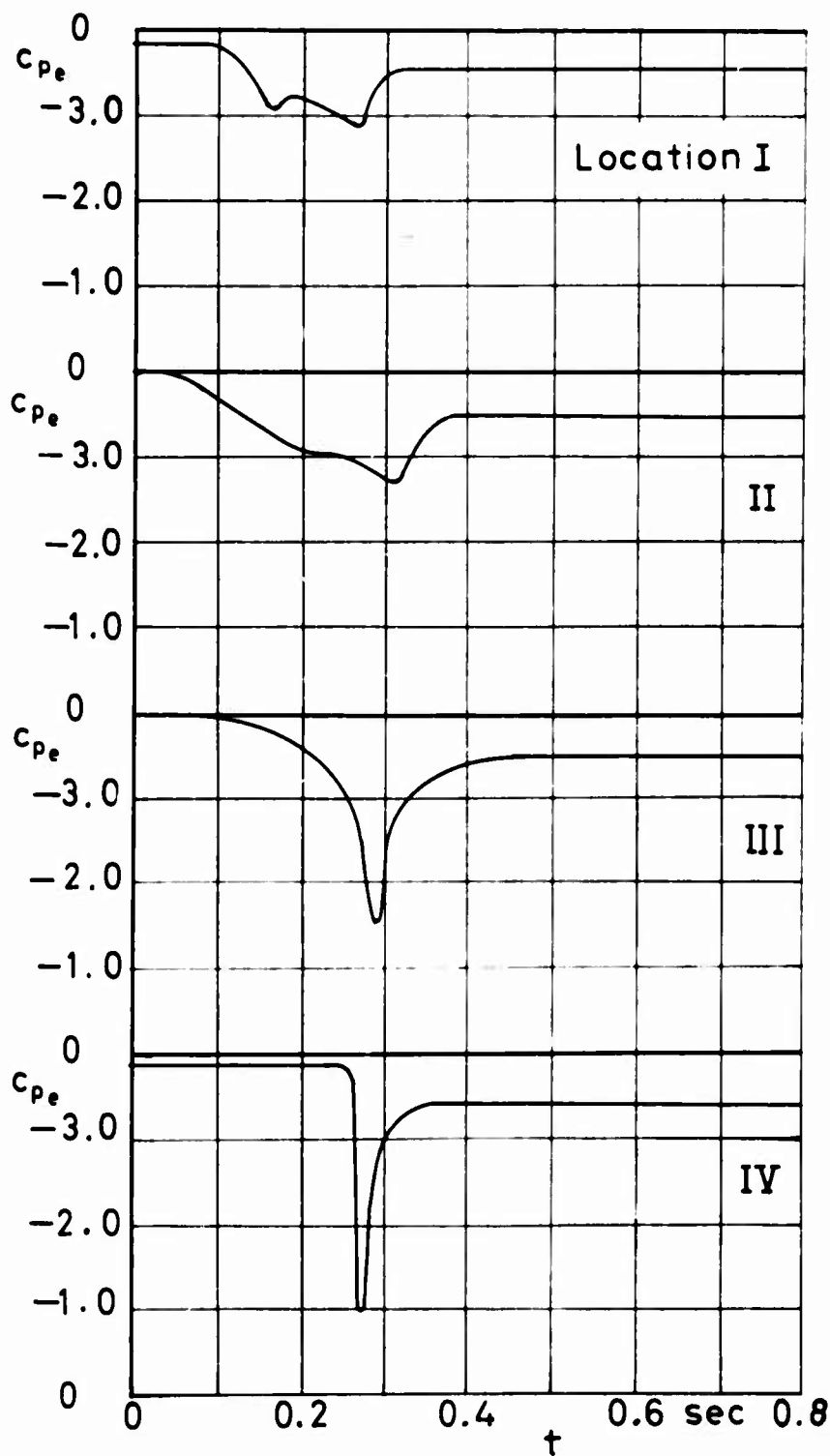


Extended Skirt

Figure 21 c_{pi}
and filling
versus time
 $v_0 = 100 \text{ ft/sec}$
Run No.160

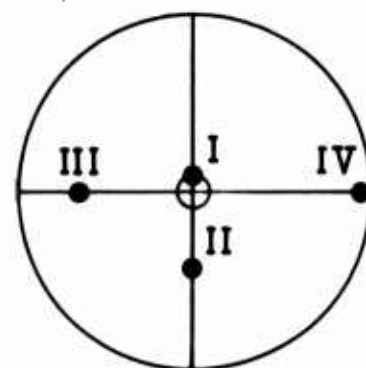
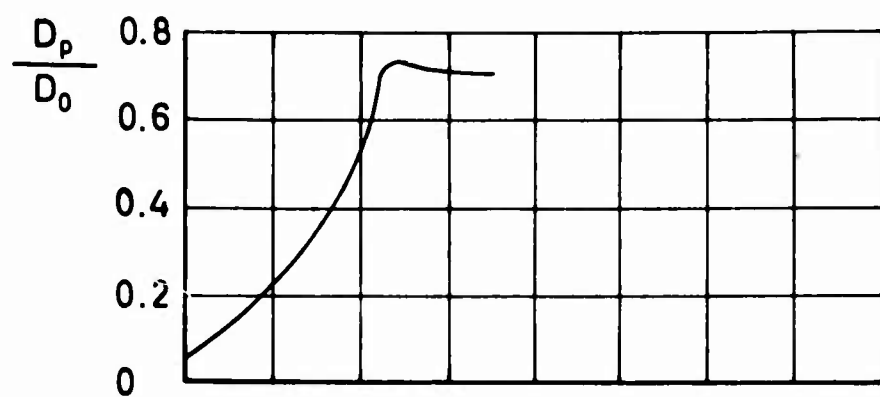


Location of
pressure trans-
ducers on
cord center line

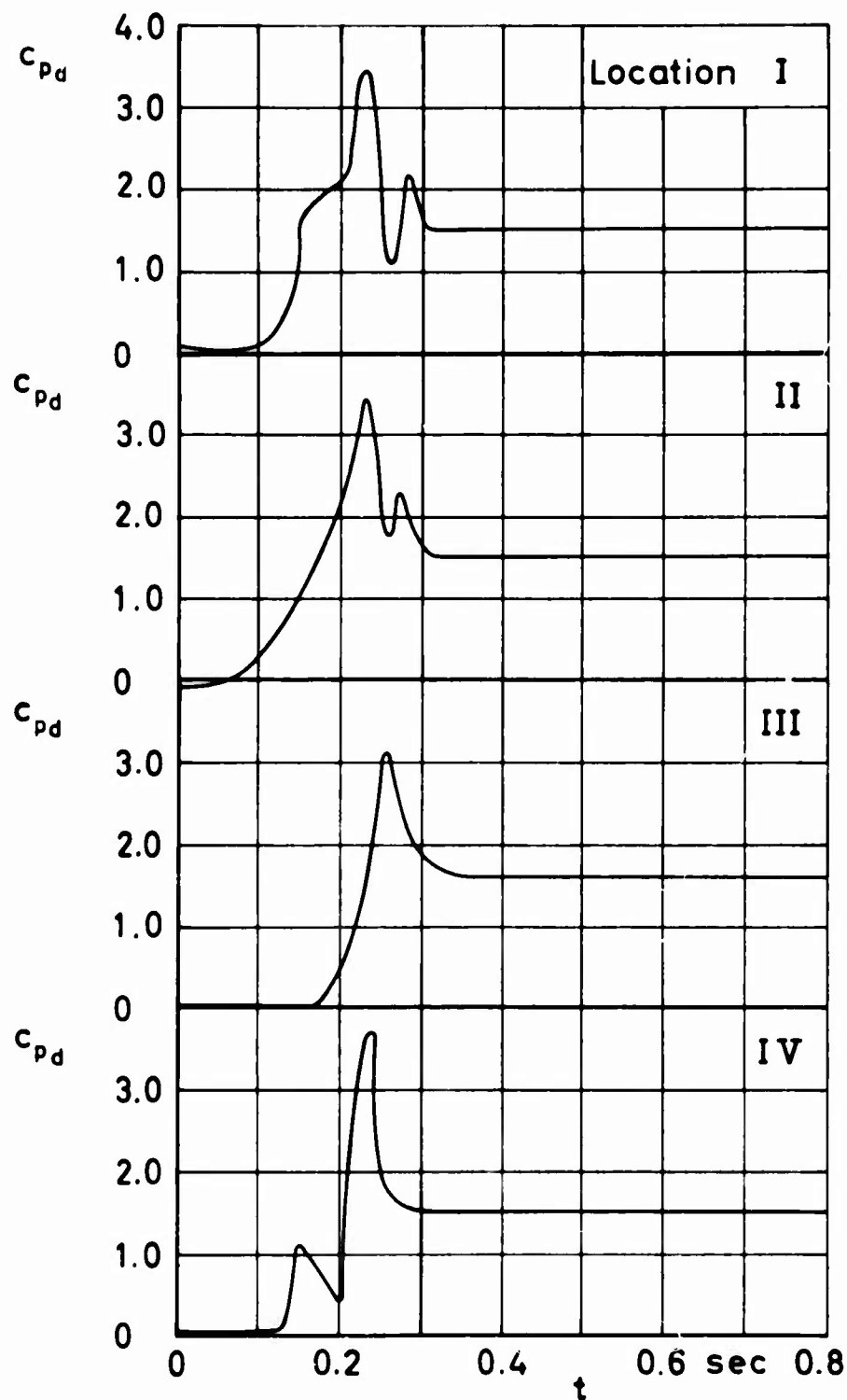


Extended
Skirt

Figure 22 c_{pe}
and filling
versus time
 $v_0 = 100 \text{ ft/sec}$
Run No 226



Location of pressure transducers on cord center line

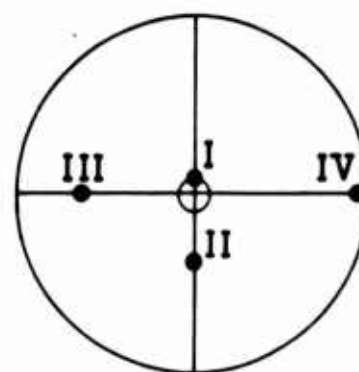
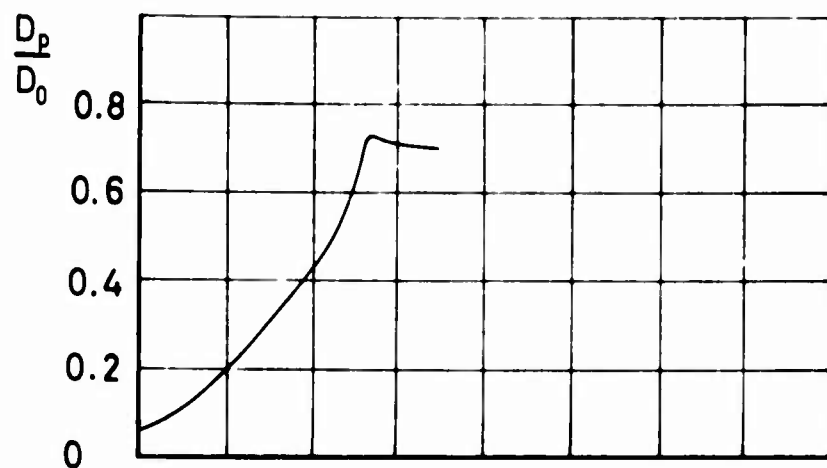


Extended Skirt

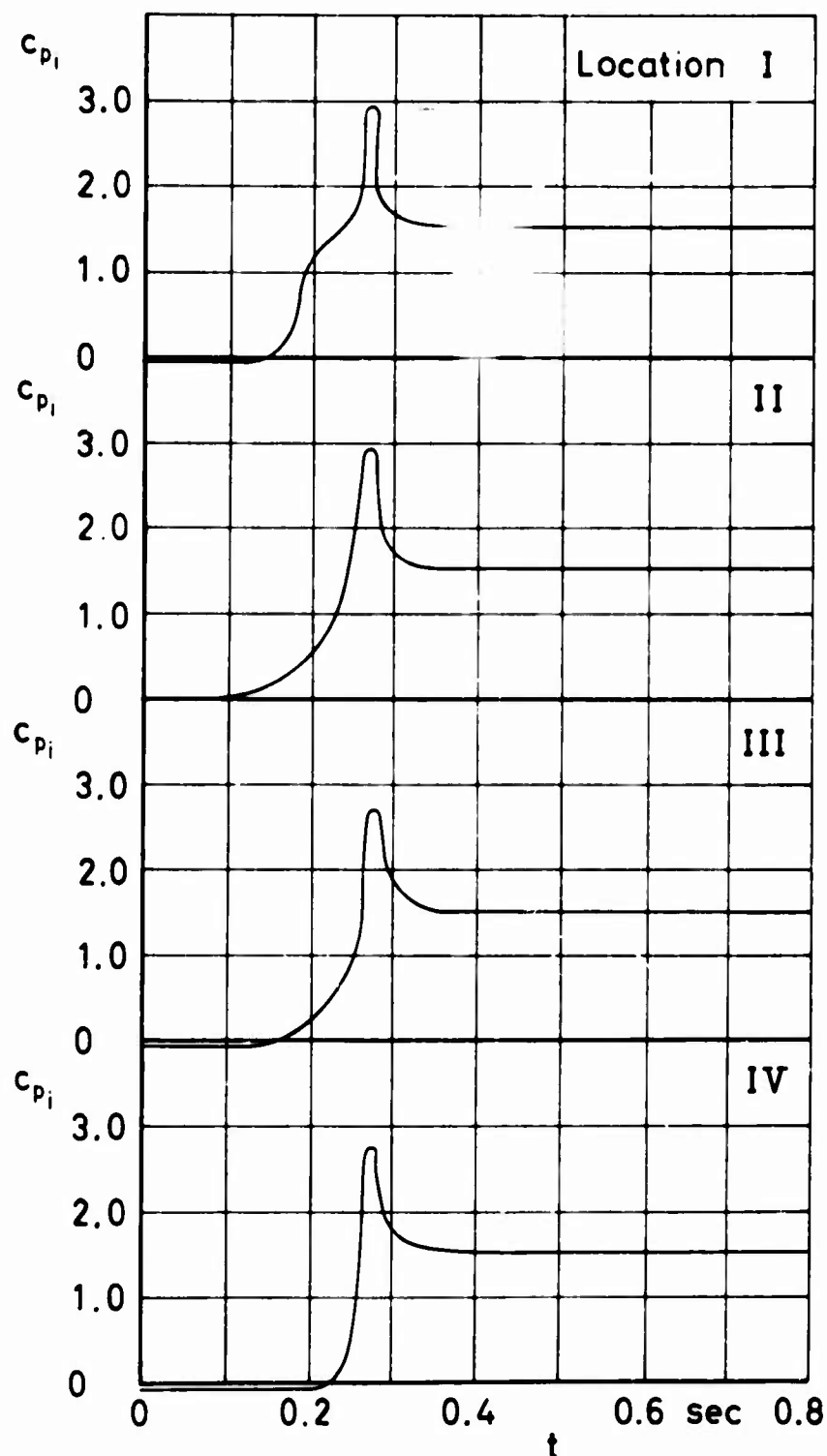
Figure 23 c_{pd} and filling versus time

$v_0 = 130 \text{ ft/sec}$

Run No. 148

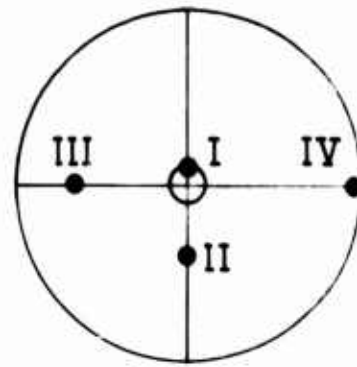
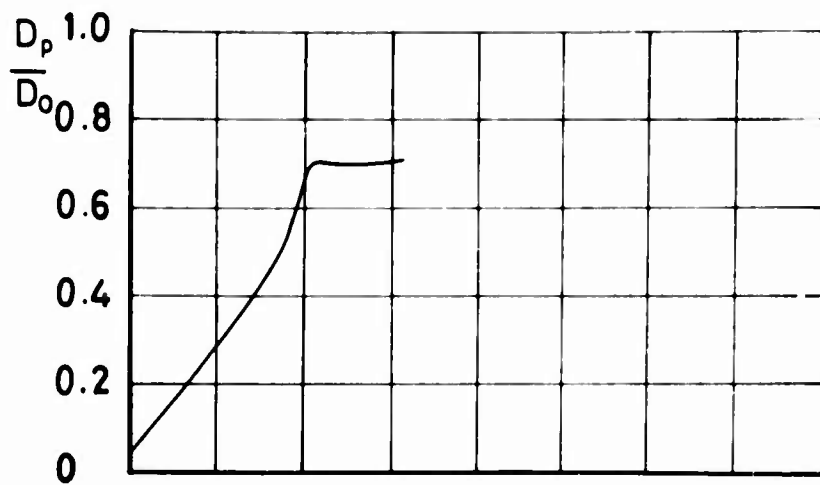


Location of
pressure trans-
ducers on
cord center line

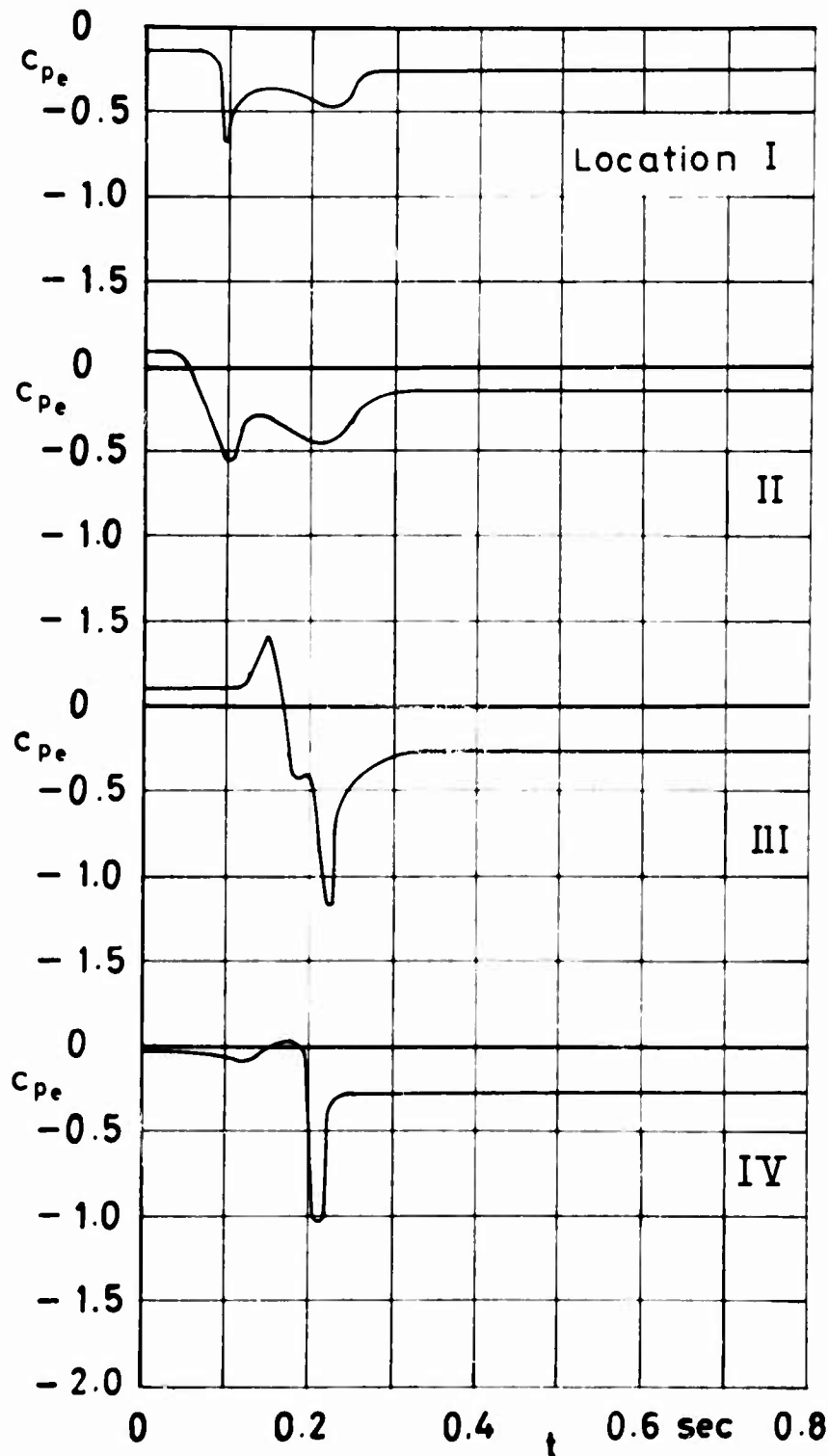


Extended
Skirt

Figure 24 c_{p_i}
and filling
versus time
 $v_0=130$ ft/sec
Run No.163

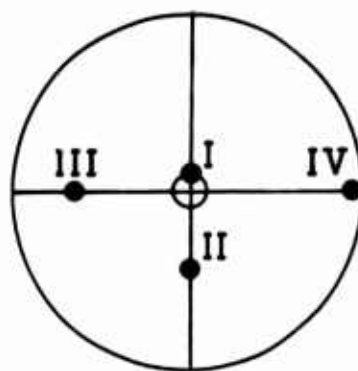
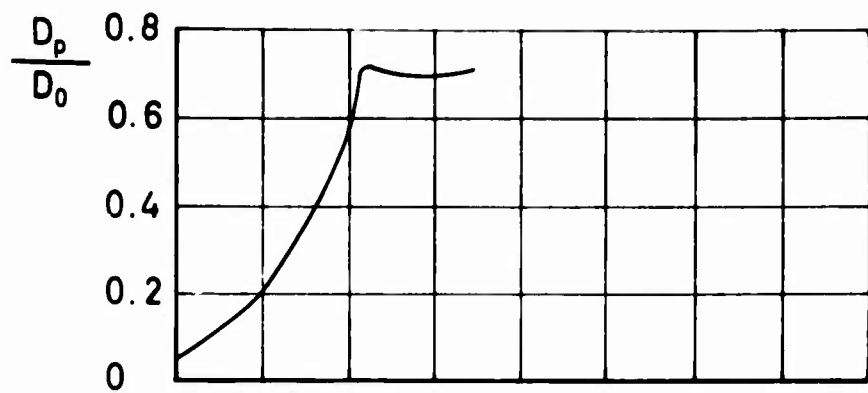


Location of
pressure trans-
ducers on
cord center line

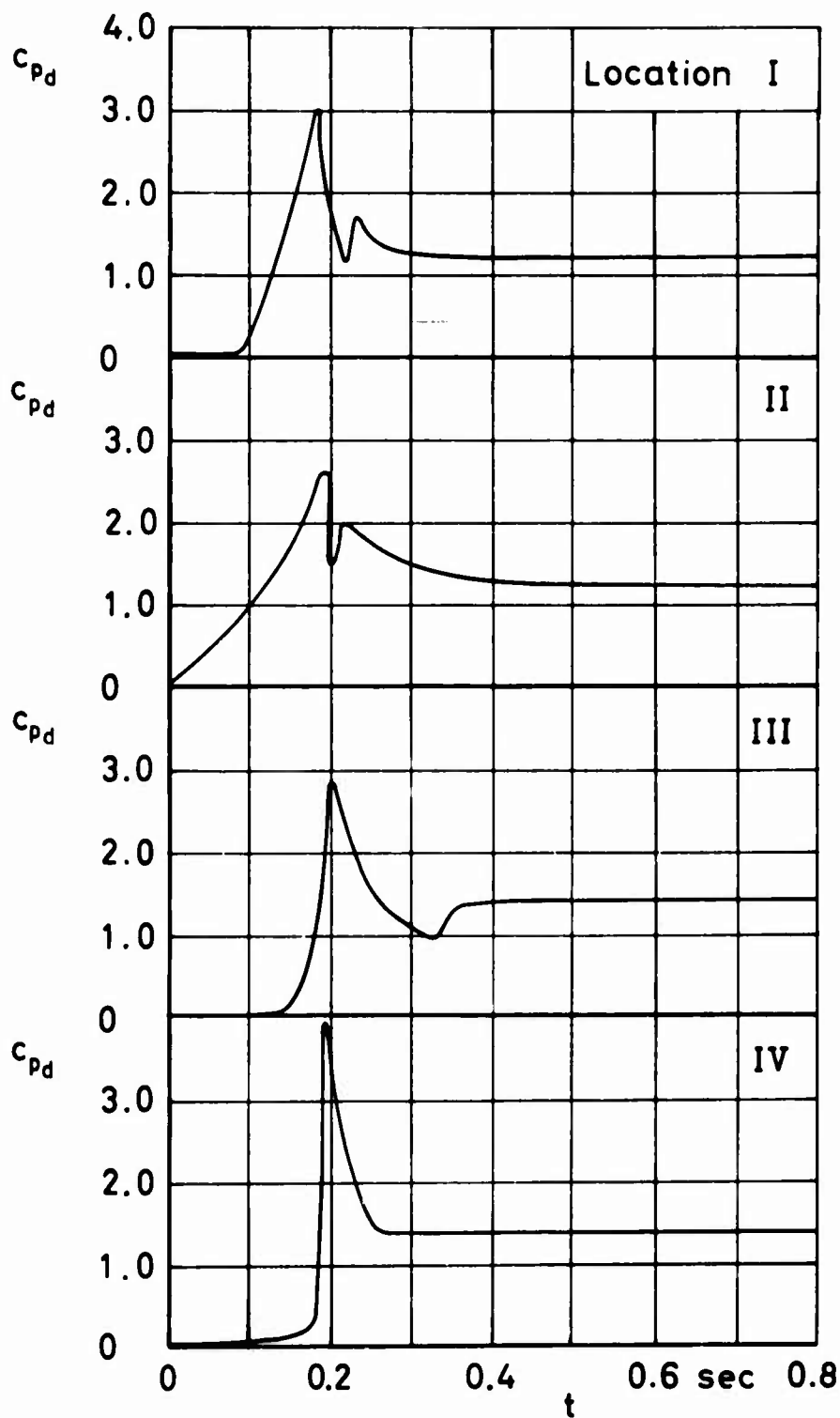


Extended
Skirt

Figure 25 c_{pe}
and filling
versus time
 $v_0 = 130$ ft/sec
Run No 231



Location of pressure transducers on cord center line

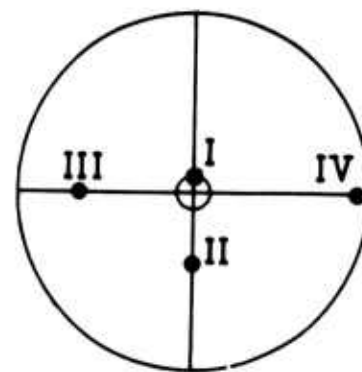
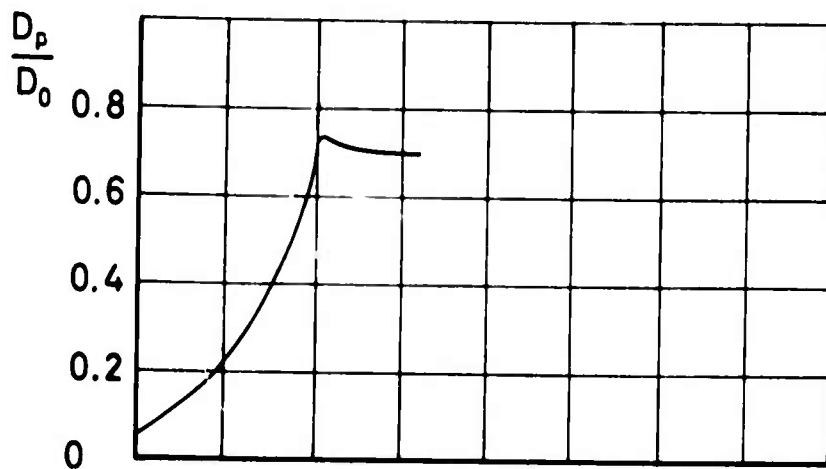


Extended Skirt

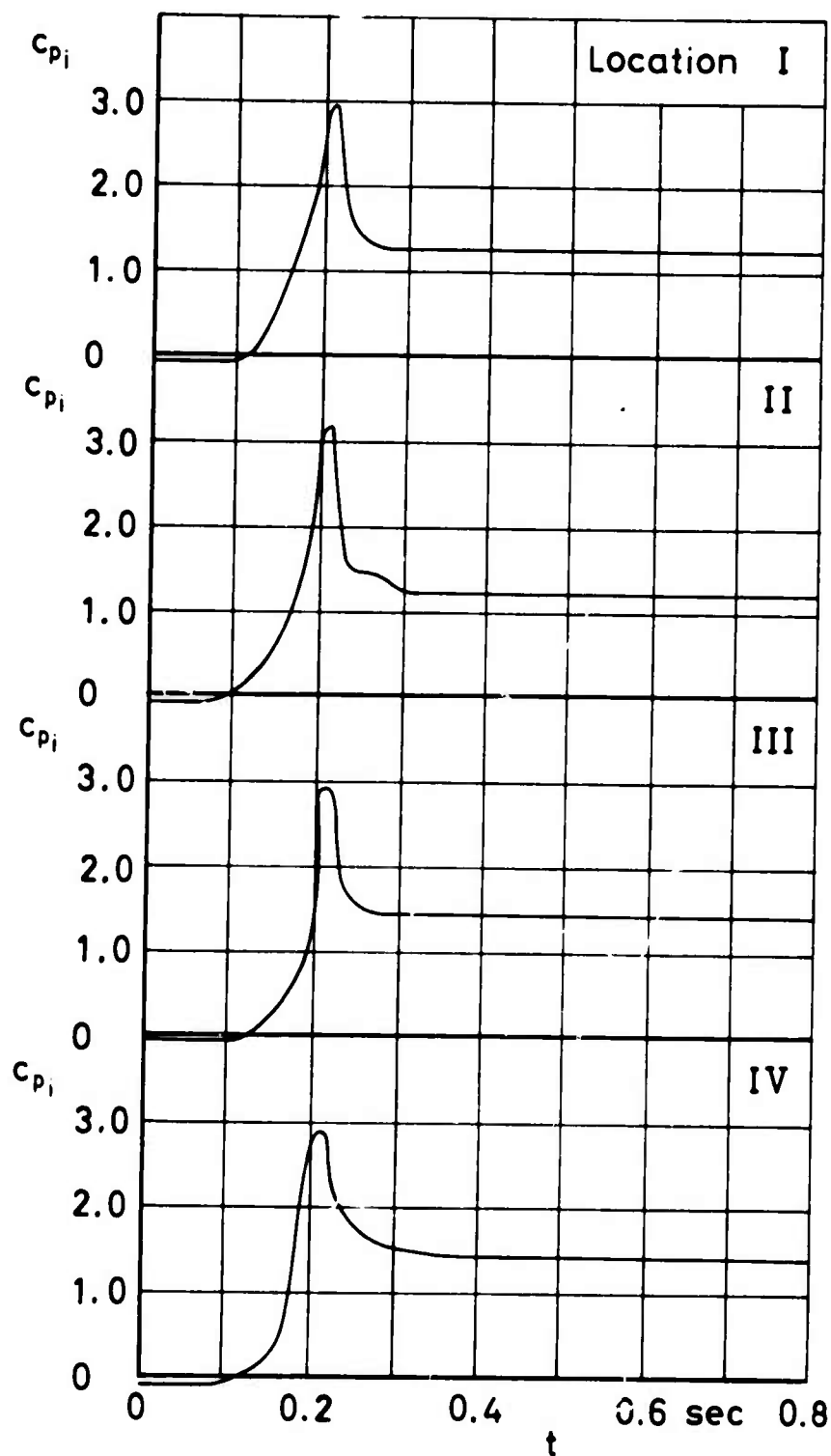
Figure 26 c_{pD} and filling versus time

$v_0 = 160 \text{ ft/sec}$

Run No. 153

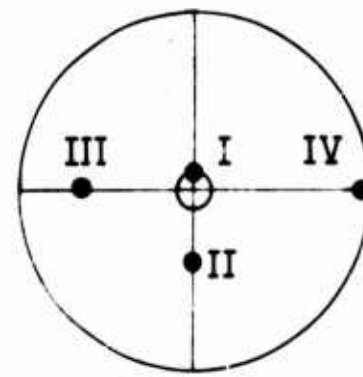
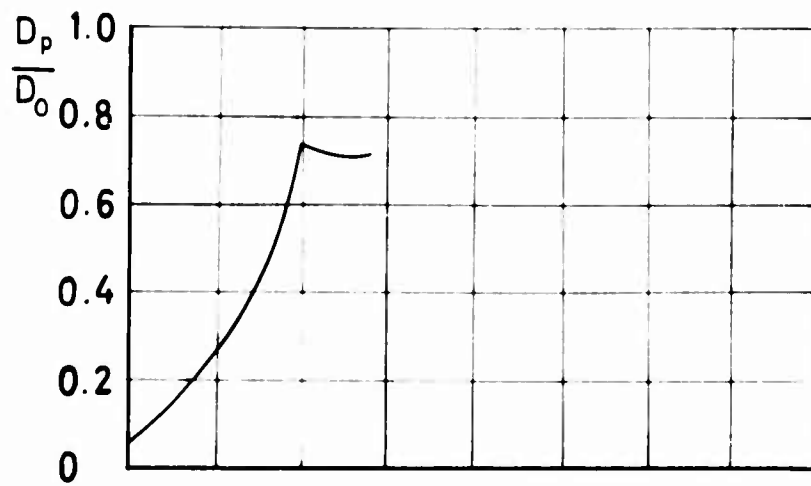


Location of
pressure trans-
ducers on
cord center line

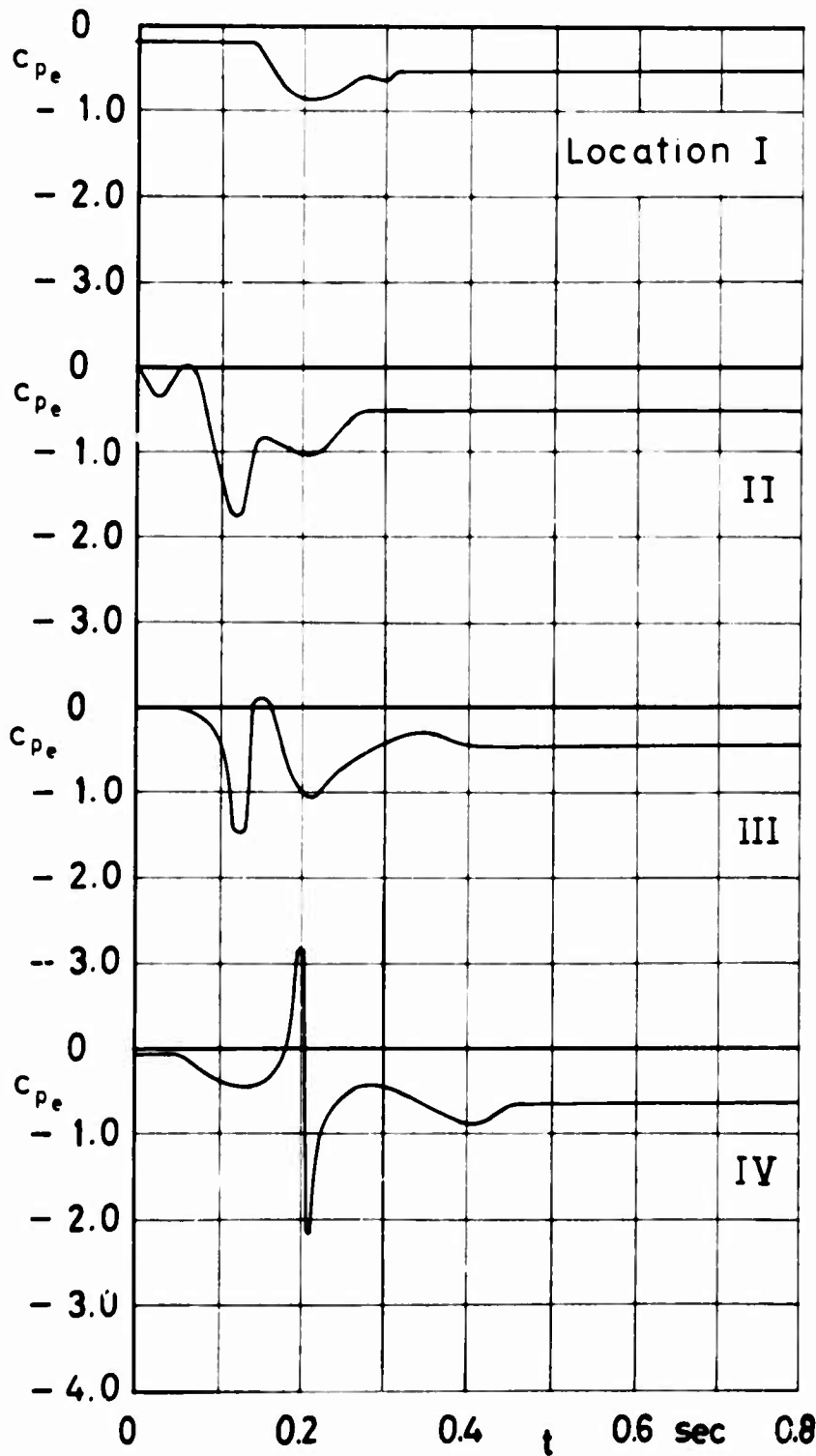


Extended Skirt

Figure 27 c_{pi}
and filling
versus time
 $v_0 = 160 \text{ ft/sec}$
R No. 166

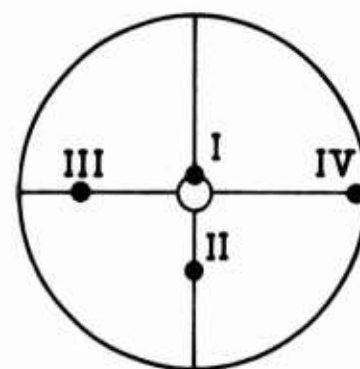
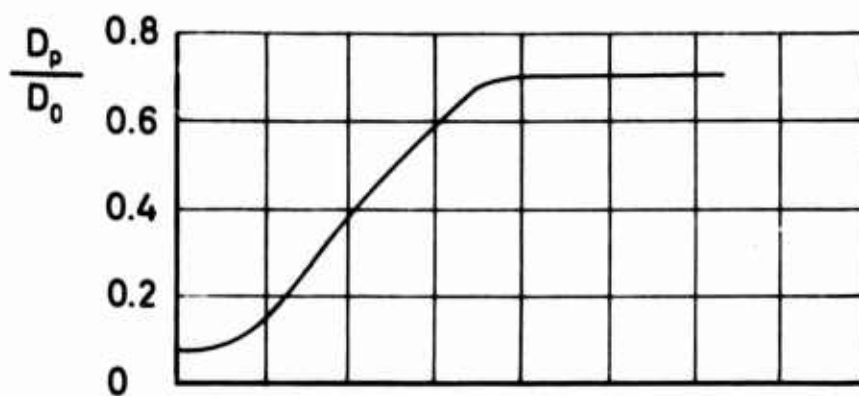


Location of
pressure trans-
ducers on
cord center line

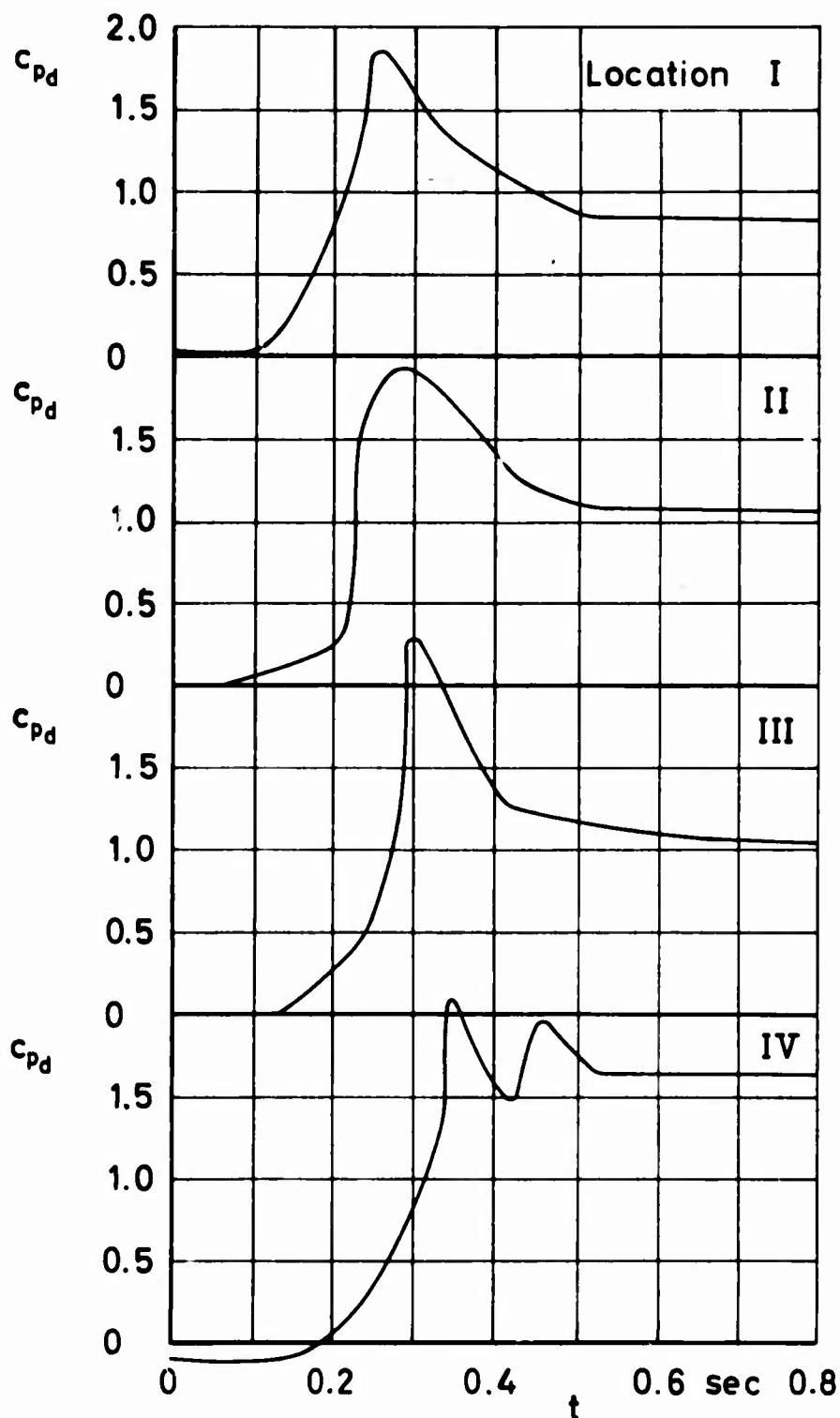


Extended
Skirt

Figure 28 c_{pe}
and filling
versus time
 $v_0 = 160 \text{ ft/sec}$
Run No 235



Location of pressure transducers on cord center line

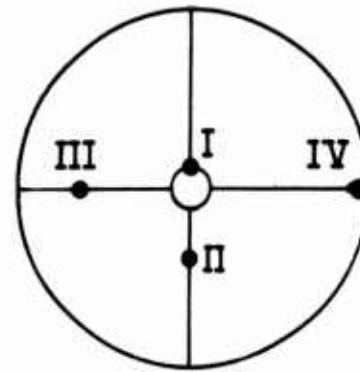
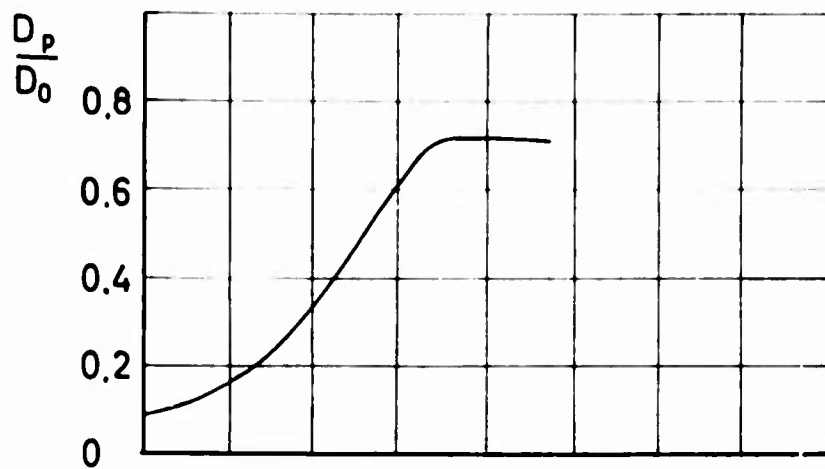


FIST

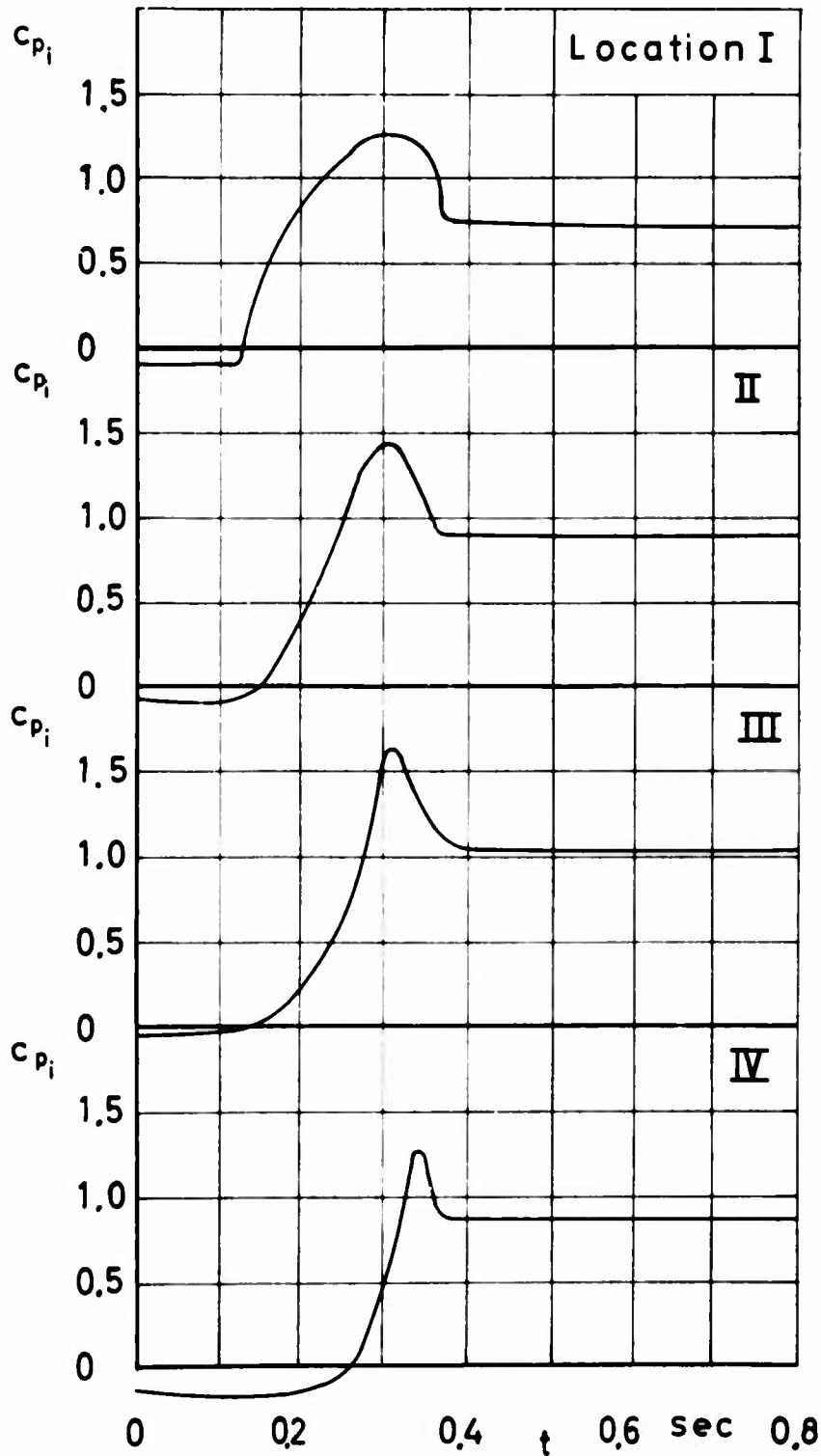
Figure 29 c_{pd} and filling versus time

$v_0 = 70 \text{ ft/sec}$

Run No.72

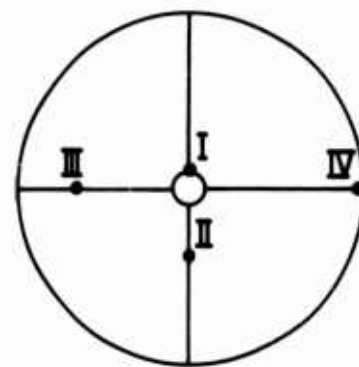
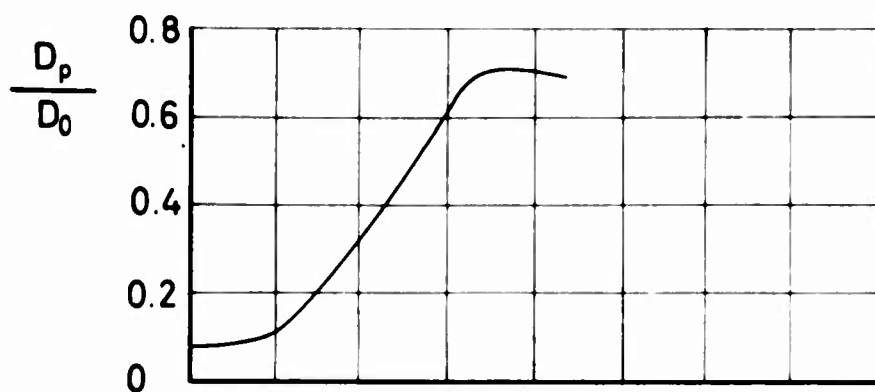


Location of
pressure trans-
ducers on
cord center line

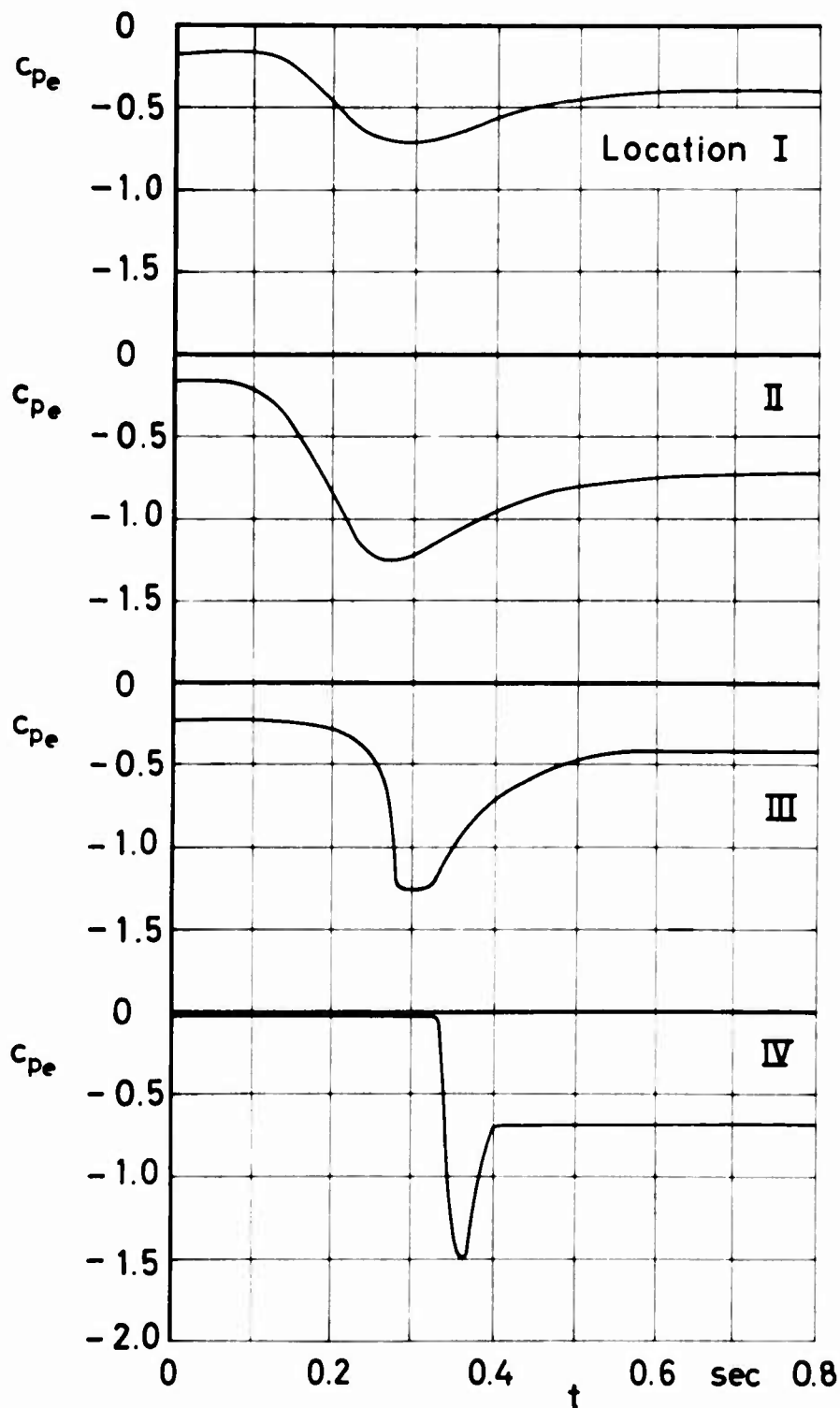


FIST

Figure 30 c_{pi}
and filling
versus time
 $v_0=70$ ft/sec
Run No 101



Location of pressure transducers on cord center line

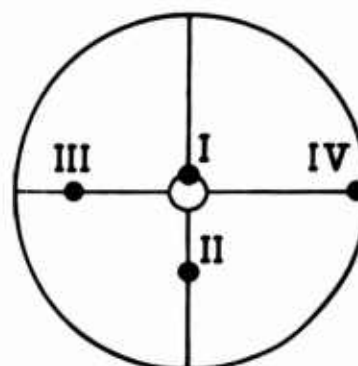
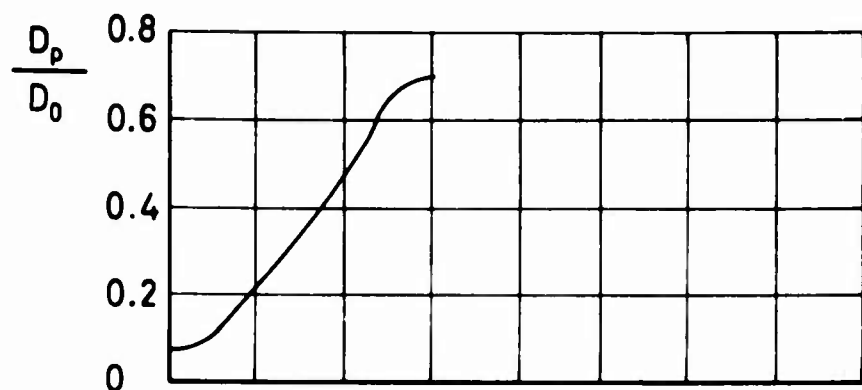


FIST

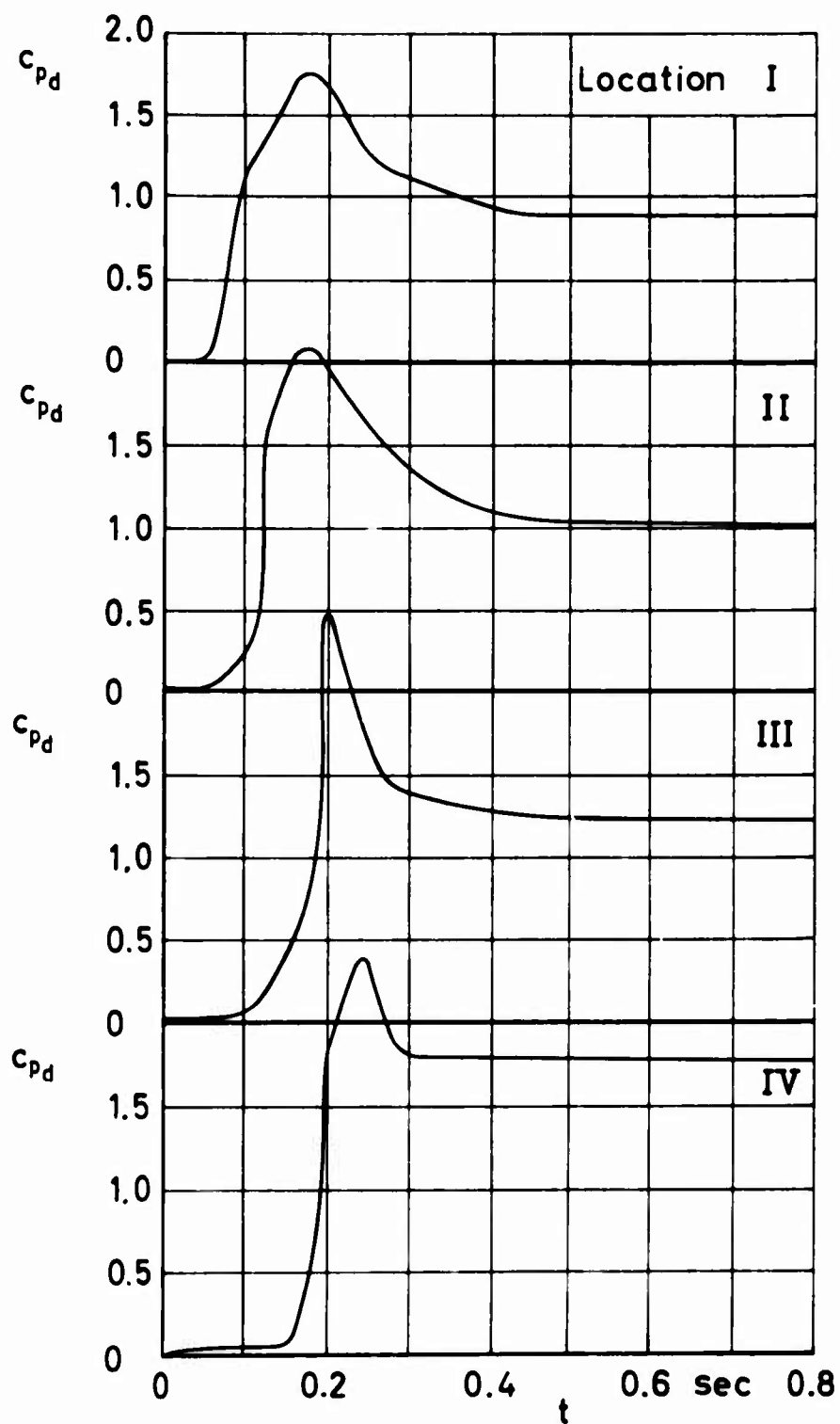
Figure 31 c_{pe} and filling versus time

$v_0 = 70 \text{ ft/sec}$

Run No. 104



Location of pressure
transducers on
cord center line

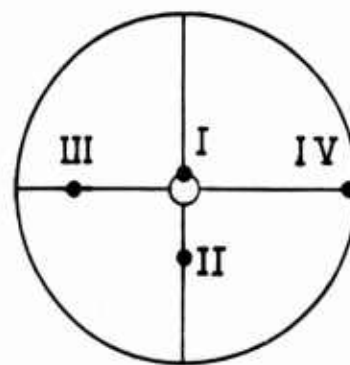
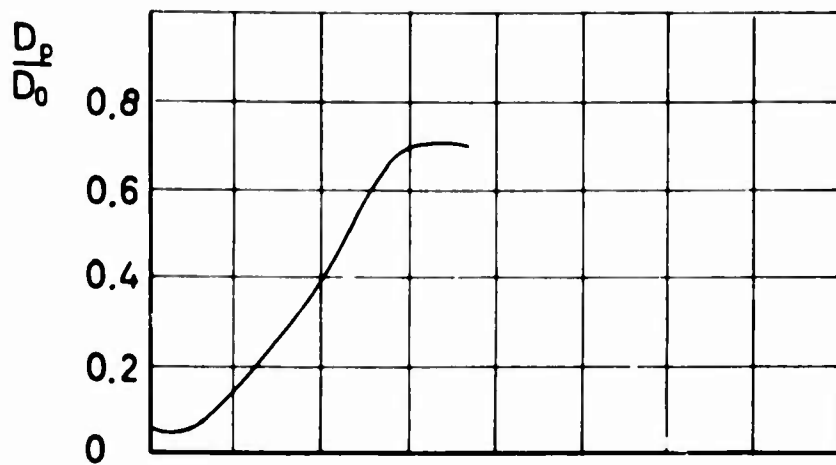


FIST

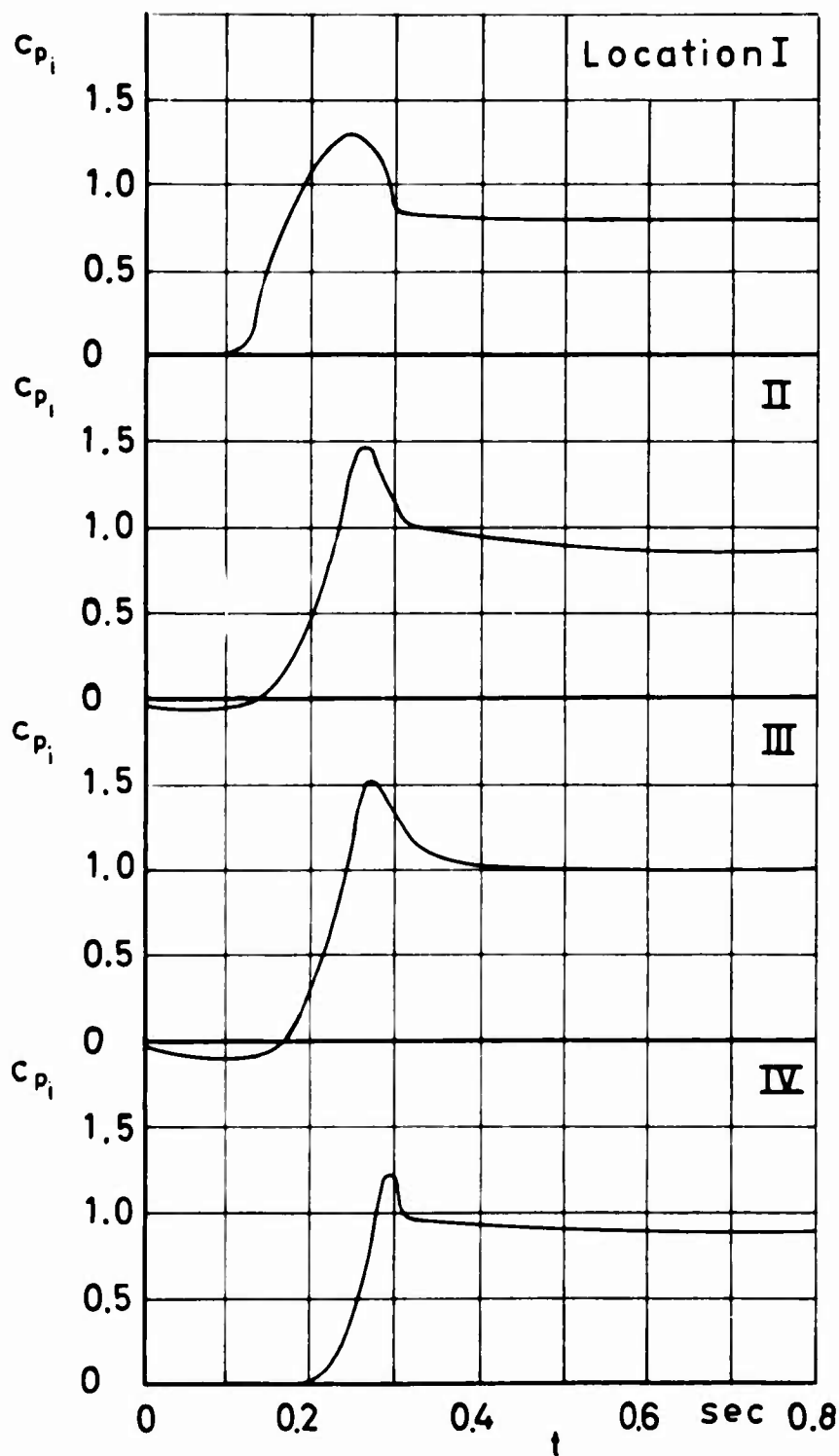
Figure 32 c_{pd} and
filling versus time

$v_0 = 100 \text{ ft/sec}$

Run No. 76

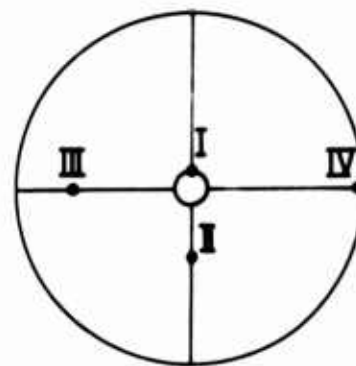
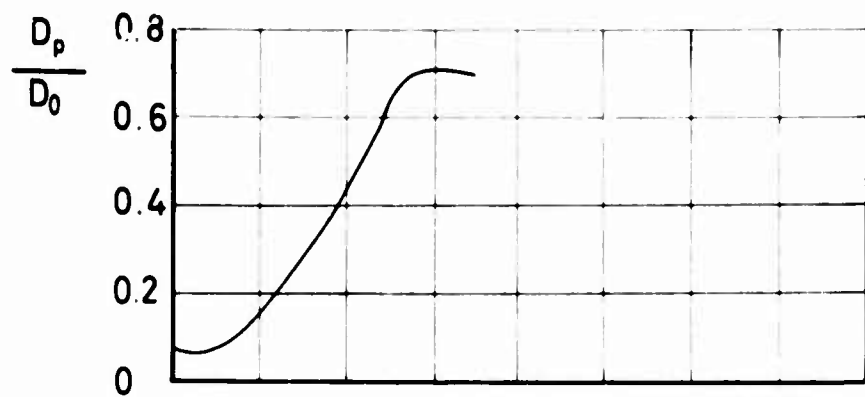


Location of
pressure trans-
ducers on
cord center line

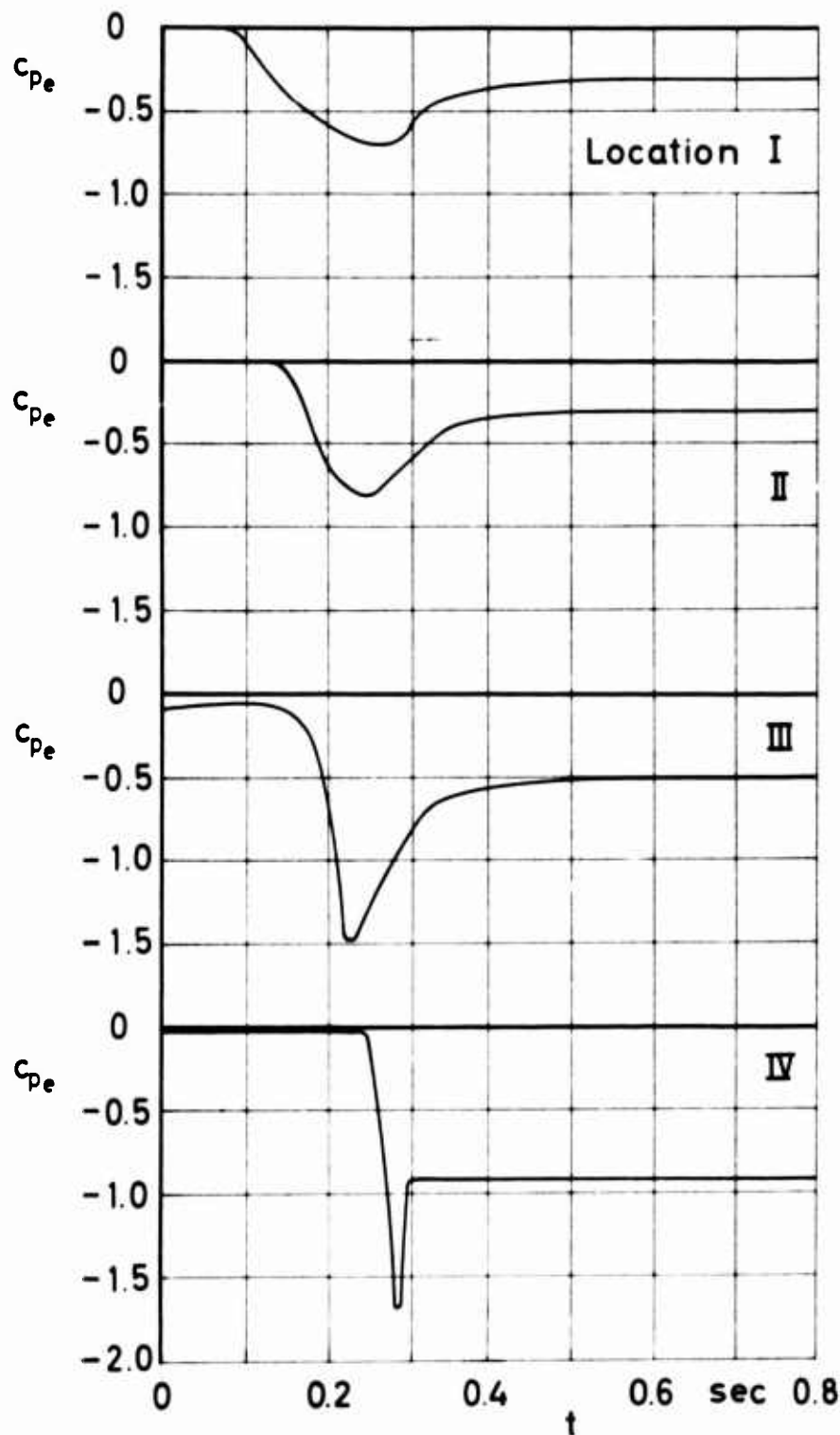


FIST

Figure 33 c_{pi}
and filling
versus time
 $v_0 = 100$ ft/sec
Run No 97



Location of pressure transducers on cord center line

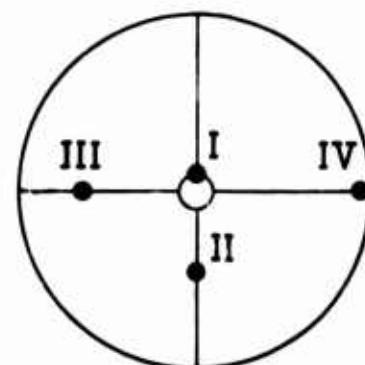
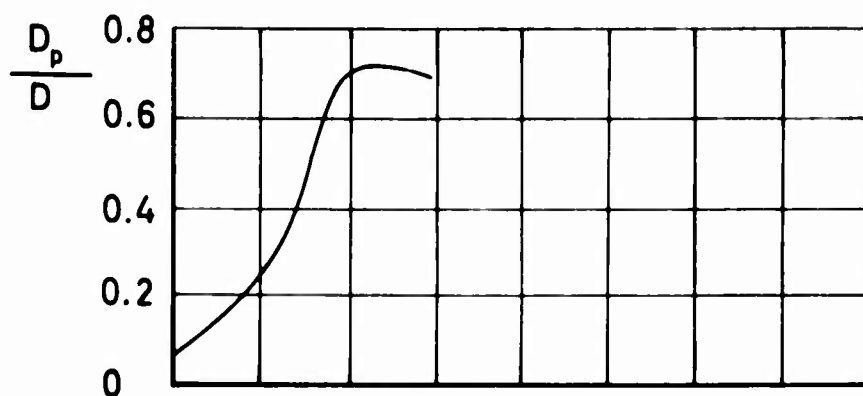


FIST

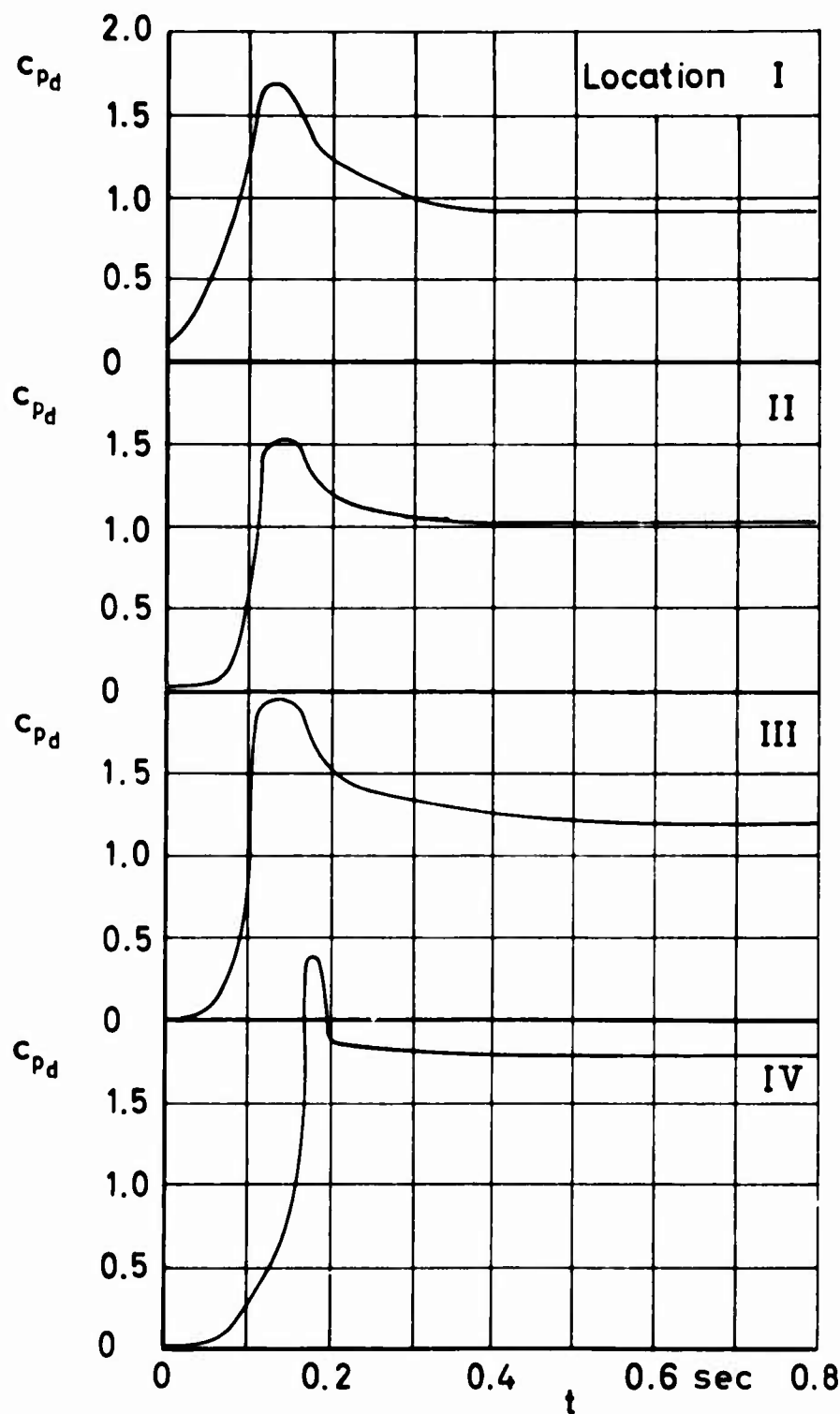
Figure 34 c_{pe} and filling versus time

$v_0 = 100 \text{ ft/sec}$

Run No. 110

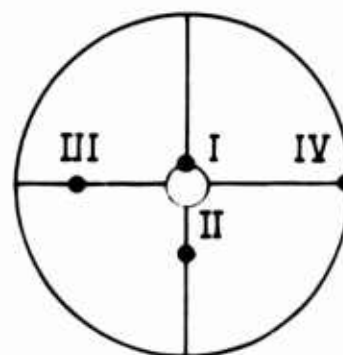
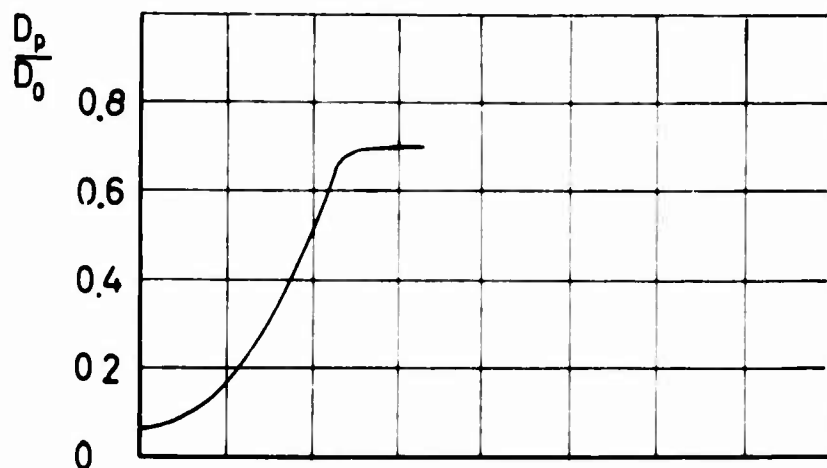


Location of pressure transducers on cord center line

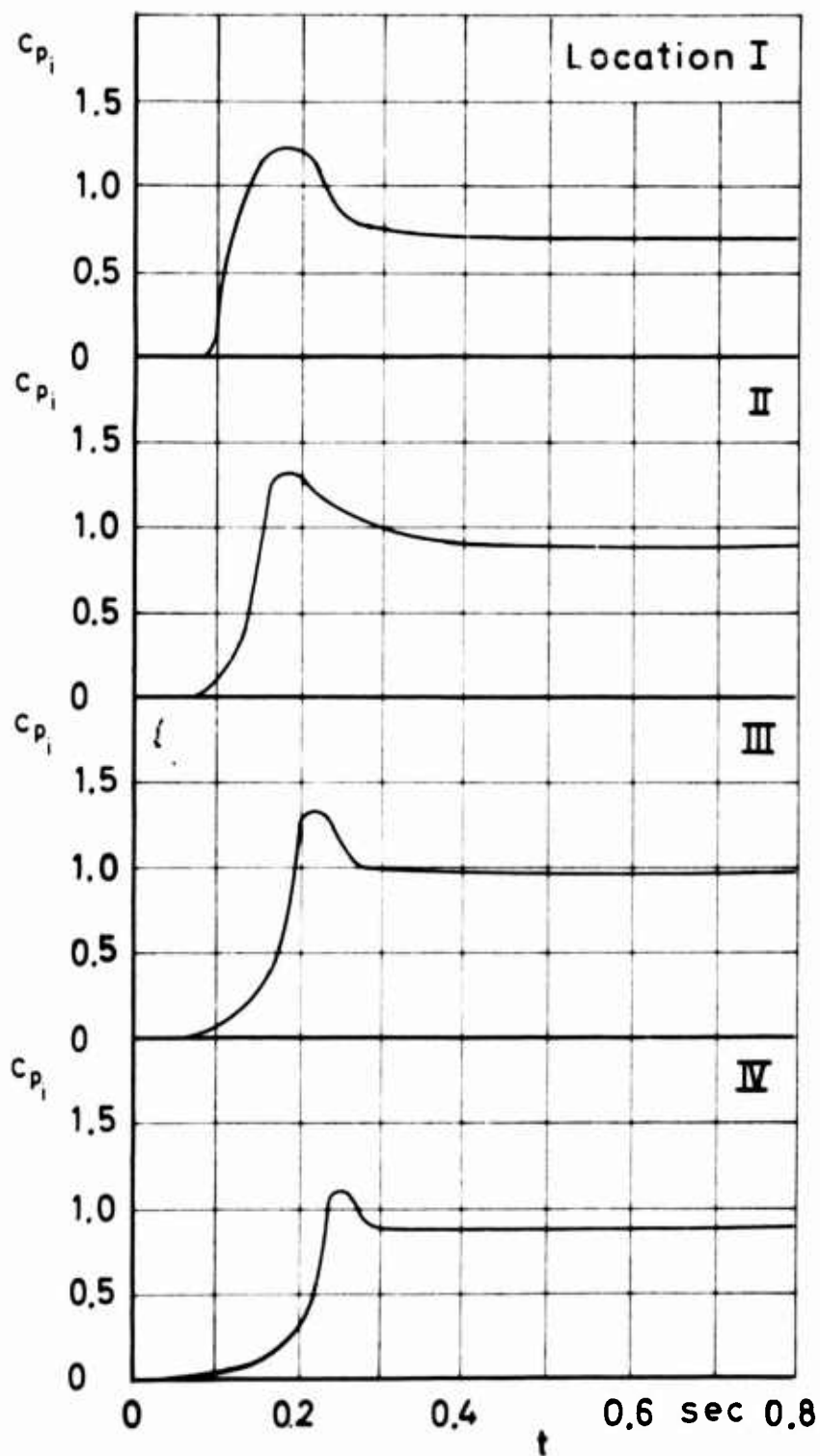


FIST

Figure 35 c_{Pd} and filling versus time
 $v_0=130\text{ft/sec}$
 Run No.82

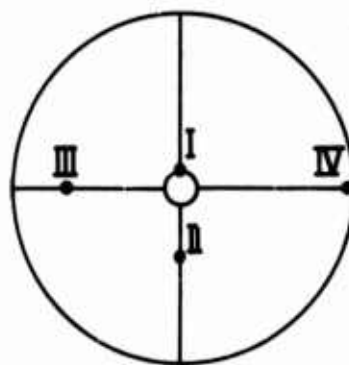
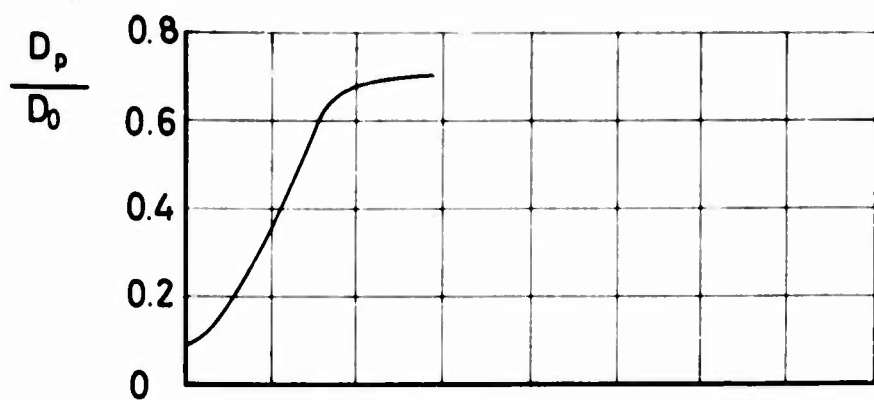


Location of
pressure trans-
ducers on
cord center line

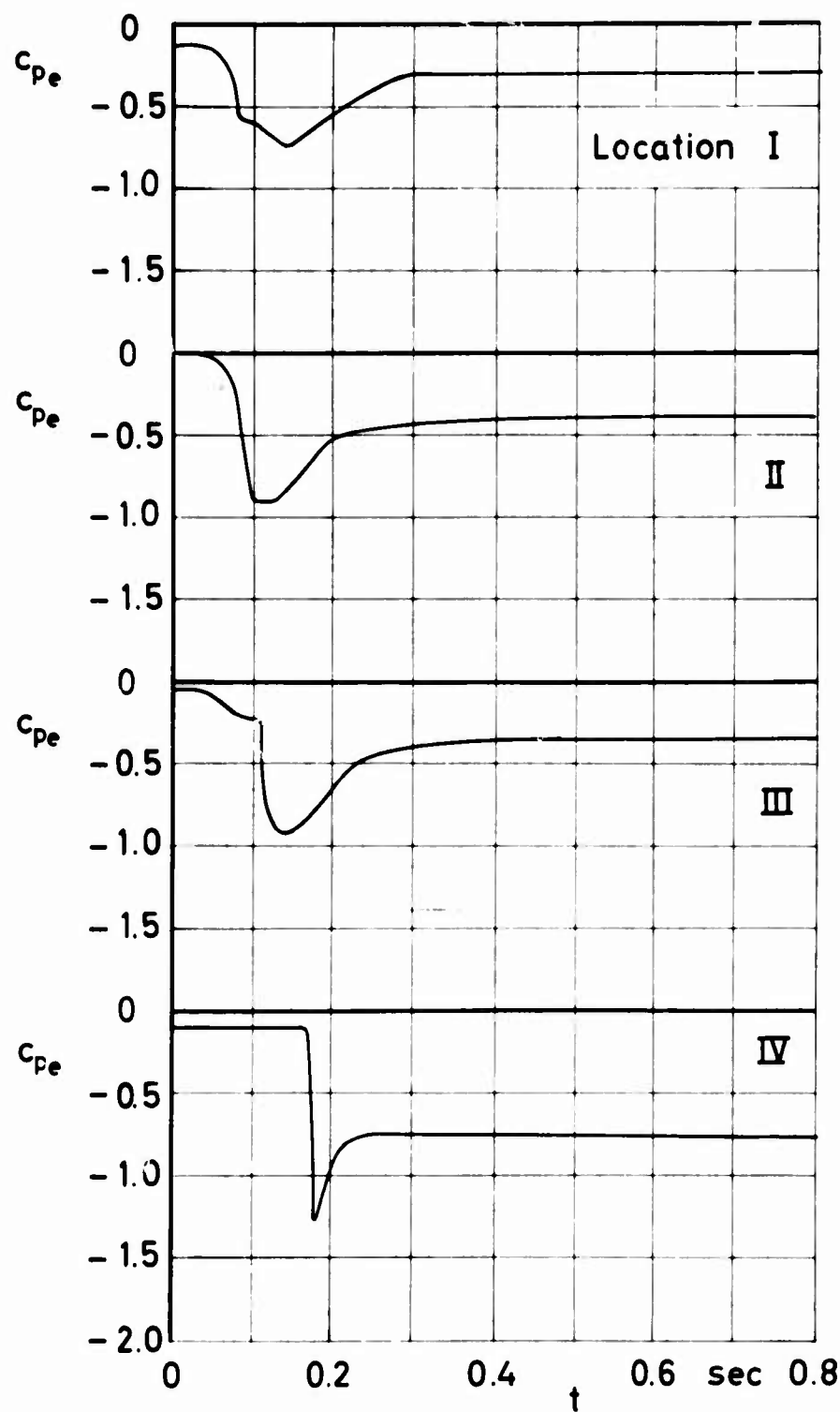


FIST

Figure 36 c_{pi}
and filling
versus time
 $v_0 = 130$ ft/sec
Run No 92



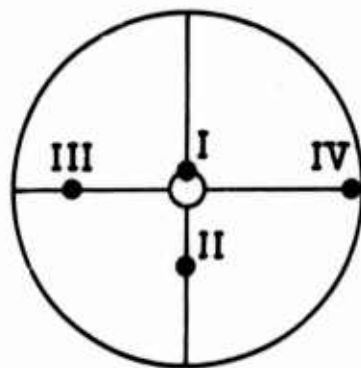
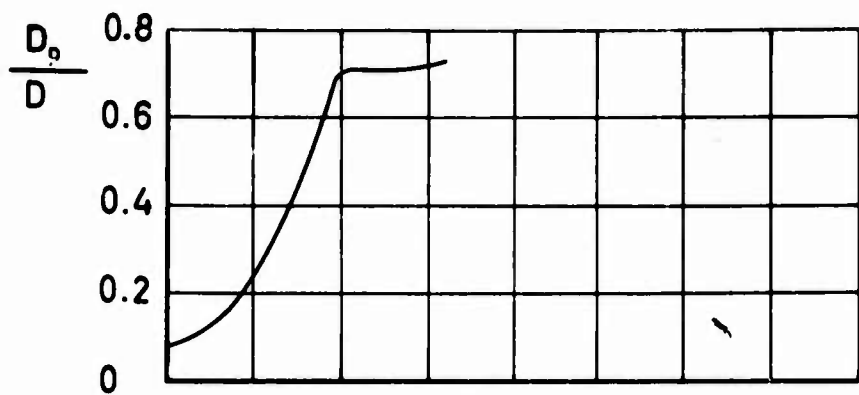
Location of pressure transducers on cord center line



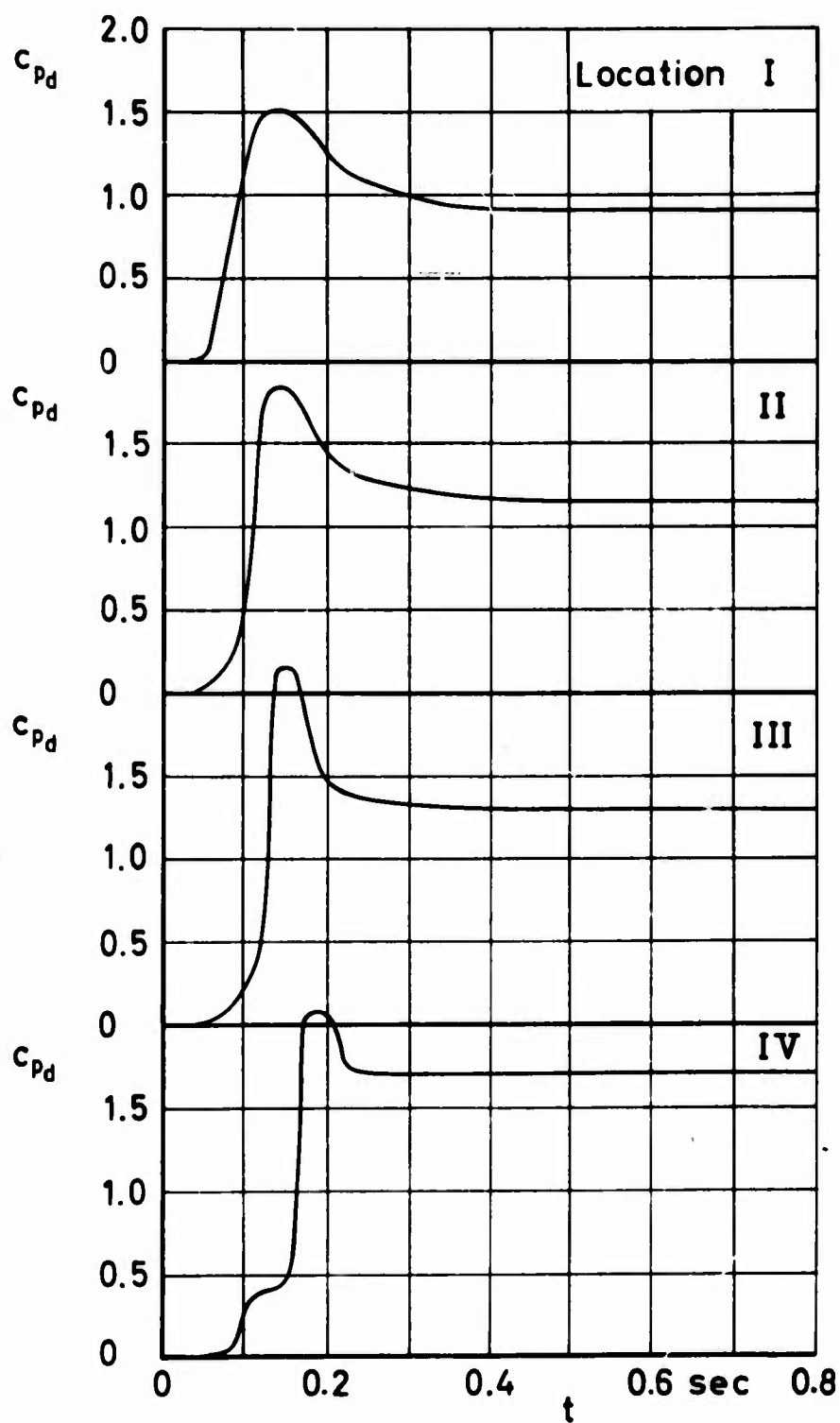
FIST

Figure 37 c_{pe} and filling versus time

$v_0 = 130 \text{ ft/sec}$
Run No. 117



Location of pressure transducers on cord center line

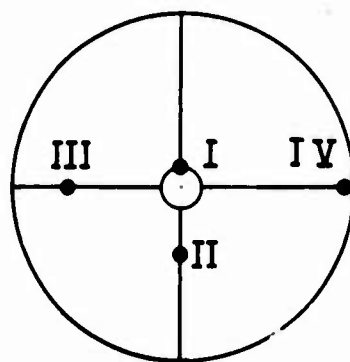
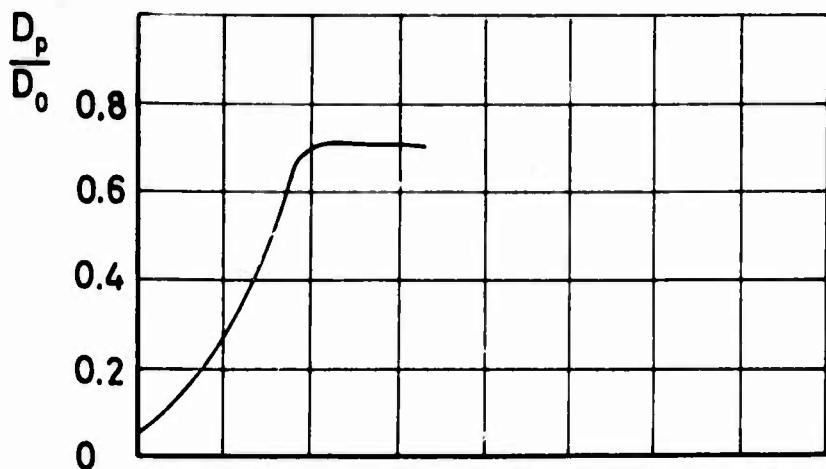


FIST

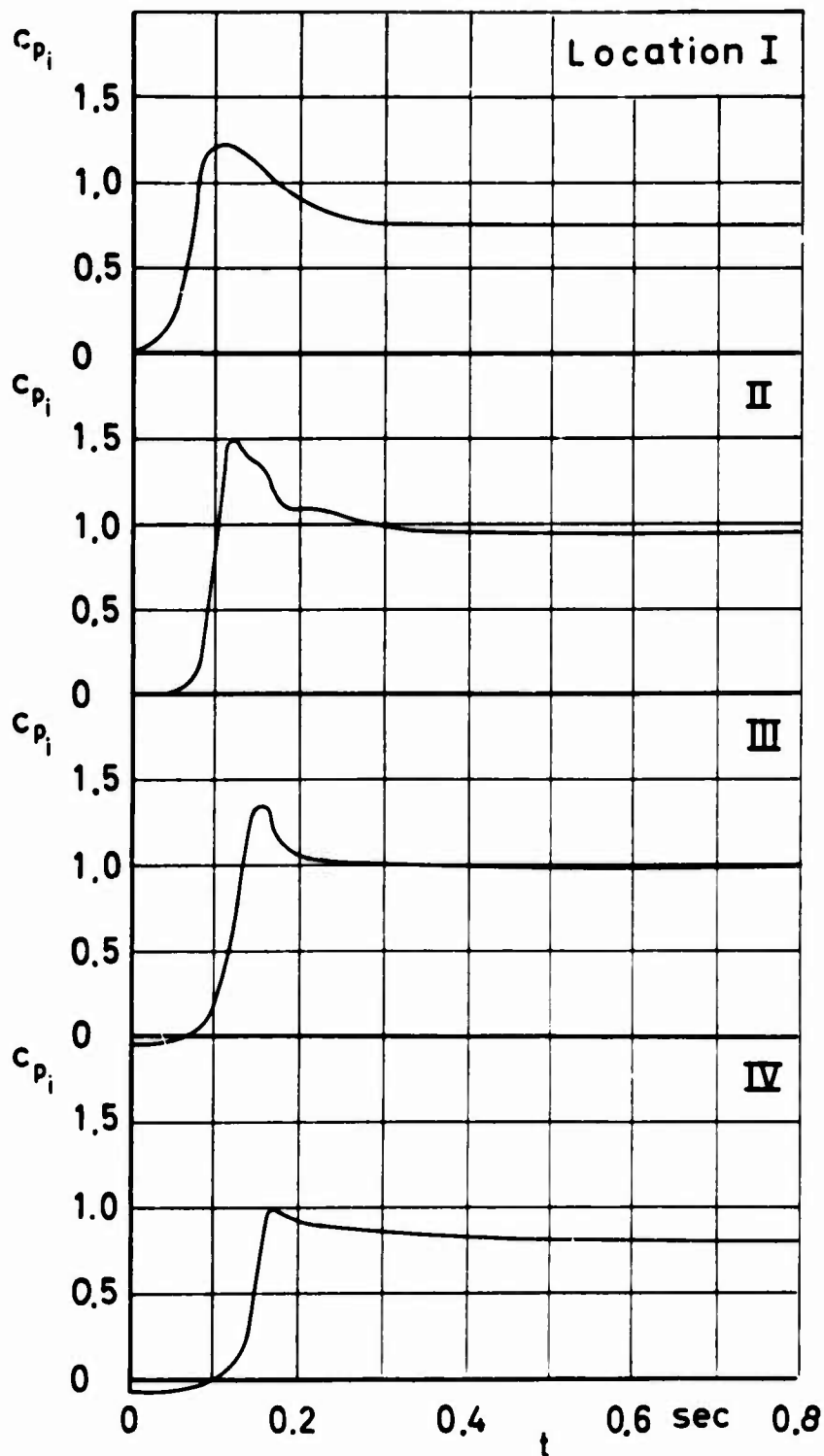
Figure 38 c_{pd} and filling versus time

$v_0 = 160 \text{ ft/sec}$

Run No. 86

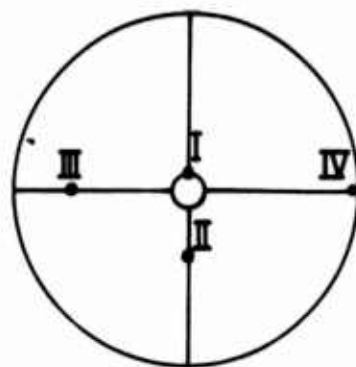
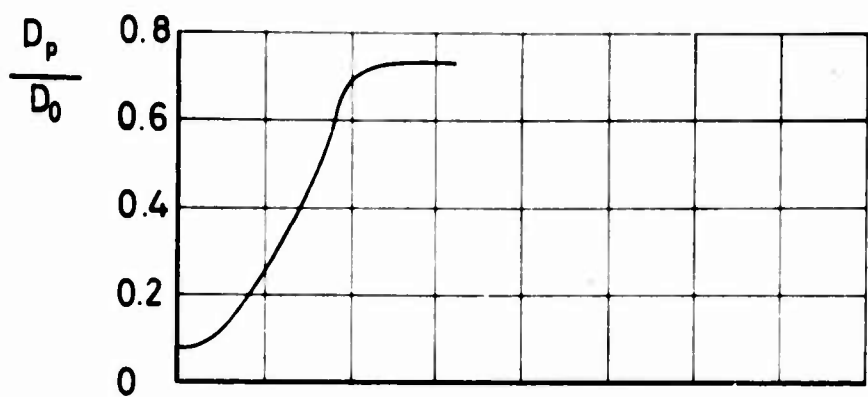


Location of
pressure trans-
ducers on
cord center line

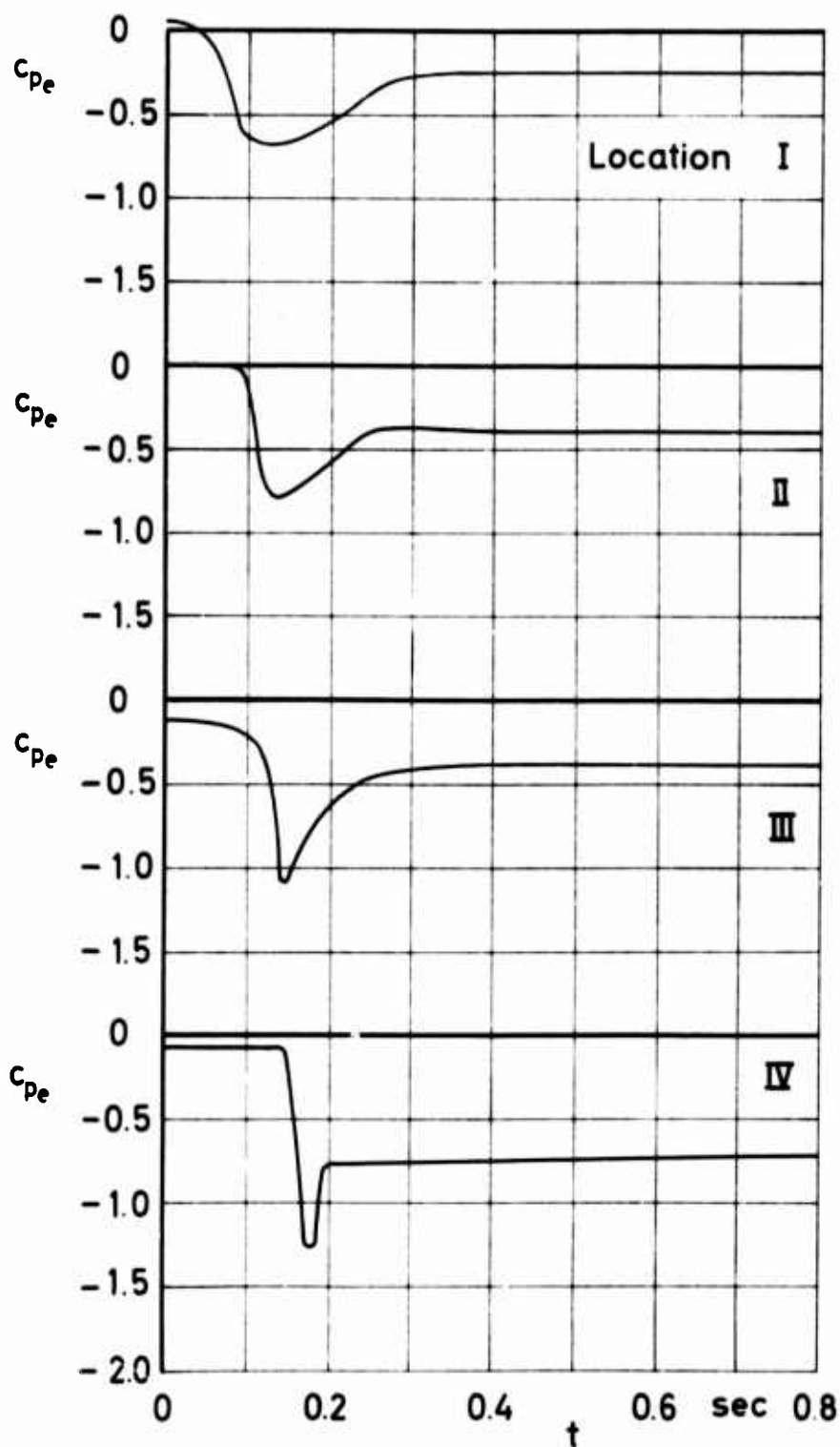


FIST

Figure 39 c_{pi}
and filling
versus time
 $v_0=160$ ft/sec
Run No 88



Location of pressure transducers on cord center line

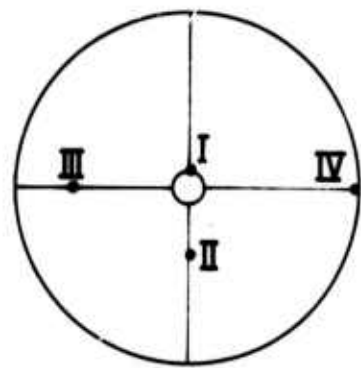
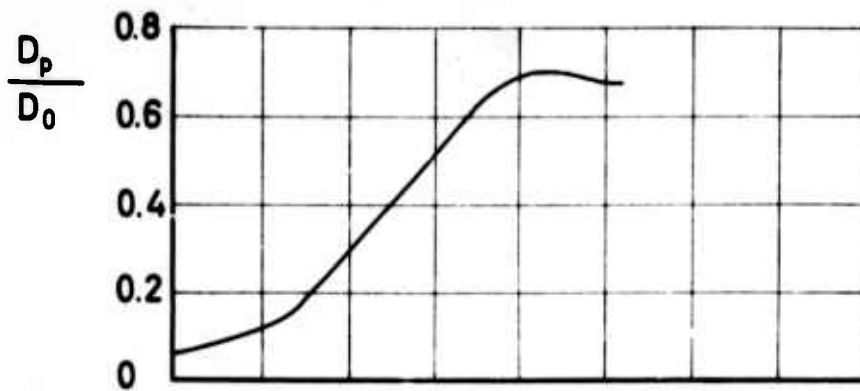


FIST

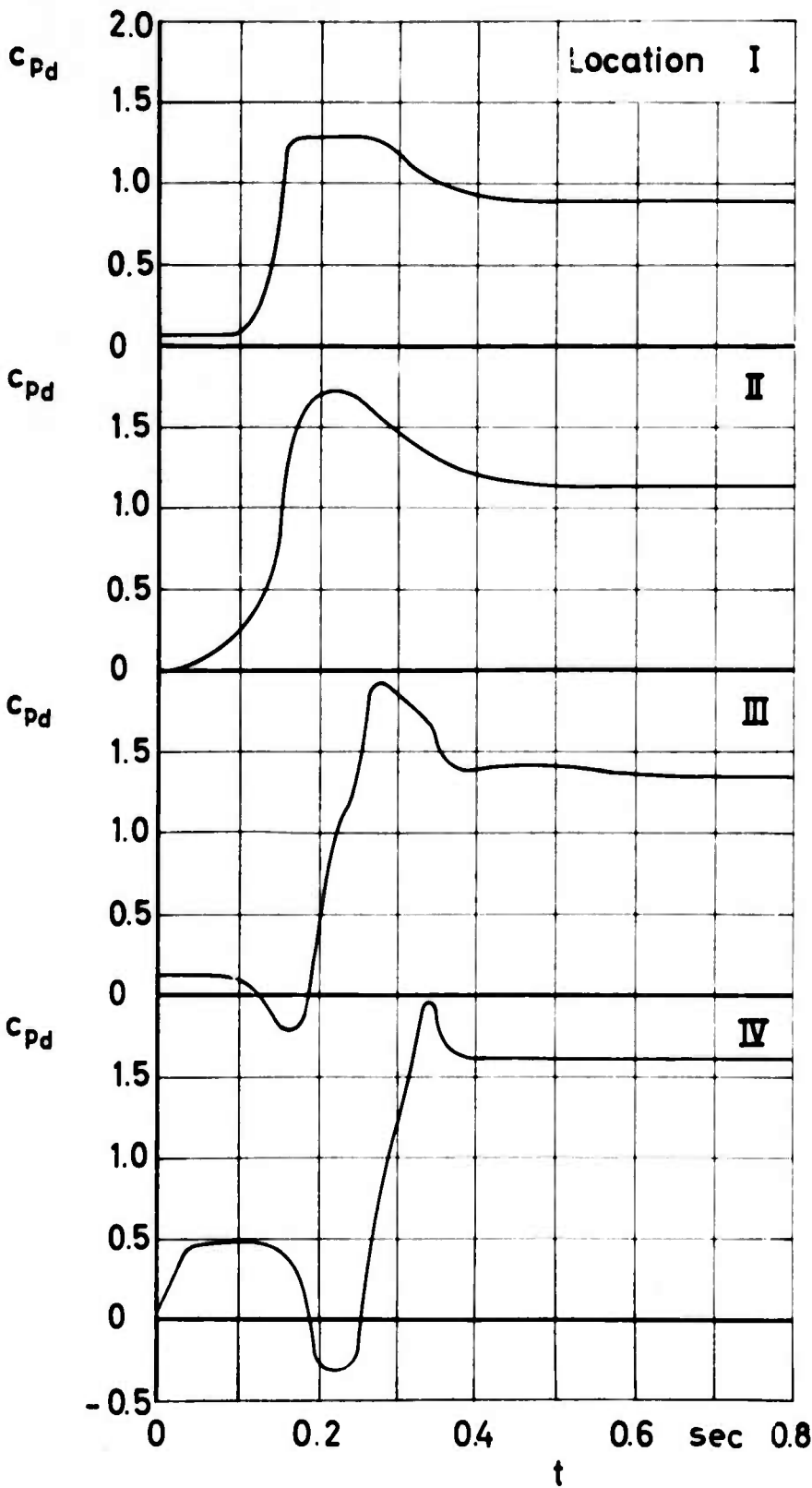
Figure 40 c_{pe} and filling versus time

$v_0 = 160 \text{ ft / sec}$

Run No. 119



Location of pressure
transducers on
cord center line

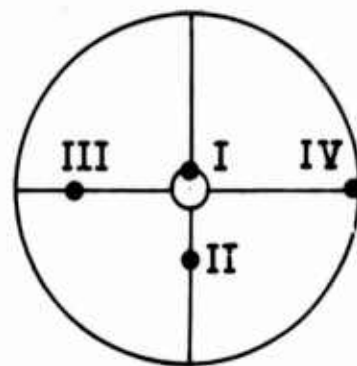
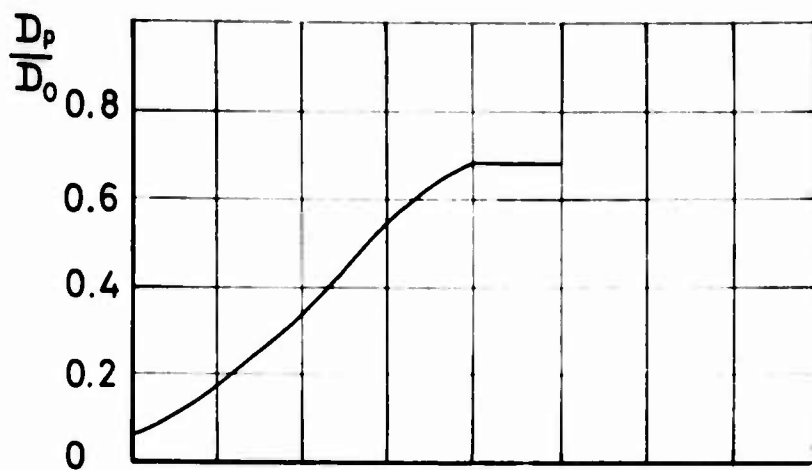


Ringslot

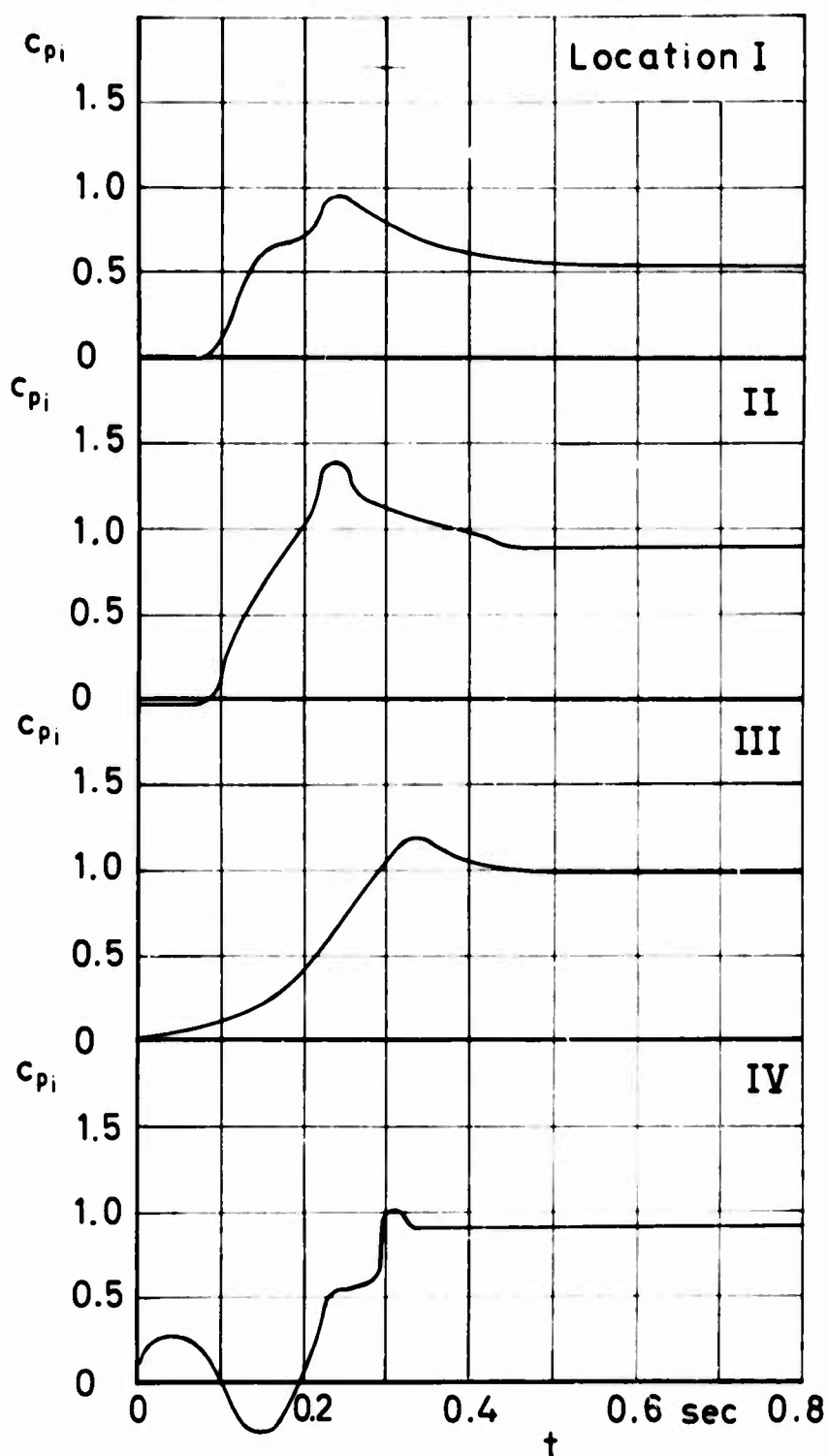
Figure 41 c_{pd} and
filling versus time

$v_0 = 70 \text{ ft / sec}$

Run No. 7

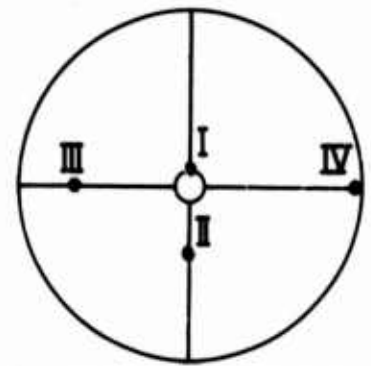
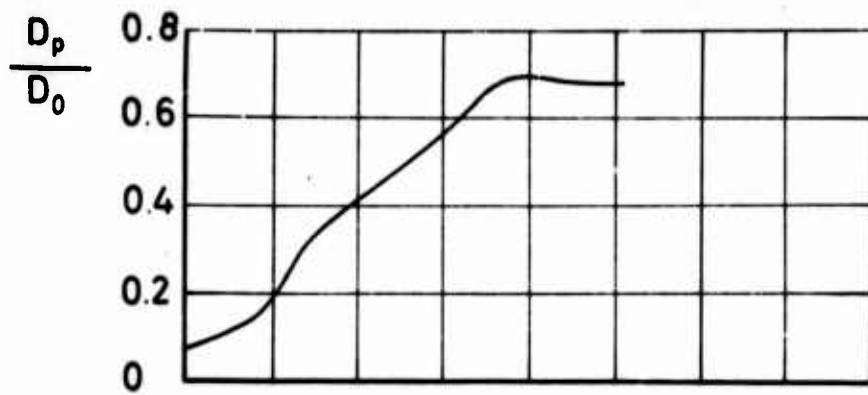


Location of
pressure trans-
ducers on
cord center line

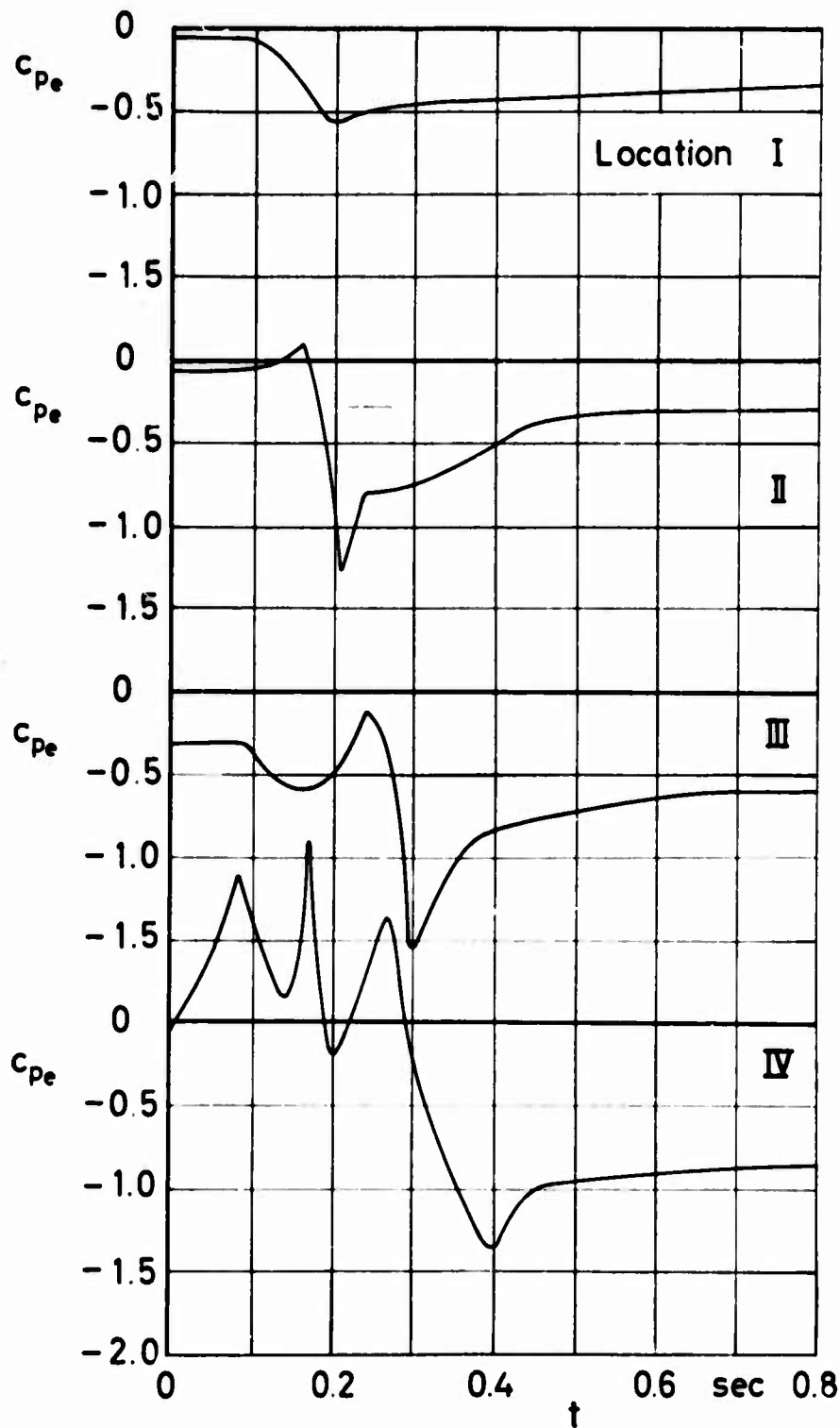


Ringslot

Figure 42 c_{pi}
and filling
versus time
 $v_0 = 70$ ft/sec
Run No 22



Location of pressure transducers on cord center line

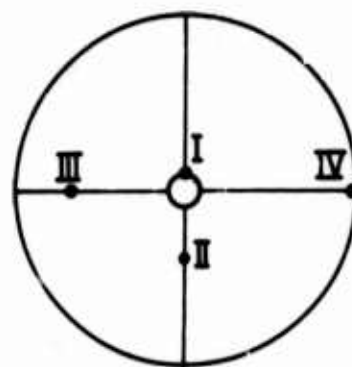
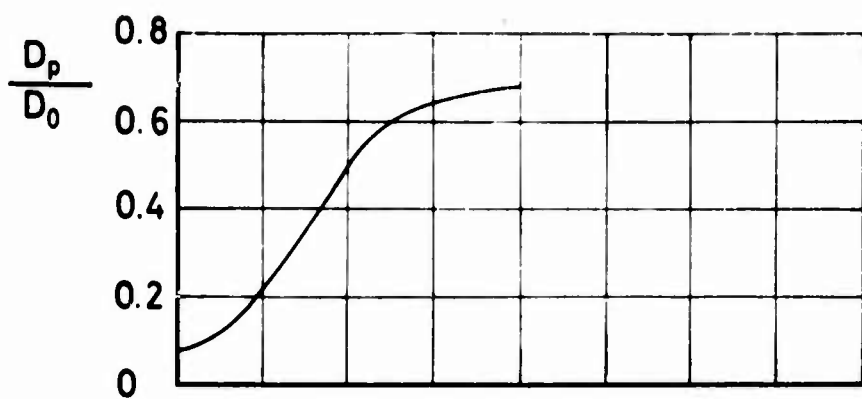


Ringslot

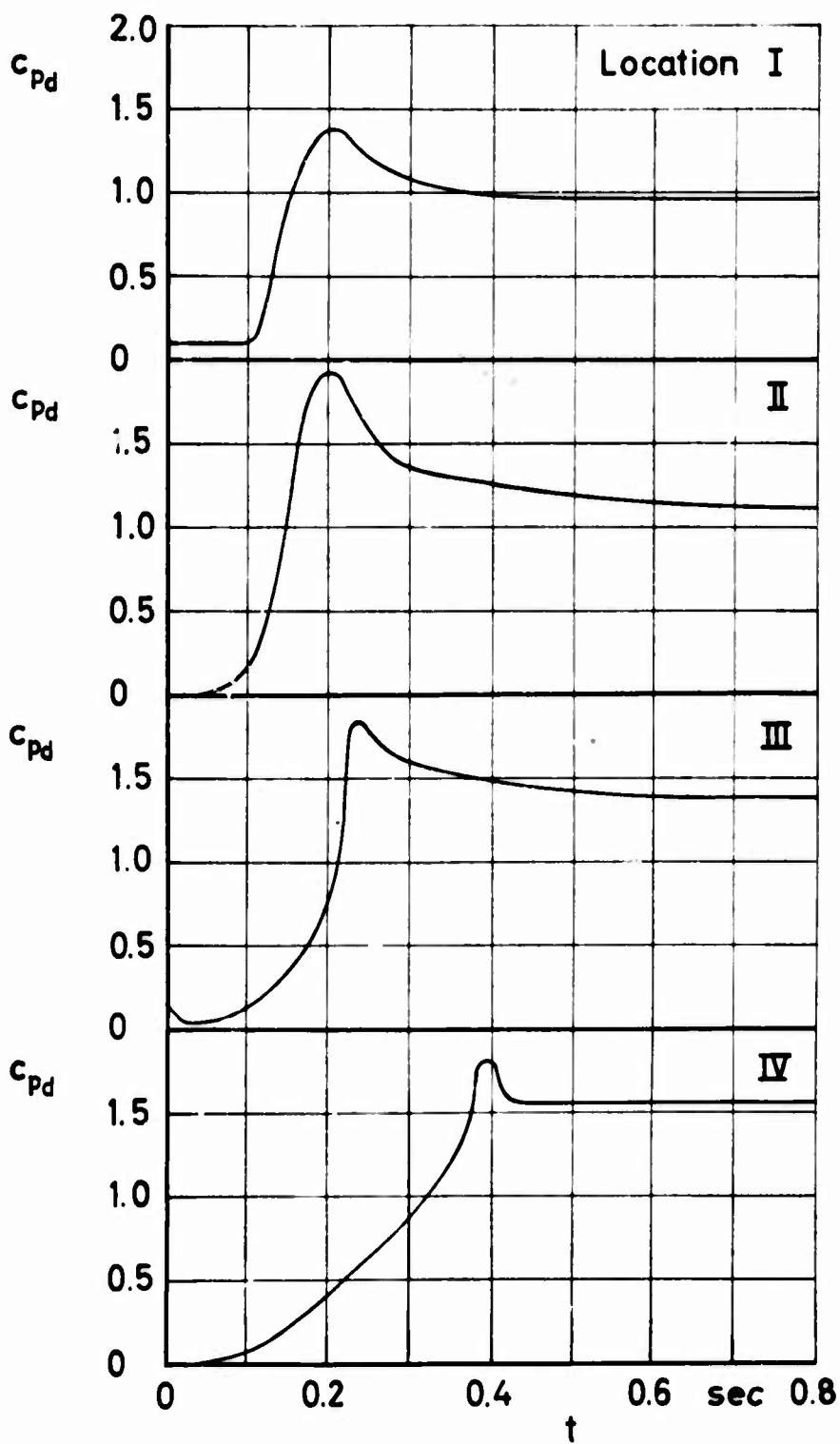
Figure 43 c_{pe} and filling versus time

$v_0 = 70 \text{ ft/sec}$

Run No. 34



Location of pressure transducers on cord center line

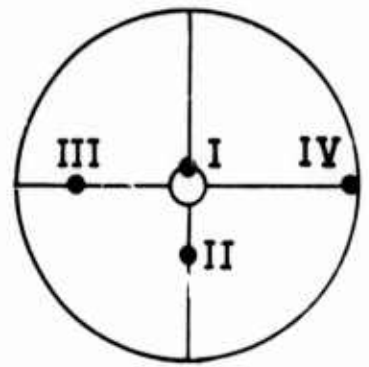
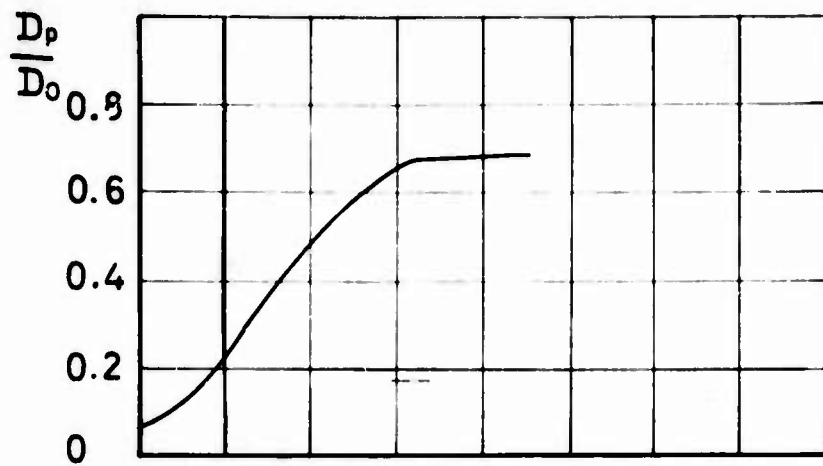


Ringslot

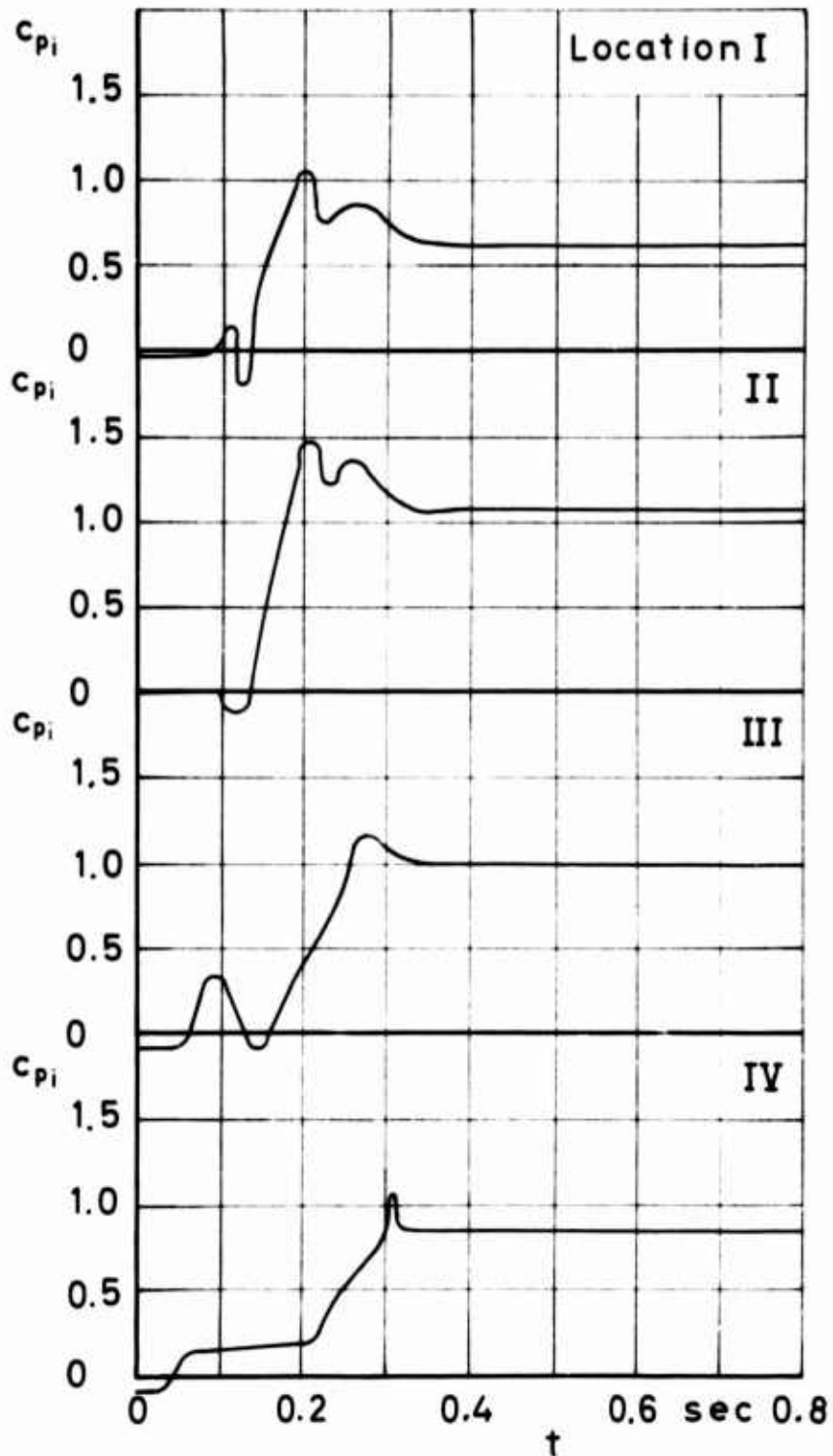
Figure 44 c_{pd} and filling versus time

$v_0 = 100 \text{ ft/sec}$

Run No. 10

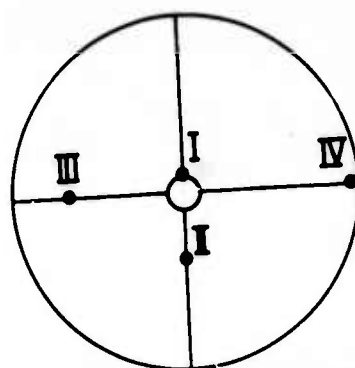
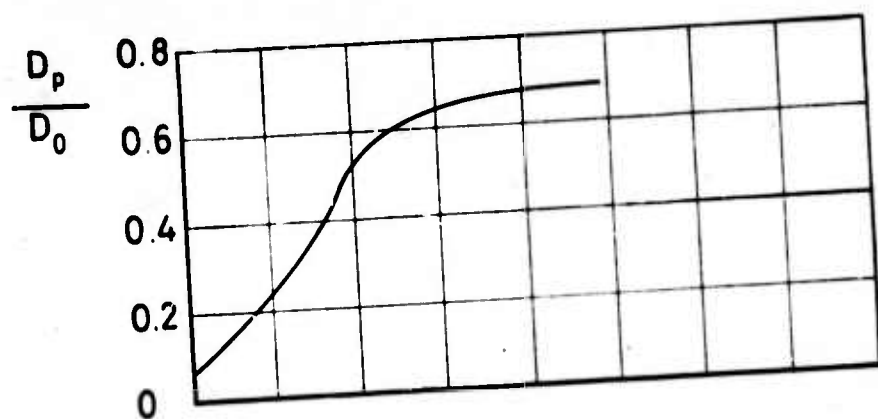


Location of
pressure trans-
ducers on
cord center line

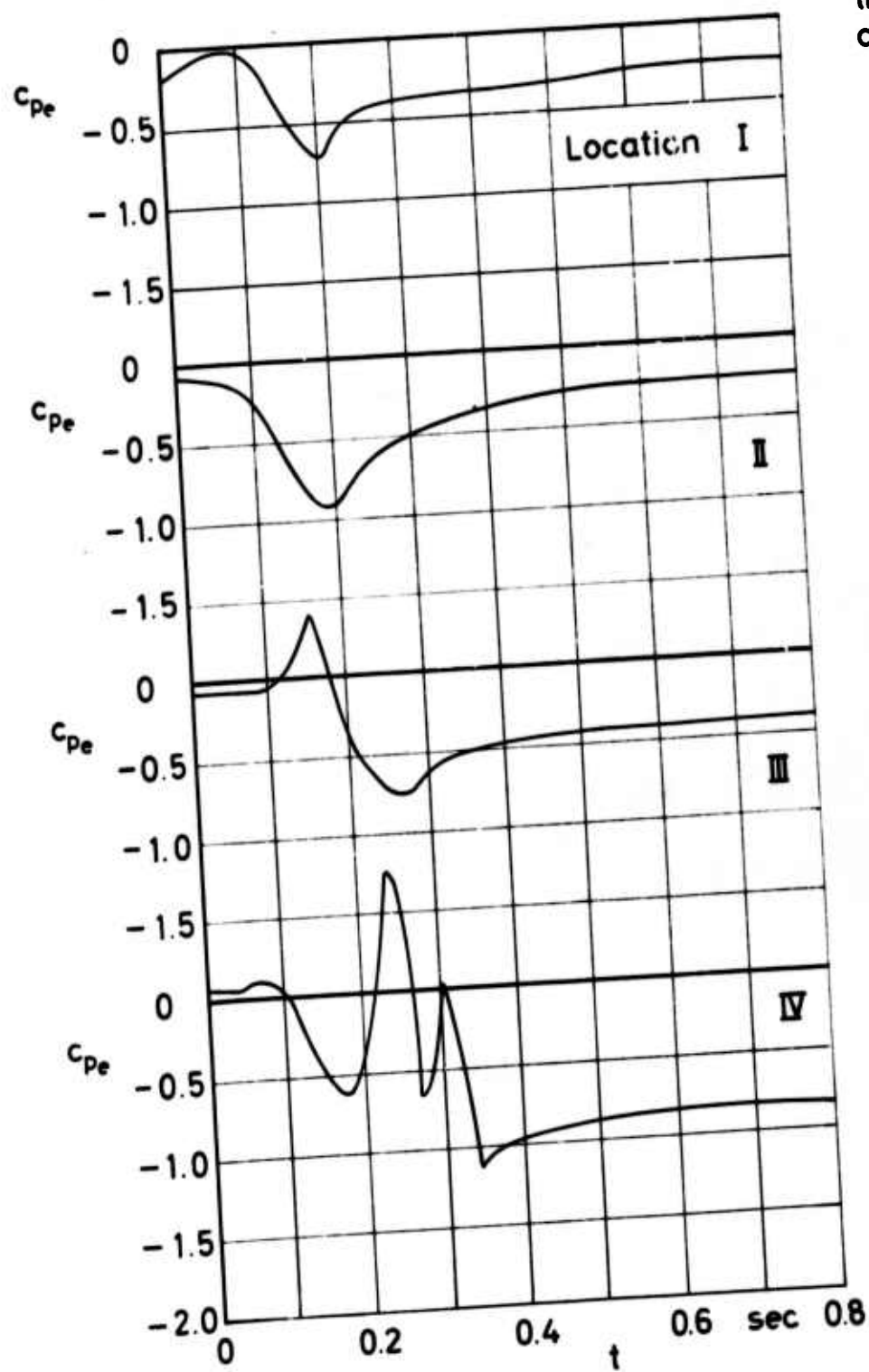


Ringslot

Figure 45 c_{pi}
and filling
versus time
 $v_0 = 100$ ft/sec
Run No 30



Location of pressure transducers on cord center line

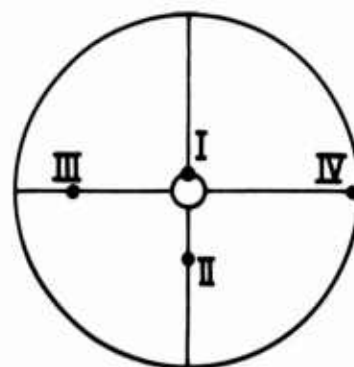
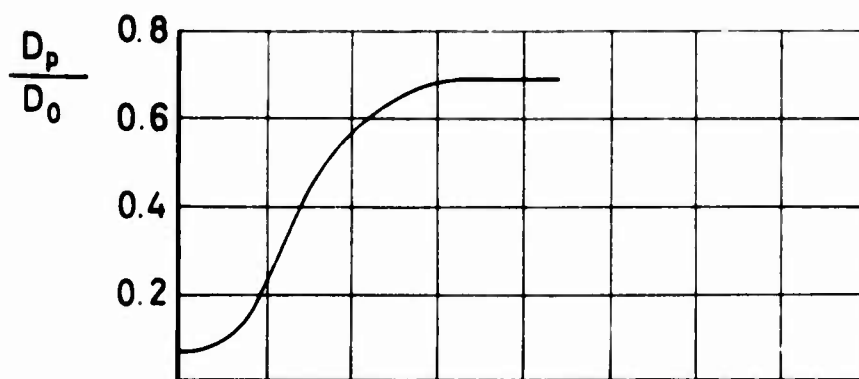


Ringslot

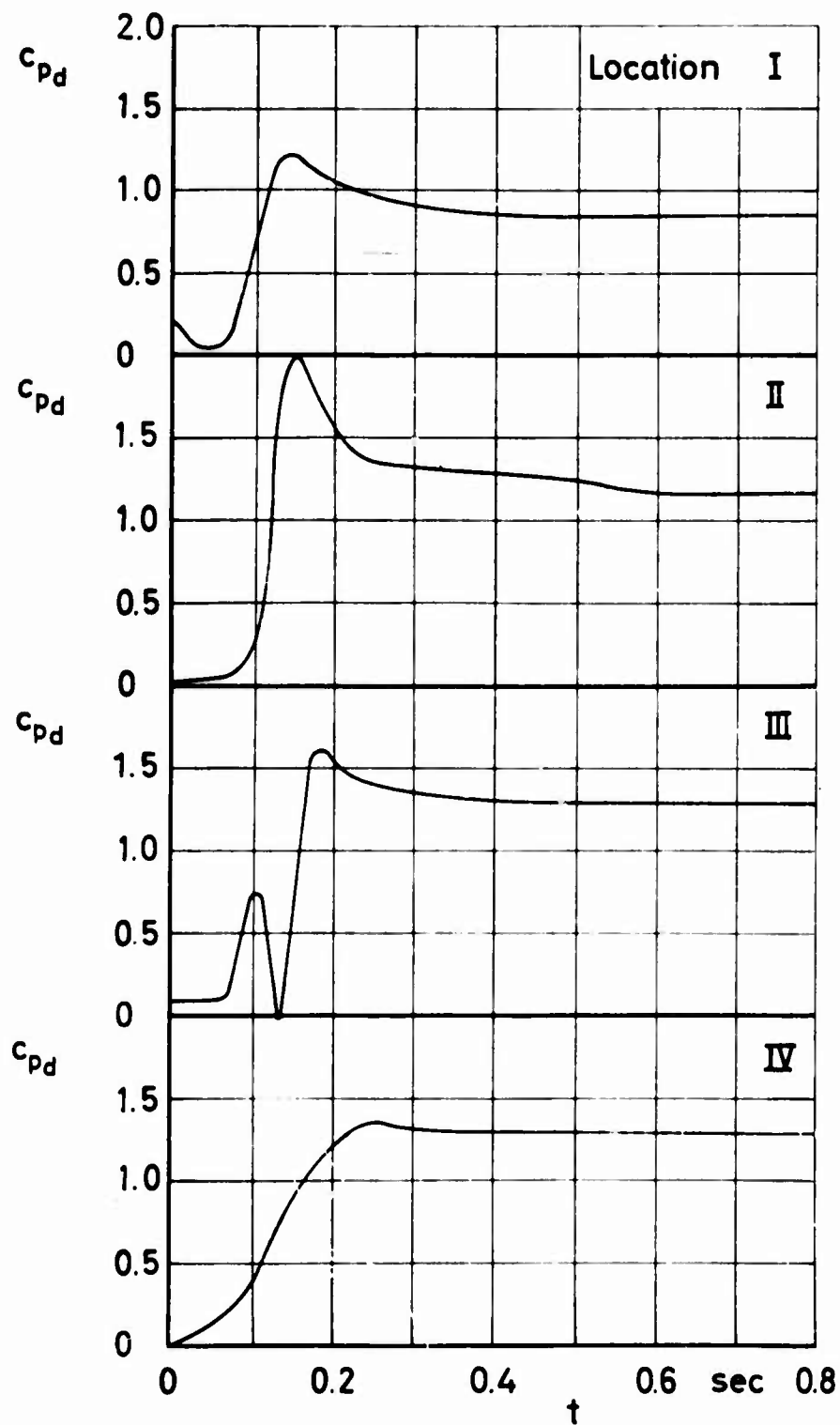
Figure 46 c_{pe} and filling versus time

$v_0 = 100 \text{ ft/sec}$

Run No. 39



Location of pressure transducers on cord center line

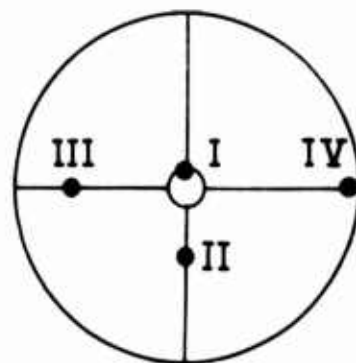
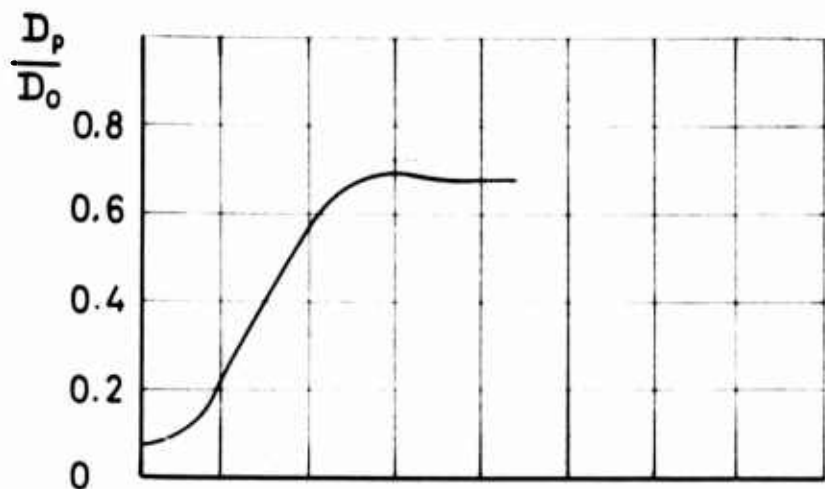


Ringslot

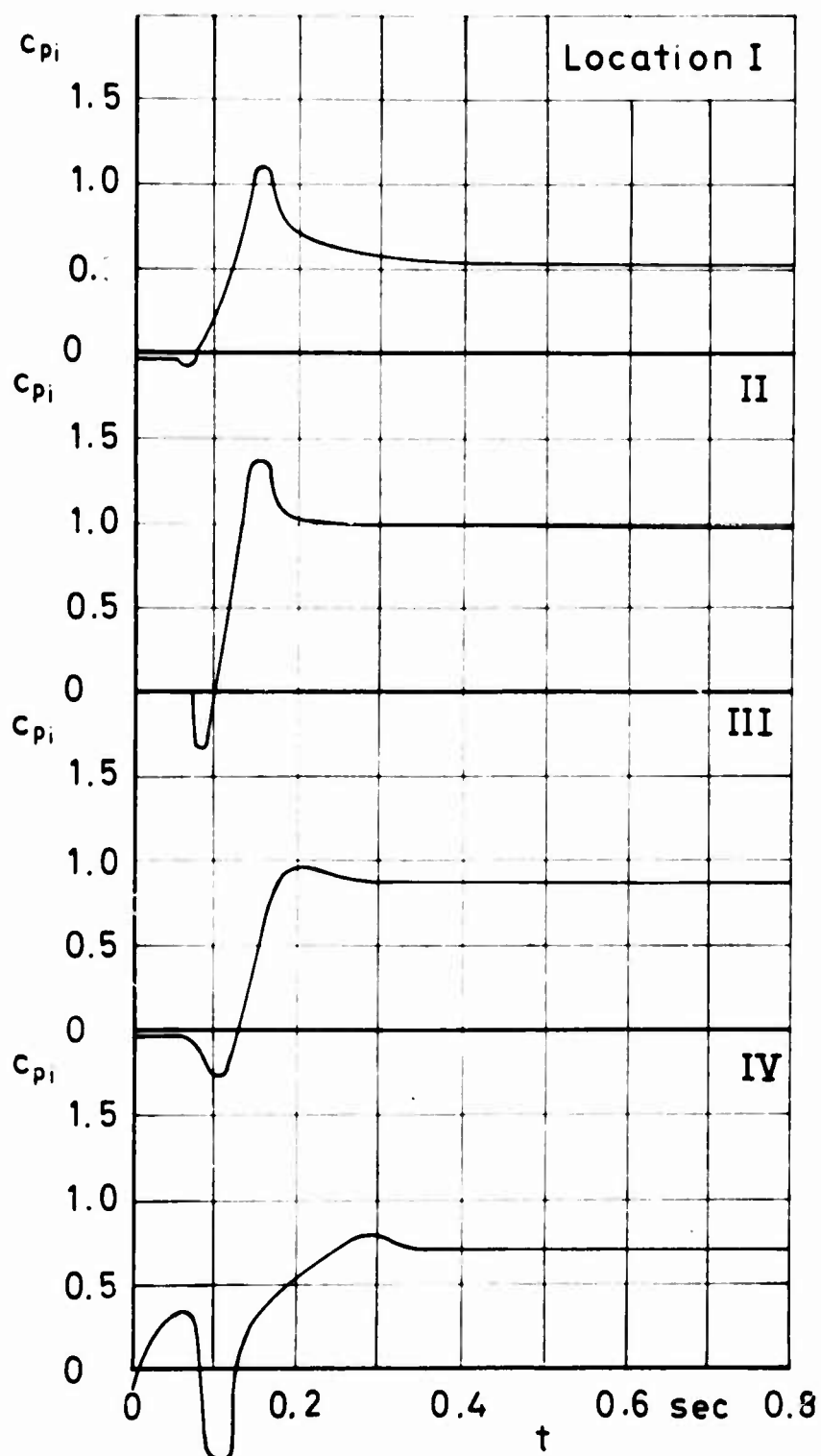
Figure 47 c_{pd} and filling versus time

$v_0 = 130 \text{ ft/sec}$

Run No. 14

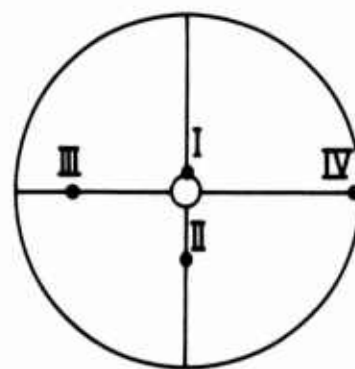
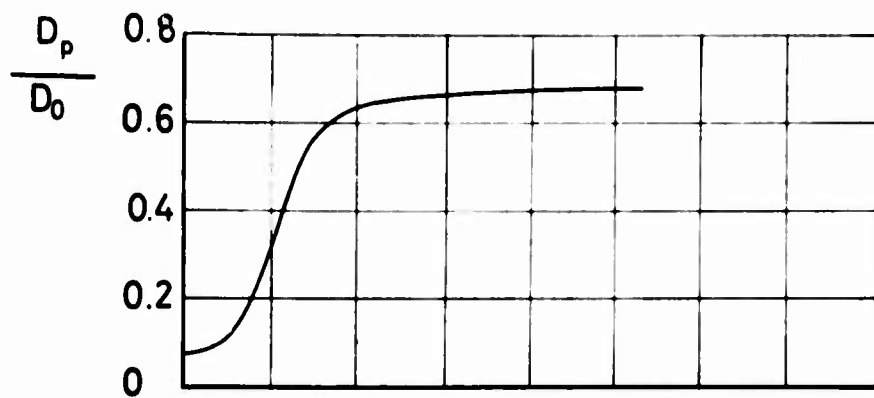


Location of
pressure trans-
ducers on
cord center line

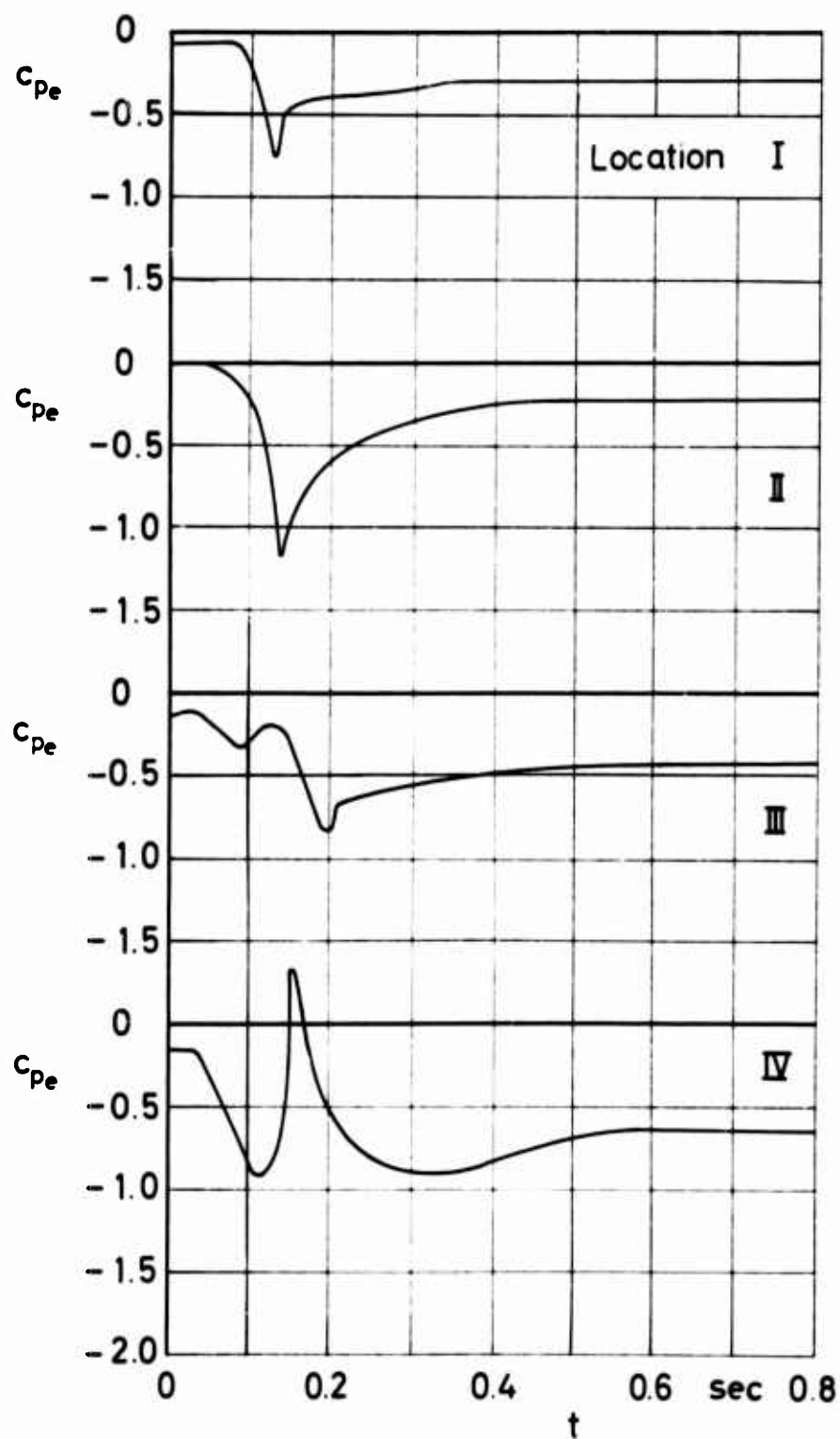


Ringslot

Figure 48 c_{pi}
and filling
versus time
 $v_0=130$ ft/sec
Run No 51



Location of pressure transducers on cord center line

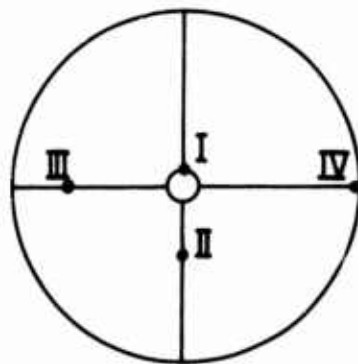
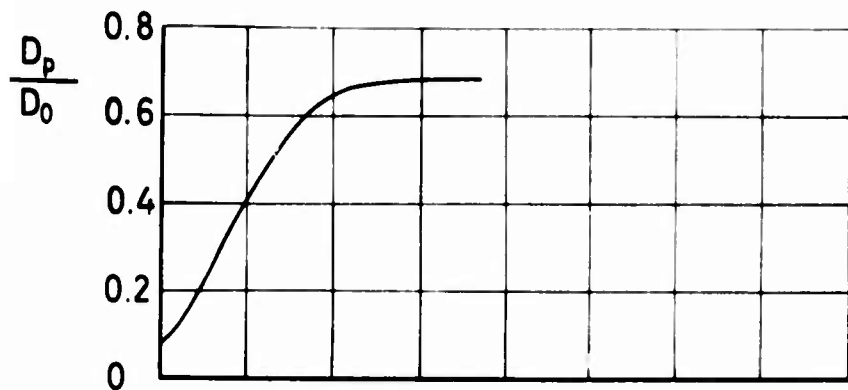


Ringslot

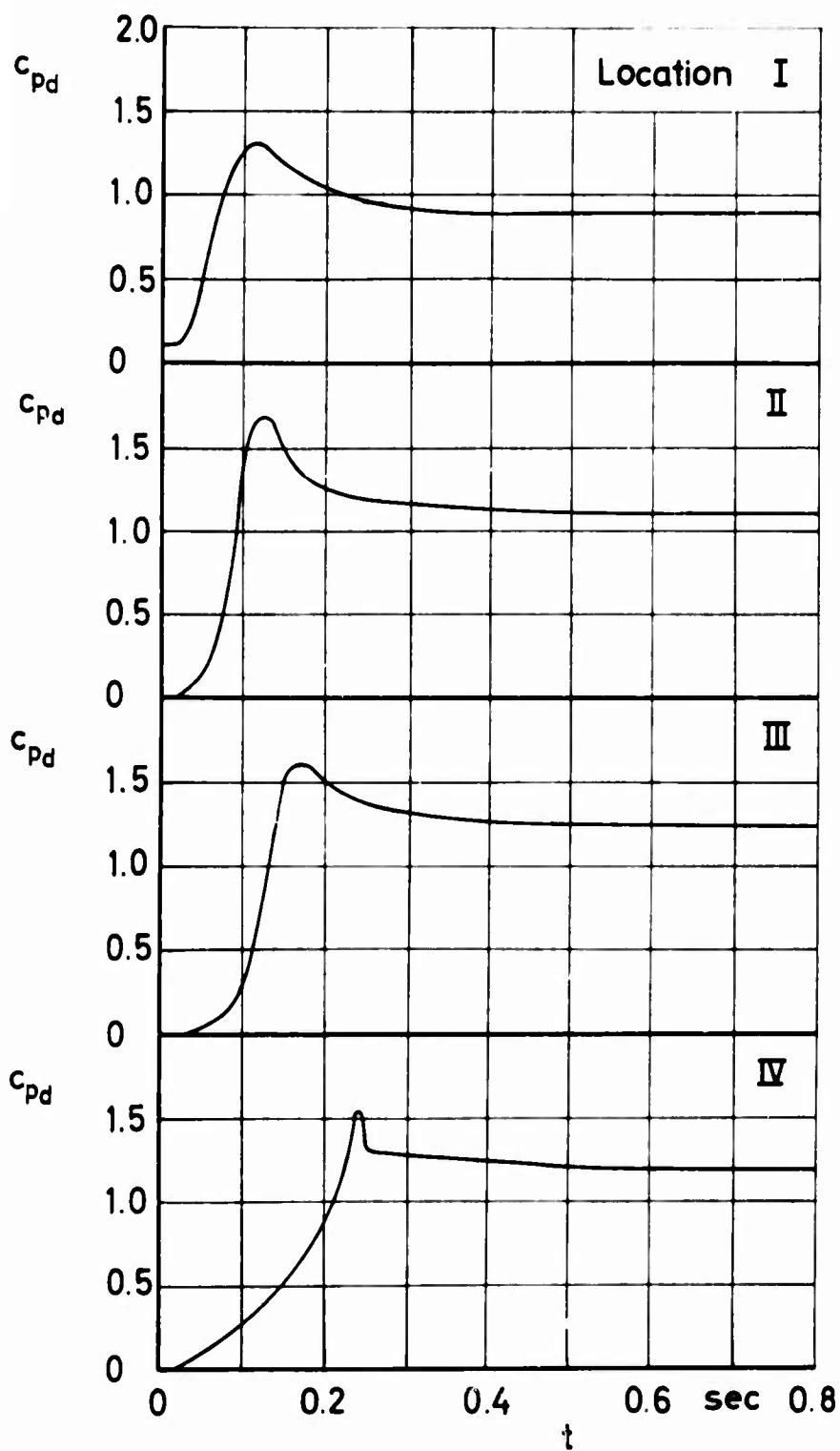
Figure 49 c_{pe} and filling versus time

$v_0 = 130$ ft/sec

Run No. 42



Location of pressure transducers on cord center line

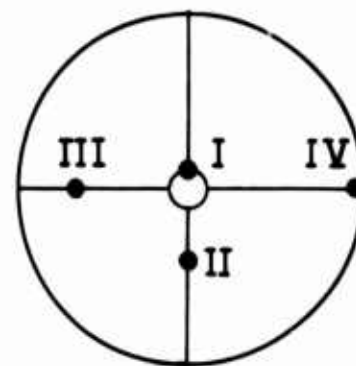
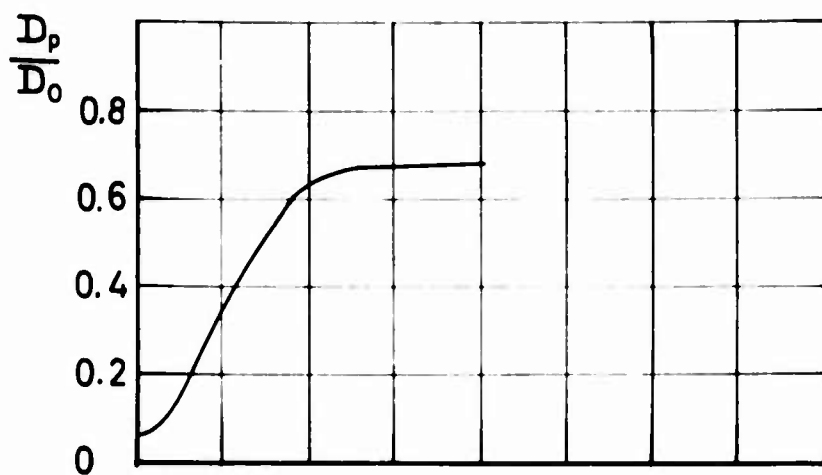


Ringslot

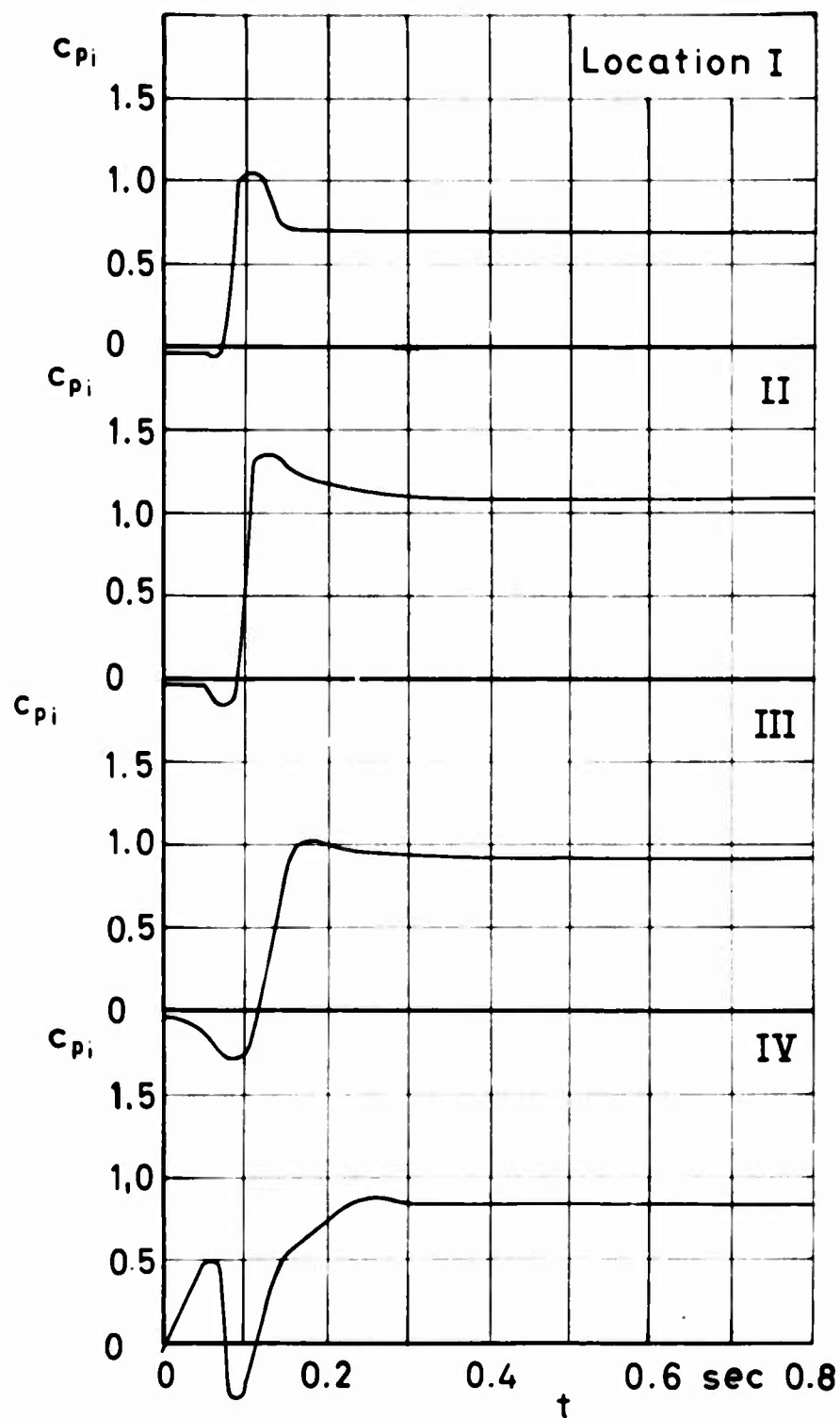
Figure 50 c_{pd} and filling versus time

$$v_0 = 160 \text{ ft/sec}$$

Run No. 18

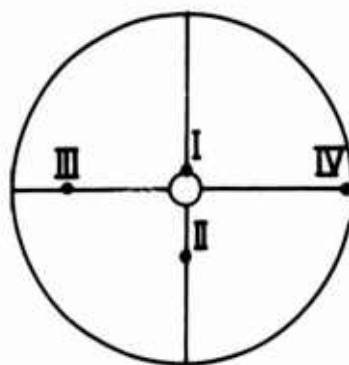
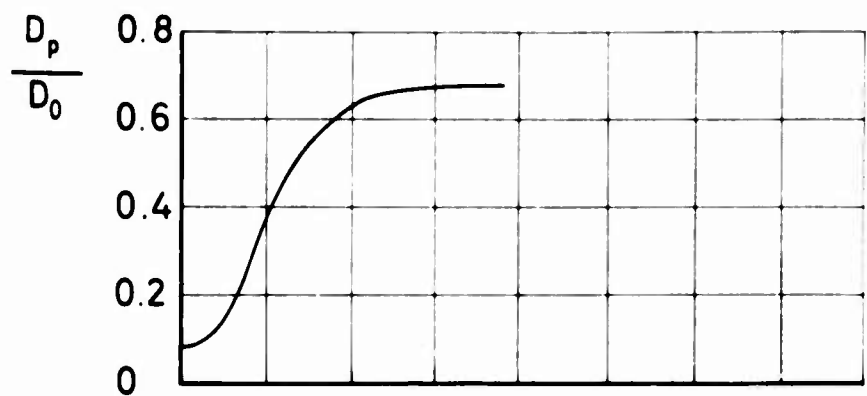


Location of
pressure trans-
ducers on
cord center line

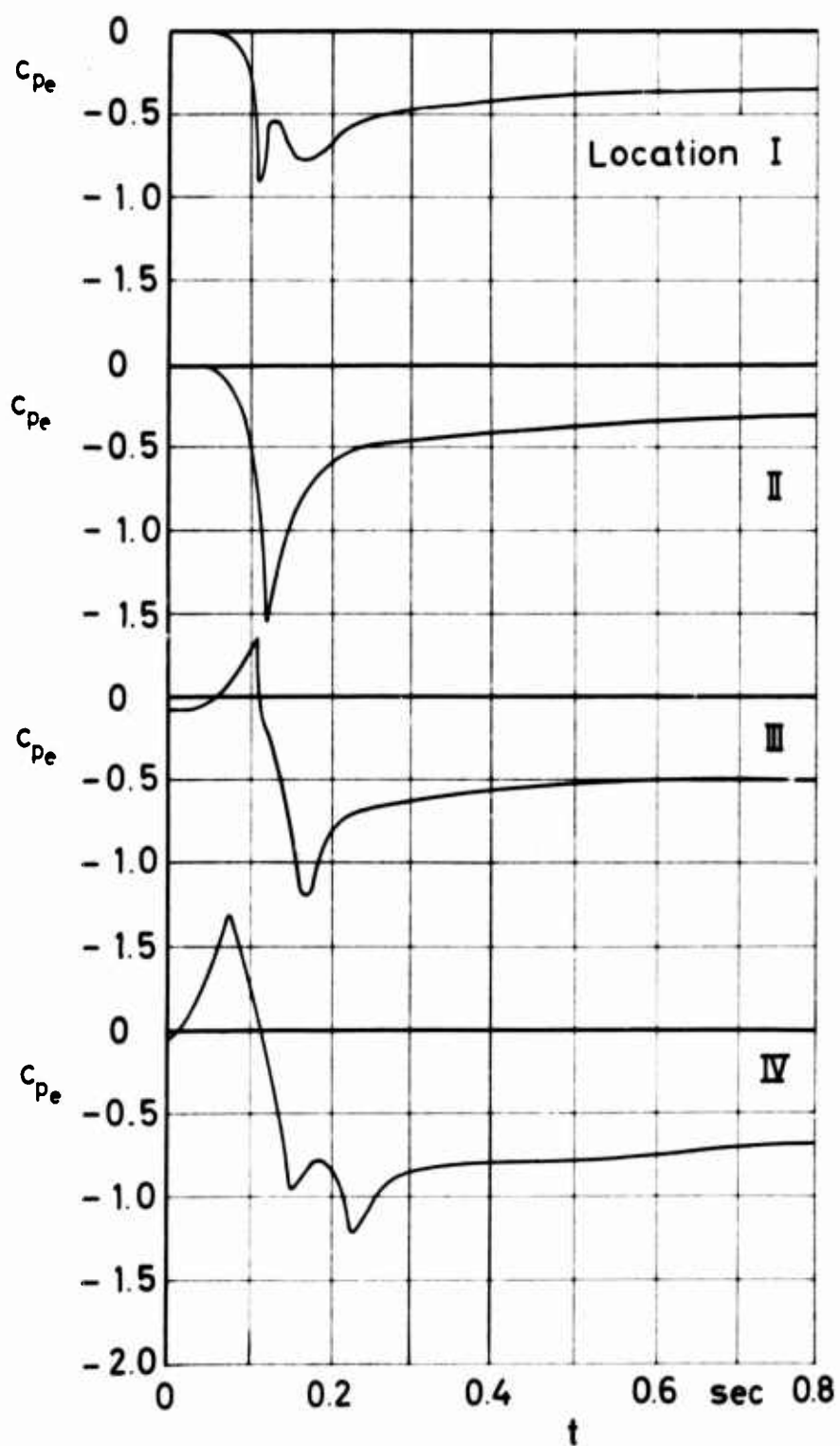


Ringslot

Figure 51 c_{pi}
and filling
versus time
 $v_0 = 160$ ft/sec
Run No 26



Location of pressure transducers on cord center line



Ringslot

Figure 52 c_{pe} and filling versus time

$v_0 = 160 \text{ ft/sec}$

Run No. 47

$v_0 = 70 \text{ ft/sec}$

$v_0 = 100 \text{ ft/sec}$

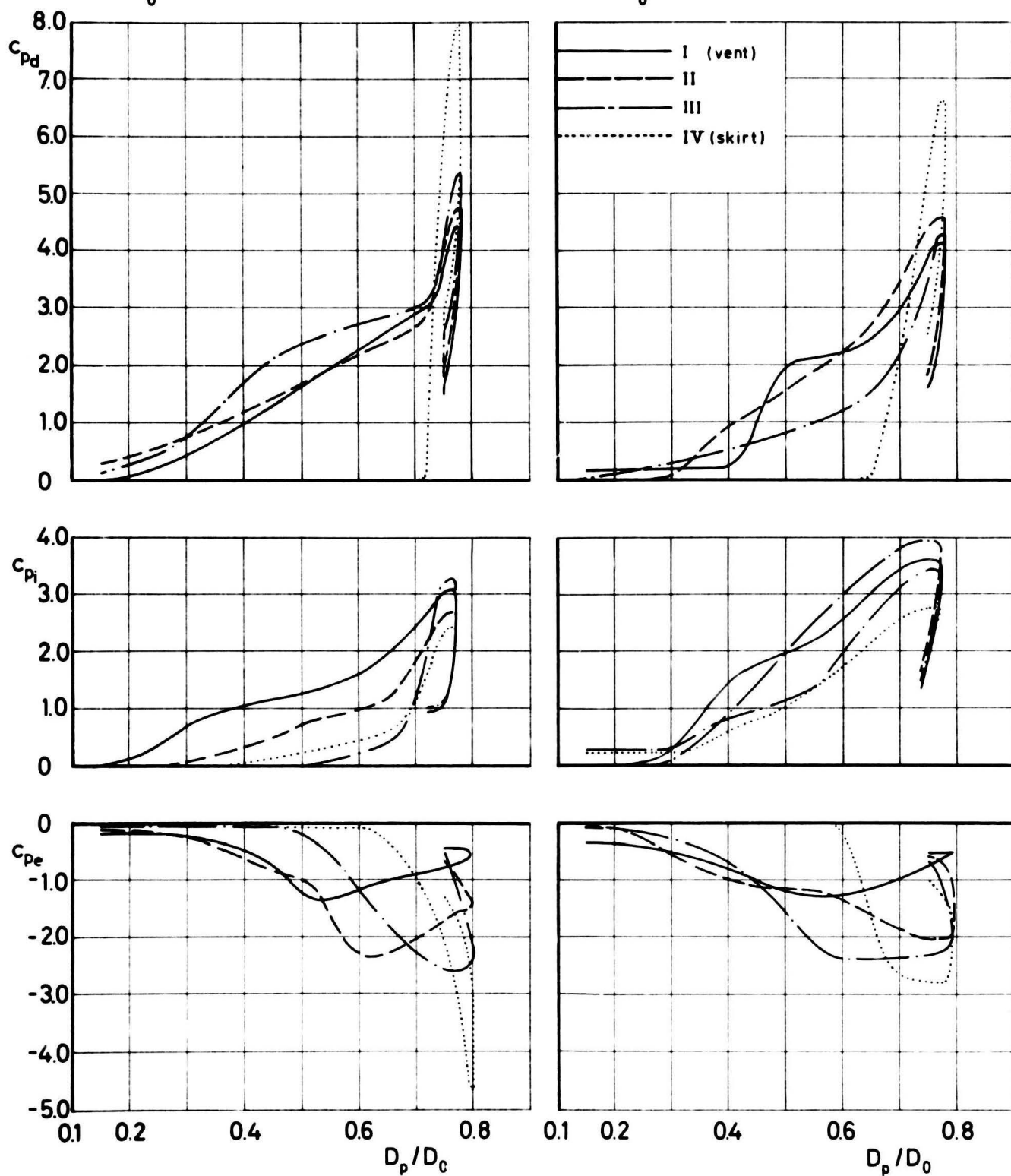


Figure 53 c_p versus D_p/D_0 for Circular Flat

Run No. 182; 194; 211; 183; 200; 216

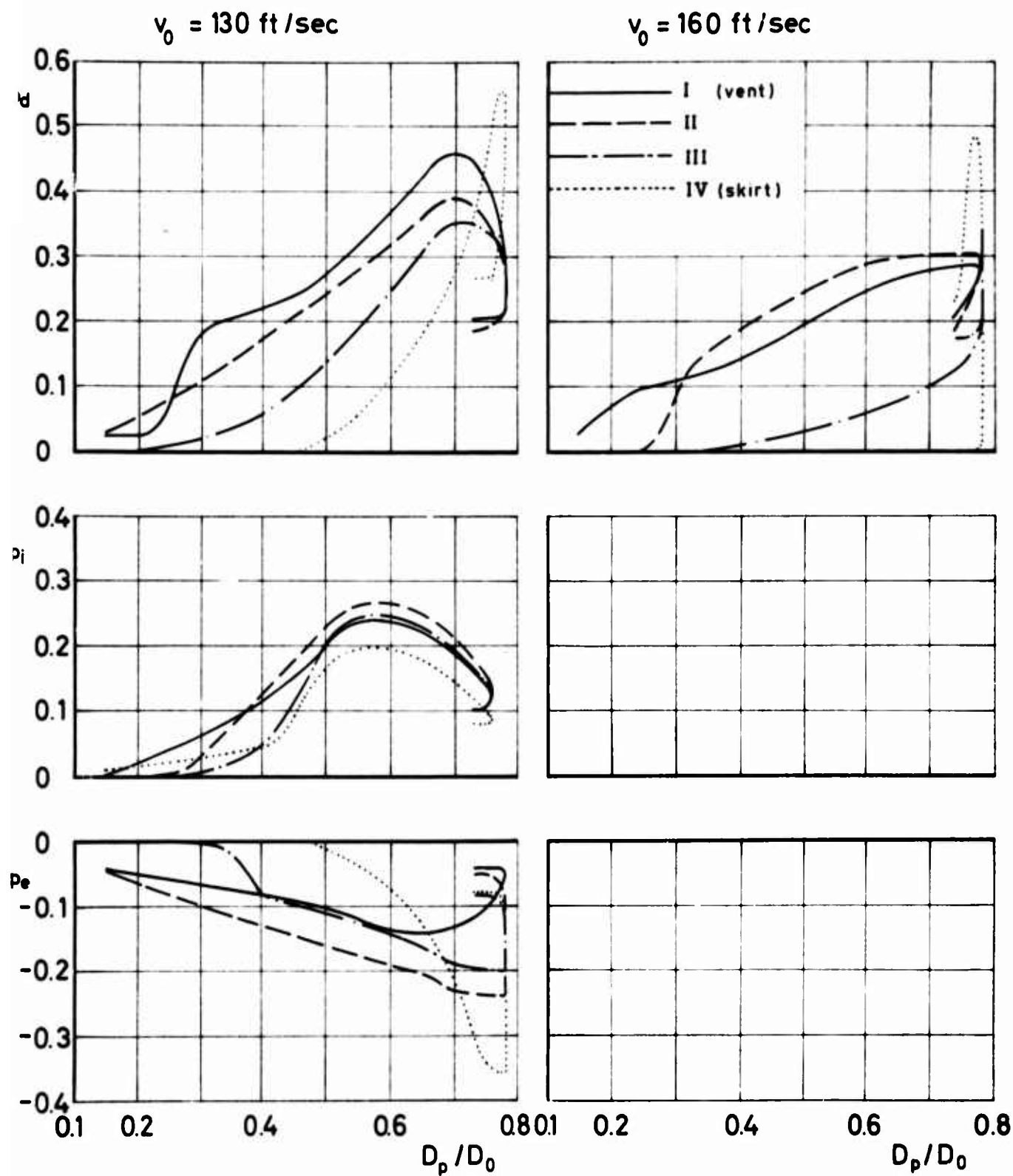


Figure 54 c_p versus D_p/D_0 for
Circular Flat
Run No. 187; 203; 218; 191

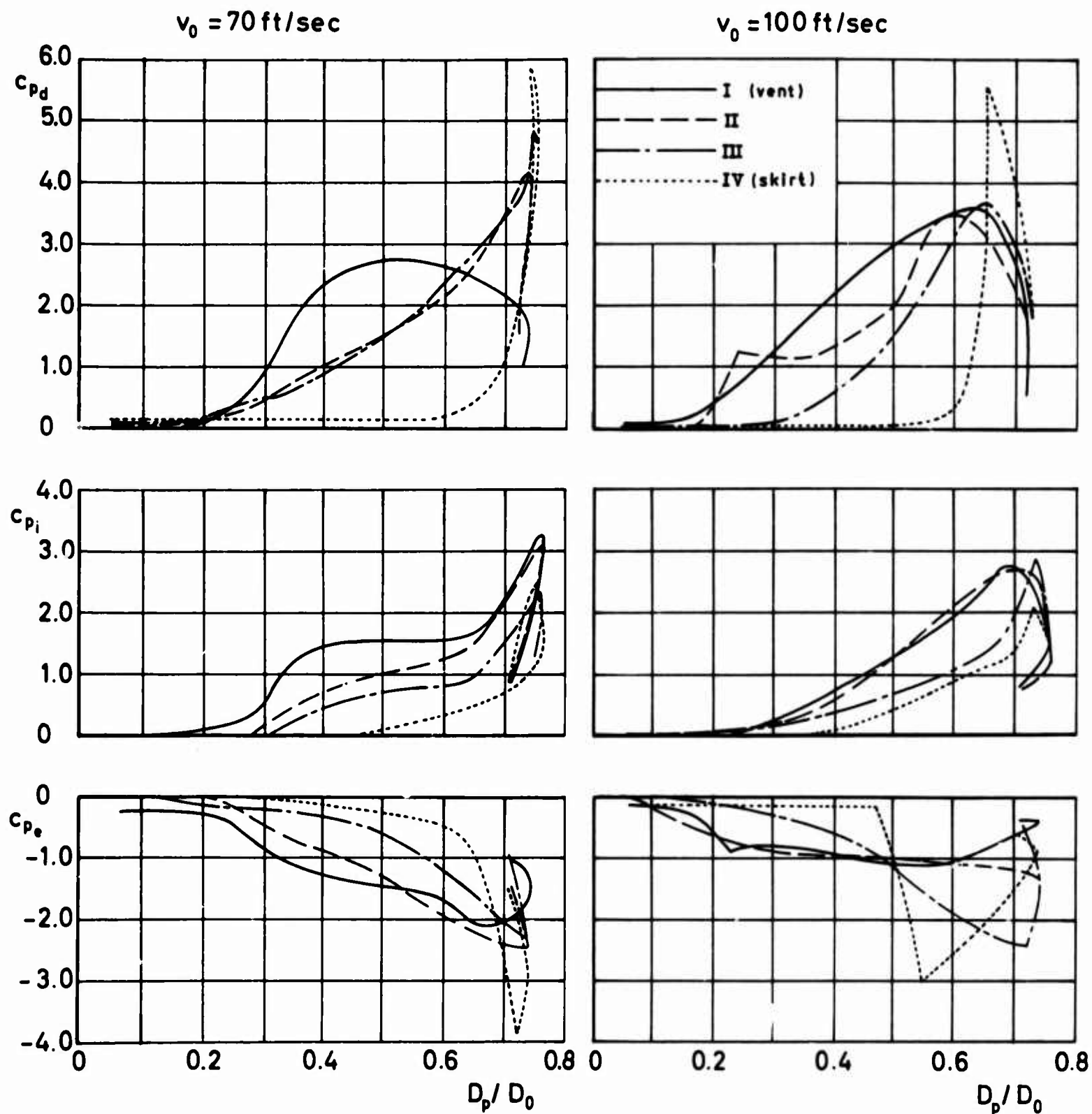


Figure 55 c_p versus D_p/D_0 for
Extended Skirt
Run No. 139; 157; 221; 144; 160; 226

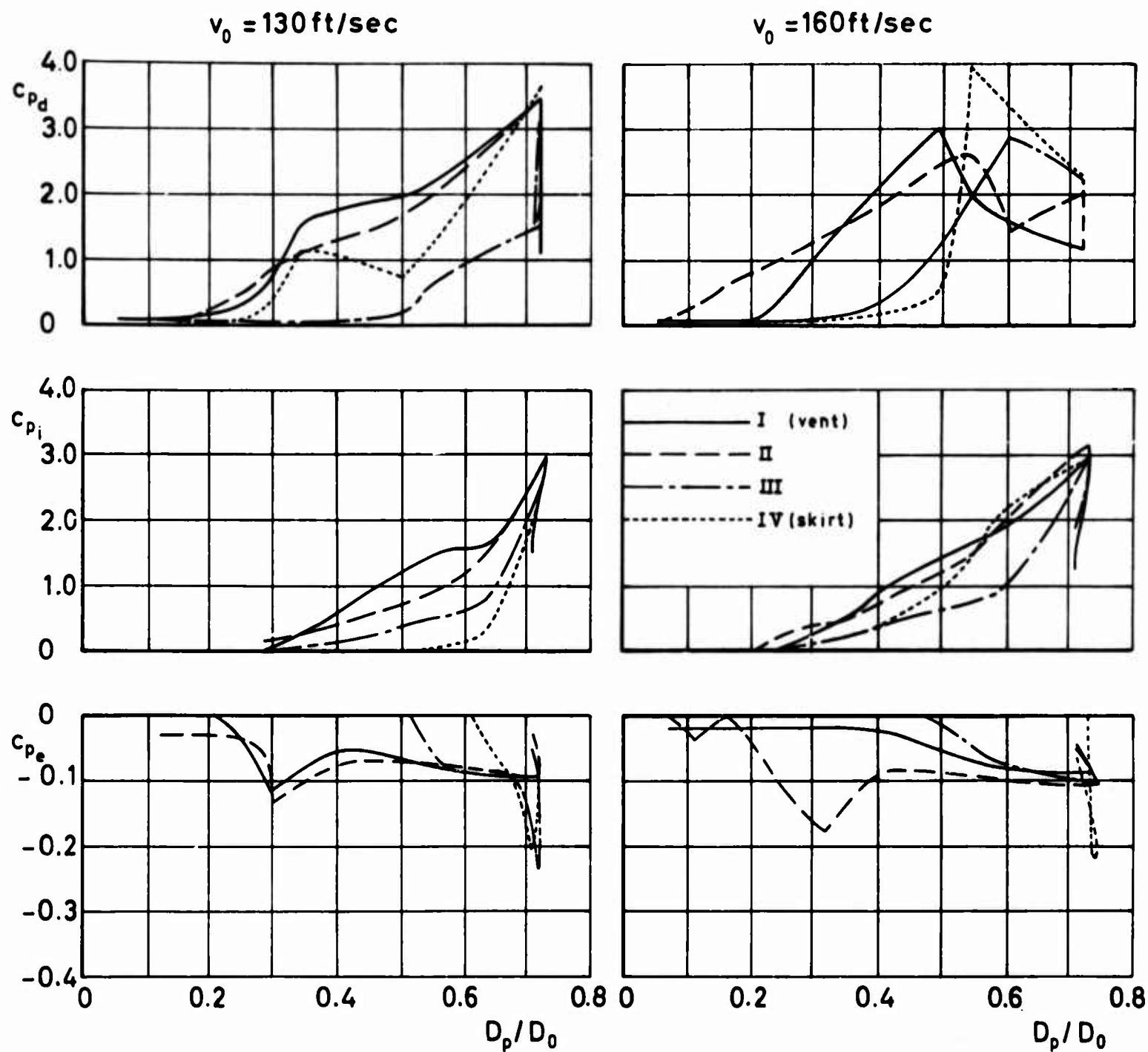


Figure 56 c_p versus D_p/D_0 for
Extended Skirt

Run No. 148; 163; 231; 153; 166; 235

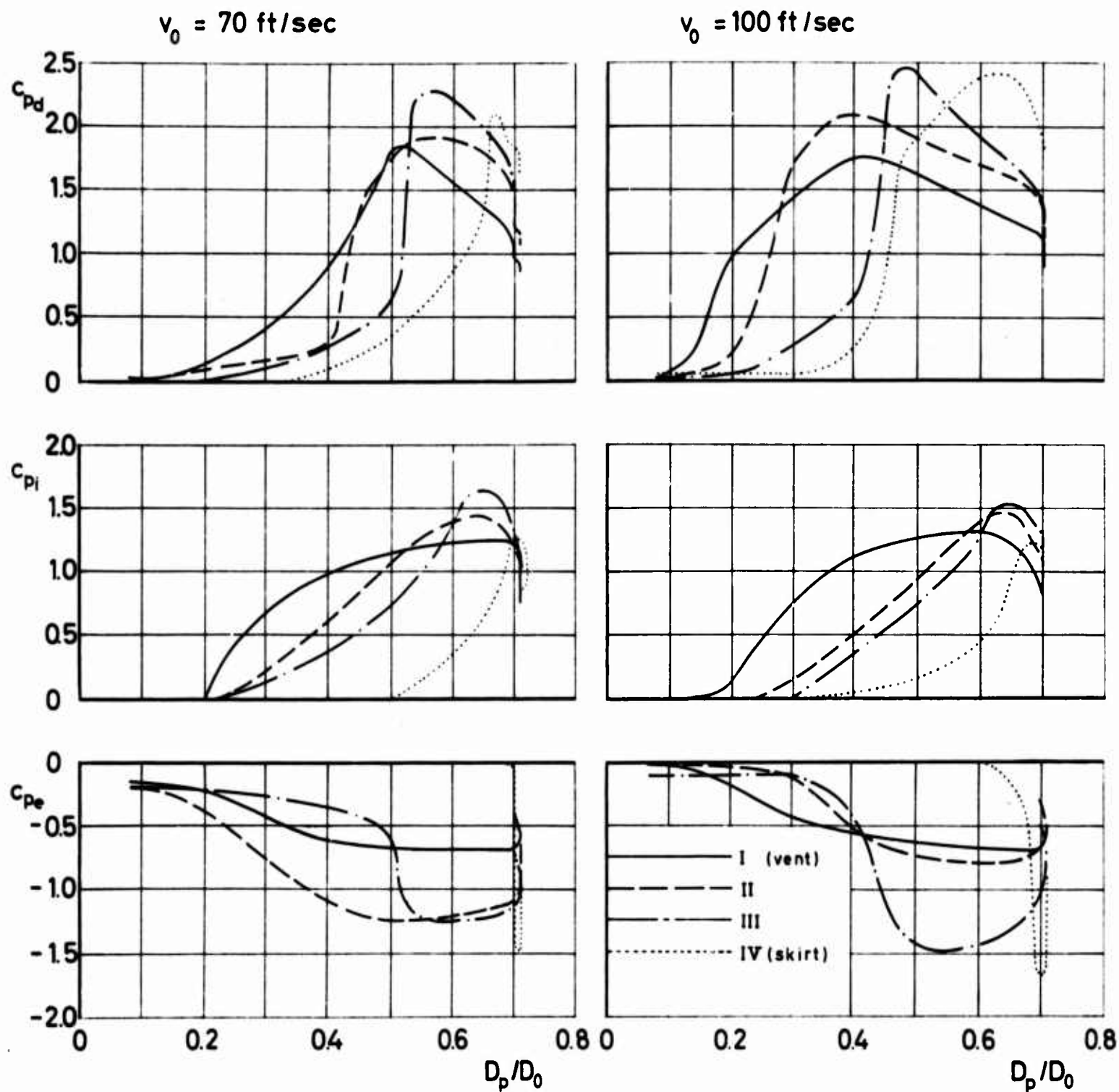


Figure 57 c_p versus D_p/D_0 for
FIST

Run No. 72; 101; 104; 76; 97; 110

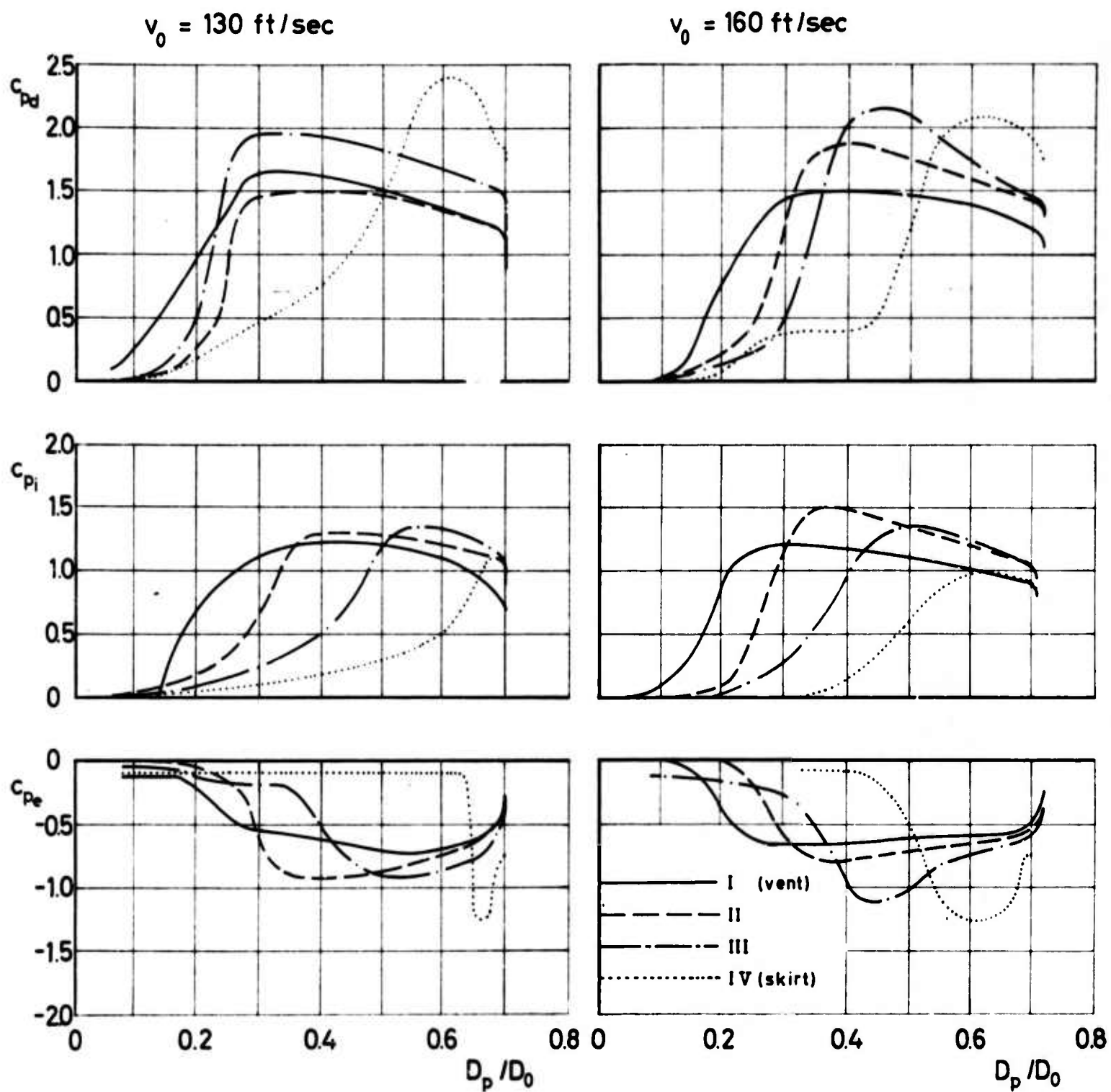


Figure 58 c_p versus D_p / D_0 for FIST

Run No. 82; 92; 117; 86; 88; 119

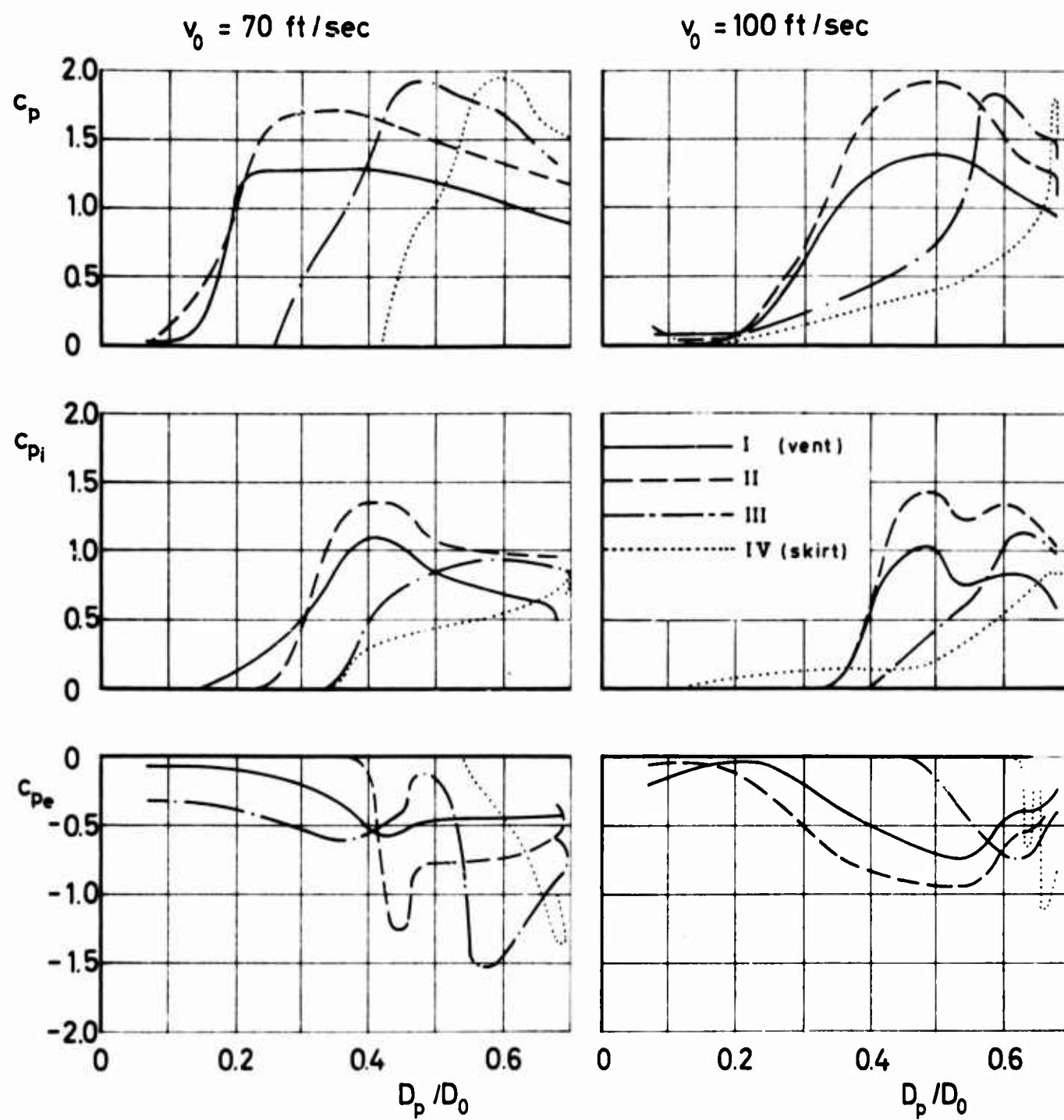


Figure 59 C_p versus D_p/D_0 for Ringslot

Run No. 7; 22; 24; 10; 30; 39

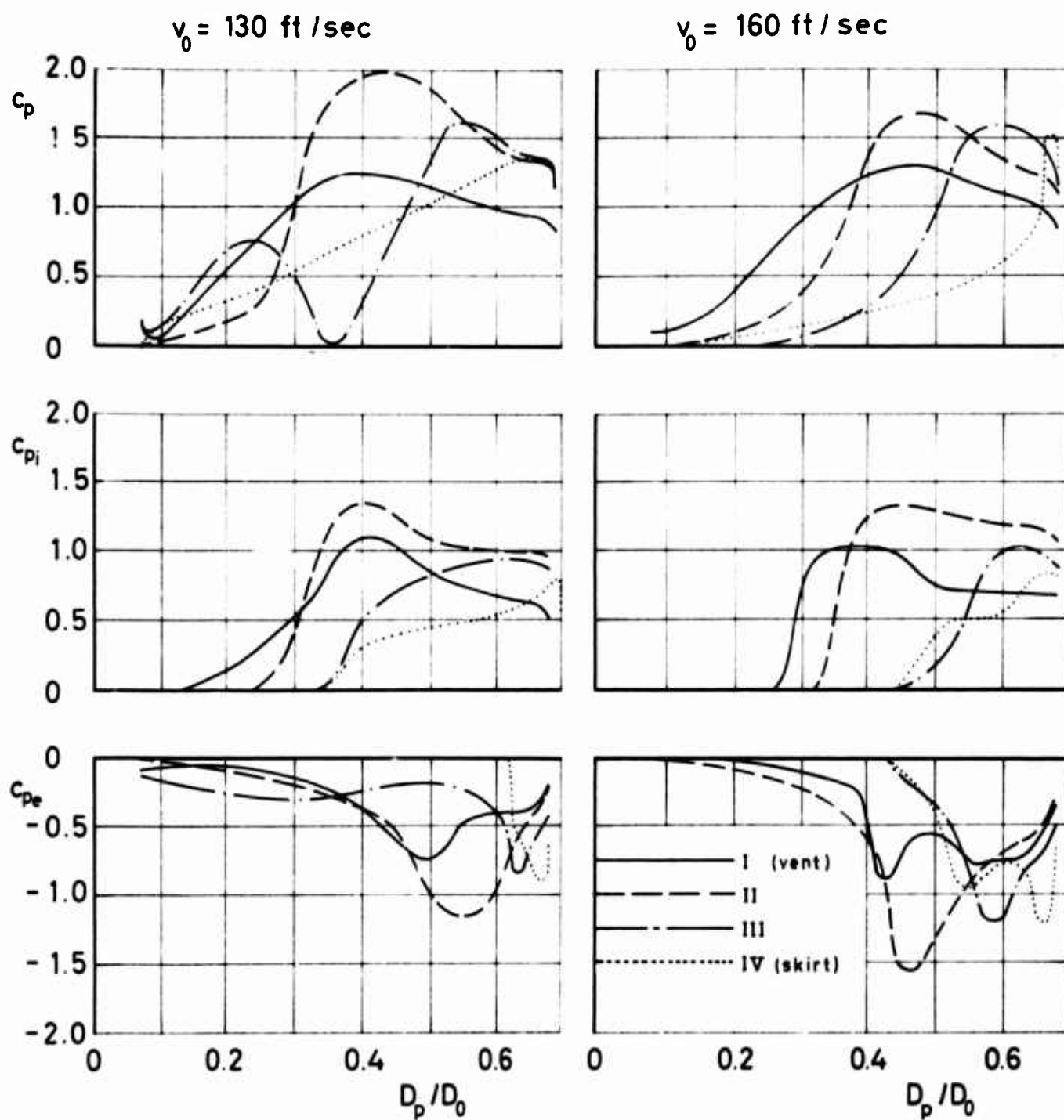


Figure 60 c_p versus D_p/D_0 for Ringslot

Run No. 14; 51; 42; 18; 26; 47

B. Canopy Shape Analysis

The objective of a "Shape Analysis" for the filling period of the parachute canopy was the mathematical description of the canopy shape as a function of time. Since the canopy is approximately rotational symmetric, it is sufficient to consider the profile views of the canopy.

To obtain representative profile views, specific frames of motion pictures taken from the side were analyzed. The profile views thus obtained yield a somewhat irregular and unsymmetric shape, as illustrated in Figures 61 and 62 by the solid lines which show an example for the circular flat type canopy. These shapes, however, can be graphically made symmetric, as is shown by the broken lines. The resulting shape shall be called the Symmetrized Photographic Shape.

This shape can be idealized in the following manner and then be described by means of specific parameters. This shape shall be called the Idealized Photographic Shape. The entire process of canopy filling may be divided into two phases. During Phase I, the canopy fills from the skirt towards the vent. The canopy shapes during this part of the filling period can then be described as consisting of four bodies of revolution depicted by the profile views in Figure 63:

1. A conical frustrum with lower base $2r$, upper base $2a$, and height ρ ,
2. An added half-ellipsoid with major semi-axis a and minor semi-axis b ,
3. An added cylinder,
4. And an added hemisphere. The height of the cylinder and added hemisphere along the axis of revolution is ρ_* , and the diameter of the cylinder is $2r_*$.

At the time where

$$\rho_* = r_* - b (1 - \sqrt{1 - r_*^2/a^2})$$

the cylinder disappears, and only the hemisphere remains added to the half-ellipsoid, meeting it with a secant equal to $2R$.

As defined by ρ_* and r_* , the radius of the hemisphere is then

$$r_{\sim} = (\sigma^2 + r_*^2)/2\sigma,$$

where

$$\sigma = \rho_* + b (1 - \sqrt{1 - r_*^2/a^2})$$

Phase II of the filling process begins at that point of time at which the canopy shape has assumed the shape of a conical frustrum to which is added a half-ellipsoid. From this point on the canopy fills from the vent towards the skirt. For the description of the canopy shape during this portion of the filling period, only four parameters are required: the lower base $2r$, the upper base $2a$, the height ρ of the conical frustrum, and the minor half-axis of the ellipsoid, b . During Phase II the canopy fills completely and opens with resulting rapid changes of $2r$ and $2a$. Phase III may be defined as the steady state period in which the canopy shape no longer changes significantly and the values of each of the four parameters only fluctuate about their steady mean values.

An approximated description of the Idealized Photographic Shape as a function of time is possible by plotting the parameters of the shape versus time. For comparative purposes, the parameters are made dimensionless by dividing by the nominal canopy diameter, D_0 . In addition, the time parameter is made dimensionless by dividing the time by a fictitious filling time t_* . This fictitious

filling time is the time from burning the wire which held the leather clamps around the stretched-out canopy to the point where the steady state mean values of the parameters were reached for the first time.

The parameters of the idealized canopy shape are now made a function of t/t_* . With this, the Idealized Photographic Shape can be constructed for any value of t/t_* for any specific deployment condition and correlated with the pressure distribution for the same time t/t_* . Figures 64 thru 79 are plottings of the parameters of the Idealized Photographic Shape obtained by this method for the four types of parachute canopies. A qualitatively similar behavior can be seen for all four types of canopies.

The parameters $2a/D_0$, $2r/D_0$, b/D_0 and ρ/D_0 increase in value during Phase I, indicating a filling of the canopy from the skirt towards the vent with simultaneous enlargement of the shape. During Phase II the values of the parameters $2a/D_0$, $2r/D_0$ and b/D_0 are increasing further until they reach the final steady state value at $t/t_* = 1$.

On the other hand, the value of the parameter ρ/D_0 decreases after reaching a maximum value. By plotting all parameters for one type of canopy for the four different deployment speeds on one graph, all points for one parameter lie relatively close together as may be seen from Figures 80 thru 83. Therefore, it may be concluded that for the infinite mass case the development of the canopy shape is primarily dependent upon the dimensionless time ratio t/t_* . This agrees with findings by Berndt [5] which indicated that for the finite mass case the growth in projected canopy area as a function of the time ratio t/t_* follows an identical relationship for a given canopy type regardless of speed and altitude of deployment.

The spread of the measured points in Figures 80 thru 83 is probably due to the inexact reproducibility of the filling process of a parachute canopy.

Table 2 Approximations to the 4th power for phase II
 $r = a_0 + a_1(t/t_0) + a_2(t/t_0)^2 + a_3(t/t_0)^3 + a_4(t/t_0)^4$

		r	a_0	a_1	a_2	a_3	a_4
Circular Flat	$v_0 = 70$ [ft/sec] $t_0 = 0.25$ [sec] $0.72 = t/t_0 = 1.00$ Run No. 182	$2a/D_0$ $2r/D_0$ b/D_0 g/D_0	-46.34 -120.12 -65.69 +61.72	+217.05 +594.60 +309.04 -288.99	-379.25 -1092.50 -543.30 +508.67	+294.30 +884.31 -423.51 -396.75	-85.02 -265.51 -123.36 +115.42
	$v_0 = 100$ [ft/sec] $t_0 = 0.20$ [sec] $0.70 = t/t_0 = 1.00$ Run No. 183	$2a/D_0$ $2r/D_0$ b/D_0 g/D_0	+56.84 +80.29 +18.21 -49.59	-284.83 -395.86 -85.69 -243.51	+531.73 +729.51 +149.49 -441.61	-436.45 -594.03 -115.31 +352.68	+133.42 +180.81 +32.11 -104.92
	$v_0 = 130$ [ft/sec] $t_0 = 0.16$ [sec] $0.69 = t/t_0 = 1.00$ Run No. 187	$2a/D_0$ $2r/D_0$ b/D_0 g/D_0	+3.64 -19.38 -3.79 -4.21	-19.17 +98.14 +18.01 +23.98	+38.77 -181.59 -32.11 -46.29	-33.71 +146.26 +26.15 +38.66	+11.11 -42.86 -8.04 -12.06
	$v_0 = 160$ [ft/sec] $t_0 = 0.14$ [sec] $0.64 = t/t_0 = 1.00$ Run No. 191	$2a/D_0$ $2r/D_0$ b/D_0 g/D_0	-18.14 +34.57 -7.64 +10.54	+83.92 -169.80 +40.04 -52.78	-141.37 +314.18 -78.03 +101.90	+103.65 -258.92 +67.47 -86.96	-27.55 +80.76 -21.64 +27.38
	$v_0 = 70$ [ft/sec] $t_0 = 0.34$ [sec] $0.56 = t/t_0 = 1.00$ Run No. 139	$2a/D_0$ $2r/D_0$ b/D_0 g/D_0	-10.68 +5.32 -1.64 +5.13	-60.42 -27.46 +11.36 -27.86	-122.67 +55.40 -26.42 +59.61	+108.67 -49.94 +26.24 -55.24	-34.90 +17.54 -9.50 +18.45
	$v_0 = 100$ [ft/sec] $t_0 = 0.29$ [sec] $0.48 = t/t_0 = 1.00$ Run No. 144	$2a/D_0$ $2r/D_0$ b/D_0 g/D_0	-3.11 -6.81 -1.62 -2.21	+19.36 +43.21 +13.42 +10.11	-42.07 -97.39 -35.38 -11.71	+40.62 +94.51 +38.80 +2.50	-13.95 -32.68 -14.98 +1.42
	$v_0 = 130$ [ft/sec] $t_0 = 0.23$ [sec] $0.48 = t/t_0 = 1.00$ Run No. 148	$2a/D_0$ $2r/D_0$ b/D_0 g/D_0	-0.60 -4.41 -1.91 -1.96	+3.52 +26.56 +12.11 +10.79	-5.21 -55.11 -27.47 -17.13	+3.59 +48.89 +27.51 +10.70	-0.47 -15.09 -9.97 -2.30
	$v_0 = 160$ [ft/sec] $t_0 = 0.21$ [sec] $0.52 = t/t_0 = 1.00$ Run No. 153	$2a/D_0$ $2r/D_0$ b/D_0 g/D_0	+9.58 +17.57 -3.68 -0.80	-56.65 -98.64 +21.96 +6.02	+124.29 +206.45 -48.47 -9.51	-117.15 -188.95 +47.55 +5.05	+40.71 +64.38 -17.10 -0.62
	$v_0 = 70$ [ft/sec] $t_0 = 0.36$ [sec] $0.50 = t/t_0 = 1.00$ Run No. 72	$2a/D_0$ $2r/D_0$ b/D_0 g/D_0	-7.06 +0.54 -2.14 +3.28	+38.82 +0.55 +11.51 -17.98	-75.99 -5.54 -21.78 +38.22	+65.86 +9.56 +18.10 -34.87	-20.94 -4.41 -5.52 +11.43
	$v_0 = 100$ [ft/sec] $t_0 = 0.26$ [sec] $0.50 = t/t_0 = 1.00$ Run No. 76	$2a/D_0$ $2r/D_0$ b/D_0 g/D_0	-4.62 -0.65 -2.36 -0.10	+25.04 +6.27 +12.42 +1.75	-47.79 -16.31 -23.36 -2.40	+40.91 +18.36 +19.53 +0.62	-12.88 -6.99 -6.05 +0.22
	$v_0 = 130$ [ft/sec] $t_0 = 0.22$ [sec] $0.50 = t/t_0 = 1.00$ Run No. 82	$2a/D_0$ $2r/D_0$ b/D_0 g/D_0	-3.27 -4.03 -6.07 +8.78	+21.60 +29.37 +36.20 -49.33	-50.76 -73.50 -78.25 +105.94	+53.34 +79.11 +73.67 -99.63	-20.23 -30.24 -25.39 +34.34
	$v_0 = 160$ [ft/sec] $t_0 = 0.20$ [sec] $0.55 = t/t_0 = 1.00$ Run No. 86	$2a/D_0$ $2r/D_0$ b/D_0 g/D_0	+1.39 -13.49 -0.59 -1.25	-4.90 +74.86 +5.05 +6.54	+6.50 -150.53 -12.81 -8.99	-2.05 +132.34 +13.71 +3.91	-0.25 -42.48 -5.16 -0.11
	$v_0 = 70$ [ft/sec] $t_0 = 0.42$ [sec] $0.52 = t/t_0 = 1.00$ Run No. 7	$2a/D_0$ $2r/D_0$ b/D_0 g/D_0	-0.64 +1.52 -4.46 +0.98	+4.37 -7.46 +24.39 -4.56	-8.92 +14.40 -48.46 +11.04	+9.91 -9.83 +42.38 -12.06	-4.04 +2.07 -13.67 +4.67
	$v_0 = 100$ [ft/sec] $t_0 = 0.32$ [sec] $0.40 = t/t_0 = 1.00$ Run No. 10	$2a/D_0$ $2r/D_0$ b/D_0 g/D_0	+2.12 +3.54 -1.08 -1.67	-12.85 -21.22 +8.24 +10.74	+30.23 +48.54 -21.52 -20.55	-27.97 -45.56 +24.37 +15.37	+9.09 +15.55 -9.86 -3.77
	$v_0 = 130$ [ft/sec] $t_0 = 0.29$ [sec] $0.41 = t/t_0 = 1.00$ Run No. 14	$2a/D_0$ $2r/D_0$ b/D_0 g/D_0	+3.23 +2.49 +8.34 -5.28	-19.94 -15.06 -49.90 +34.77	+47.81 +36.53 +109.95 -78.96	-46.59 -35.82 -104.07 +75.98	+16.13 +122.23 +35.83 -26.41
	$v_0 = 160$ [ft/sec] $t_0 = 0.25$ [sec] $0.28 = t/t_0 = 1.00$ Run No. 18	$2a/D_0$ $2r/D_0$ b/D_0 g/D_0	+0.38 +1.08 +0.15 +0.16	-2.70 -6.64 -0.67 +1.29	+11.63 +18.59 +2.57 -4.78	-14.75 -19.11 -3.27 +5.65	+6.06 +6.75 +1.33 -2.20

The parameters of the Idealized Photographic Shape can also be mathematically expressed as a function of t/t_* forming a polynomial in t/t_* . The coefficients of this polynomial are obtained by the method of least squares.

A regression to the fourth power was made for Phase II of the filling process for all four types of parachute canopies and for the four deployment velocities. Table II shows the results for each parameter in the form

$$f = a_0 + a_1 t/t_* + a_2 (t/t_*)^2 + a_3 (t/t_*)^3 + a_4 (t/t_*)^4$$

The shape can be described approximately by the parameters of the Idealized Photographic Shape stated in graphic form or in terms of a polynomial.

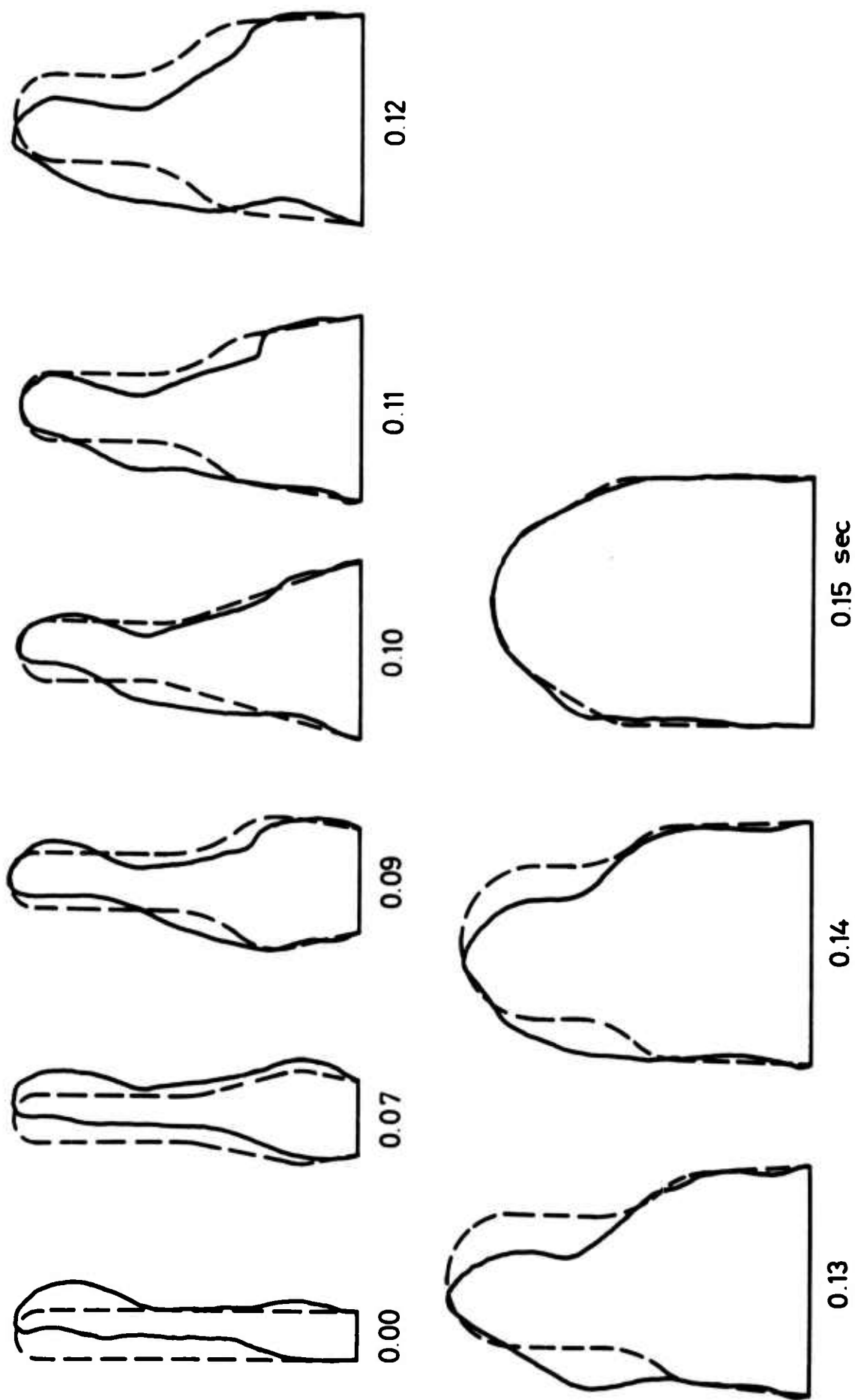
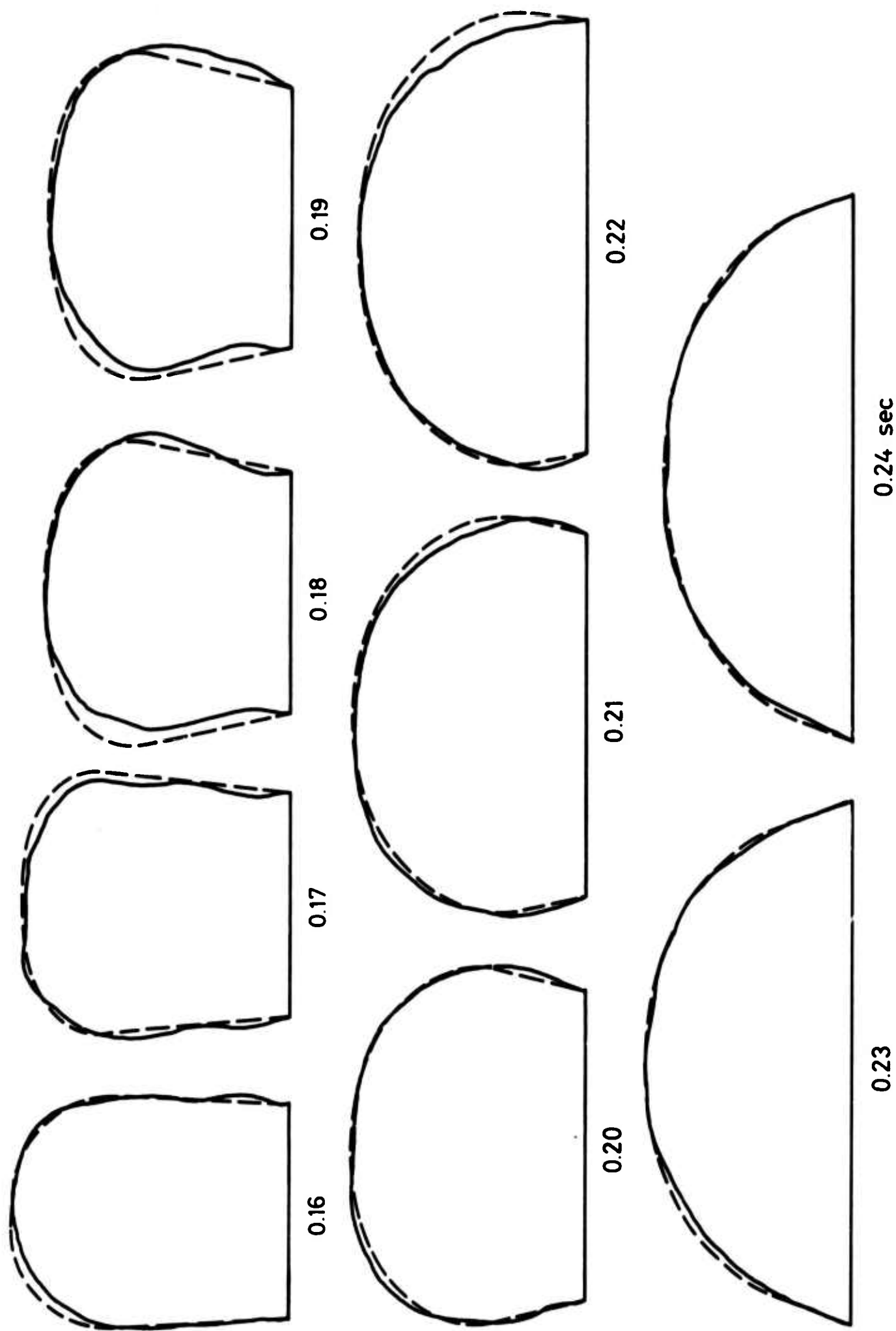


Figure 61 Photographic Shape (---symmetrized) Phase I for
Circular Flat, $v_0 = 70$ ft/sec, Run No. 194



0.23 0.24 sec
 Figure 62 Photographic Shape (---symmetrized) Phase II for
 Circular Flat, $v_0 = 70$ ft/sec, Run No. 194

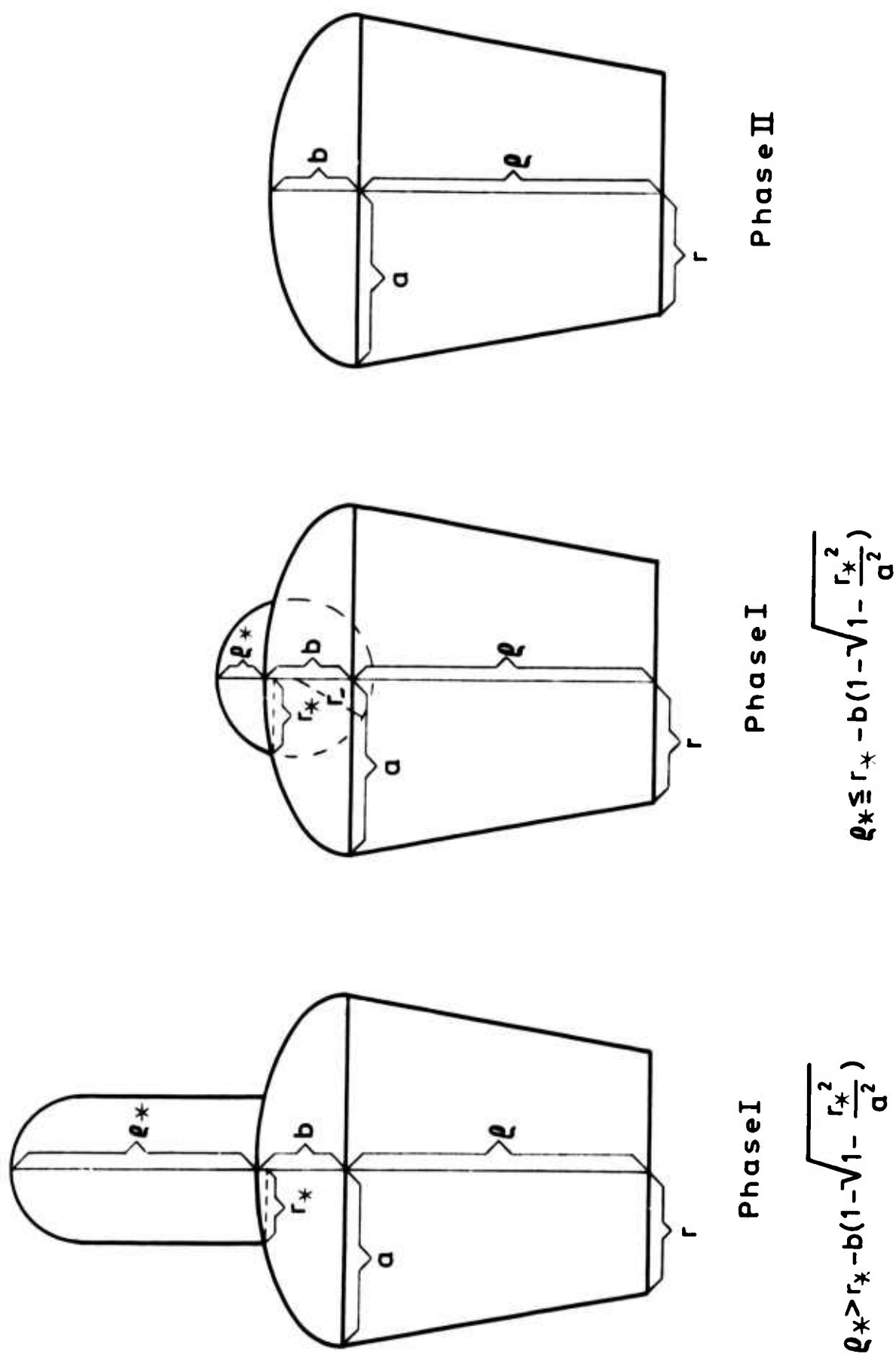


Figure 63 Idealized Photographic Shape Symbols

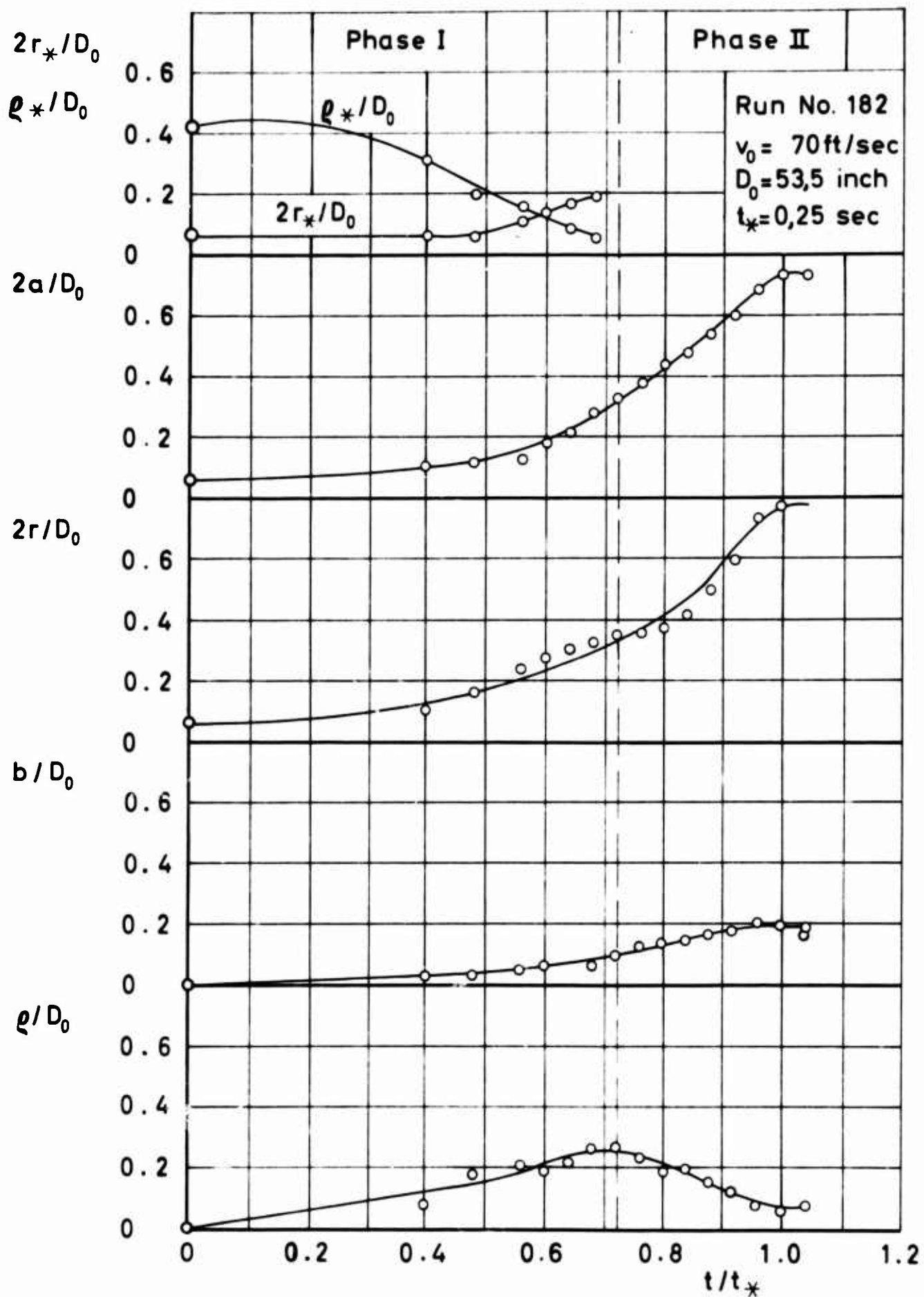


Figure 64 Parameters of Idealized Photographic Shape Versus Time for Circular Flat

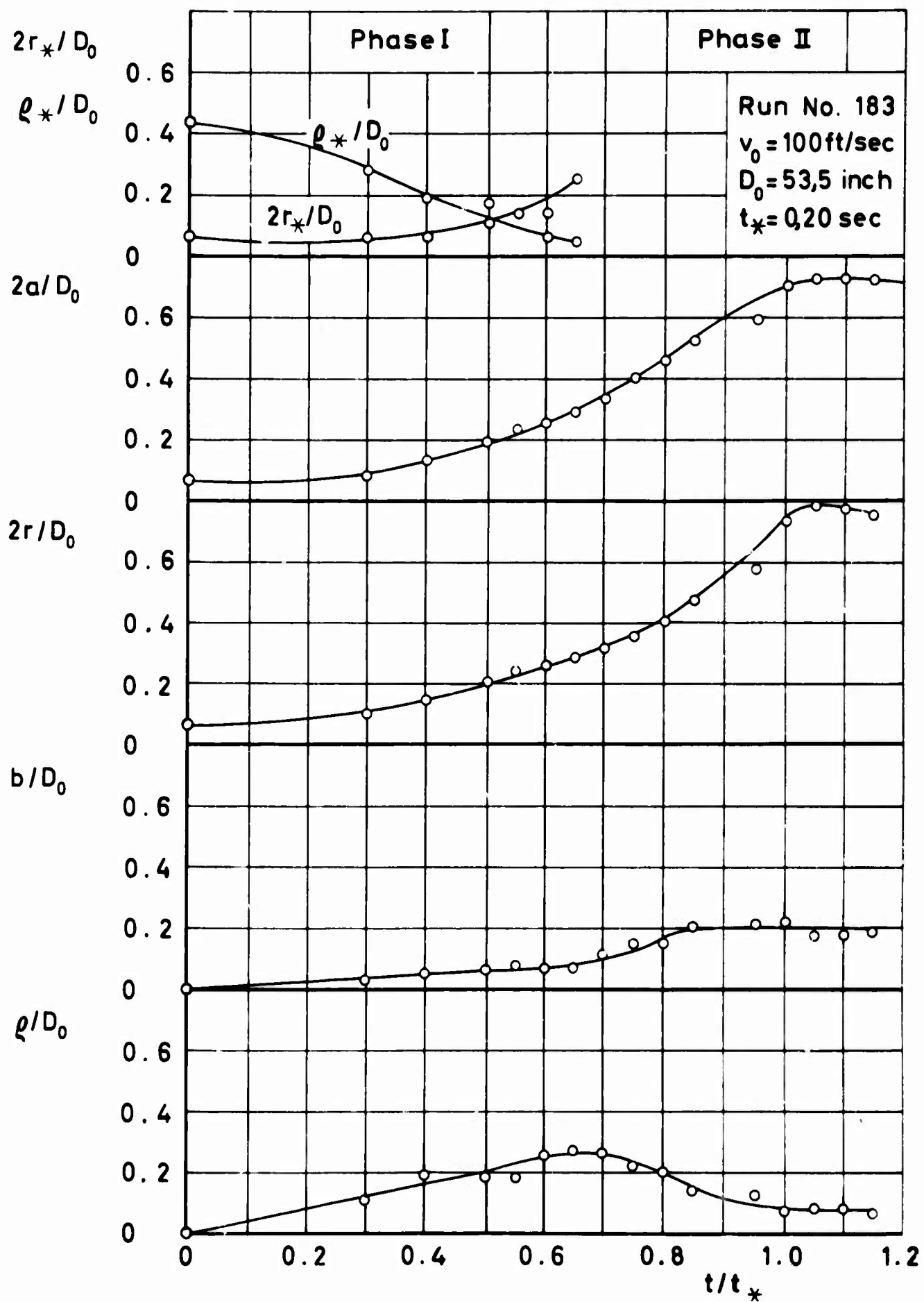


Figure 65 Parameters of Idealized Photographic Shape Versus Time for Circular Flat

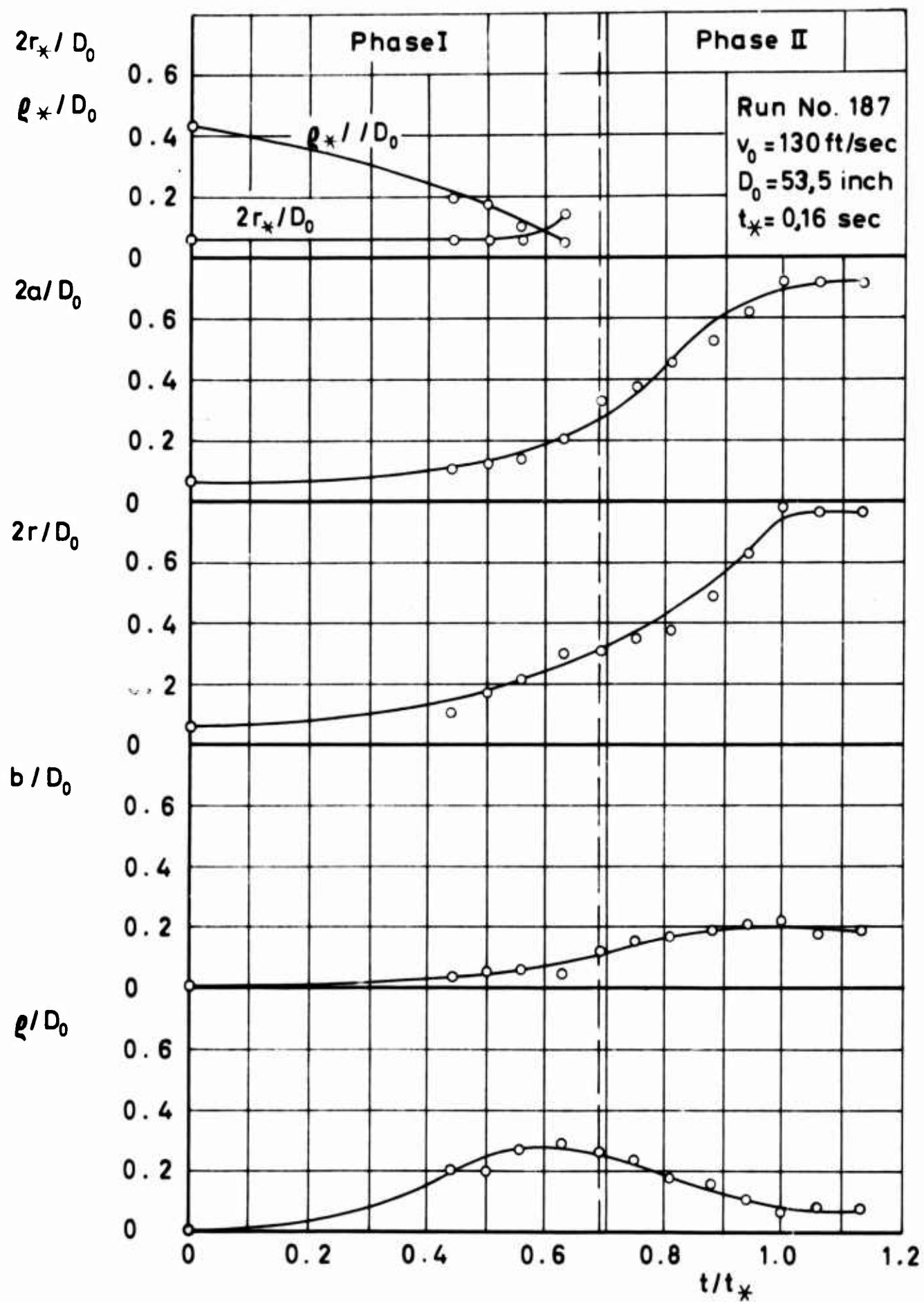


Figure 66 Parameters of Idealized Photographic Shape Versus Time for Circular Flat

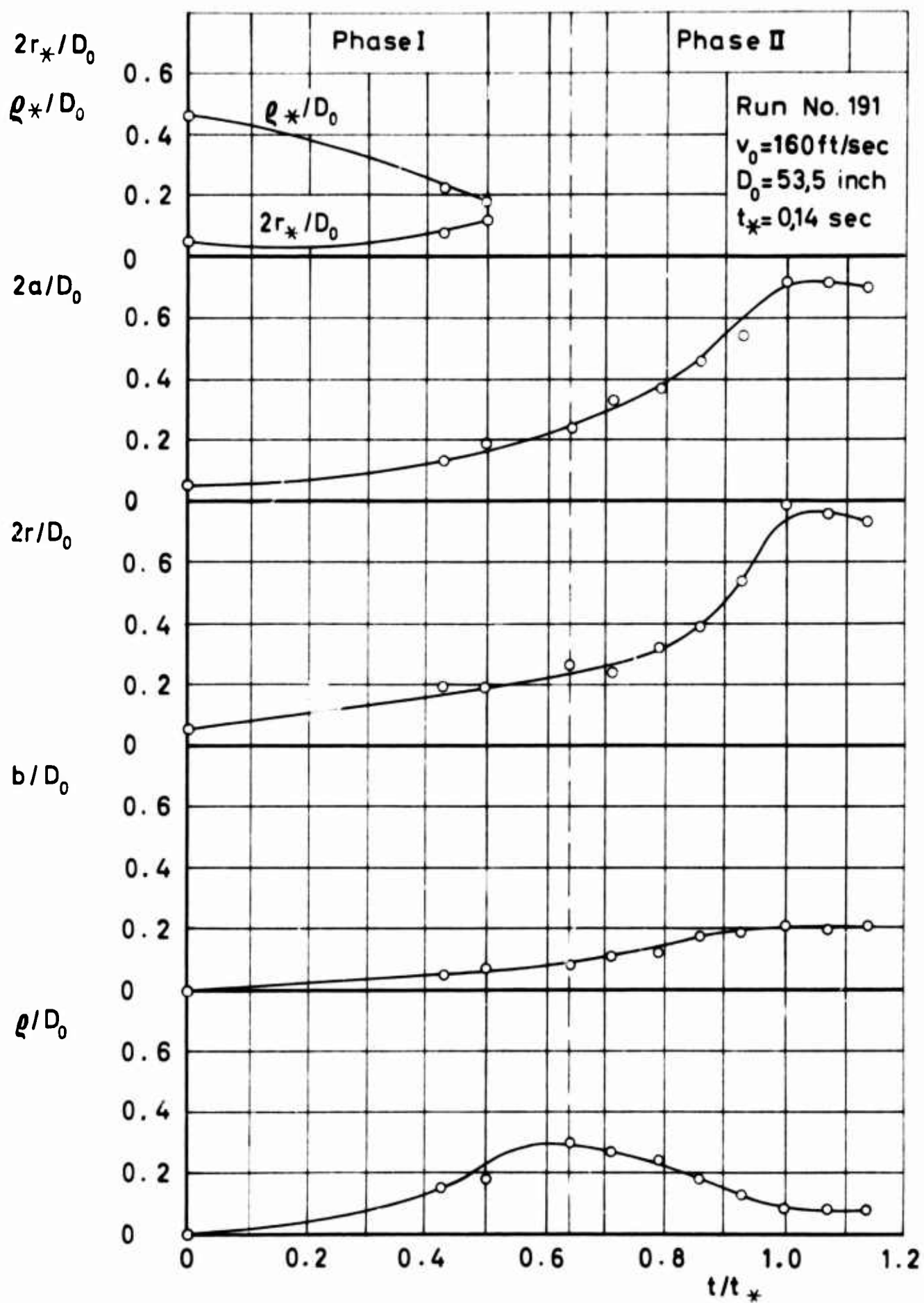


Figure 67 Parameters of Idealized Photographic Shape Versus Time for Circular Flat

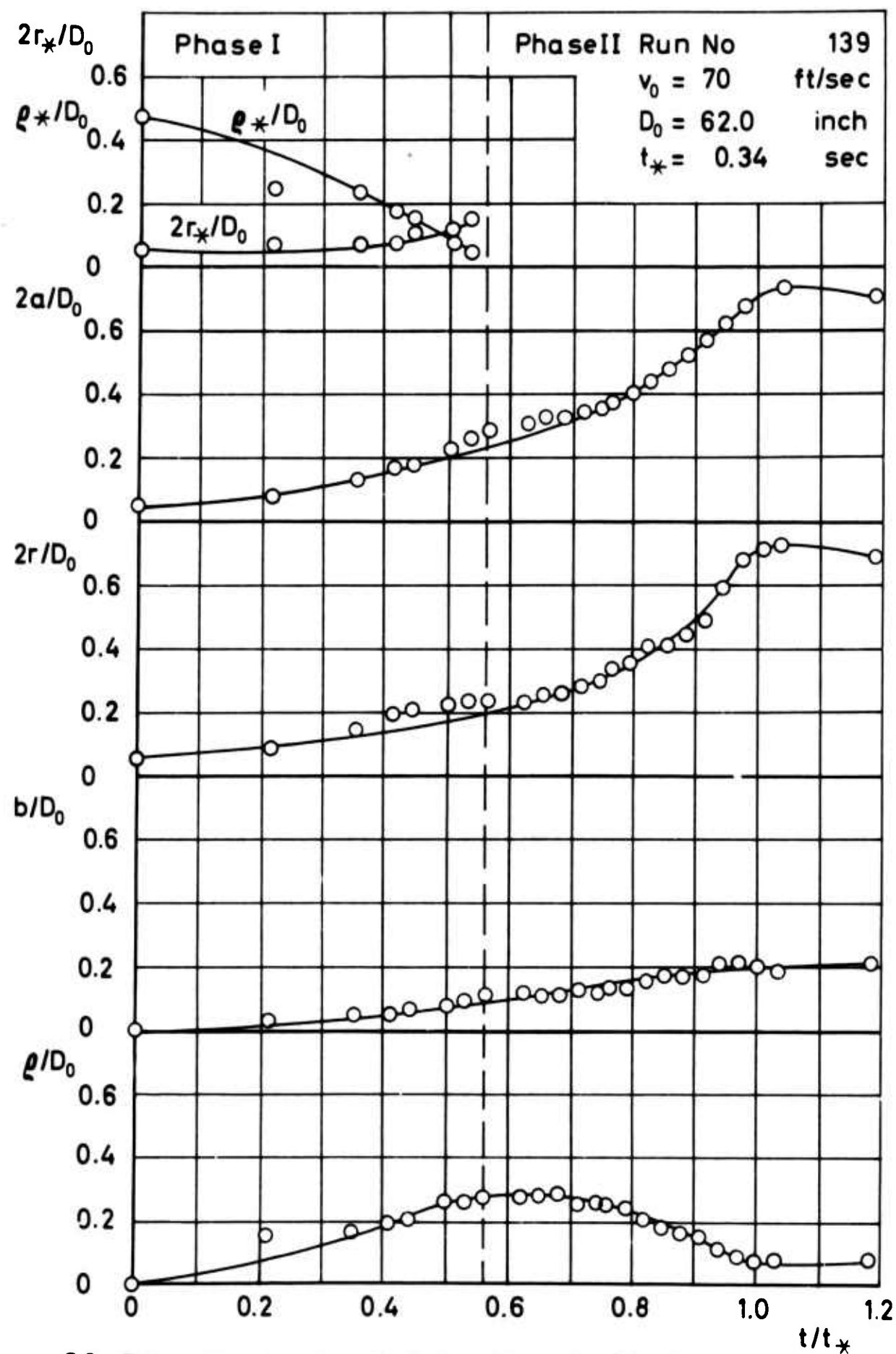


Figure 68 Parameters of Idealized Photographic Shape Versus Time for Extended Skirt

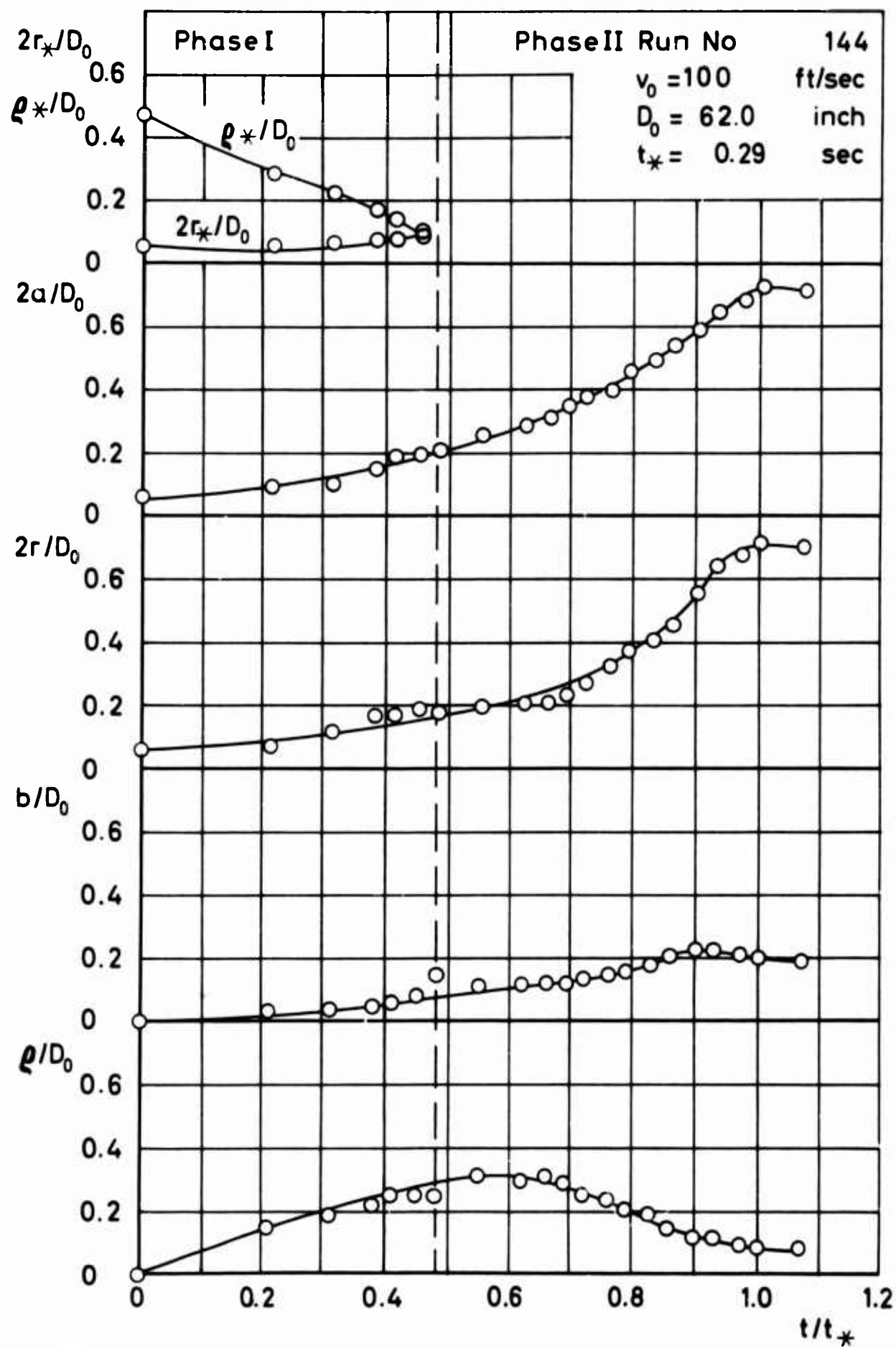


Figure 69 Parameters of Idealized Photographic Shape Versus Time for Extended Skirt

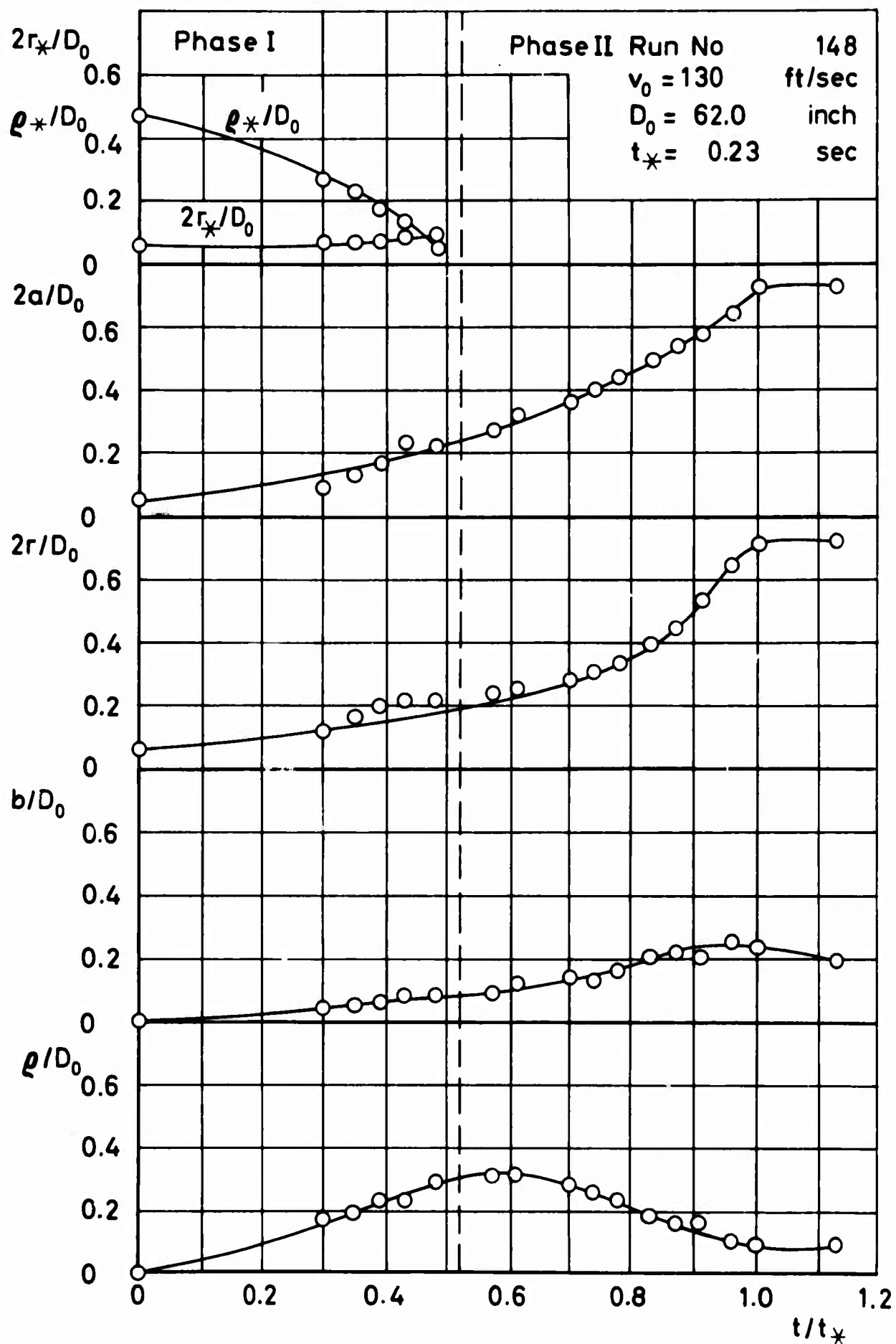


Figure 70 Parameters of Idealized Photographic Shape Versus Time for Extended Skirt

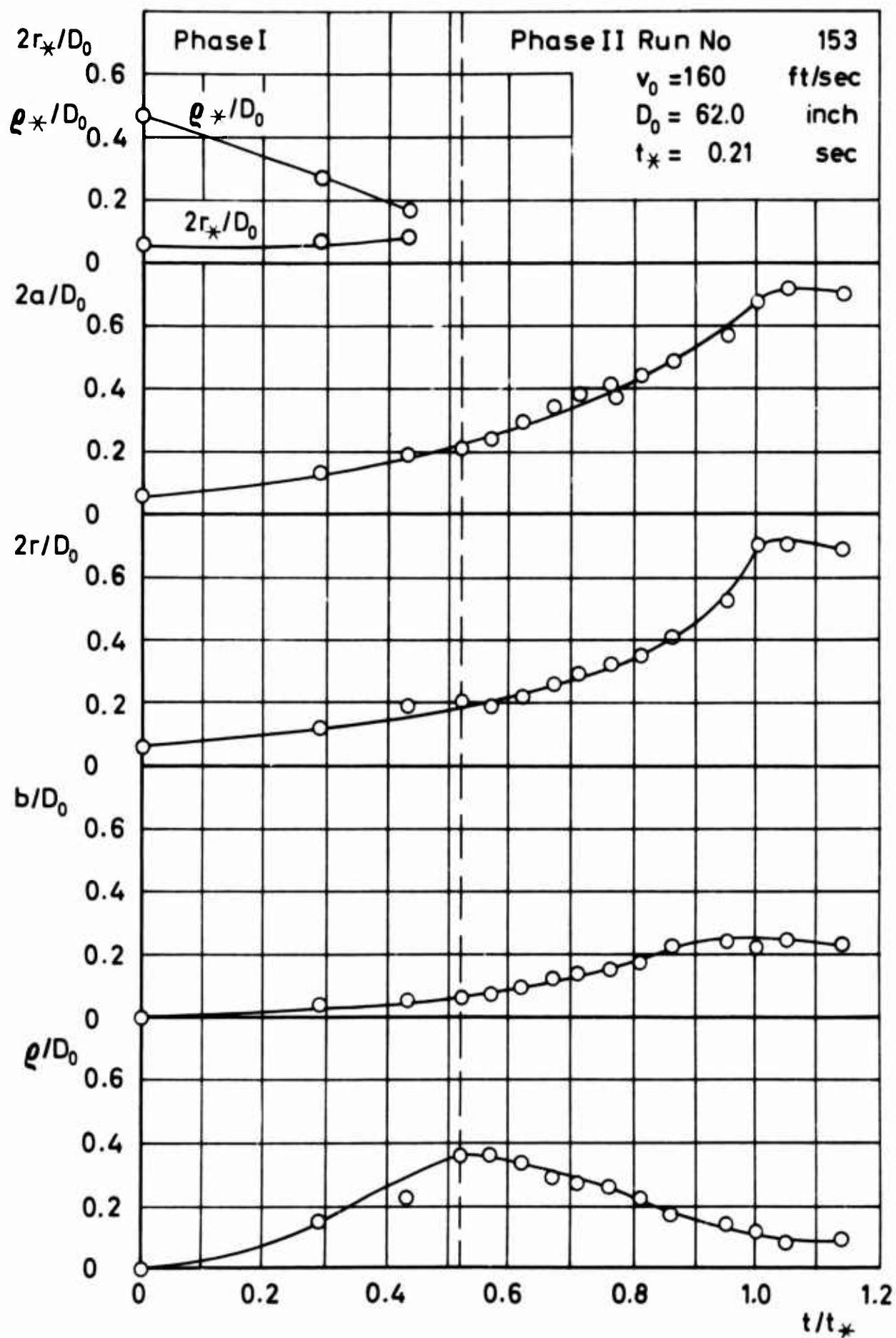


Figure 71 Parameters of Idealized Photographic Shape Versus Time for Extended Skirt

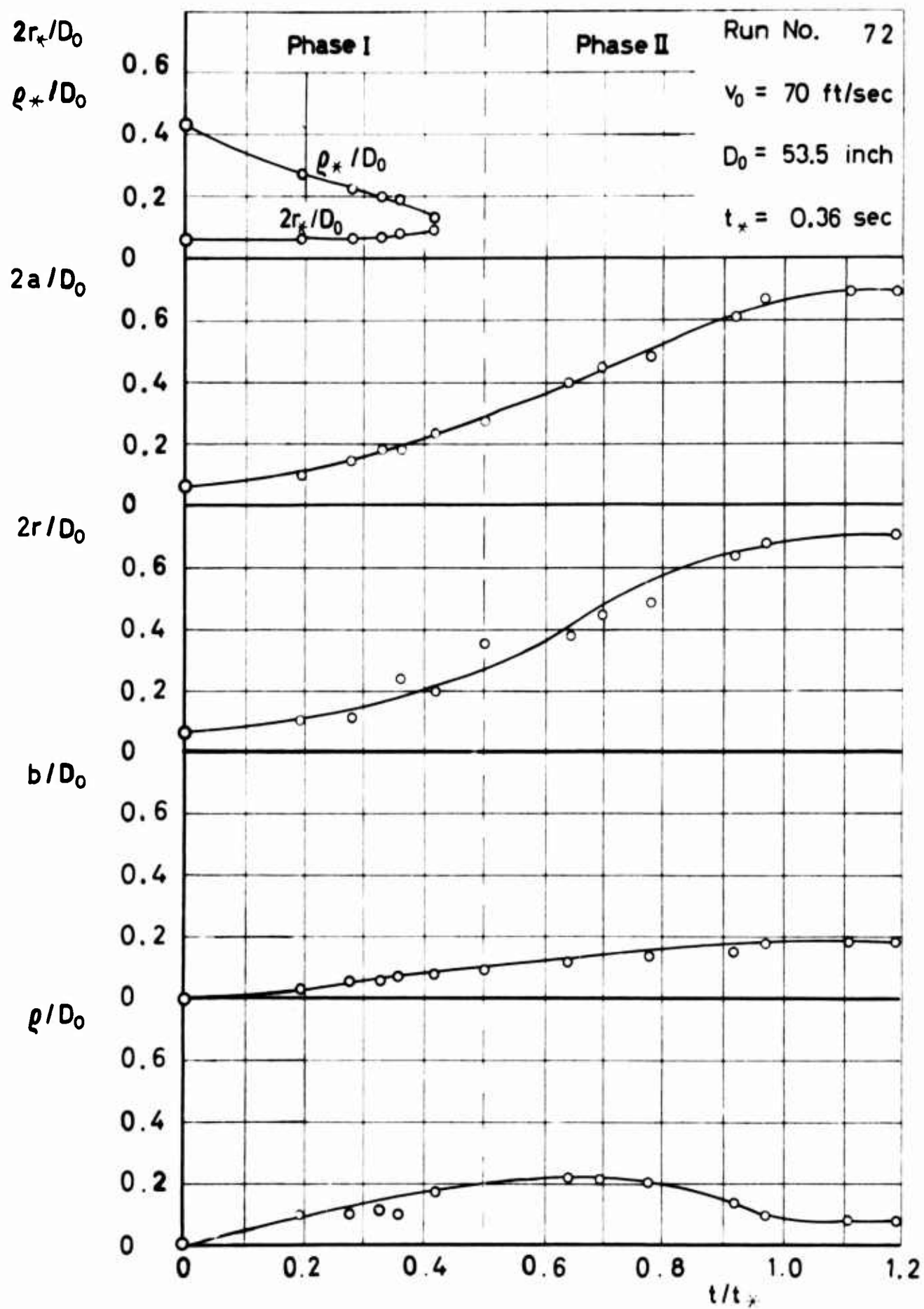


Figure 72 Parameters of Idealized Photographic Shape Versus Time for FIST

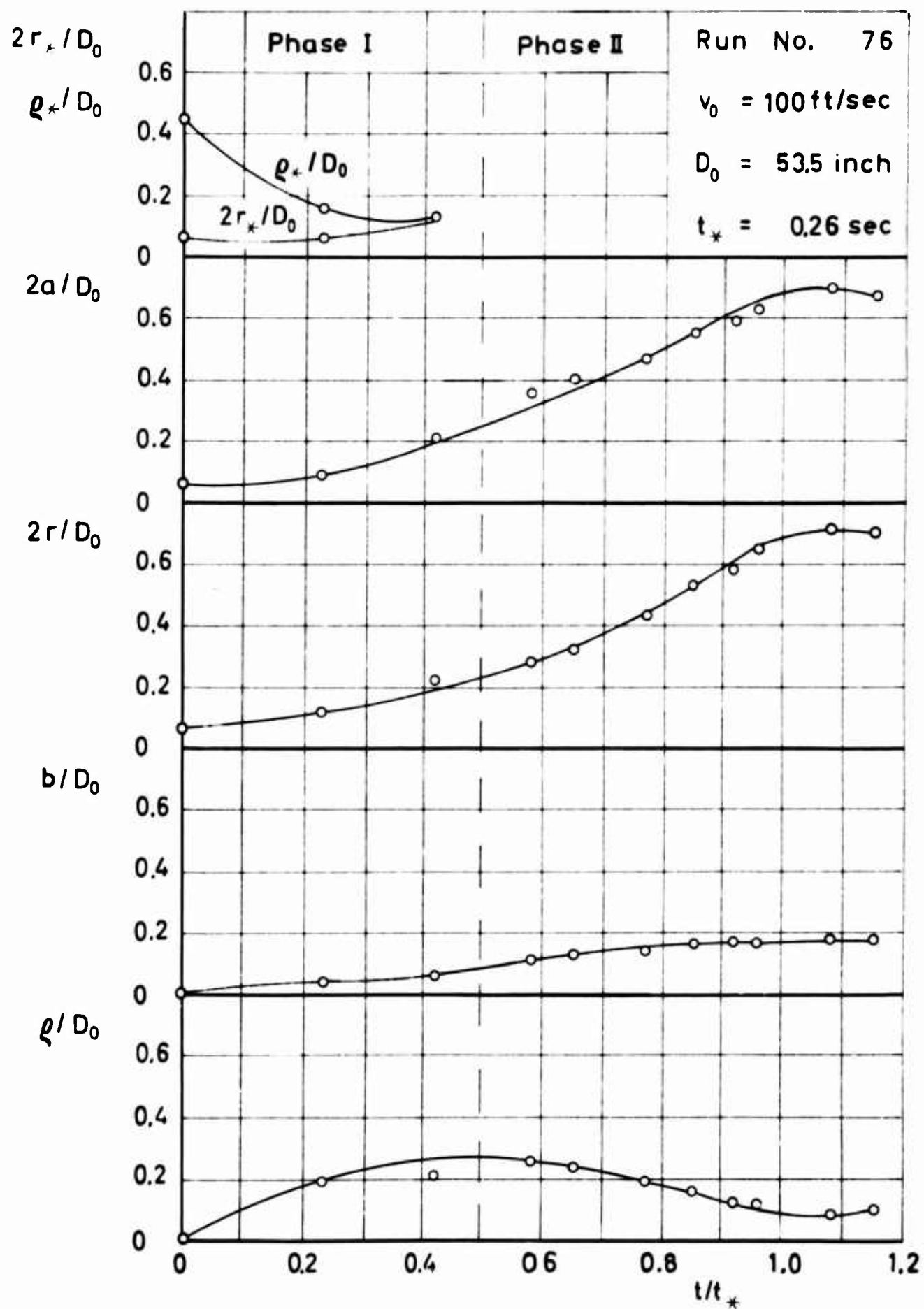


Figure 73 Parameters of Idealized Photographic Shape Versus Time for FIST

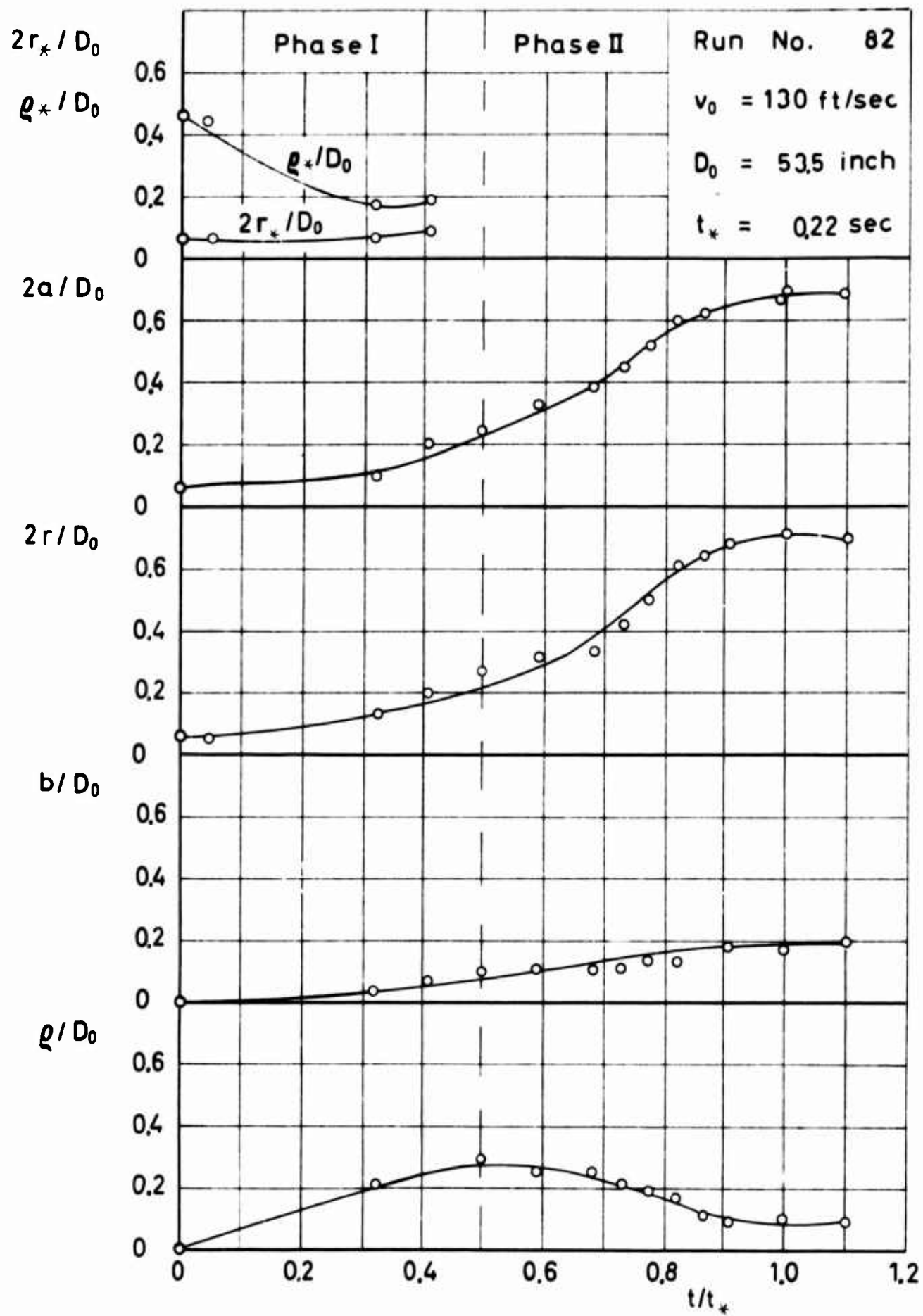


Figure 74 Parameters of Idealized Photographic Shape Versus Time for FIST

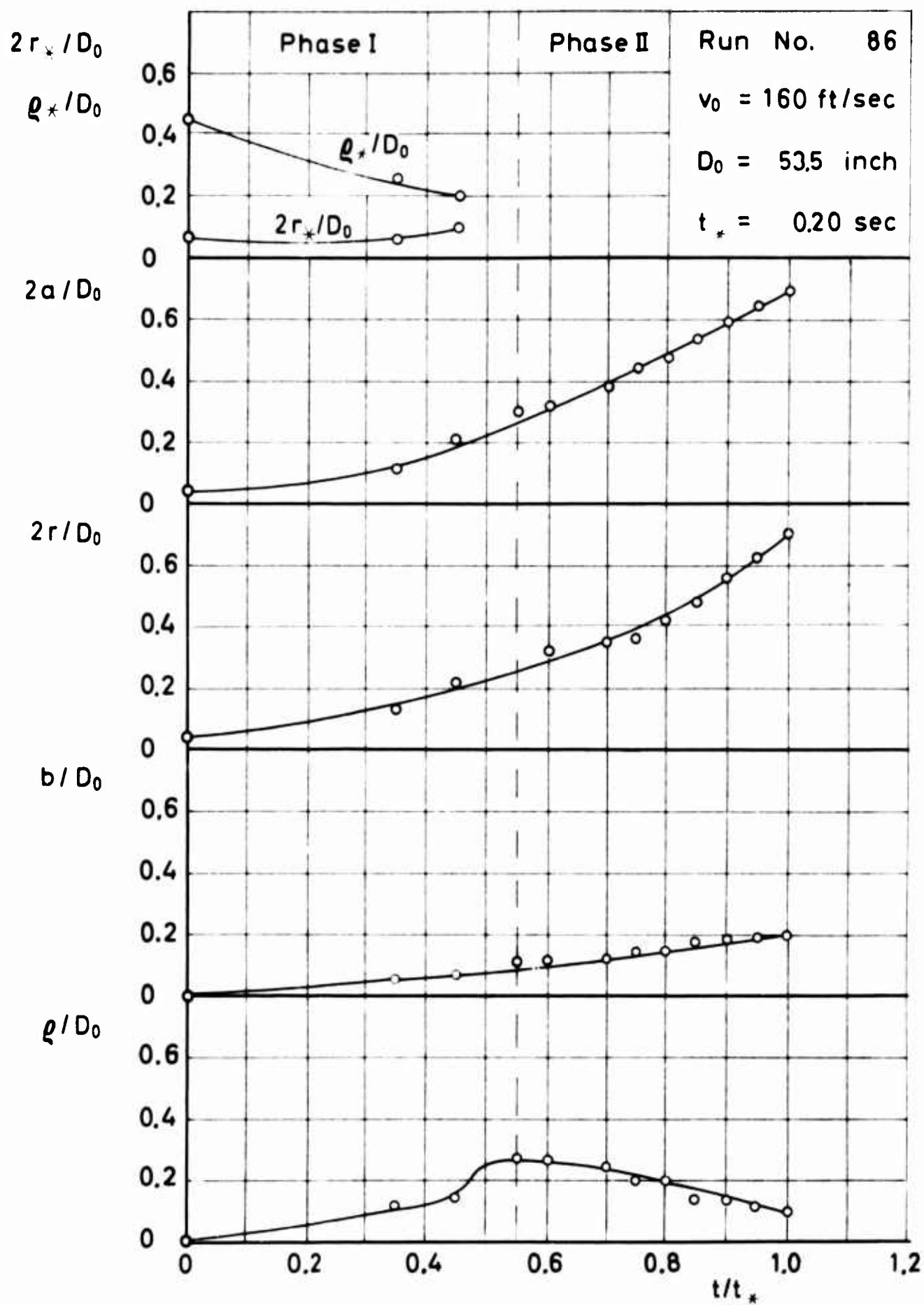


Figure 75 Parameters of Idealized Photographic Shape Versus Time for FIST

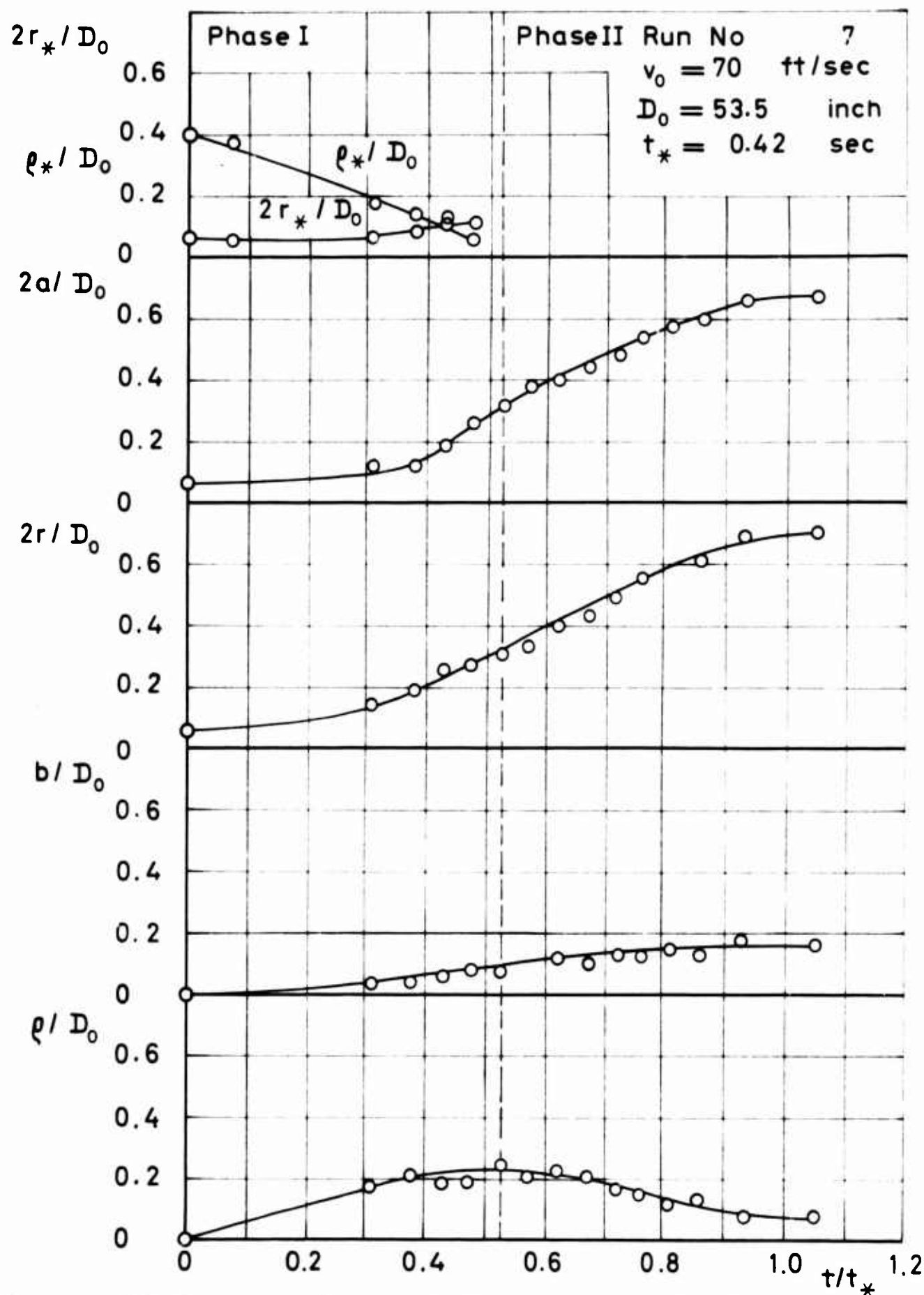


Figure 76 Parameters of Idealized Photographic Shape Versus Time for Ringslot

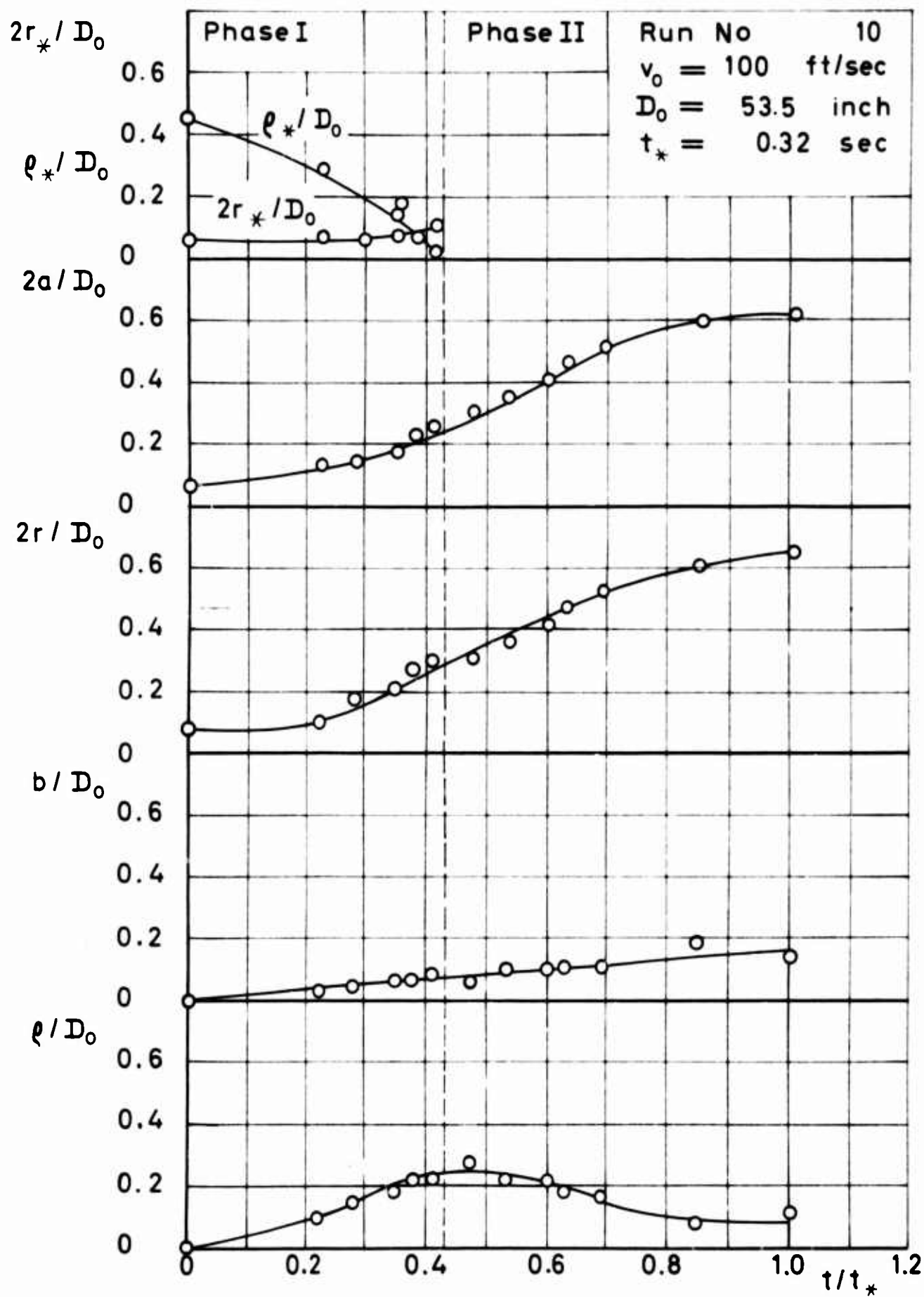


Figure 77 Parameters of Idealized Photographic Shape Versus Time for Ringslot

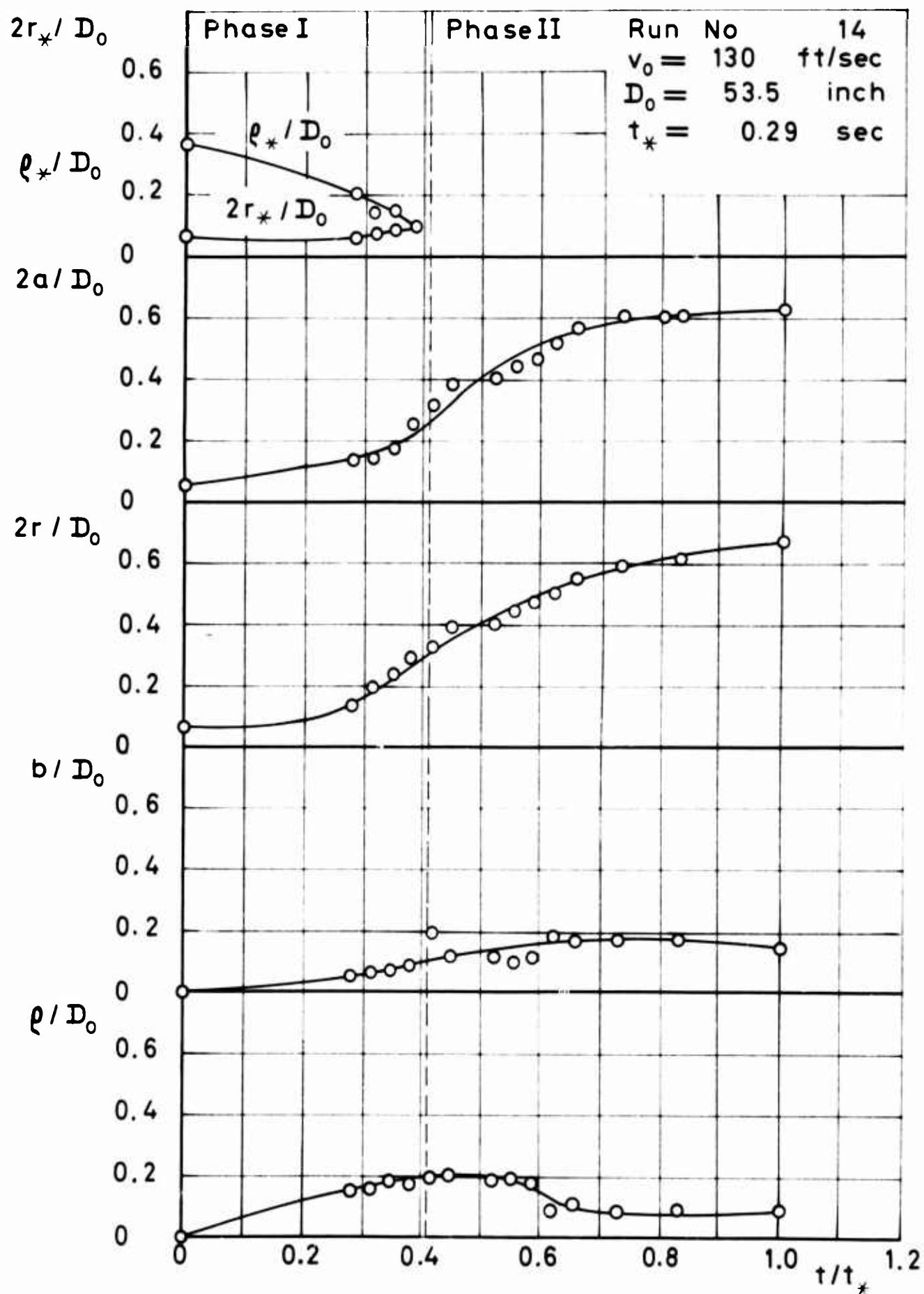


Figure 78 Parameters of Idealized Photographic Shape Versus Time for Ringslot

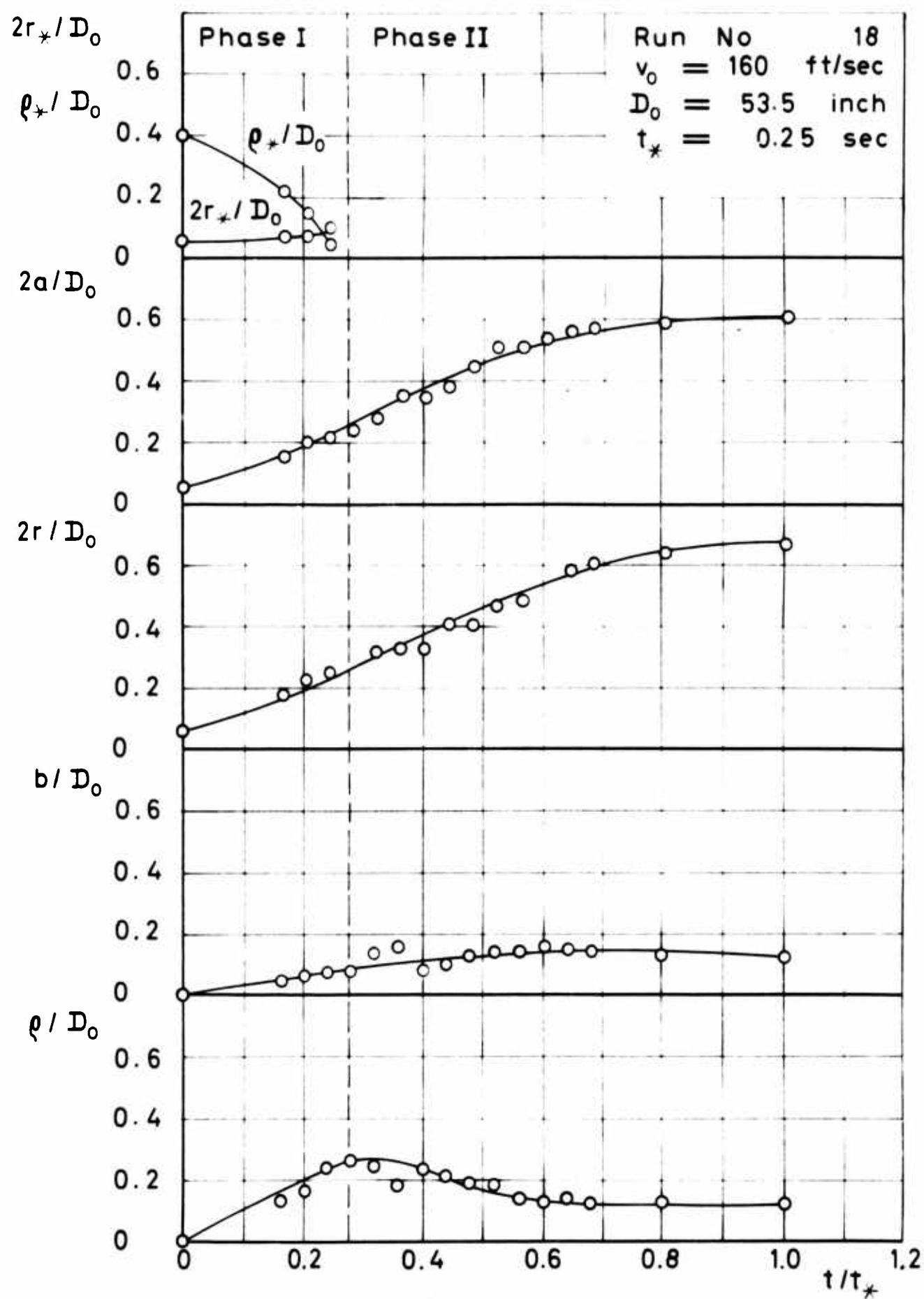


Figure 79 Parameters of Idealized Photographic Shape Versus Time for Ringslot

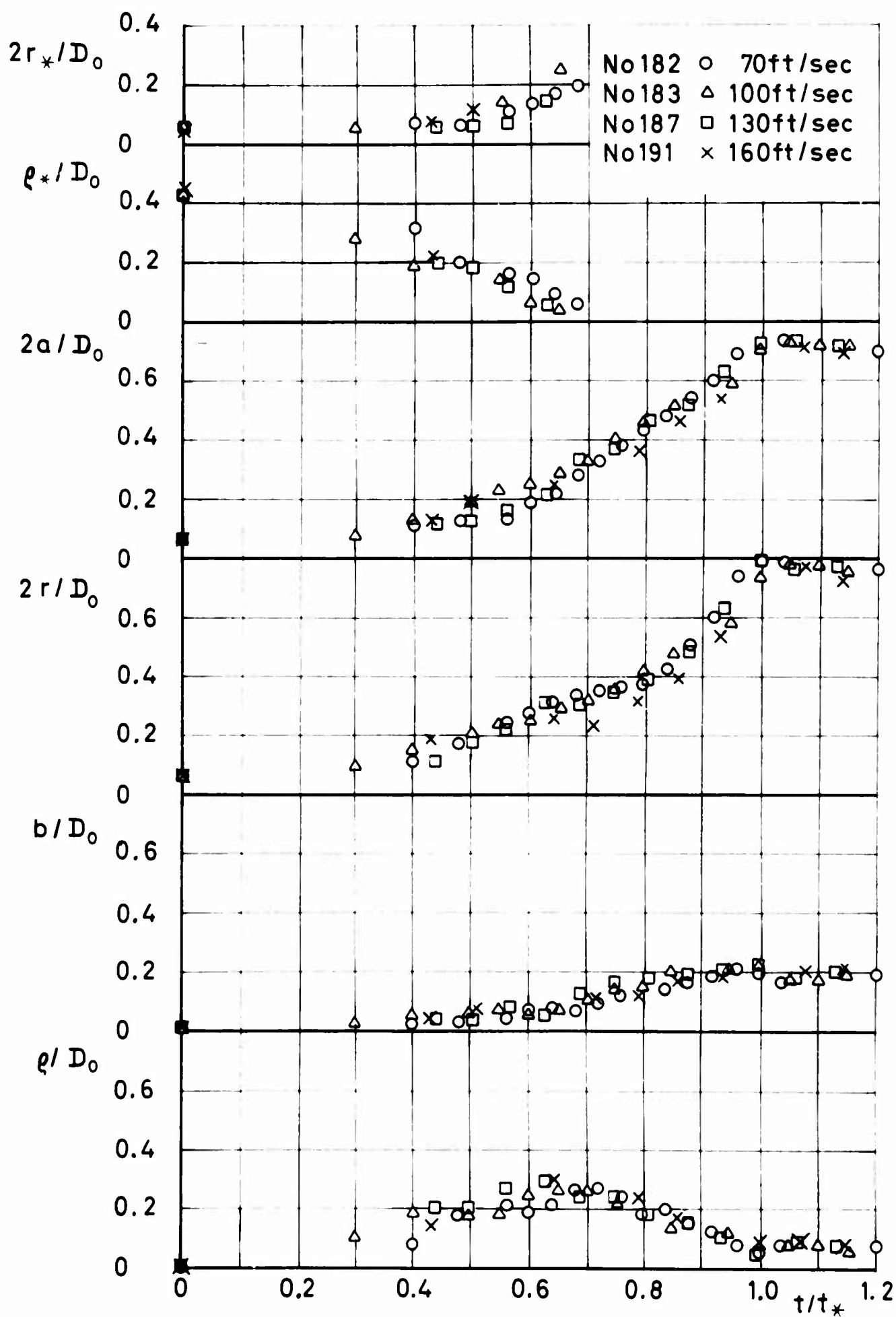


Figure 80 Parameters of Idealized Photographic Shape Versus Time for Circular Flat

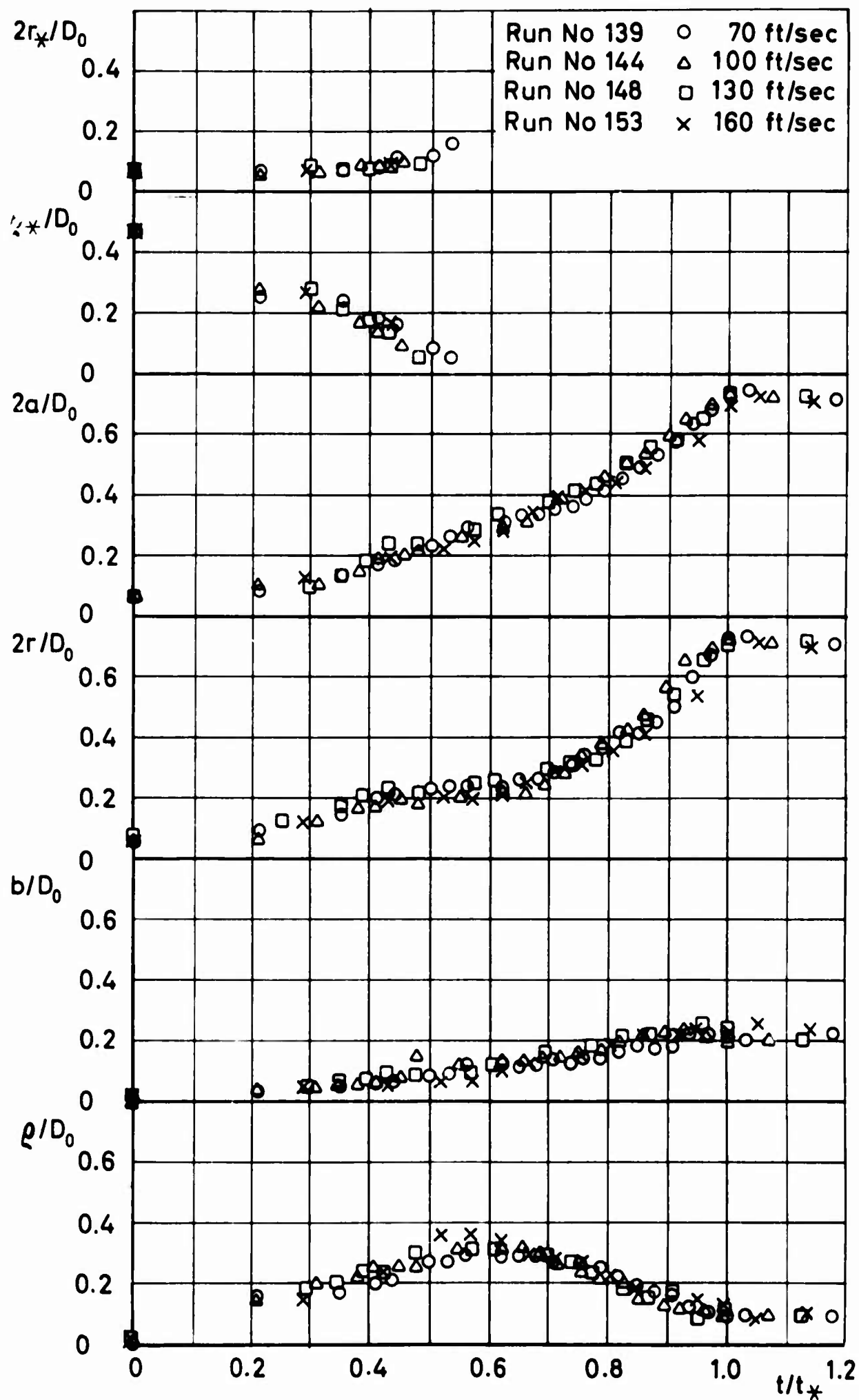


Figure 81 Parameters of Idealized Photographic Shape Versus Time for Extended Skirt

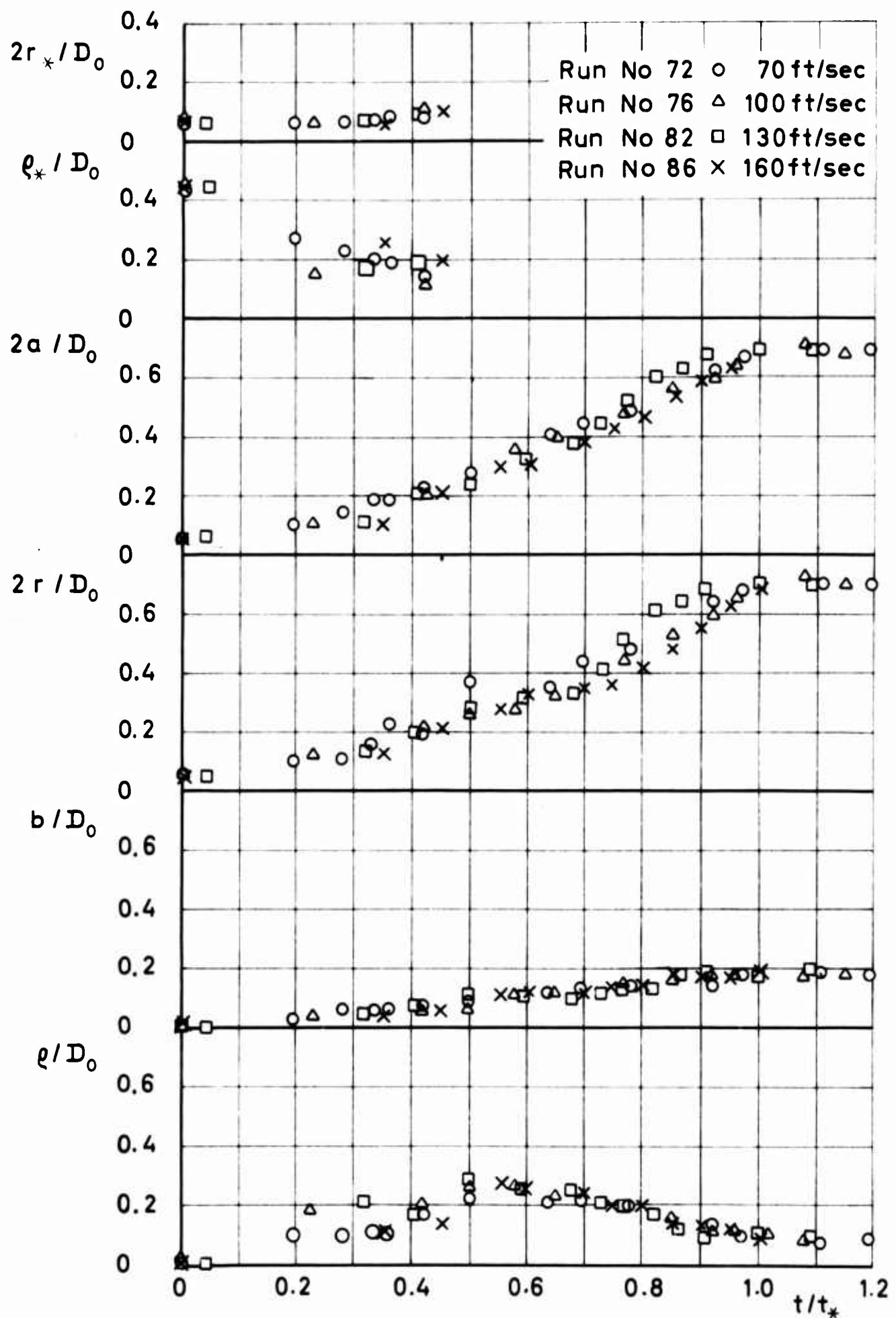


Figure 82 Parameters of Idealized Photographic Shape Versus Time for FIST

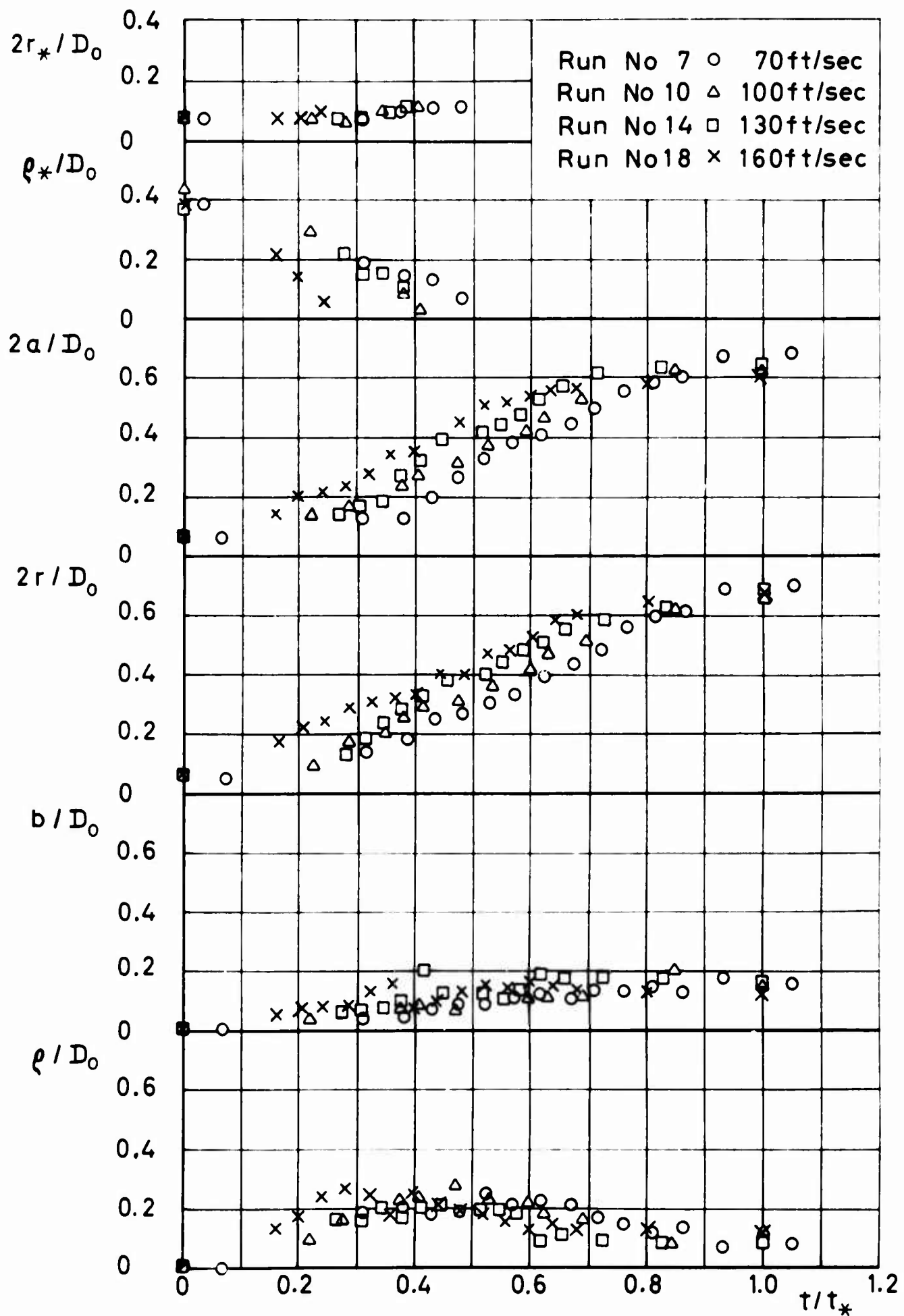


Figure 83 Parameters of Idealized Photographic Shape Versus Time for Ringslot

4. SUMMARY AND RECOMMENDATIONS

The change of the pressure distribution over the surface of four different types of parachute canopies during the period of inflation was experimentally determined for the infinite mass operating condition during low speed wind tunnel tests. The changing canopy shape during inflation was also determined and correlated to the changing pressures.

The results are presented in detail and provide for the first time a good knowledge of this vital relationship. In order to develop an analytical relationship between the changing pressure and the changing canopy shape, many more experimental tests will be required. These are necessary to eliminate abnormal variations in test conditions and canopy deployment.

In order to substantiate the findings obtained on canopy models, additional measurements of the dynamic pressure distribution should be performed on full scale canopies during free-flight tests.

For the finite mass operating case, quite different results and relationships may be expected. The two different operating modes should therefore be separated during further investigations.

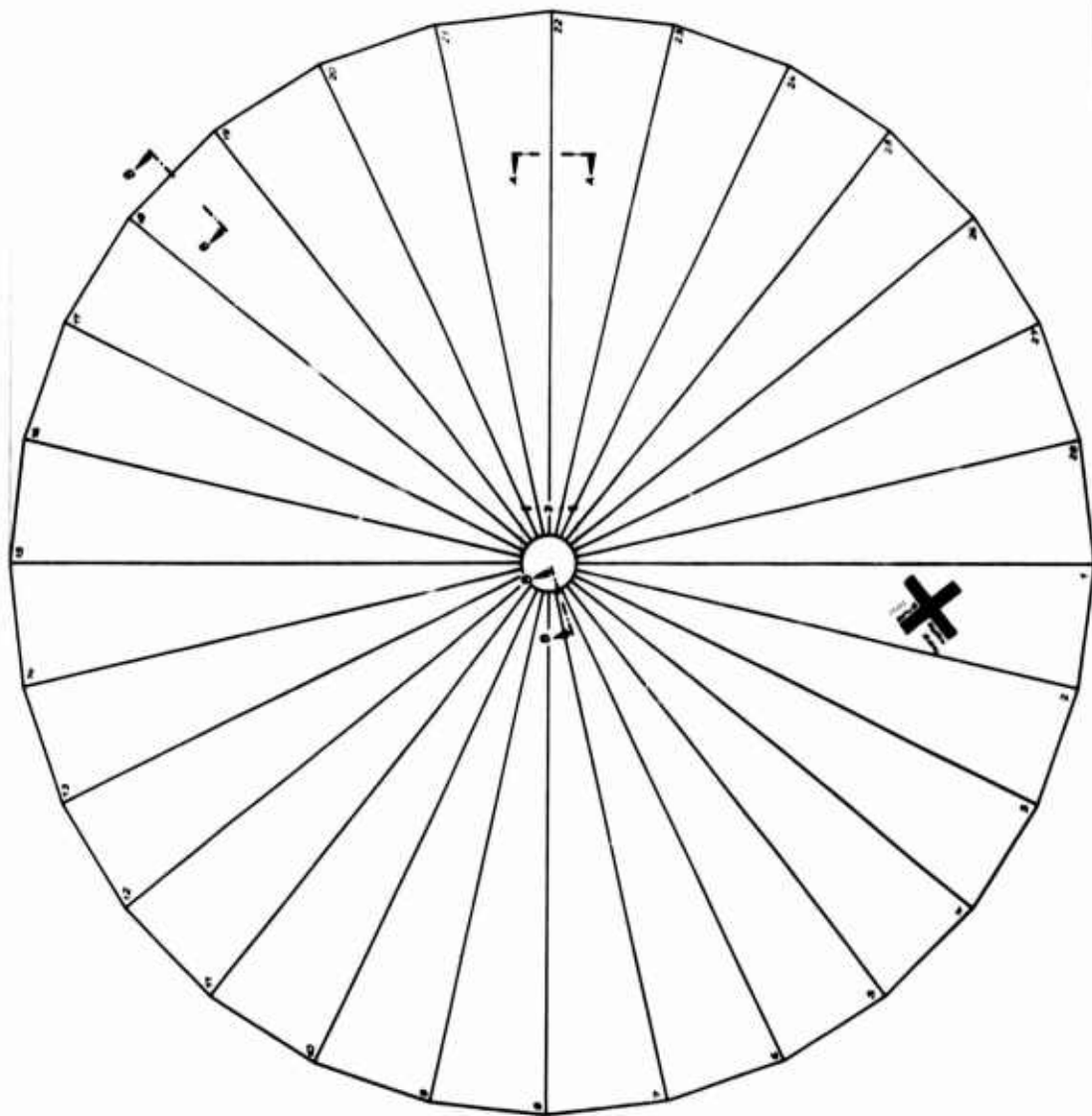
5. REFERENCES

- [1] Jones, R. A., On the Aerodynamic Characteristics of Parachutes. British ARC Report R & M No 862, June 1923.
- [2] Topping, A. D. et al., A Study of Canopy Shapes and Stresses for Parachutes in Steady Descent. WADC-TR-55-294, Oct. 1955.
- [3] Heinrich, H. G., Jamison L. R., Parachute Stress Analysis During Inflation and at Steady State. AIAA Entry Technology Conference, Williamsburg, Oct. 1964.
- [4] Performance of and Design Criteria for Deployable Aerodynamic Decelerators. ASD-TR-61-579, Dec. 1963.
- [5] Berndt, R. J., Experimental Determination of Parameters for the Calculation of Parachute Filling Times. German WGL-Jahrbuch 1964.
- [6] Melzig, H. D., The Change of Pressure Distribution on Parachute Canopies During Inflation. Final Phase Aerodynamic Deceleration Course, University of Minnesota, July 1965.

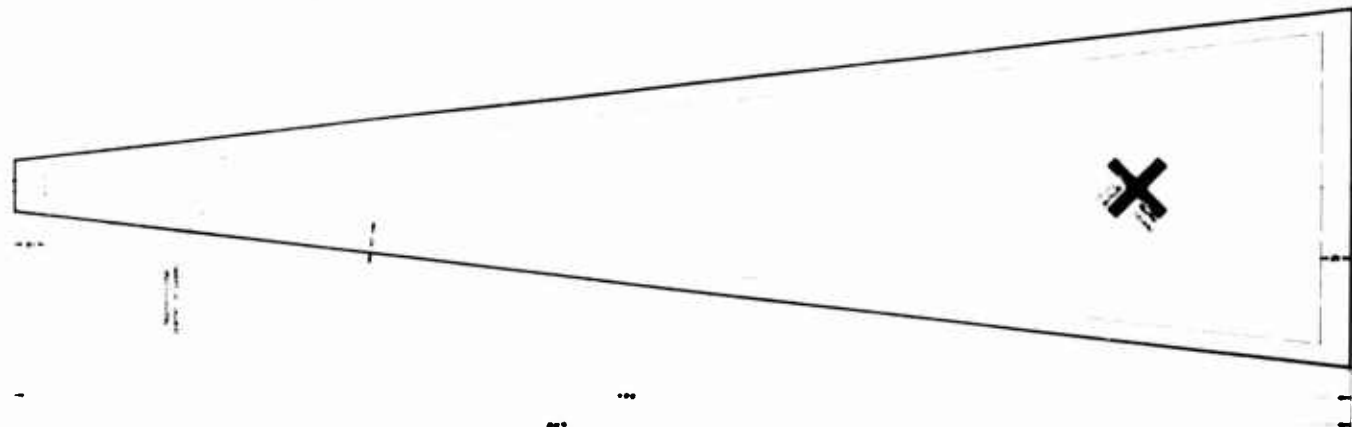
APPENDIX I

PARACHUTE CANOPY MODELS

Detail drawings of the four canopy models used during the experimental test program are shown in Figures 84 thru 87.



Model M 12.5
Scale 1:100

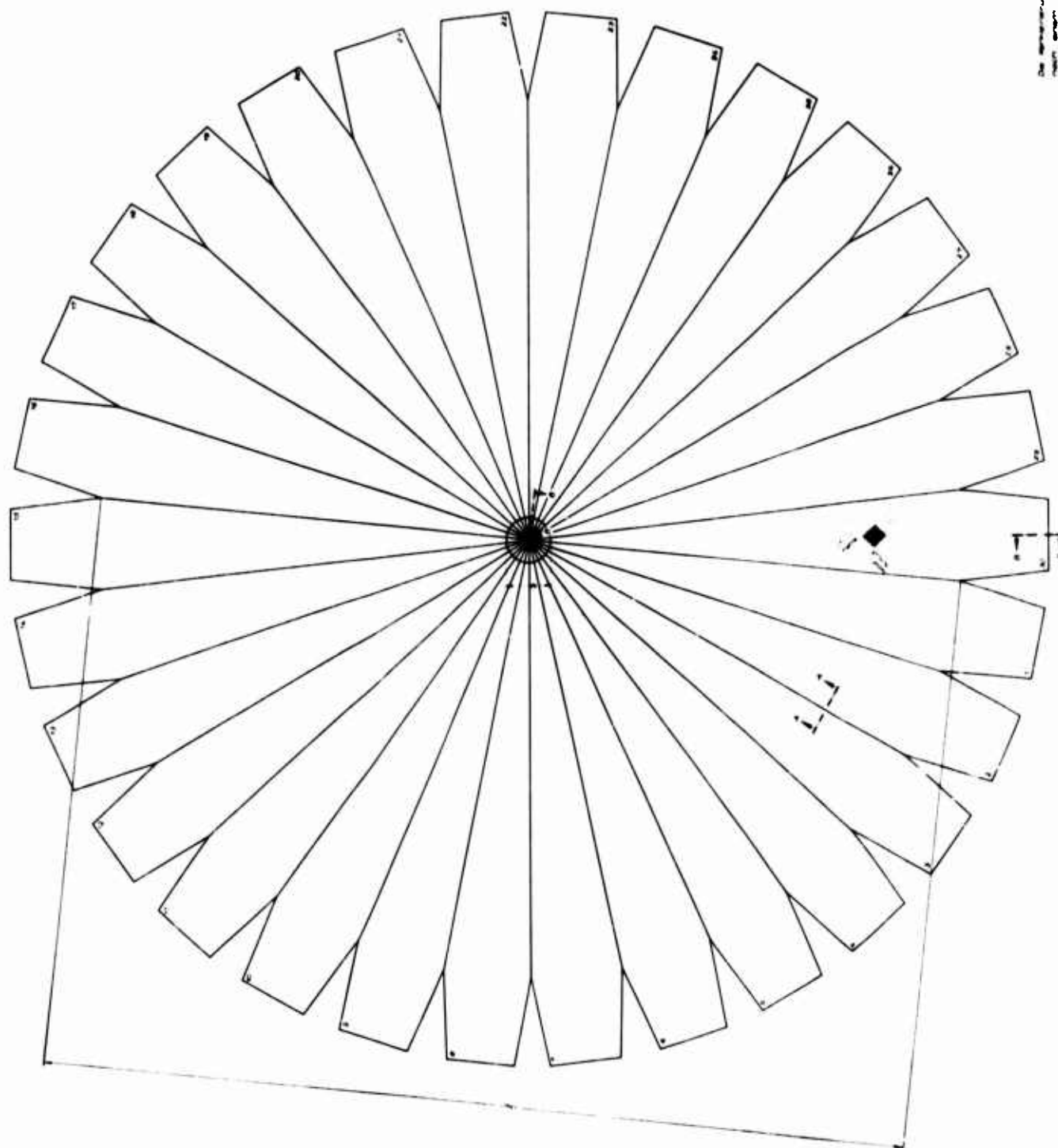


Model M 12.5
Scale 1:100

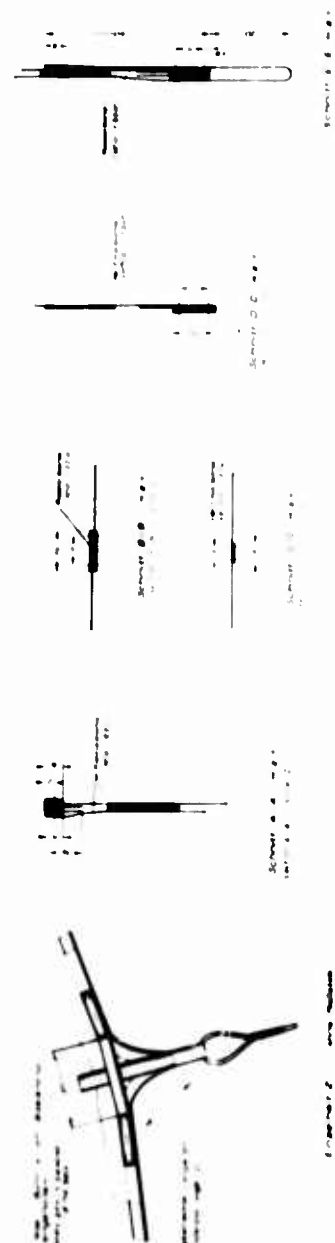
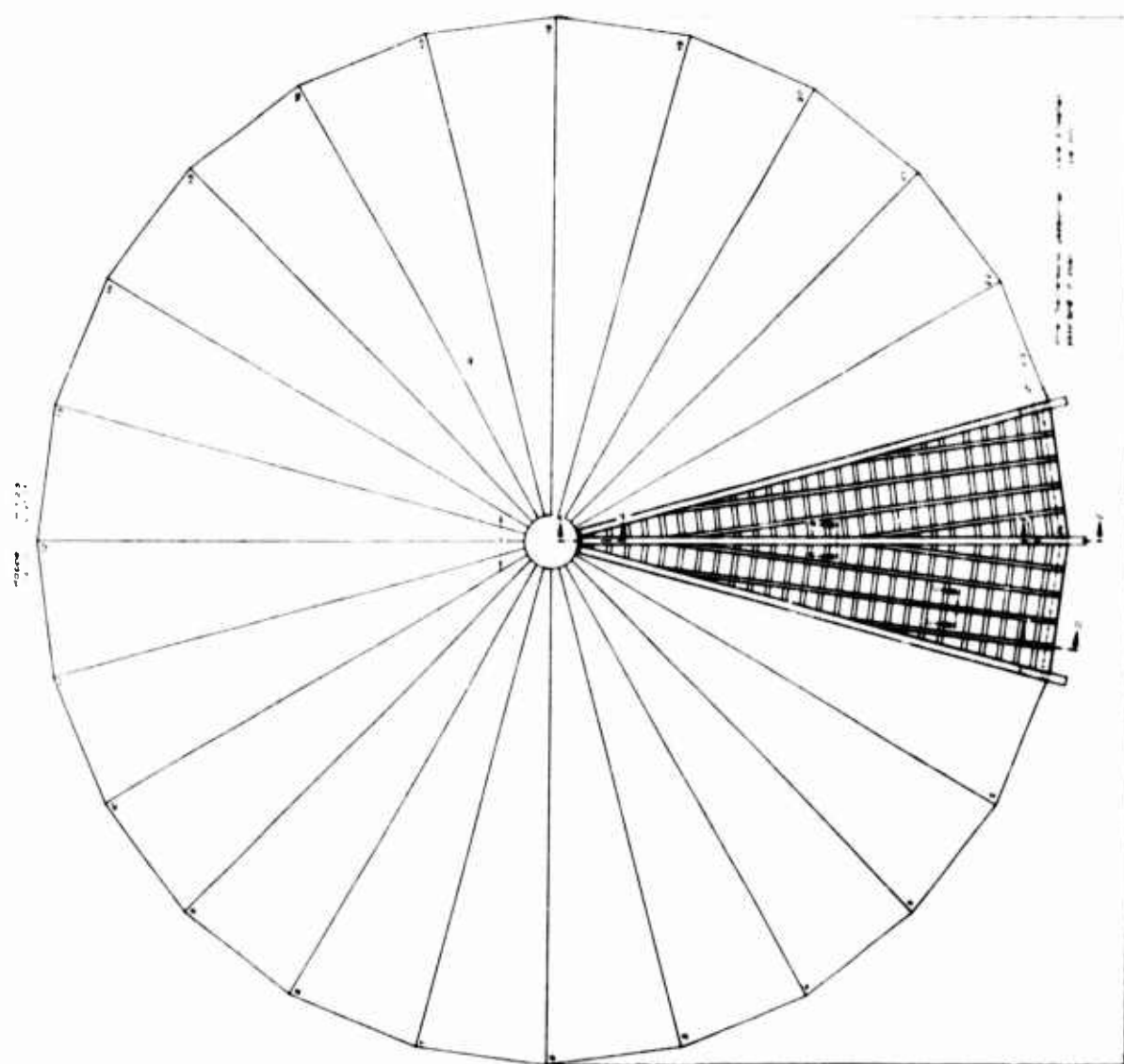
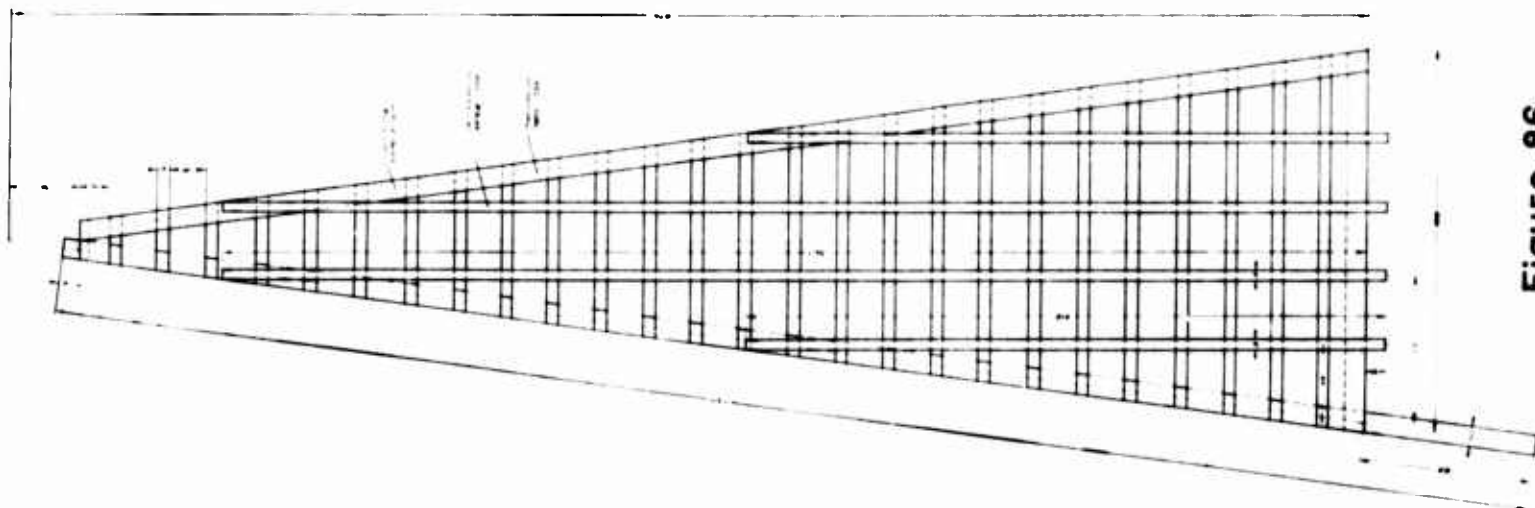
Model M 12.5
Scale 1:100

Model	M 12.5
Scale	1:100
Material	CS-30 127
Color	Black
Weight	0.15 kg
Length	1.5 m
Width	0.1 m
Area	0.15 m²
Volume	0.00225 m³
Mass	0.0225 kg
Force	0.225 N
Pressure	1.5 N/m²
Stress	1.5 N/m²
Strain	0.0015
Modulus	100 N/m²
Frequency	1.5 Hz
Wavelength	0.133 m
Speed	1.5 m/s
Acceleration	1.5 m/s²
Deceleration	1.5 m/s²
Velocity	1.5 m/s
Displacement	1.5 m
Time	1.5 s
Angle	1.5 rad
Frequency	1.5 Hz
Wavelength	0.133 m
Speed	1.5 m/s
Acceleration	1.5 m/s²
Deceleration	1.5 m/s²
Velocity	1.5 m/s
Displacement	1.5 m
Time	1.5 s
Angle	1.5 rad

Figure 84



535 Model of a
Circular Flat
FIST Parachute



Project	525	Model of	525
Sheet	1	Scale	1/4" = 1'-0"
Date		Drawn by	
Checked by		Engineer	
Approved by		Architect	

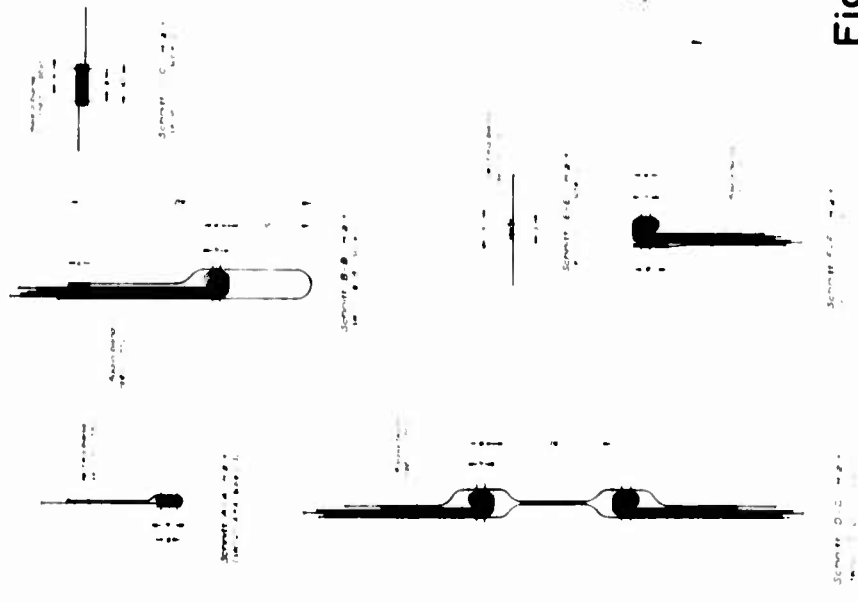
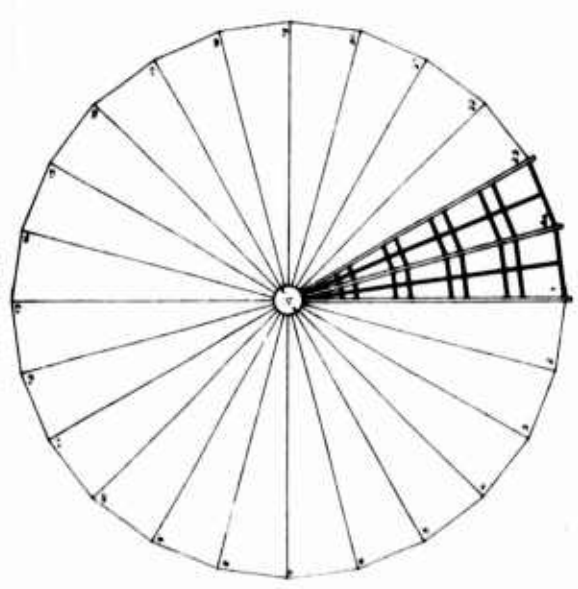
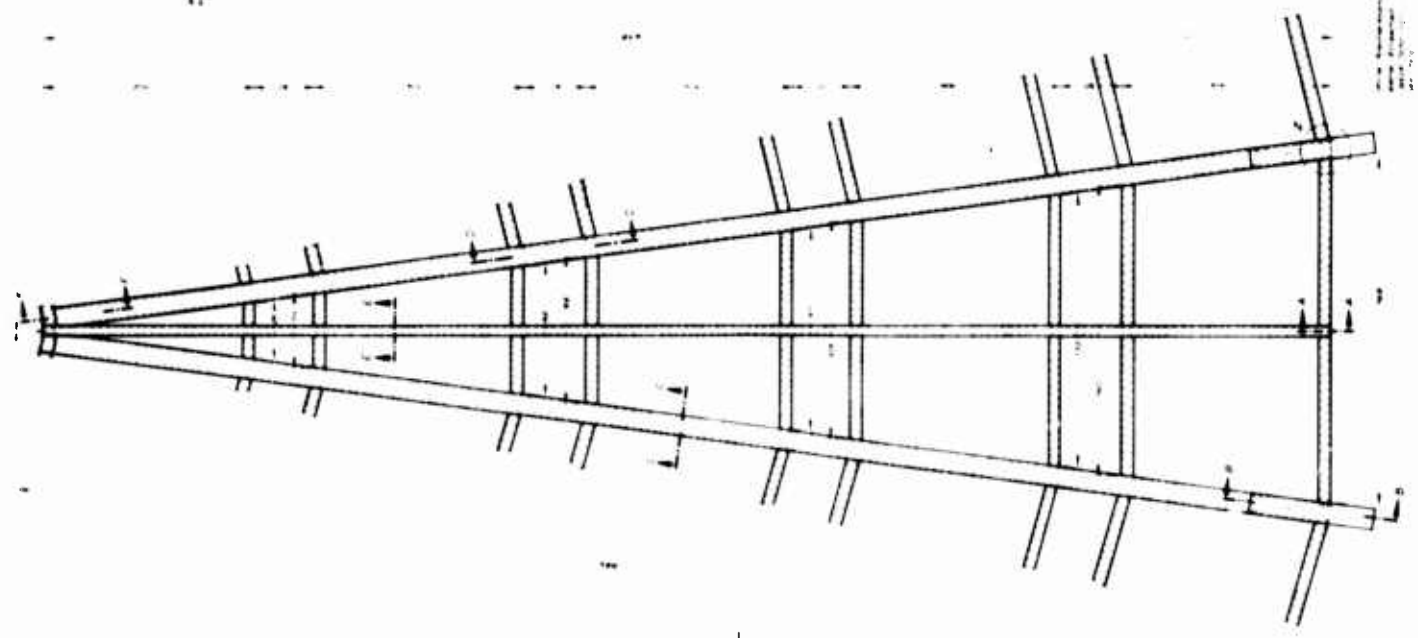
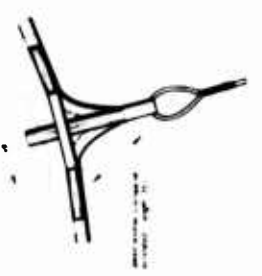
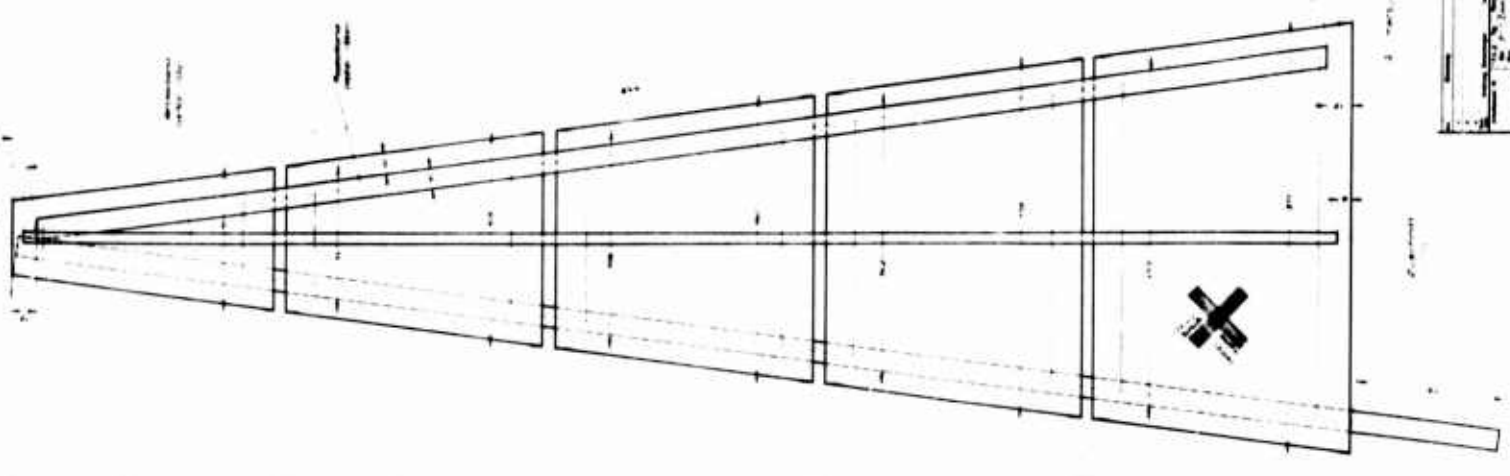


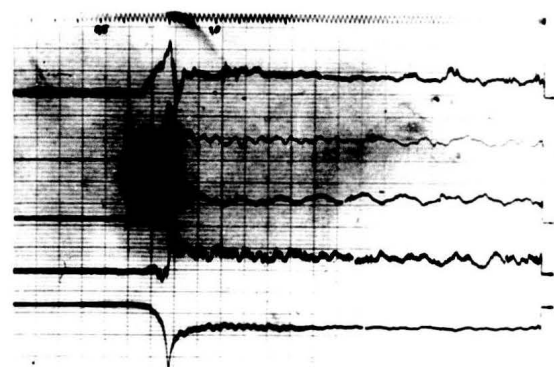
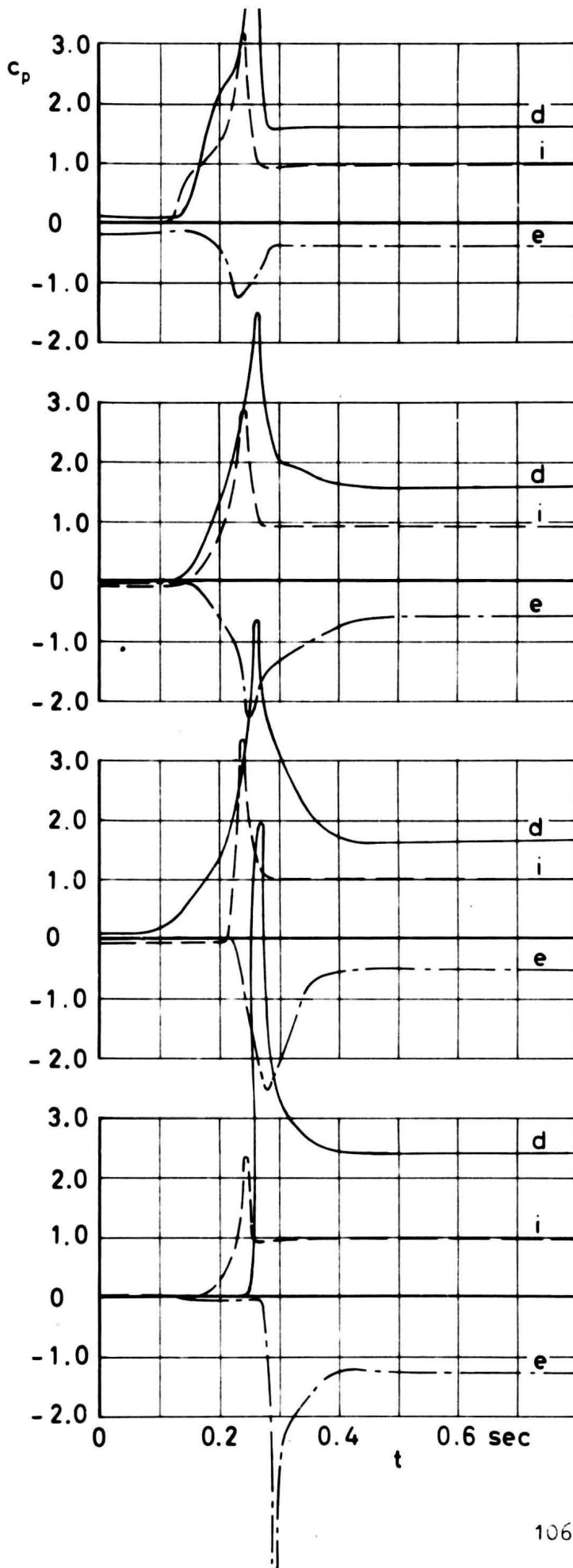
Figure 87

APPENDIX II

COMPARATIVE PRESSURE COEFFICIENT VERSUS TIME RELATIONSHIPS

A complete picture of the pressure versus time relationships for each canopy type and deployment velocity is presented in Figures 88 thru 102 in which the differential, internal and external pressure coefficients are plotted versus a common time base. Since the plottings are based upon smoothed data, reproduction of the original oscillograph traces are presented also to show the fluctuations in pressures actually encountered.

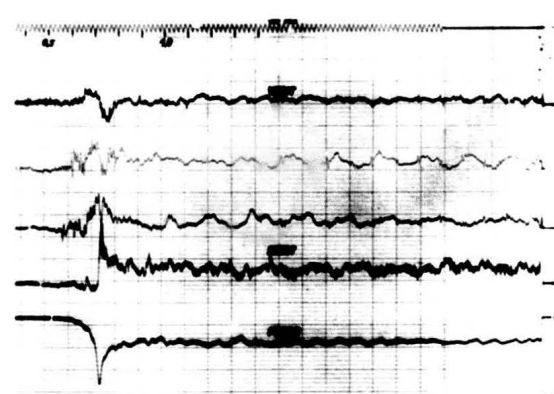
As may be seen on the original traces, a recording of the force generated by the canopy model during inflation was made during each run. Although a numerical evaluation of the force traces was not performed, they are presented here for correlative purposes.



No.182 p_d differential pressure



No.194 p_i internal pressure

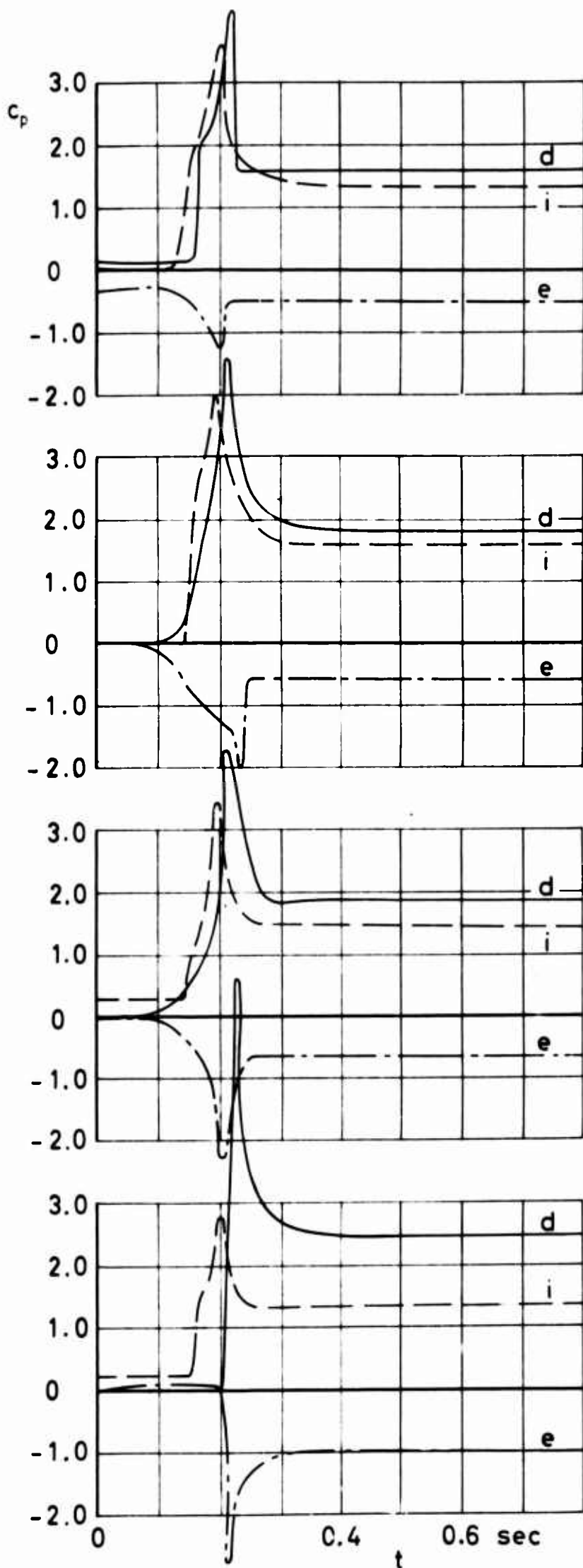


No.211 p_e external pressure

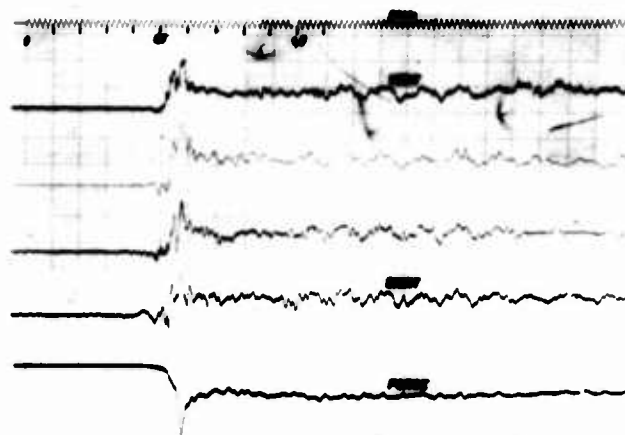
Figure 88 c_p versus time for differential, internal and external pressure

$v_0 = 70$ ft/sec

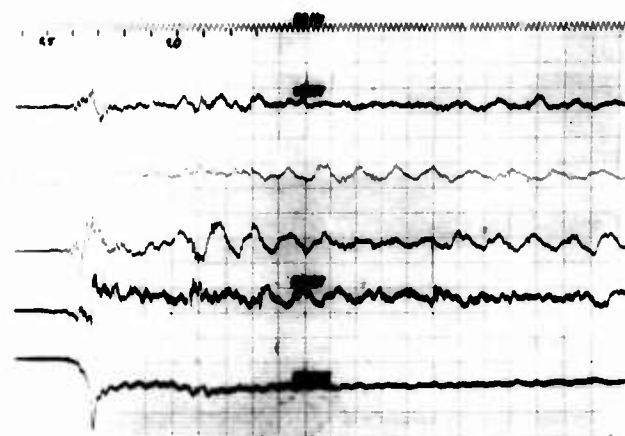
Type: Circular Flat



No. 183 p_d



No. 200 p_i

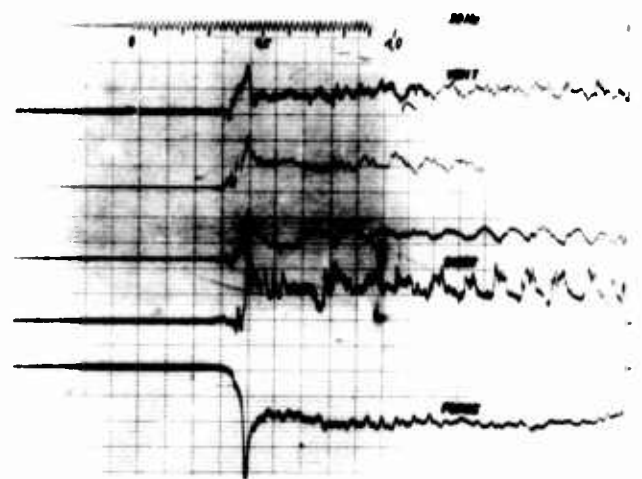
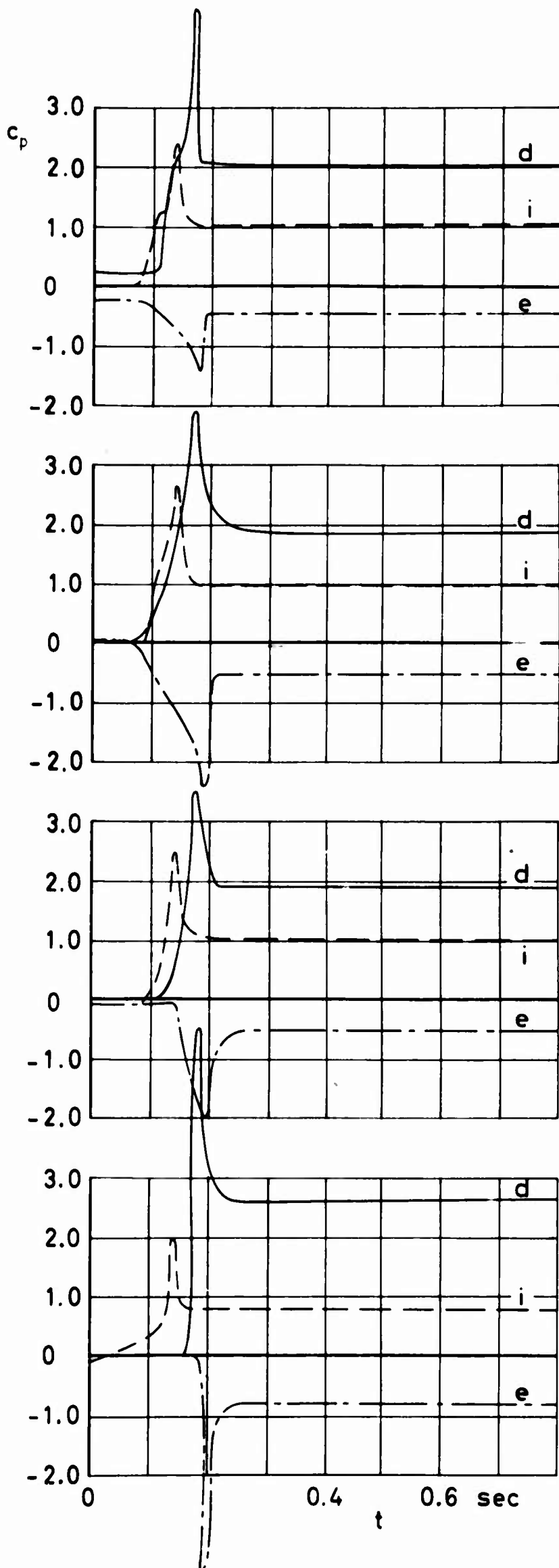


No. 216 p_e

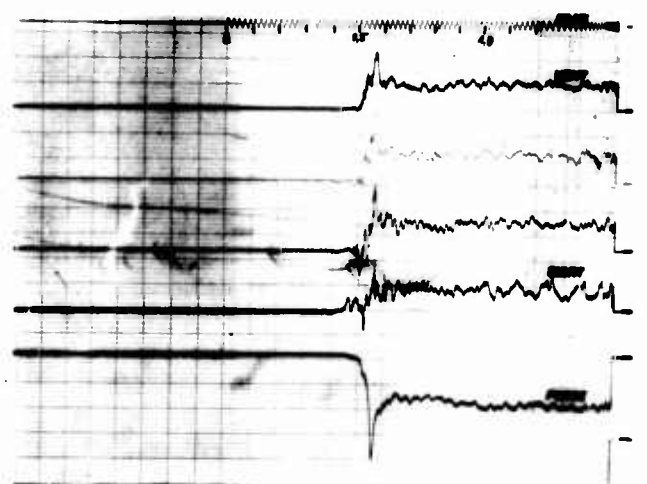
Figure 89 c_p versus time for differential, internal and external pressure

$v_0 = 100 \text{ ft/sec}$

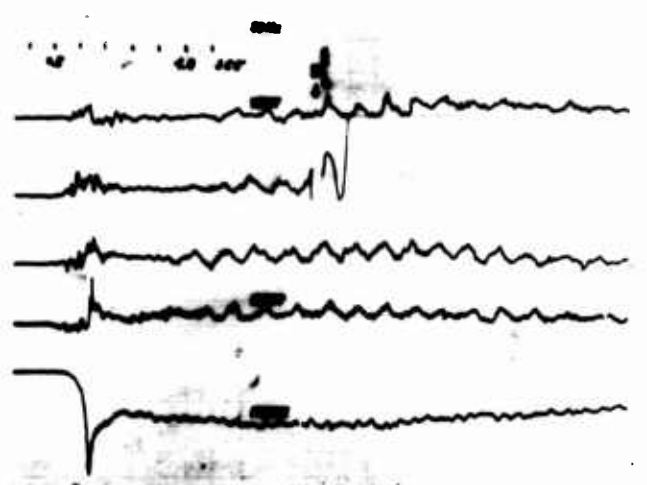
Type: Circular Flat



No.187 p_d



No.203 p_i

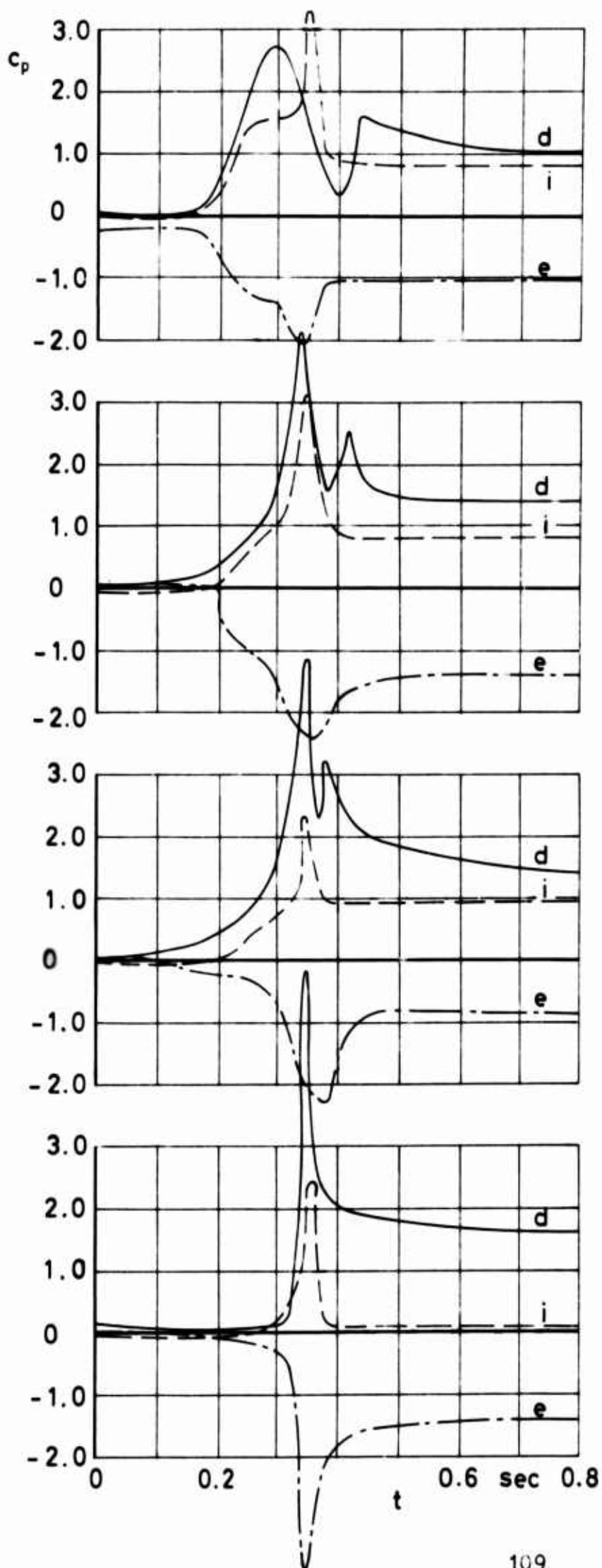


No.218 p_e

Figure 90 c_p versus time for
differential, internal and
external pressure

$v_0 = 130 \text{ ft/sec}$

Type: Circular Flat



No.139 p_d differential pressure

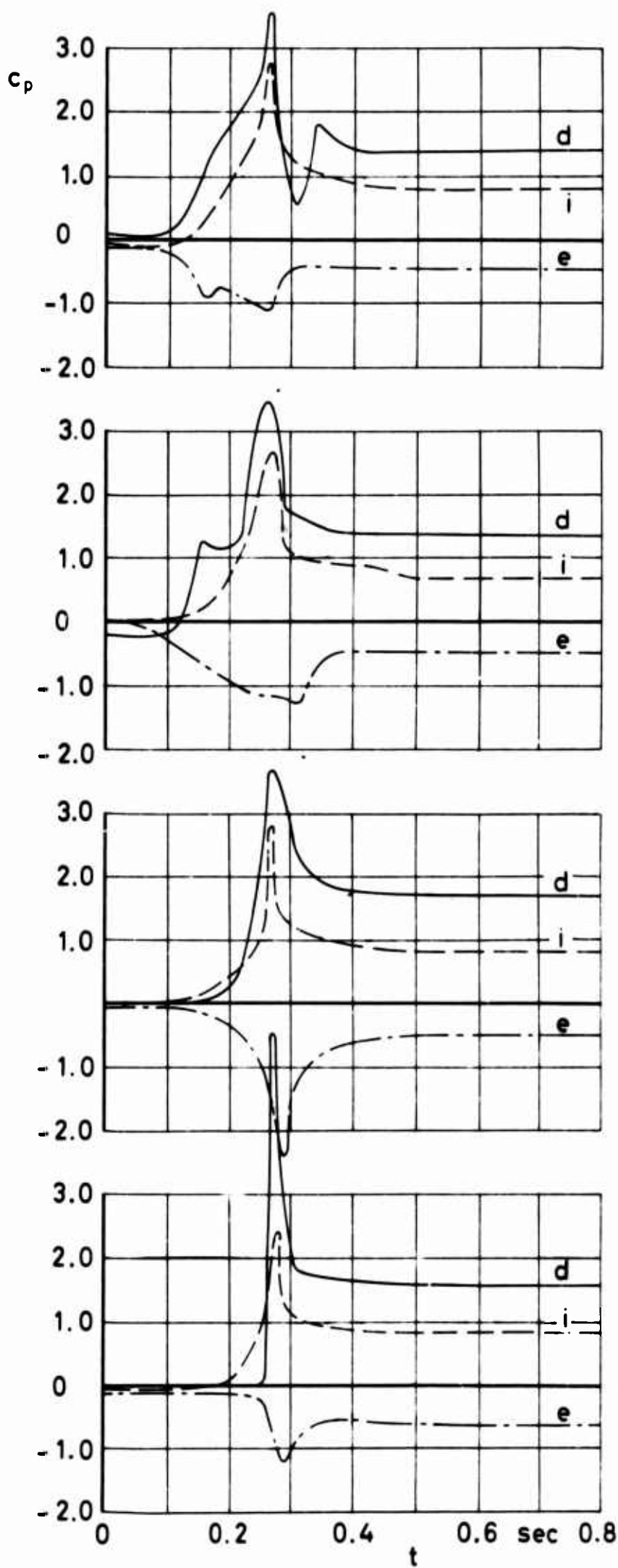
No.157 p_i internal pressure

No.221 p_e external pressure

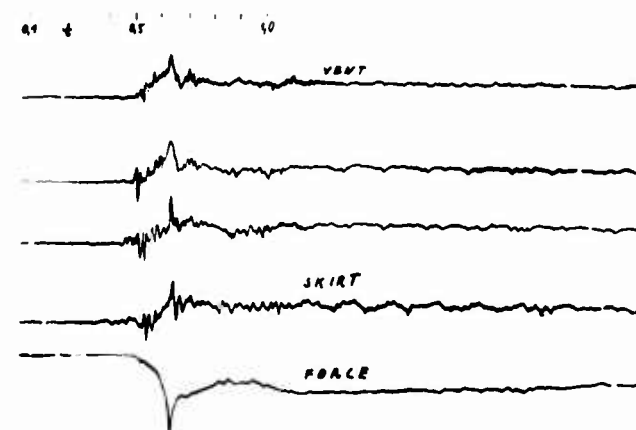
Figure 91 c_p versus time for differential, internal and external pressure

$v_0 = 70$ ft/sec

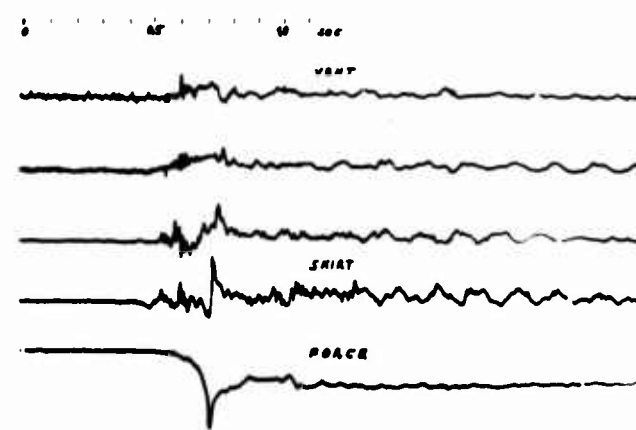
Type: Extended Skirt



No.144 p_d



No.160 p_i

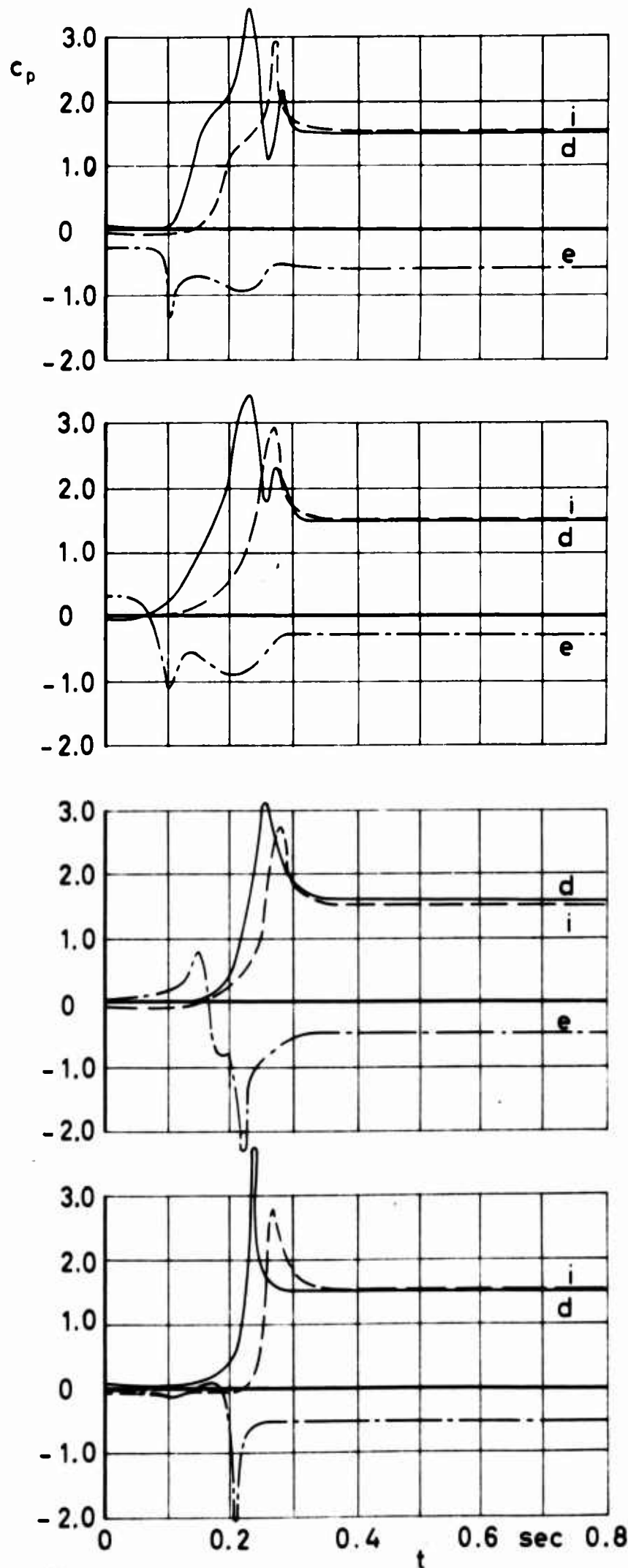


No.226 p_e

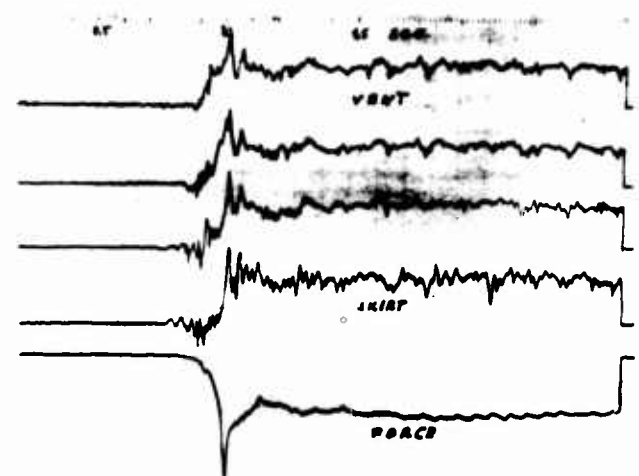
Figure 92 c_p versus time for differential, internal and external pressure

$v_0 = 100$ ft/sec

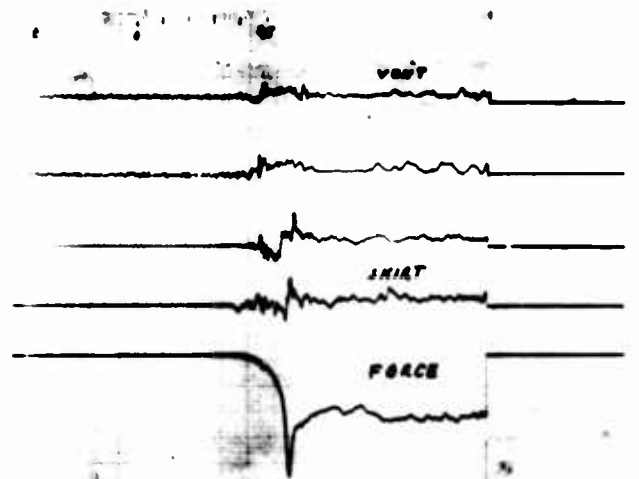
Type: Extended Skirt



No.148 p_d



No.163 p_i

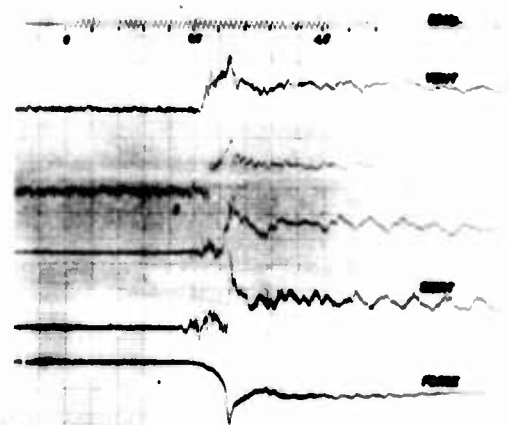
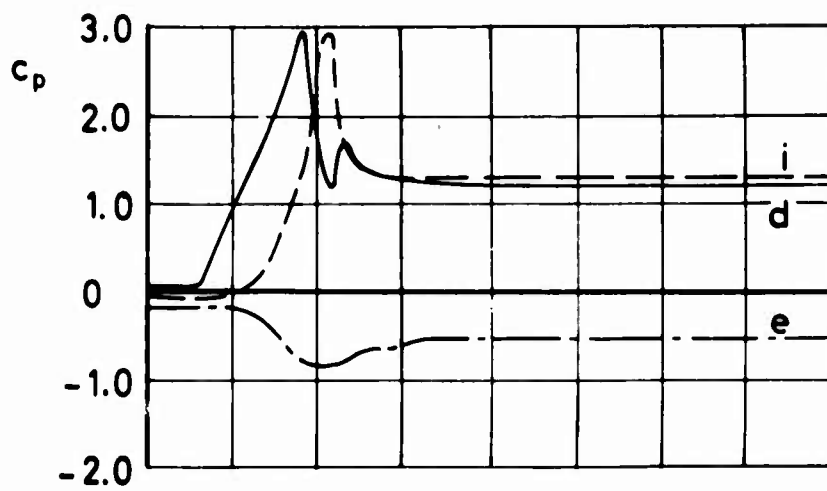


No.231 p_e

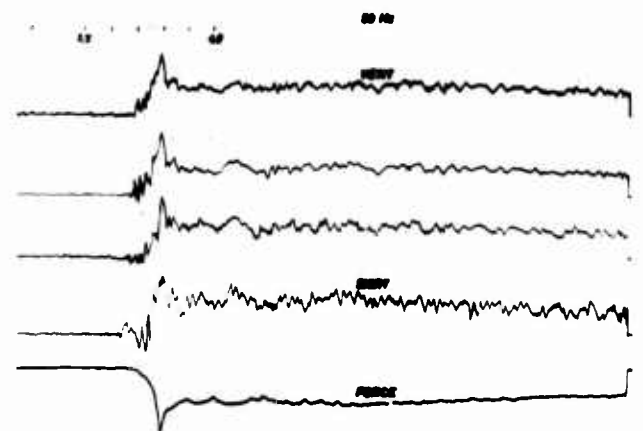
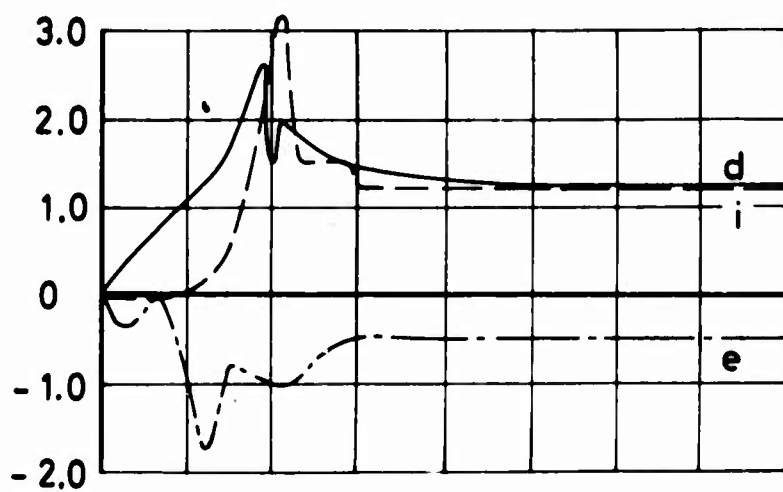
Figure 93 c_p versus time
differential, internal and
external pressure

$v_0=130$ ft/sec

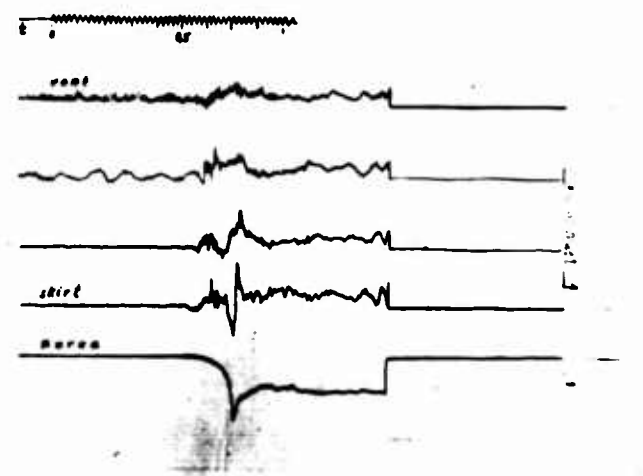
Type: Extended Skirt



No. 153 p_d



No. 166 p_i



No. 235 p_e

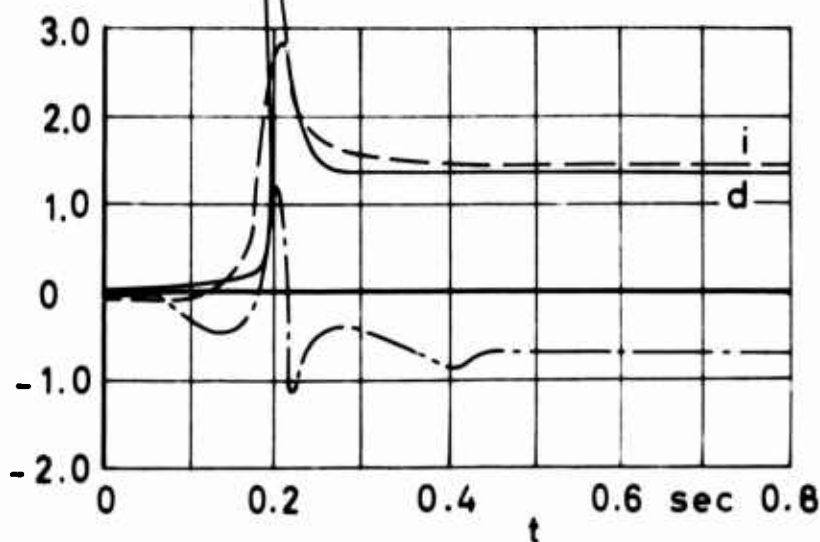
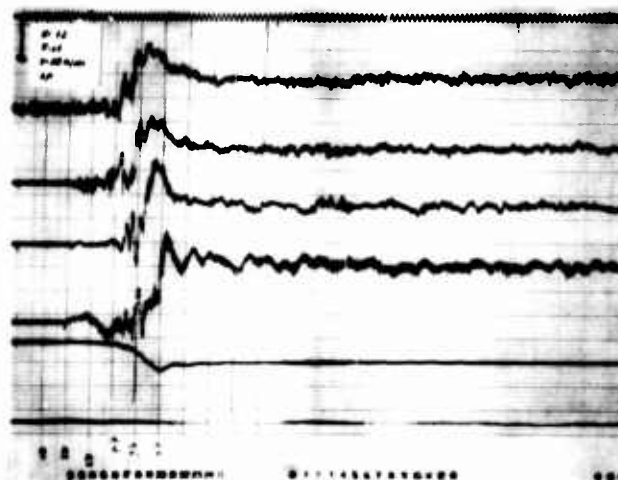
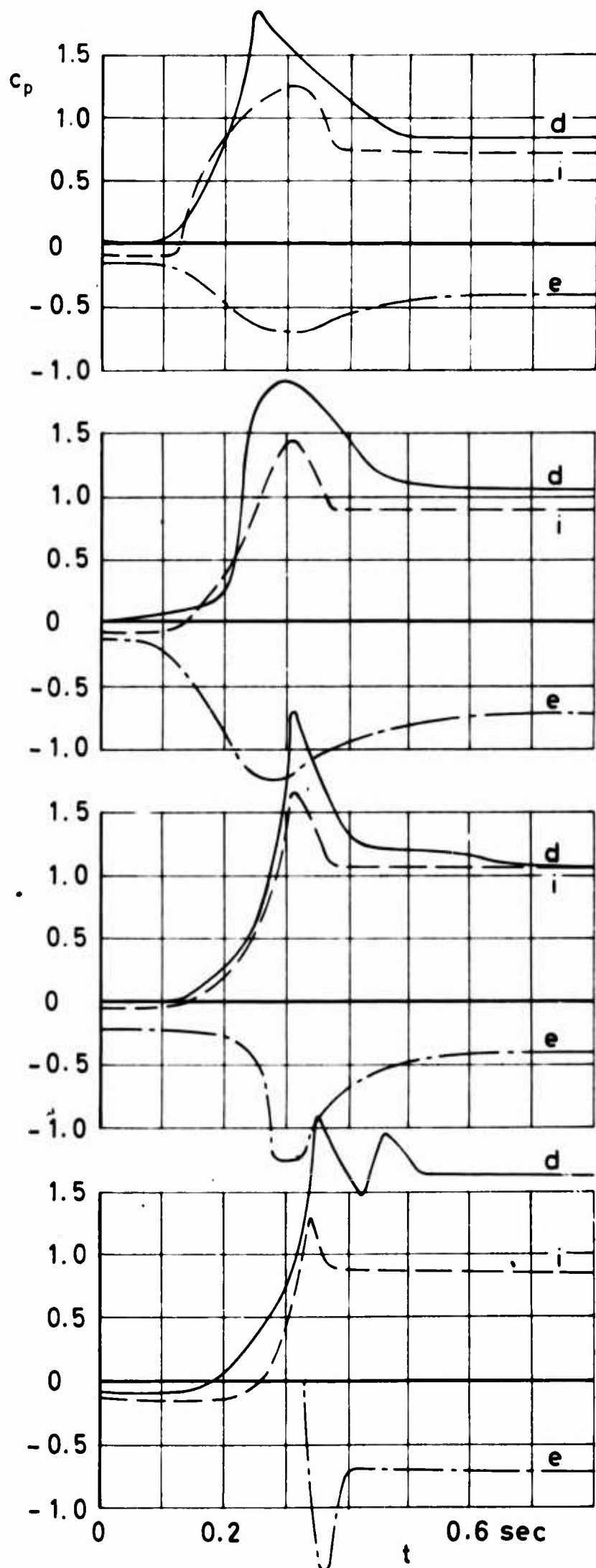


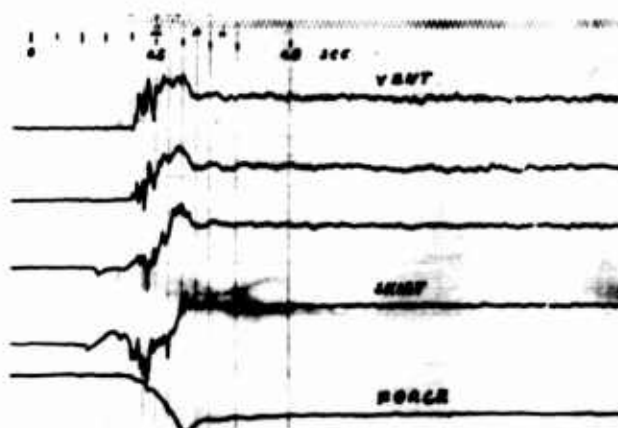
Figure 94 c_p versus time for differential, internal and external pressure

$v_0 = 160$ ft/sec

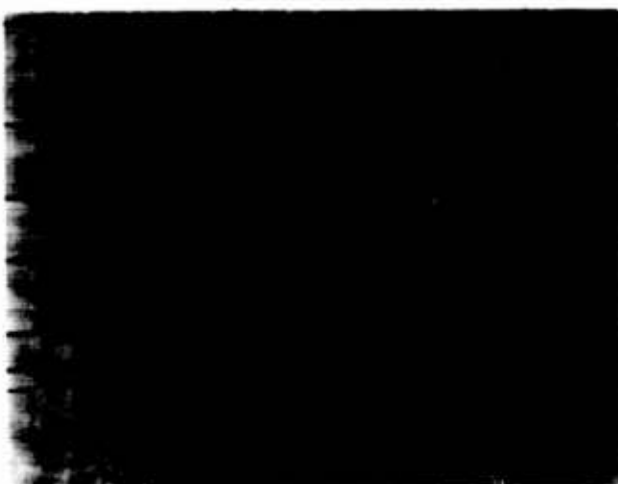
Type: Extended Skirt



No. 72 p_d differential pressure



No. 101 p_i internal pressure

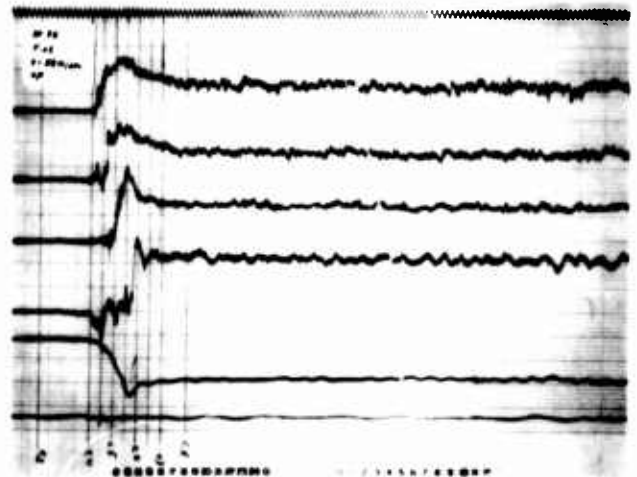
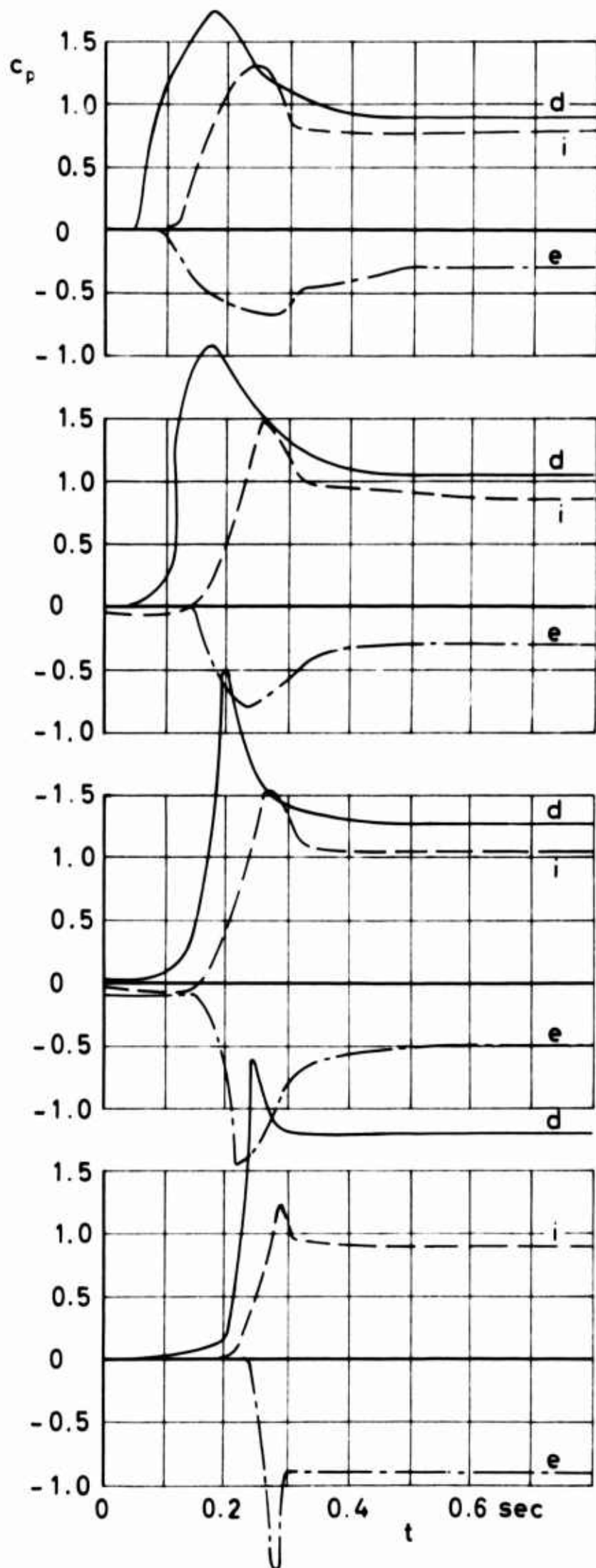


No. 104 p_e external pressure

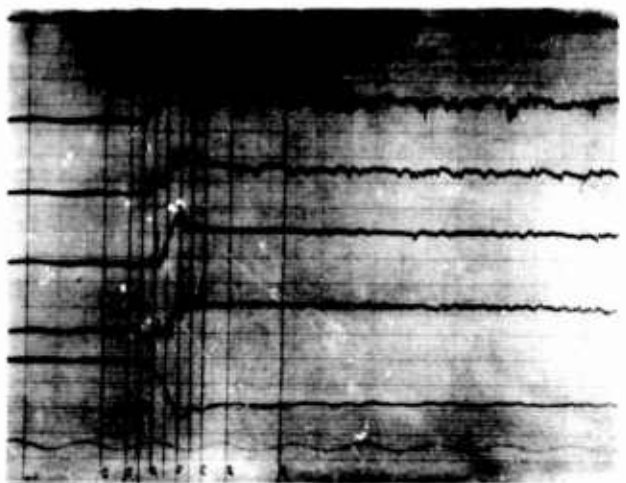
Figure 95 c_p versus time for differential, internal and external pressure

$v_0 = 70 \text{ ft/sec}$

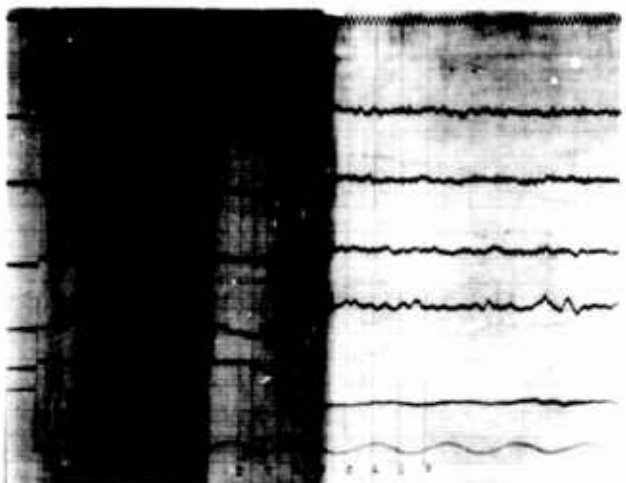
Type: Fist



No. 76 p_d



No. 97 p_i

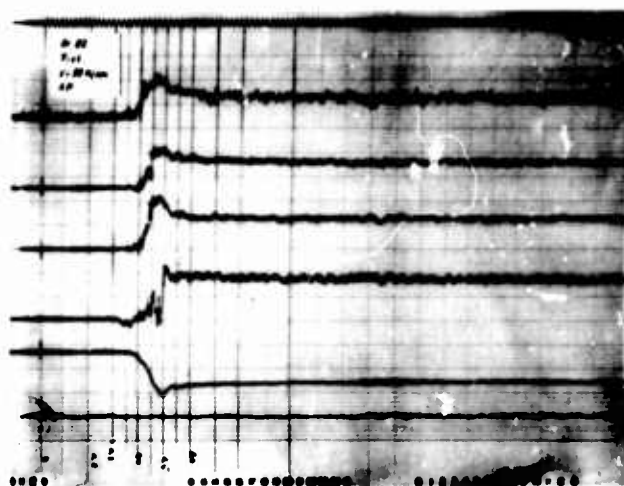
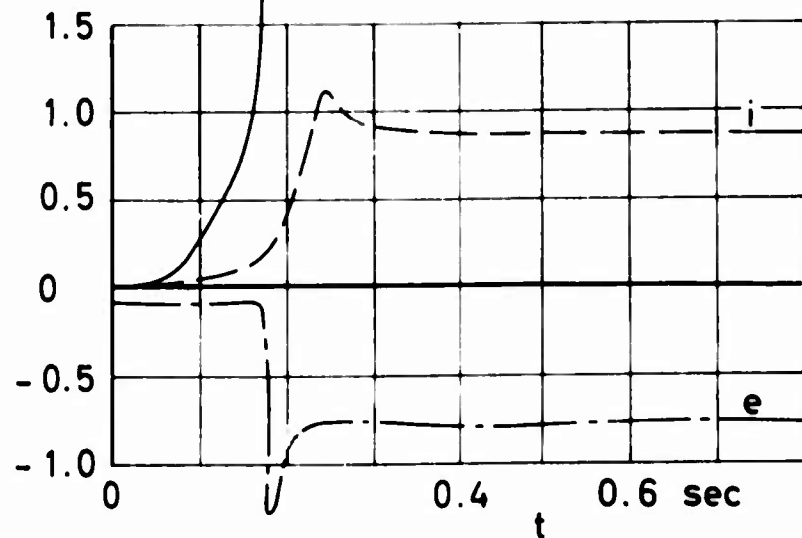
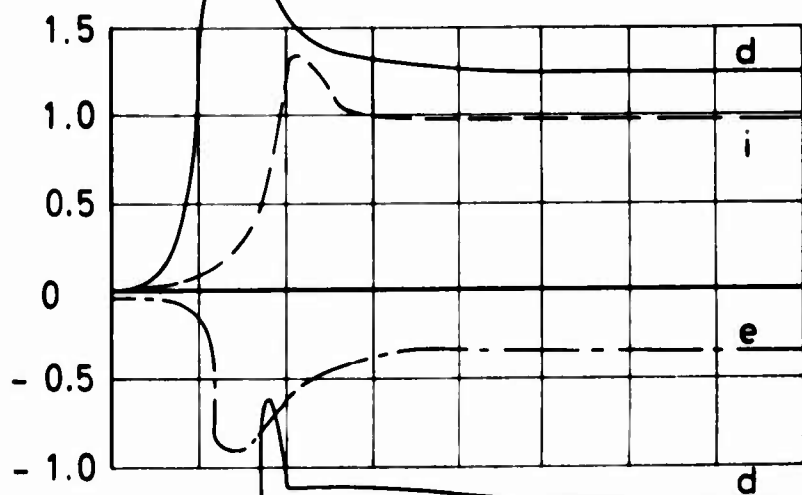
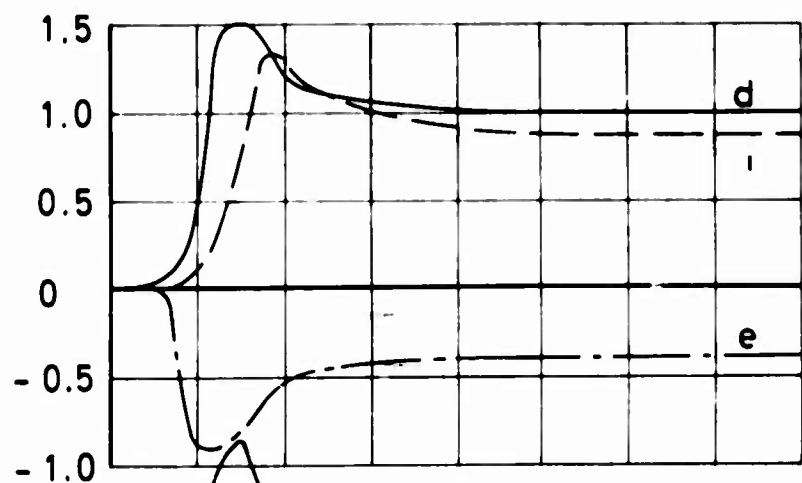
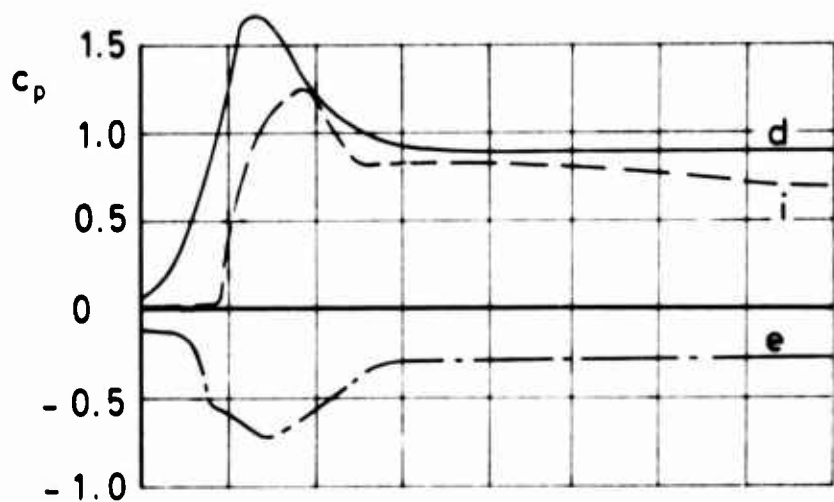


No. 110 p_e

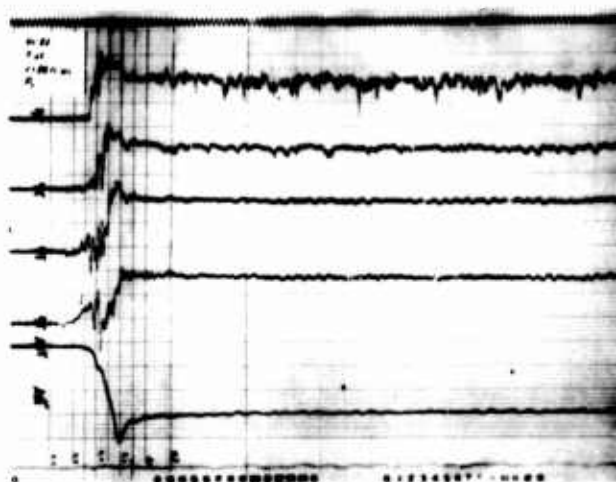
Figure 96 c_p versus time for differential, internal and external pressure

$v_0 = 100$ ft/sec

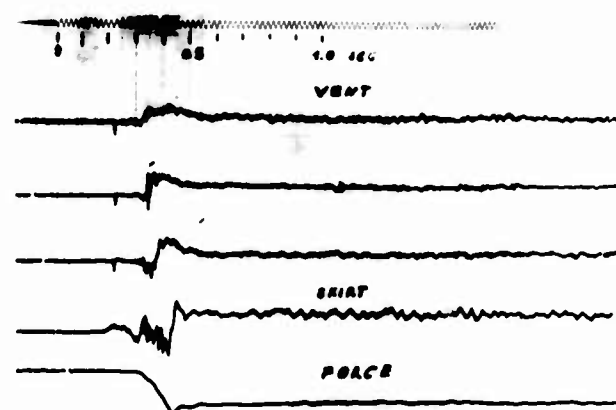
Type: Fist



No. 82 p_d



No. 92 p_i

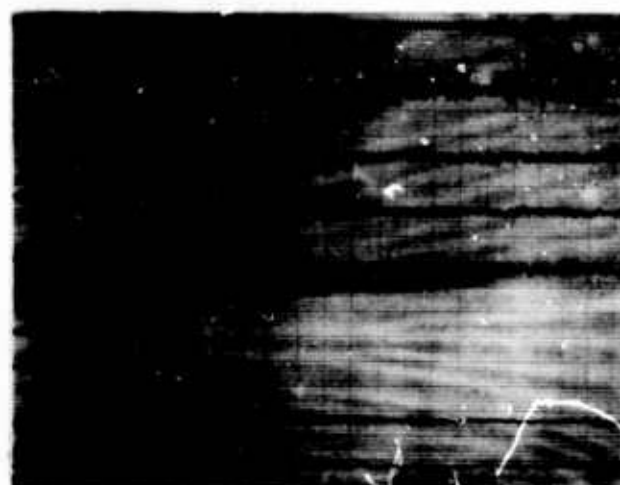
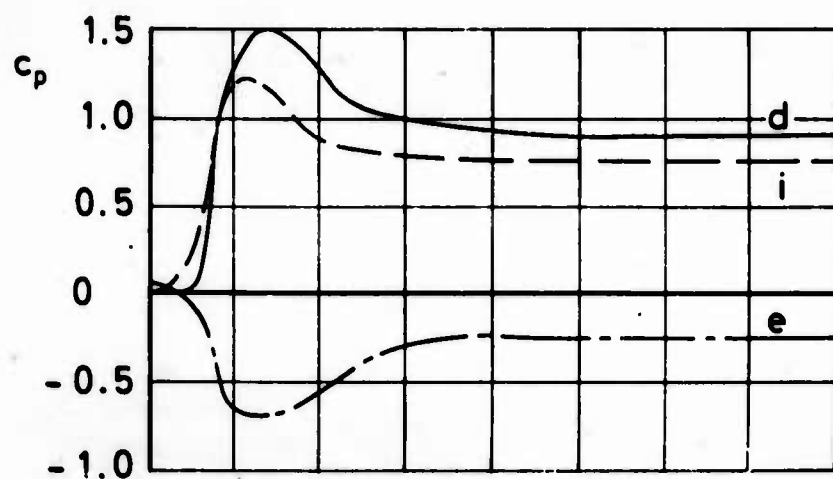


No. 117 p_e

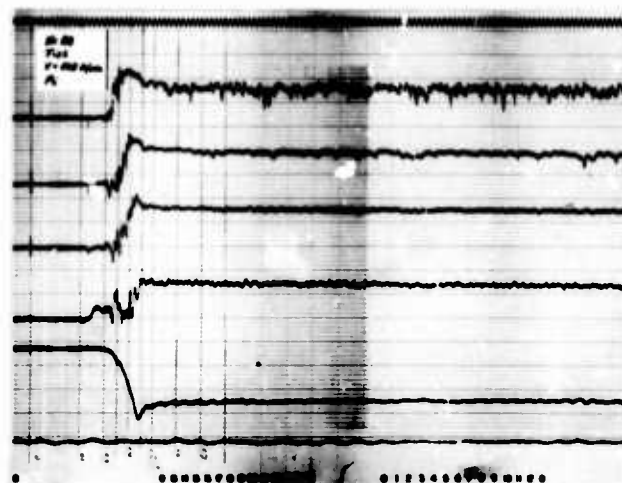
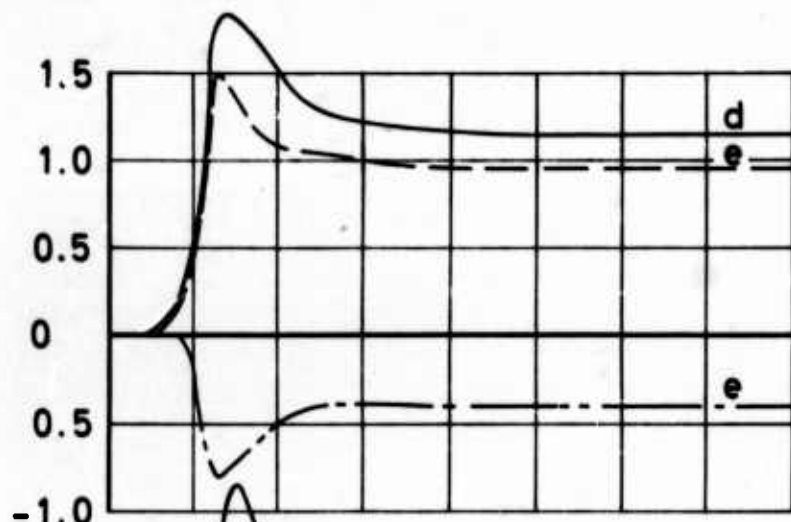
Figure 97 c_p versus time for differential, internal and external pressure

$v_0 = 130 \text{ ft/sec}$

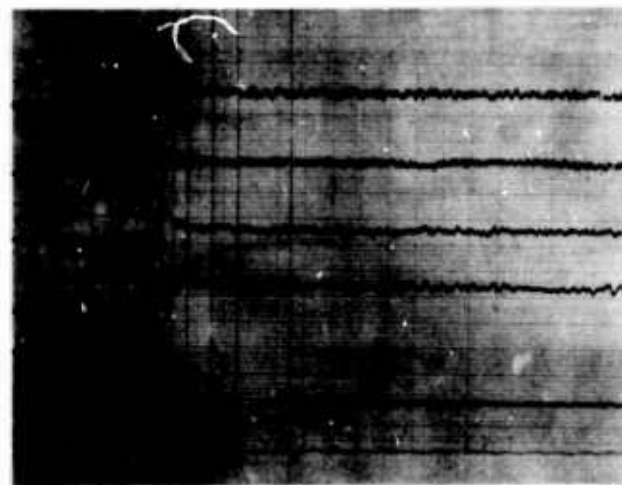
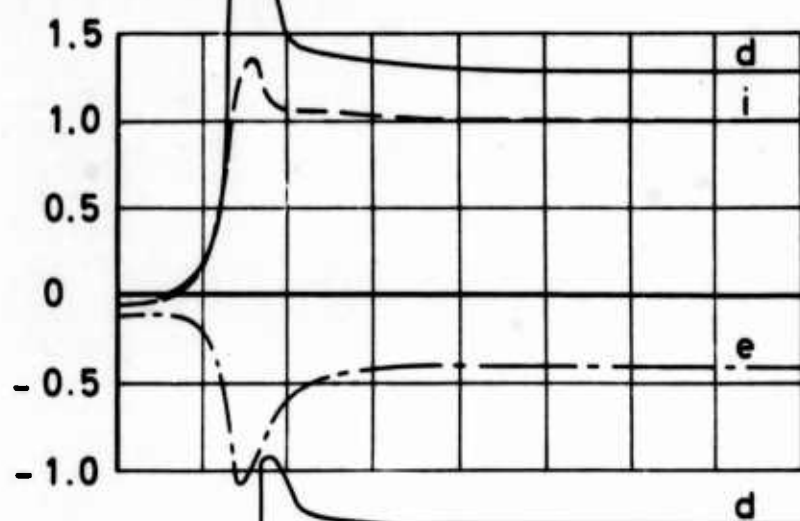
Type: Fist



No. 86 p_d



No. 88 p_i



No. 119 p_e

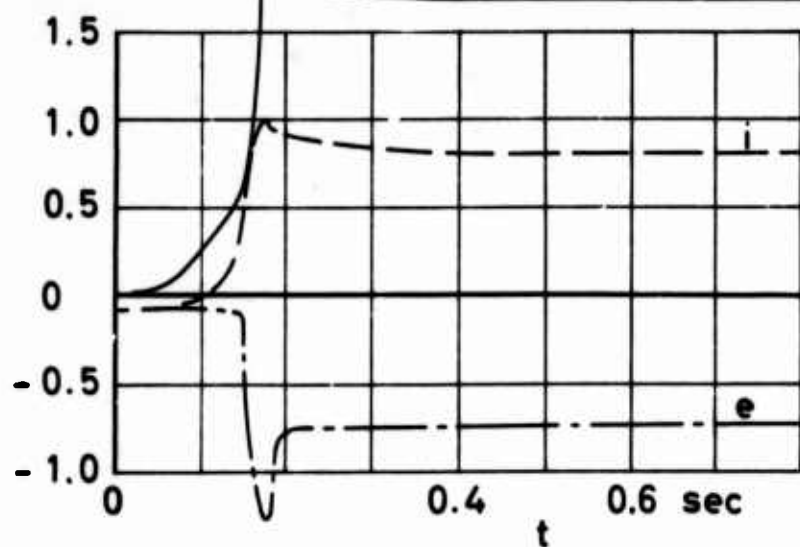
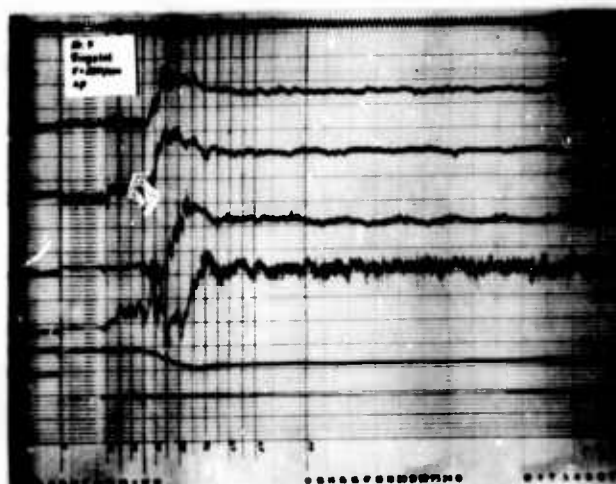
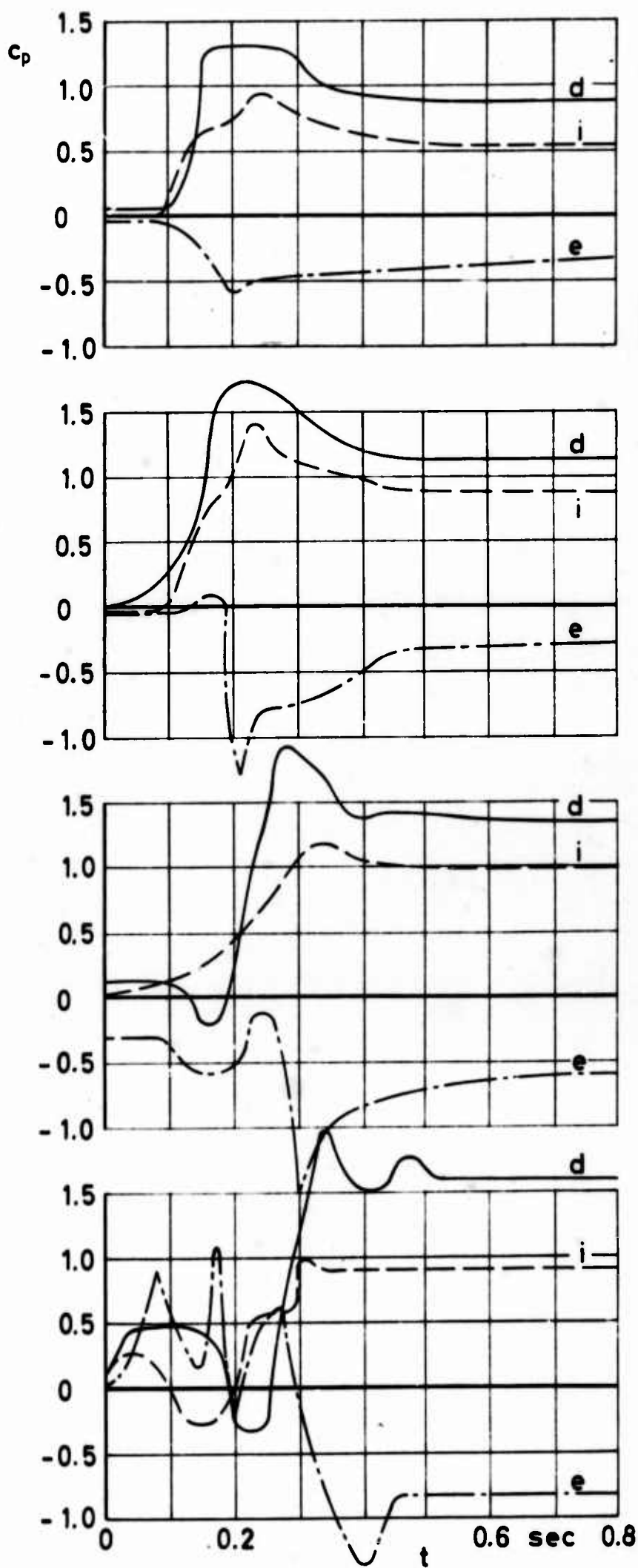


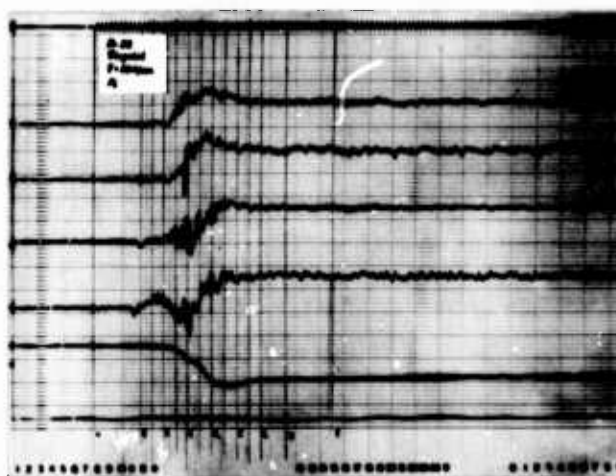
Figure 98 c_p versus time for
differential, internal and
external pressure

$v_0 = 160 \text{ ft/sec}$

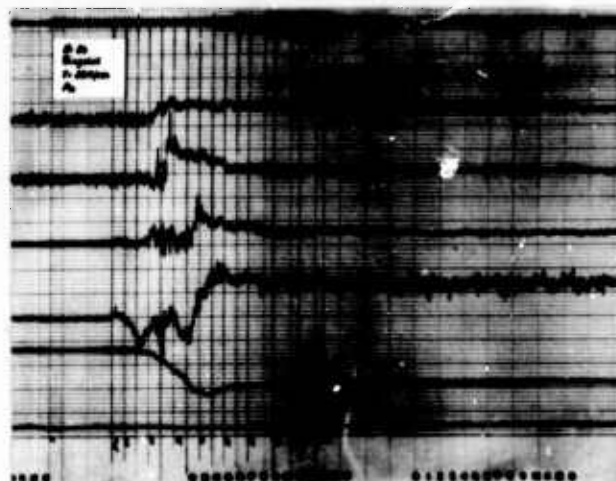
Type: Fist



No. 7 p_d differential pressure



No. 22 p_i internal pressure

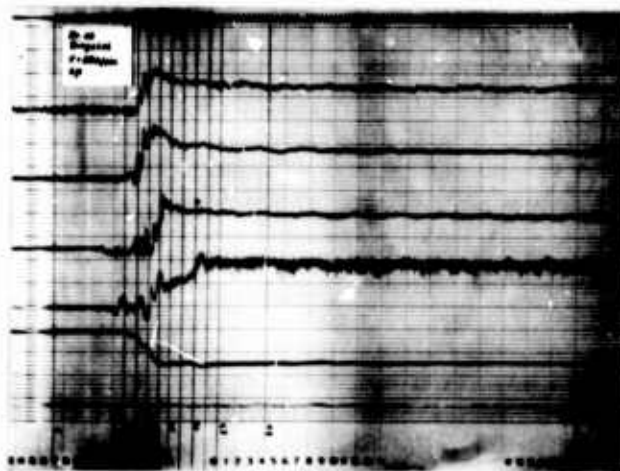
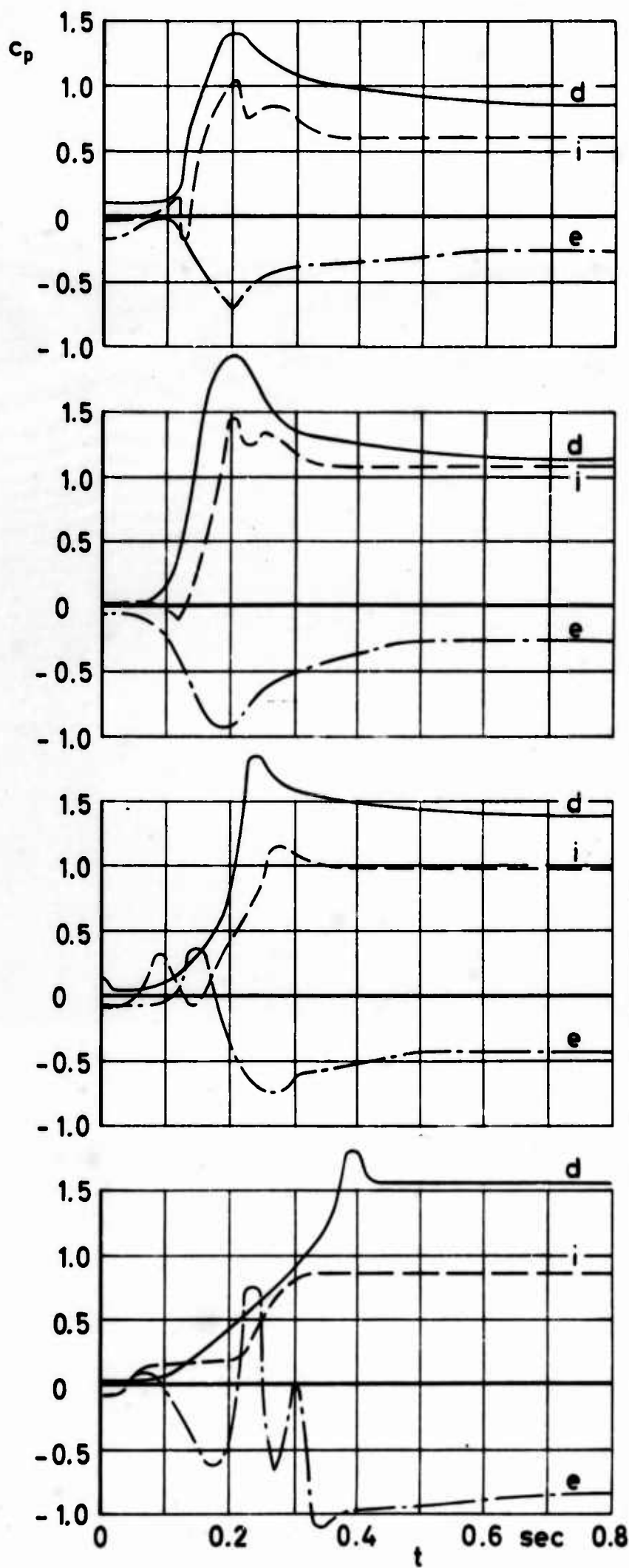


No. 34 p_e external pressure

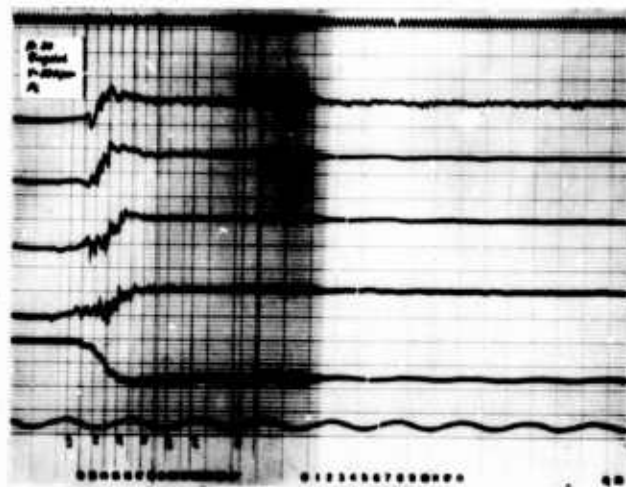
Figure 99 c_p versus time for differential, internal and external pressure

$v_0 = 70$ ft/sec

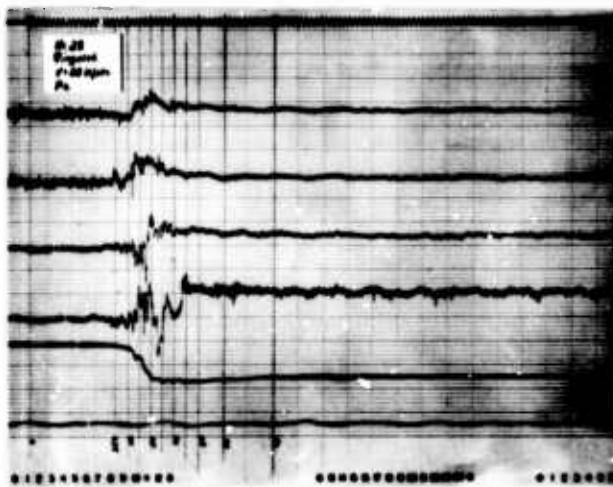
Type: Ringslot



No. 10 p_d



No. 30 p_i

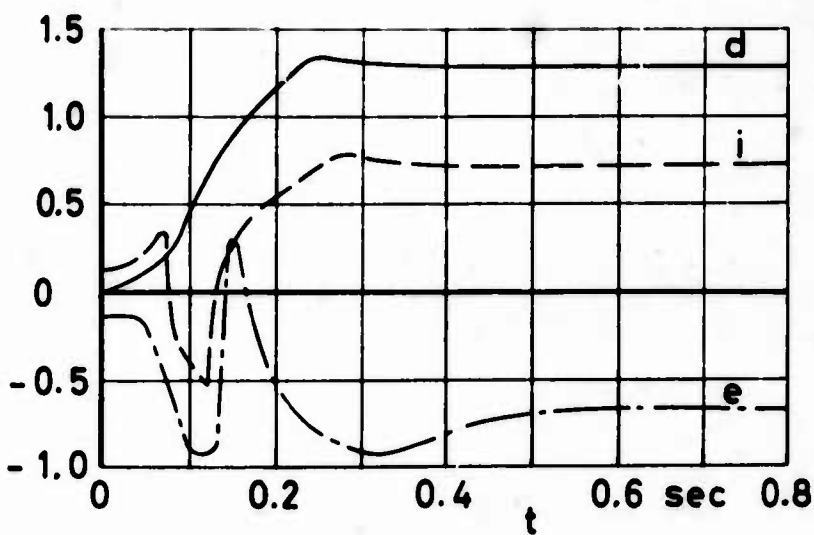
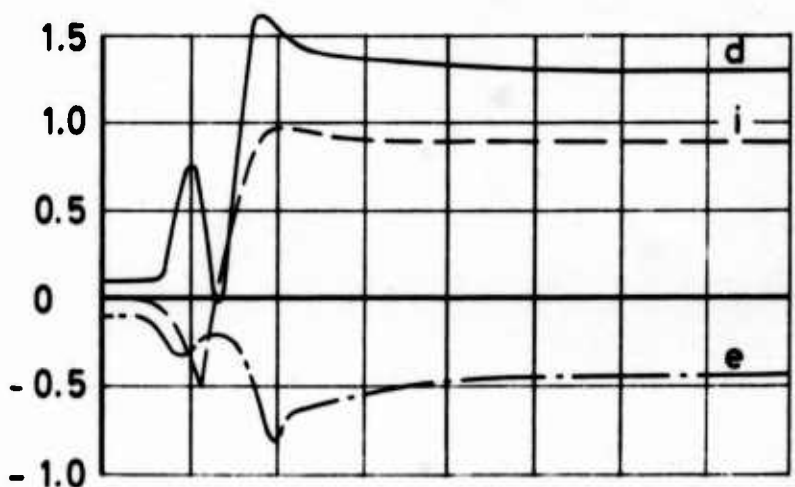
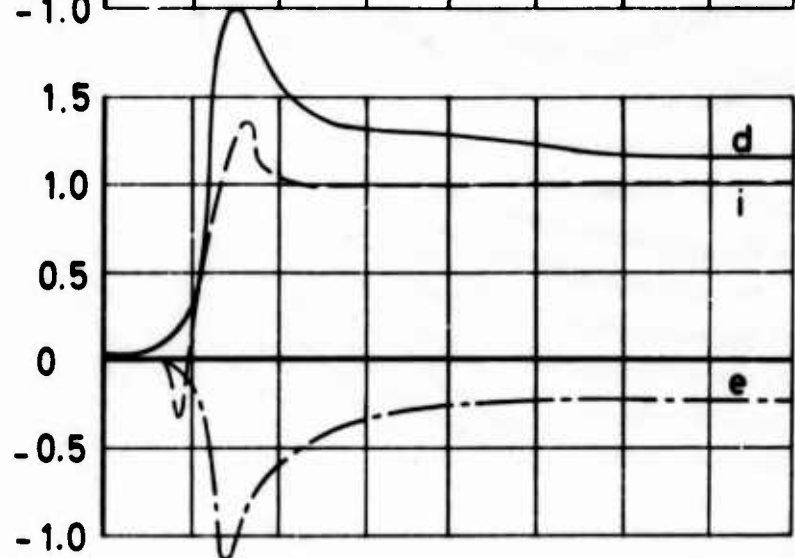
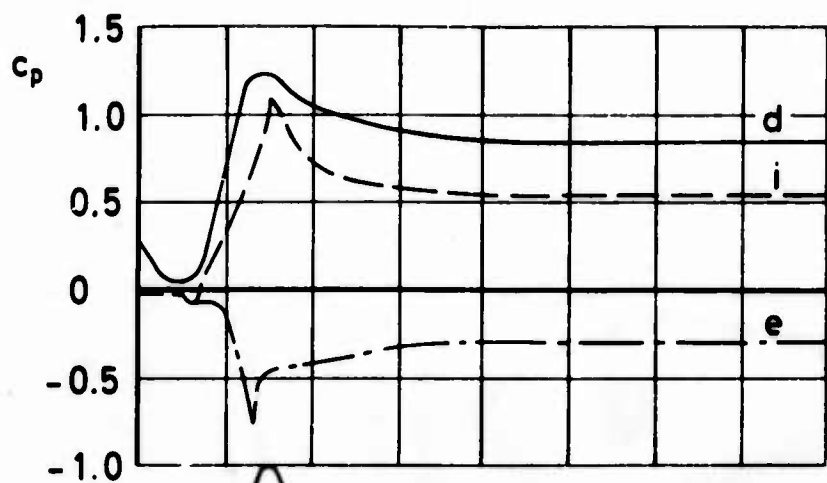


No. 39 p_e

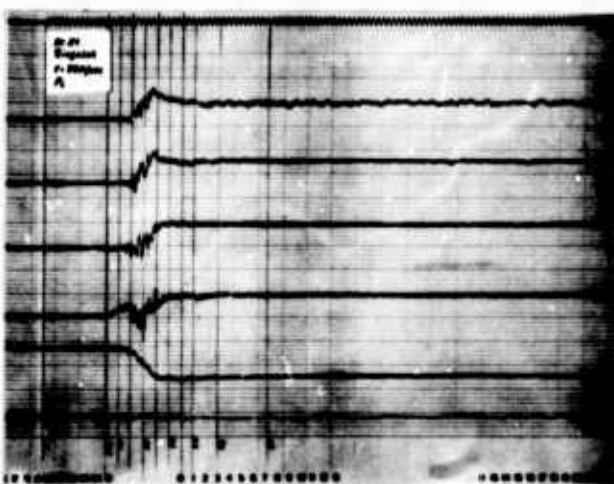
Figure 100 c_p versus time for differential, internal and external pressure

$v_0 = 100$ ft/sec

Type: Ringslot



No. 14 p_d



No. 51 p_i

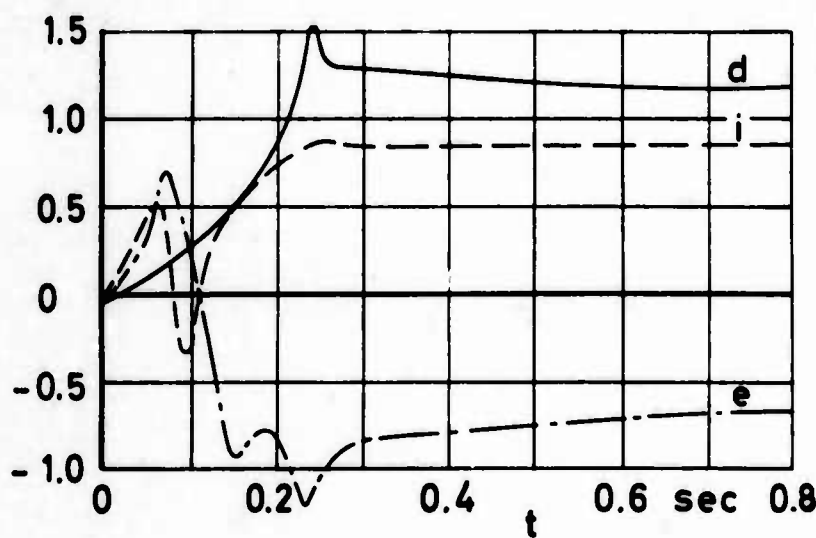
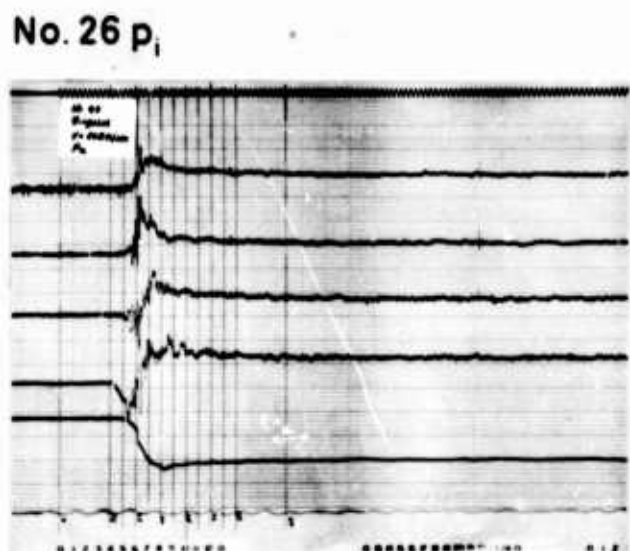
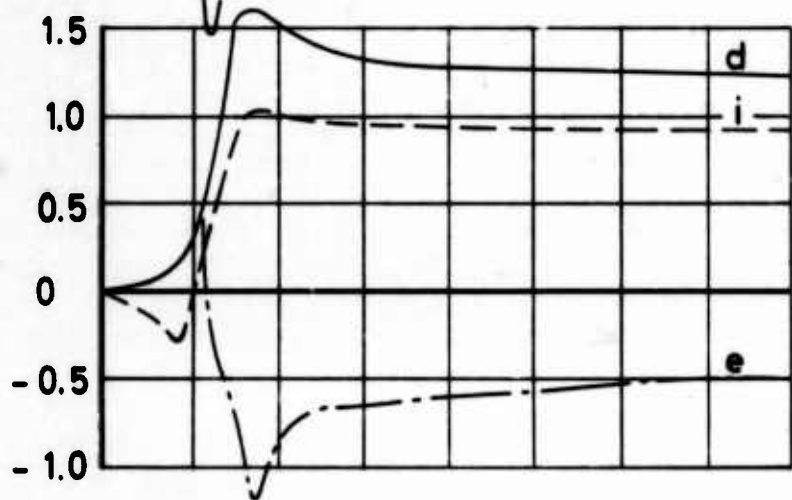
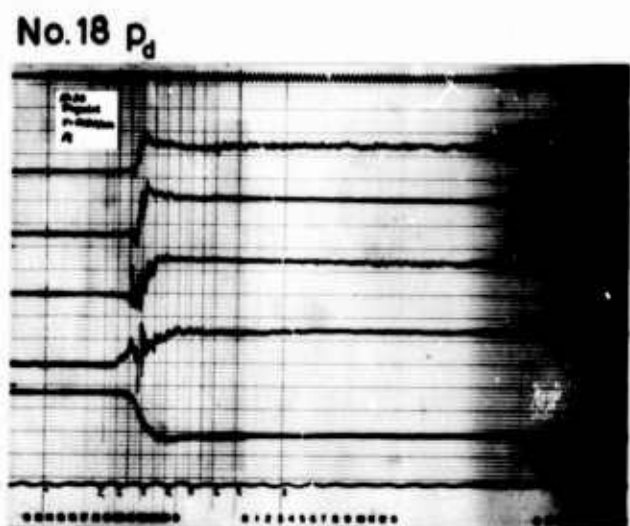
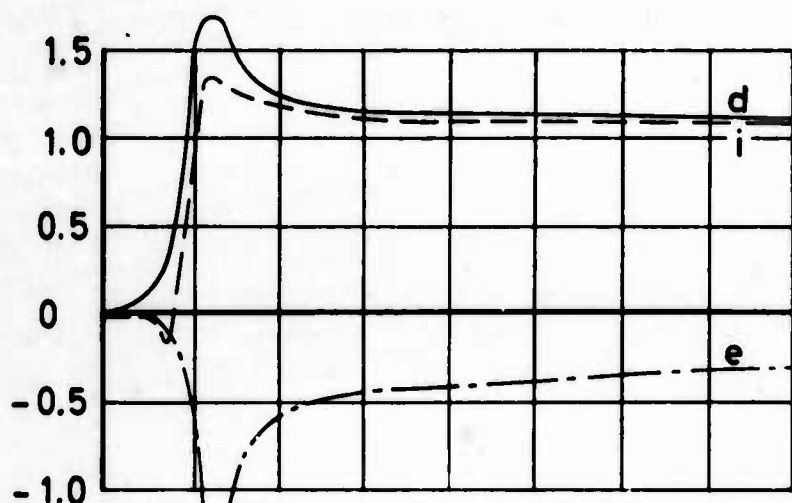
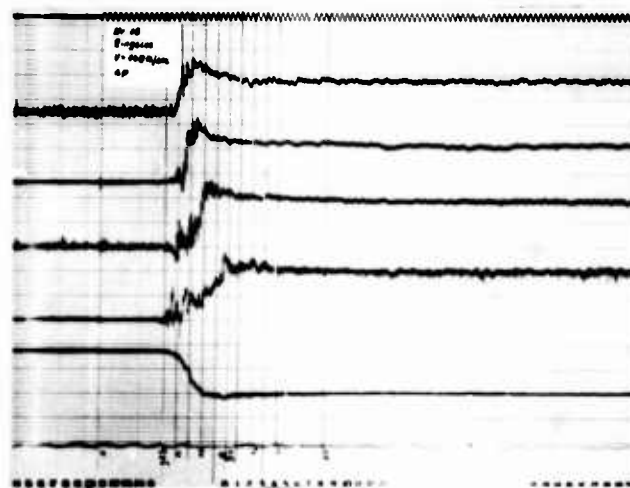
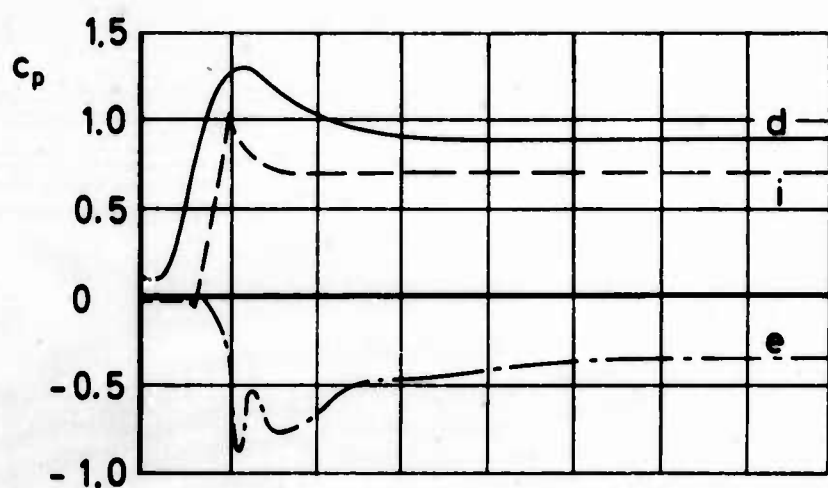


No. 42 p_e

Figure 101 c_p versus time for differential, internal and external pressure

$v_0 = 130$ ft/sec

Type: Ringslot



No. 47 p_e

Figure 102 c_p versus time for
differential, internal and
external pressure

$v_0 = 160 \text{ ft/sec}$

Type: Ringslot

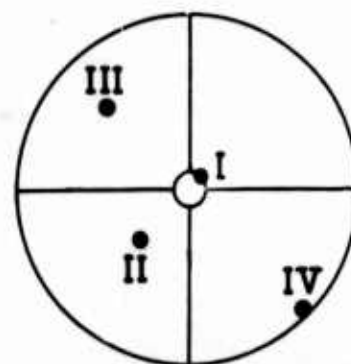
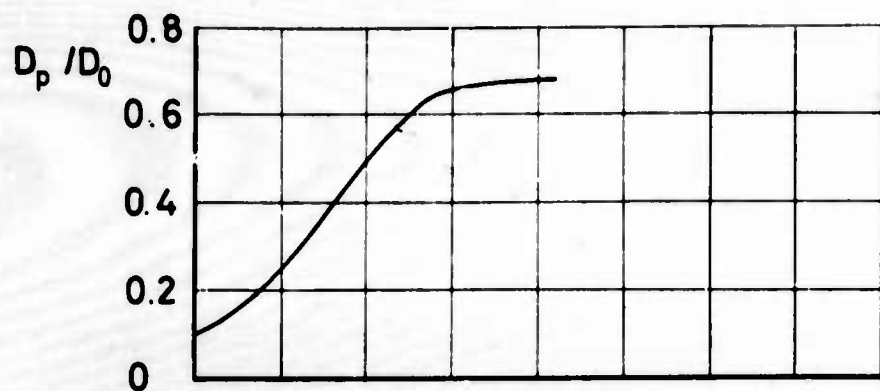
APPENDIX III

GORE CENTER LINE PRESSURE MEASUREMENTS

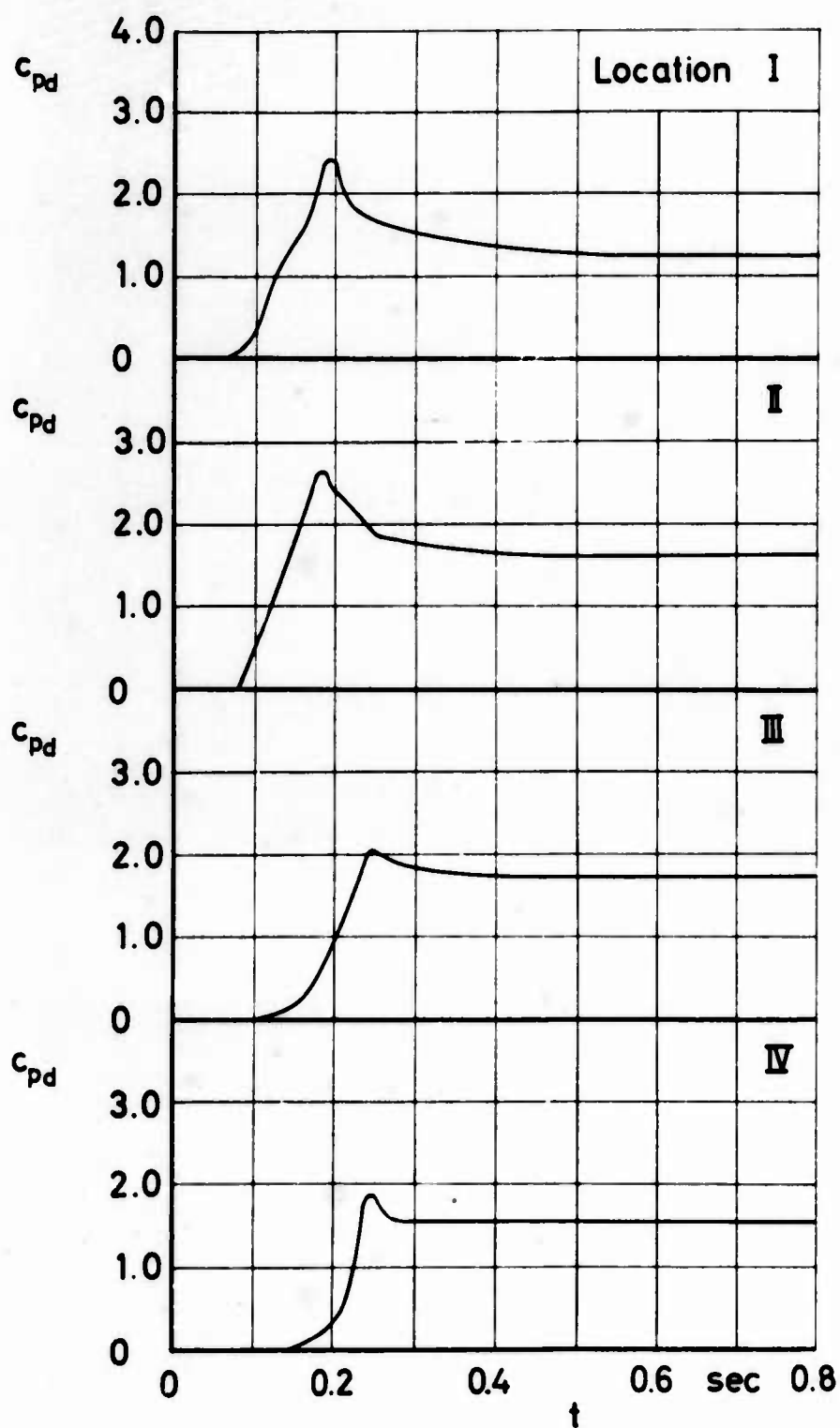
Additional wind tunnel tests were conducted to determine the magnitude and time relationship of local pressures at locations other than along the canopy cord centerline. During these tests, the four pressure transducers were located on the gore center line, spaced 90 degrees apart over the surface of the canopy, and arranged in a similar manner as for the previous tests.

Analyzing all data obtained, no significant difference in either the magnitude or time relationship of the pressures as compared to the measurements along the cord centerline were detected.

A typical example of the pressure data obtained during this test series is presented in Figures 103 thru 105. These graphs show the relationship between the differential pressure coefficient, c_{pd} , and time for each of the four locations on a ringslot type canopy deployed at a free stream velocity of 100 ft/sec.



Location of pressure transducers on gore center line

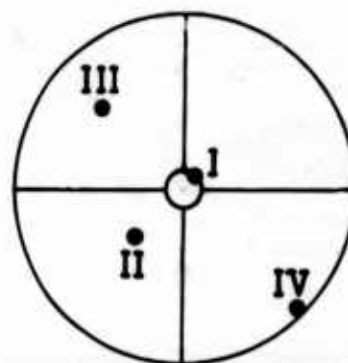
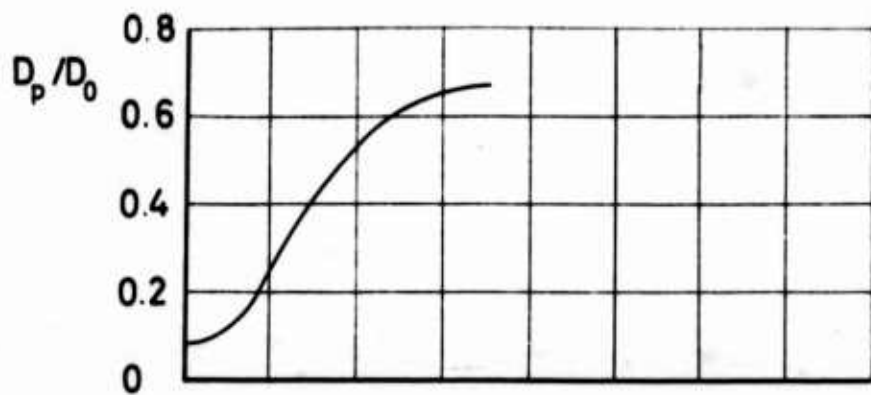


Ringslot

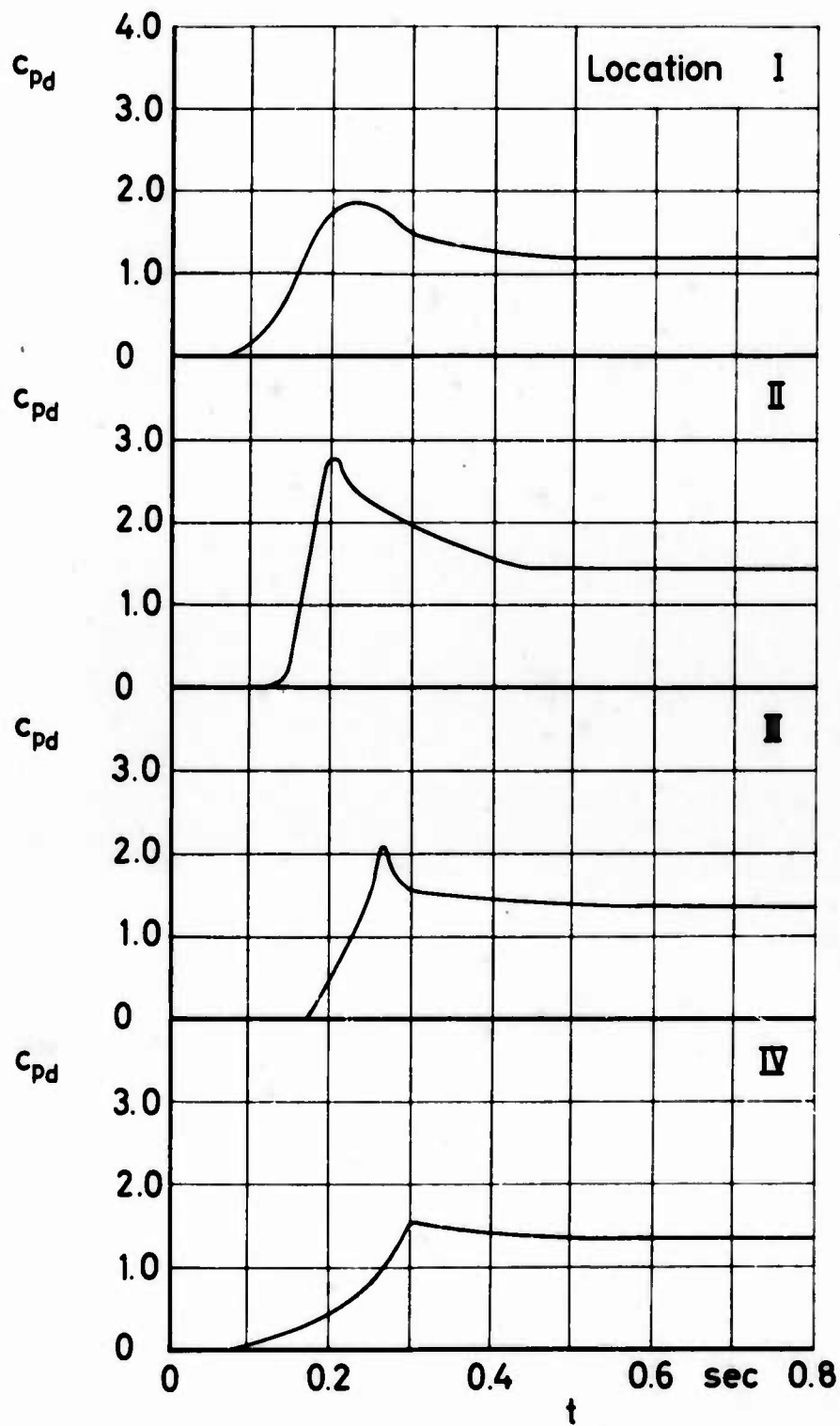
Figure 103 c_{pd} and filling versus time

$v_0 = 100$ ft/sec

Run No. 173



Location of pressure transducers on gore center line

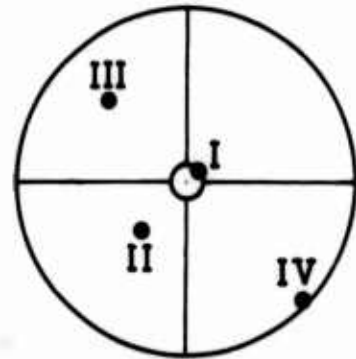
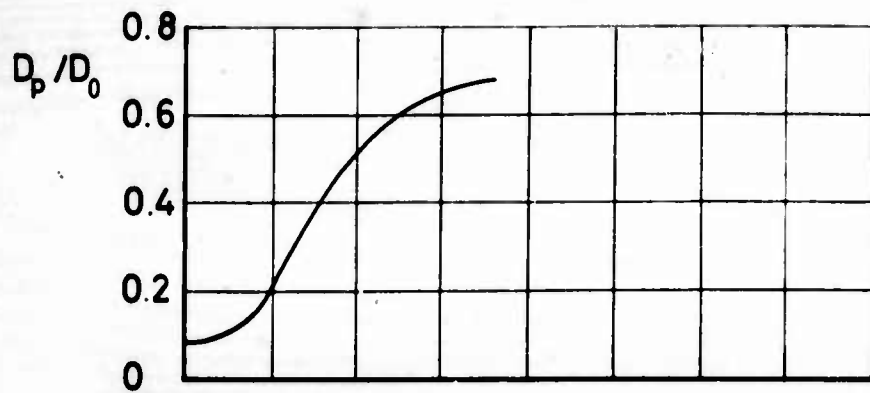


Ringslot

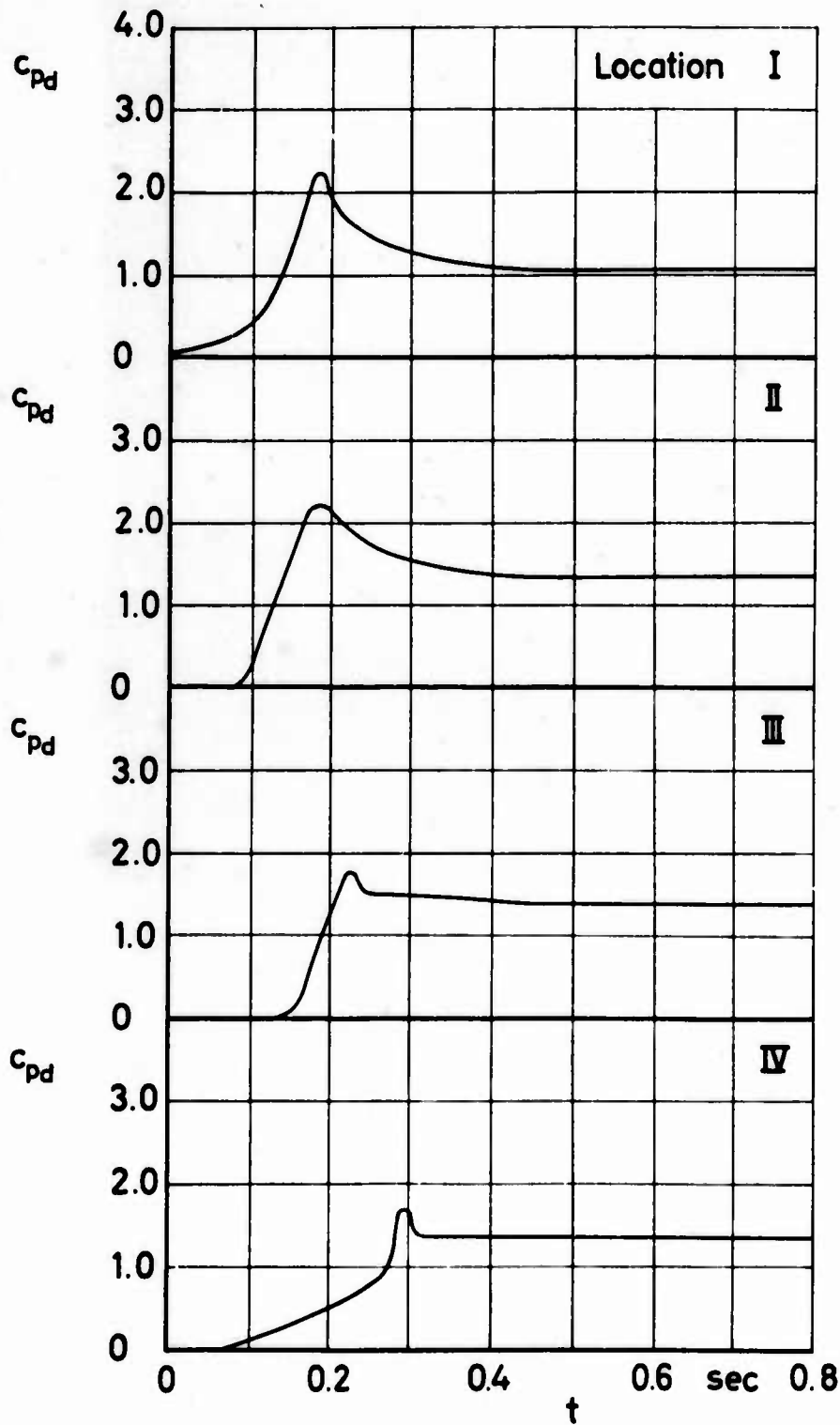
Figure 104 c_{pD} and filling versus time

$v_0 = 100 \text{ ft/sec}$

Run No. 174



Location of pressure transducers on gore center line



Ringslot

Figure 105 c_{pd} and filling versus time

$v_0 = 100 \text{ ft/sec}$

Run No. 175